The Build up of Stars and Dust in Nearby Galaxies

Simon Paul Schofield

A Thesis submitted to Cardiff University
for the degree of Doctor of Philosophy

November 2016

Author: Simon Paul Schofield
Title: The Build up of Stars and Dust in Nearby Galaxies
Date of submission: November 2016

Permission is granted to Cardiff University to circulate and to have copied for non-commercial purposes, at its discretion, the above title upon the request of individuals or institutions. The author reserves other publication rights, and neither the thesis nor extensive extracts from it may be printed or otherwise reproduced without the author's written permission.

Copyright © 2017 by Simon Paul Schofield

Declaration

This work has not been submitted in substance for any other degree or award at this or any other university or place of learning, nor is being submitted concurrently in candidature for any degree or other award.

Signed: _____ (candidate) **Date:** _____

Statement 1

This thesis is being submitted in the partial fulfilment of the requirements for the degree of PhD.

Signed: _____ (candidate) **Date:** _____

Statement 2

This thesis is the result of my own independent work/investigation, except where otherwise stated, and the thesis has not been edited by a third party beyond what is permitted by Cardiff University's Policy on the Use of Third Party Editors by Research Degree Students. Other sources are acknowledged by explicit references. The view expressed are my own.

Signed: _____ (candidate) **Date:** _____

Statement 3

I hereby give consent for my thesis, if accepted, to be available online in the University's Open Access repository and for inter-library loan, and for the title and summary to be made available to outside organisations.

Signed: _____ (candidate) **Date:** _____

Statement 4: Previously Approved Bar on Access

I hereby give consent for my thesis, if accepted, to be available online in the University's Open Access repository and for inter-library loans **after expiry of a bar on access previously approved by the Academic Standards & Quality Committee**

Signed: _____ (candidate) **Date:** _____

'Come in! Come in! And know me better man!'

Charles Dickens, A Christmas Carol

Abstract

In this thesis I took a combined sample of dust-selected galaxies (from Clark et al. 2015) and HI-selected galaxies (from De Vis et al. 2016). The dust selected sample contains a large fraction of intriguing galaxies dubbed the 'Blue And Dusty Gas Rich Sources' (BADGRS), while the HI selected sources revealed another population of blue and gas rich systems which are instead dust-poor. I investigated whether the unique properties of these galaxies could be explained by variations in their recent star formation activity. I showed that the BADGRS are younger, and have typically experienced more recent bursts of star formation compared to the non-BADGRS. Splitting the sample into dust-rich and dust-poor sources showed that both sub-populations are of similar age, although the dust-rich sources have experienced a burst of star formation more recently.

I took the chemical evolution model of Morgan & Edmunds (2003), used more recently used in Rowlands et al. (2014), and updated many of the functions and libraries in line with recent literature. I then produced a suite of models to investigate the dust and metal properties of 425 Herschel sources. These models showed (i) a delayed star formation history is required to match the observed star formation rates; (ii) inflows and outflows are required to explain the observed metallicities at low gas fractions; (iii) a significantly reduced contribution of dust from supernovae is necessary to explain the dust poor sources with high gas fractions. We also showed the dust-to-metal ratio is not definitively constant in all galaxies, and that there is evidence for a decrease in the dust-to-metals ratio towards lower metallicity. This thesis proposes a model in which the dust, gas, metals and stars can be modelled in a consistent and coherent manner, and gains insight into the dust-to-gas evolution at early epochs.

Extended Summary

One of the main challenges for extragalactic astronomy is to understand how galaxies evolve from simple clouds of unenriched atomic gas into complex systems consisting of stars, dust, metals, and the different gas phases we observe today. This transformation is caused by the ongoing star formation in galaxies. The atomic gas cools and condenses into molecular clouds that then collapse and form new stars. During this process, the InterStellar Medium (ISM) is enriched by heavy elements that have been synthesised in stellar cores and expelled into the galactic environment at the end of the stars' lives. At the same time, interstellar dust is formed in the winds of evolved low to intermediate mass stars. One can learn about dust sources and sinks by comparing models of the build up of dust, gas and metals with the observed properties of galaxies.

In this thesis I first took a combined sample of dust-selected galaxies (from Clark et al. 2015) and HI-selected galaxies (from De Vis et al. 2016). Together these samples provide a complementary view of dust and gas in the local universe, compared to previously studied stellar mass or optically selected samples. The dust selected sample contains a large fraction of intriguing galaxies dubbed the 'Blue And Dusty Gas Rich Sources' (BADGRS), while the HI selected sources revealed another population of similarly blue and gas rich systems that are dust poor compared to the BADGRS. I investigated whether the unique properties of these galaxies could be explained by differences in their recent star formation activity. Individual star formation histories were derived from modelling the spectral energy distribution of the galaxies (using the model of da Cunha et al. 2008). I showed that the BADGRS have typically experienced more recent significant bursts of star formation (in the last ~ 0.9 Gyr) compared to the non-BADGRS (in the last ~ 1.9 Gyr). The BADGRS also appear younger, with a light weighted mean age of ~ 1.9 Gyr compared to the non-BADGRS ~ 5.3 Gyr. When splitting the sample into dust-rich and dust-poor sources,

I showed that both sub-populations are of similar age, although the dust-rich sources appear to have experienced a burst of star formation more recently ($\sim 0.6\,\mathrm{Gyr}$) than the dust-poor sources ($\sim 1.4\,\mathrm{Gyr}$). I also showed that the physical properties of this population of local galaxies are poorly represented in current SED fitting libraries, and suggested methods to resolve this issue. The optical spectra of both the BADGRS and the dust-rich population of galaxies also exhibit enhanced OIII and H_α emission lines, which principle component analysis shows are indicative of a recent starburst. This may suggest a link between bursts of star formation and a dust-rich galaxy.

Chemical evolution modelling can be used to investigate how the build up of dust and metals in galaxies relates to their star formation history. I took the model of Morgan & Edmunds (2003), which was more recently used in Rowlands et al. (2014), and updated many of the functions and libraries in line with recent literature. This included updating (i) the dust yield from high mass stars and (ii) the remnant mass equation, accounting for the fact that stars $> 40\,\mathrm{M}_\odot$ form a black hole at the end of their lifetime and only produce gas, dust and metals in the pre-supernova stage. I also identified and resolved two errors in the model which (i) prevented high mass stars contributing to metal mass at times $> 0.6\,\mathrm{Gyr}$ and (ii) lead to an underestimate of the dust production timescale in the ISM. The code was rewritten in python, and developed as an open source package for the community. I then explored the implications of these changes on the production of metals and dust in the model.

Combining samples of nearby galaxies with *Herschel* photometry provides us with an opportunity to discriminate between different dust sources in the earliest stages of galaxy evolution. Using the chemical evolution code developed in this thesis I produced a suite of models to investigate the dust and metal properties of 425 *Herschel* sources. These models showed that (i) a delayed star formation history is required to match the observed star formation rates; (ii) inflows and outflows are required to explain the observed metallicities at low gas fractions; (iii) a significantly reduced contribution of dust from supernovae (by up to a factor of 25 compared to the input libraries) is necessary to explain the dust poor sources with high gas fractions. We also showed that the BADGRS and dust-poor HI selected galaxies share similar properties to galaxies from the Dwarf Galaxy Survey (DGS), but require both different star formation histories and much more moderate inflows and outflows of gas compared to the DGS. By increasing the sample size of galaxies at low metallicity, we

also showed the dust-to-metal ratio is not definitively constant in all galaxies, and that there is evidence for a decrease in the dust-to-metal ratio towards lower metallicity. The low-stellar mass, metal-poor galaxies contained in the samples modelled in this thesis cover a wider range of gas fraction, and therefore larger evolutionary state, of nearby galaxies than studied before (by a factor of ~ 3). This thesis proposes a model in which the dust, gas, metals and stars can be modelled in a consistent and coherent manner, and gains insight into the dust-to-gas evolution at early epochs.

Publications

Schofield, S. P., Gomez, H. L., Dunne, L., Rowlands, K., De Vis, P., Clark, C. J. R., Maddox, S., Wild, V., da Cunha, E., *Understanding the Star Formation Histories of Nearby Dusty Blue Galaxies*, in prep. (Results from Chapters 2 and 3 are to be published in this paper)

De Vis, P., **Schofield, S. P.**, Dunne, L., Maddox, S., Gomez, H. L., Gomez, E. L., Cigan, P., Lara-Lopez, M., Owers, M., *Herschel-ATLAS: Revealing dust build up and decline across gas, dust and stellar mass selected samples: II. disentangling dust sources*, in prep. (Results from Chapters 5 and 6 are to be published in this paper)

Clark, C. J. R., **Schofield, S. P.**, Gomez, H. L., Davies, J. I., *An empirical determination of the dust mass absorption coefficient, κ_d, using the Herschel Reference Survey*, MNRAS 459, 1646 (Results from Chapter 2 are published in this paper)

De Vis, P., Dunne, L., Maddox, S., Gomez, H. L., Clark, C. R. J., Bauer, A. E., Viaene, S., **Schofield, S. P.**, Baes, M., Baker, A. J., Bourne, N., Driver, S. P., Dye, S., Eales, S., Furlanetto, C., Ivison, R. J., Robotham, A. S. G., Rowlands, K., Smith, D. J. B., Smith, M. W. L., Valiante, E., Wright, A. H., *Herschel-ATLAS: Revealing dust build-up and decline across gas, dust and stellar mass selected samples: I. Scaling relations*, accepted, MNRAS (Results from Chapter 4 and 6 are published in this paper)

Clark, C.J.R., Dunne, L., Gomez, H.L., Maddox, S., De Vis, P., Smith, M. W. L., Eales, S. A., Baes, M., Bendo, G. J., Bourne, N., Driver, S. P., Dye, S., Furlanetto, C., Grootes, M. W., Ivison, R., J., **Schofield, S. P.**, Robotham, A. S. G., Rowlands, K., Valiante, E., Vlahakis, C., van der Werf, P., Wright, A. H., de Zotti, G., *Herschel-ATLAS: the surprising diversity of dust-selected galaxies in the local submillimetre*

Universe, MNRAS 452, 397 (Results from Chapter 5 and 6 are published in this paper)

Eales, S., De Vis, P., Dunne, L., Appiah, K., Ciesla, L., Duffield, C., **Schofield, S. P.**, Smith, M. W. L., *The Extended Galaxy Main Sequence*, accepted, MNRAS 2016

Contents

Abstract vii

Extended Summary ix

Publications xiii

List of Tables xix

List of Figures xx

1 Introduction 1

1.1 Interstellar Dust . . . 2

1.1.1 History of interstellar dust . . . 4

1.1.2 Dust life-cycle . . . 6

1.1.3 Dust emission . . . 9

1.1.4 Dust and other Tracers of Star Formation . . . 11

1.2 Observing Dust . . . 13

1.2.1 Ground based Infrared Observations . . . 13

1.2.2 Space based Infrared Observations . . . 14

1.2.3 Herschel Space Observatory . . . 15

1.3 Herschel Surveys . . . 16

1.3.1 Herschel-ATLAS . . . 16

1.3.2 Herschel Reference Survey . . . 17

1.3.3 Dwarf Galaxy Survey . . . 18

1.4 An overview of SED modelling . . . 19

1.4.1 Stellar Spectra . . . 19

1.4.2 Simple Stellar Populations . . . 21

1.4.3 Composite Stellar Populations . . . 22

1.4.4 Age metallicity degeneracy . . . 23
1.4.5 The Star Formation History of Galaxies . . . 23
1.4.6 MAGPHYS . . . 26
1.5 Chemical Evolution Modelling . . . 28
1.5.1 Simple Picture for the Evolution of a Galaxy . . . 29
1.6 Aims of the Thesis . . . 31
1.7 Overview of Thesis Structure . . . 31

2 Investigating Nearby Galaxies Using MAGPHYS: Limitations of the Mode 33

2.1 Introduction . . . 33
2.2 The Galaxy Samples . . . 33
2.3 Spectral Energy Distribution With MAGPHYS . . . 37
2.3.1 SED Modelling Results with MAGPHYS (A First Attempt) . . . 38
2.3.2 Including IRAS 60 μm data for the HAPLESS sample: Constraining the MAGPHYS FIT . . . 42
2.3.3 Extending the cold dust priors . . . 48
2.4 How to constrain the Star Formation History from MAGPHYS . . . 50
2.4.1 Inspecting the Probability Distribution . . . 52
2.4.2 Creating a Stacked SFH for each Galaxy . . . 53
2.5 Final SED Fits- MAGPHYS Parameters . . . 56
2.6 Star Formation Rates in MAGPHYS . . . 69
2.6.1 Smoothed Star Formation Rates . . . 70
2.6.2 Results From Smoothing The Star Formation Histories . . . 72
2.7 Investigating the MAGPHYS parameter space . . . 74
2.7.1 Using other model libraries . . . 77
2.8 Conclusion . . . 81

3 The Average Star Formation Properties of Dust Rich and Blue Galaxies in the Local Universe 83

3.1 Introduction . . . 83
3.2 Sample Split: BADGRS vs non-BADGRS . . . 84
3.2.1 Average Spectral Energy Distributions: BADGRS and non-BADGRS . . . 84

3.2.2 Average Star Formation Histories: BADGRS and non-BADGRS 87
3.3 Sample Split: Dust-Rich vs Dust-Poor . . . 89
3.3.1 Defining A Dust Rich Galaxy . . . 90
3.3.2 Average Spectral Energy Distributions: dust-rich and dust-poor 91
3.3.3 Average Star Formation Histories: dust-rich and dust-poor . . 92
3.4 What can we learn from optical spectra of our sample . . . 95
3.4.1 Optical Spectra as a Tool to learn about Star Formation . . . 96
3.4.2 The Optical Spectra of HIGH and HAPLESS . . . 97
3.4.3 Removing AGN from our Sample . . . 109
3.4.4 Creating a stacked optical spectrum . . . 110
3.4.5 Advanced Analysis of the Spectra . . . 116
3.5 Conclusion . . . 118

4 The Chemical Model I: Introduction, Libraries and Tests 121
4.1 Introduction . . . 121
4.2 Modelling dust, gas and stars using an analytic approach . . . 122
4.3 The Chemical Evolution Model . . . 127
4.4 Libraries and Inputs of the Chemical Evolution Model . . . 130
4.4.1 Initial Mass Function . . . 131
4.4.2 Metal and Dust Yields . . . 133
4.4.3 Stellar Lifetimes and Remnant Mass . . . 141
4.4.4 Dust Destruction . . . 144
4.4.5 Grain Growth . . . 146
4.5 Conclusion . . . 148

5 Chemical Model II: results from using fiducial galaxies 151
5.1 Introduction . . . 151
5.2 Star Formation History . . . 151
5.2.1 Dust Production of Different Initial Mass Functions . . . 152
5.2.2 Dust Production and Stellar Lifetime . . . 154
5.2.3 Metal Production of Different Initial Mass Functions . . . 155
5.2.4 Understanding the Evolution of Dust Mass with Gas Fraction 157
5.2.5 Comparing the Dust Production of High and Low Mass Stars 158
5.3 Conclusion . . . 162

6 Chemical Evolution of HAPLESS and HIGH **163**
6.1 Introduction . . . 163
6.2 The Additional Herschel Samples of Galaxies . . . 165
6.2.1 A quasi-stellar mass selected sample . . . 165
6.2.2 The dwarf galaxy survey (DGS) . . . 166
6.2.3 An aside on the metallicities . . . 170
6.3 The Chemical Evolution models . . . 170
6.3.1 The simple model in C15 and DV16 . . . 171
6.3.2 Relaxing the closed box model . . . 175
6.3.3 Star formation rates and gas mass . . . 177
6.3.4 The metallicity versus gas fraction . . . 179
6.3.5 Dust-to-gas with metallicity . . . 183
6.3.6 A different model for dwarf galaxies from the DGS . . . 185
6.4 The Dust to Metal Ratio . . . 186
6.5 Caveats . . . 192
6.6 Conclusion . . . 193

7 Conclusion and Future Work **197**
7.1 Summary of the thesis . . . 197
7.1.1 Limitations of Spectral Energy Distribution Modelling using MAGPHYS . . . 198
7.1.2 The Impact of the Star Formation History on the Physical Properties of Nearby Galaxies . . . 199
7.1.3 The Chemical Evolution Model . . . 200
7.1.4 Chemical Evolution Modelling of a Large Sample of Herschel Galaxies . . . 201
7.2 Future Work . . . 202

Bibliography **204**

List of Tables

2.1 Table displaying key properties of the 42 HAPLESS galaxies, from Clark et al. (2015) . . . 36
2.2 Table displaying key properties of the 16 HiGH galaxies from De Vis et al. (2016) . . . 37
2.3 Table displaying the IRAS 60 and 100 μm flux measurements obtained for the HAPLESS galaxies . . . 47
2.4 Table displaying best fit parameters derived from MAGPHYS of the 42 HAPLESS galaxies . . . 57
2.5 Table displaying best fit parameters derived from MAGPHYSfor the 16 HiGH galaxies . . . 58

3.1 The ID and PCA classification of each galaxy in HIGH and HAPLESS (into BADGRS/non-BADGRS and dust-rich/dust-poor) . . . 119

4.1 Summary of the stellar yields for stars of mass $0.9-120\,M_{\odot}$, with initial metallicity of $Z = 0.02$, which are input to the chemical evolution model 139

6.1 The average properties for the DGS, HiGH-low, HiGH-high and HRS (LTGs) samples used in this work quoted as the mean (with range shown by standard deviation) . . . 169
6.2 Parameters for the different chemical evolution models used. . . . 169
6.3 Average dust-to-metal ratio for the different galaxy samples quoted as mean $\pm$ standard deviation . . . 191

List of Figures

1.1 Comparison between the ultraviolet and optical light (from stars) and the far-infrared and submillimetre light (from dust grains) 3

1.2 Dust lanes in the Milky Way 4

1.3 Cartoon depiction of the life cycle of dust grains 7

1.4 The atmospheric transmission at infrared wavelengths 14

1.5 *Herschel*-SPIRE image of the GAMA 09 field from the *Herschel*-ATLAS survey 17

1.6 *Herschel* 3-colour image of 66 galaxies from the Herschel Reference Survey 18

1.7 Cartoon depiction of the attenuation of starlight in MAGPHYS 25

1.8 Cartoon depiction of a galaxy Spectral Energy Distribution modelled by MAGPHYS 27

1.9 Flow chart demonstrating the different stages a galaxy progresses through in a chemical evolution model 29

2.1 Example MAGPHYS spectral energy distribution for two galaxies from HiGH and HAPLESS 39

2.2 Example probability distribution functions for a selection of parameters output by MAGPHYS for a single galaxy. 40

2.3 Stacked probability distribution function of cold dust for HAPLESS . 41

2.4 Selection of best-fit star formation histories obtained from MAGPHYS 42

2.5 Comparison between IRAS and PACS 100 μm flux values for HAPLESS 43

2.6 Comparison between the stacked spectral energy distribution for the HAPLESS sample, with and without IRAS 60 μm data 44

2.7 Comparison of the optical depth and specific star formation rate parameters output by MAGPHYS for HAPLESS, shown with and without IRAS 60 μm data 45
2.8 Stacked spectral energy distribution for the HAPLESS sample obtained from MAGPHYS using extended cold priors 46
2.9 Stacked probability distribution function of cold dust for HAPLESS, with and without extended cold priors 49
2.10 The change in the dust mass when the cold dust priors have been extended for the HAPLESS galaxies 50
2.11 Example probability distribution of the top 100 best-fitting star formation histories for a single galaxy from our sample 51
2.12 Demonstration of normalising and re-sampling a single star formation history from MAGPHYS onto a standard time grid 54
2.13 Example of the median fit star formation history obtained from MAGPHYS, with the associated uncertainty estimate, compared to the best-fit star formation history for that galaxy 55
2.14 MAGPHYS fits (best-fit spectral energy distribution, best-fit and median star formation history) obtained for the combined HIGH and HAPLESS sample 59
2.15 Comparison of star formation rate from MAGPHYS against the star formation rate from Clark et al. (2015) 70
2.16 Smoothing bursts in the star formation histories using a range of timescales 71
2.17 Comparison of the smoothed star formation rate from MAGPHYS against the star formation rate from Clark et al. (2015) for the bimodal sources 73
2.18 Smoothed median star formation history, with associated uncertainty, for a single galaxy from our sample 74
2.19 Location of the bursts in the top best-fitting models compared to the single best-fit star formation history fro a single galaxy in our sample 75
2.20 Distribution of all models in the MAGPHYS libraries, across the full range of parameter space, compared to the median and best fit values obtained for galaxy in our sample 76

2.21 Comparison of the original MAGPHYS parameter space to the extended library used in da Cunha et al. (2015) 78
2.22 Comparison of the original MAGPHYS parameter space to the extended library used in Rowlands et al. (2014) 79

3.1 The stacked best-fit SEDs of the combined HIGH and HAPLESS samples obtained from MAGPHYS separated into BADGRS and non-BADGRS. 85
3.2 Recovered stellar emission for HIGH and HAPLESS samples separated into BADGRS and non-BADGRS 86
3.3 Stacked best-fit star formation history of the HIGH and HAPLESS galaxies separated into BADGRS and non-BADGRS 88
3.4 Comparison of the average physical parameters output by MAGPHYS for the HIGH and HAPLESS galaxies separated into BADGRS and non-BADGRS 89
3.5 Comparison of $\log(M_{\rm d}/M_{\rm HI})$ against $\log(M_{\rm d}/M_{\rm s})$ for the HIGH and HAPLESS sources 91
3.6 Comparison of the stacked best-fit spectral energy distributions for HIGH and HAPLESS separated into dust-rich and dust-poor sub-samples 93
3.7 Comparison of the stacked best-fit star formation histories for HIGH and HAPLESS separated into dust-rich and dust-poor sub-samples 94
3.8 Comparison of the average physical parameters output by MAGPHYS for HIGH and HAPLESS separated into dust-rich and dust-poor sources 95
3.9 The HAPLESS galaxies shown in GALEX FUV, SDSS 3-colour optical, VIKING NIR and *Herschel* FIR and the region covered in the fibre optical spectra (superimposed on a 5 colour band SDSS image) 99
3.10 Same as Figure 3.9, but for the galaxies from the HIGH sample. The GALEX FUV, SDSS 3-colour optical, VIKING NIR and *Herschel* FIR images are from De Vis et al. (2016). No spectrum was available for HIGH 16. 106
3.11 BPT style diagram to identify spectra dominated by AGN emission . 109
3.12 Individual spectra of the BADGRS from SDSS and GAMA. Galaxies have been normalised and offset for clarity (the absolute flux is arbitrary) 111

3.13 Individual spectra of the non-BADGRS from SDSS and GAMA. Galaxies have been normalised and offset for clarity (the absolute flux is arbitrary) . . . 112
3.14 The stacked spectra for BADGRS (top) and non-BADGRS (bottom) 113
3.15 Stacked optical spectra for HiGH and HAPLESS (similar to Figure 3.14), but where the galaxies have been split into the dust-rich and dust-poor sub-samples . . . 115
3.16 Principle Component Analysis of the strength of the 4000 Å break against the strength of the Balmer absorption lines in our galaxies . . 116

4.1 Solutions from an analytical chemical evolution for a test galaxy . . . 126
4.2 Comparison of different stellar IMFs which are described in the text . 132
4.3 Comparison of the different mass yields of low to intermediate mass stars from various works in the literature . . . 135
4.4 How the stellar yield varies with initial stellar mass for a fixed metallicity 136
4.5 Comparison between the total dust production of high and low mass stars against time . . . 138
4.6 Comparison of the metal mass of a galaxy over time in Gyr for the old Fortran model . . . 142
4.7 Same as Figure 4.6, but now using the correct metal yields from Maeder 1992 . . . 143
4.8 Testing the effect different remnant mass equations have on the amount of gas and dust which are produced . . . 145

5.1 Different 'fiducial' SFHs used to investigate the effect that the SFH has on the dust and metal content of a galaxy in this chapter . . . 153
5.2 The dust mass production from different stellar IMFs present in the literature . . . 154
5.3 The lowest mass of star that can contribute to the dust budget over the lifetime of a galaxy . . . 155
5.4 The gaseous metal fraction, against gas fraction, for a Milky Way type SFH . . . 156
5.5 Comparison of metallicity against gas fraction for different IMFs using our model . . . 157

5.6 The dust mass (red) and gas mass (black) in a Milky Way type galaxy against gas fraction. The dust mass rises quickly (in terms of gas fraction)to a maximum around a gas fraction of 0.70, while the gas mass declines as stars are being created. 158
5.7 Here we show the total dust mass contribution of different mass stars over the evolution of a galaxy 159
5.8 The ratio of freshly formed dust, normalised by the returned gas from stars in a Milky Way type galaxy as the gas fraction declines 161

6.1 Comparison of the dust mass which has been derived for the DGS in this work against the dust mass published for the DGS in previous work 166
6.2 Comparison of stellar mass for the HiGH-high (red) and HiGH-low (blue) sources with DGS galaxies (black). Stellar masses were obtained from the MAGPHYS UV-submm SED-fitting routine. The DGS stellar masses from Rémy-Ruyer et al. (2013) have been scaled by a factor of 3.2 to be consistent with the MAGPHYS estimates. 167
6.3 Star formation histories used in this work 170
6.4 Variation of $M_{\rm d}/M_{\rm bary}$ with gas fraction for different samples observed with *Herschel*, including HAPLESS, HRS and HiGH 172
6.5 $M_{\rm d}/M_{\rm bary}$ ratio against gas fraction for the chemical model used in this work and three analytical models (based on instantaneous recycling technique) 174
6.6 Variation of $M_{\rm d}/M_{\rm bary}$ with the gas fraction 176
6.7 SFR$/M_{\rm bary}$ against the gas fraction for the samples compared to models with different SFHs to illustrate how the evolution of sources in this parameter space depends on their SFH 178
6.8 Metallicity variation with gas fraction for the different samples using the three different metallicity calibrations 181
6.9 Metallicity against gas fraction for a top-heavy stellar IMF 182
6.10 Metallicity variation with gas-to-dust ratio with the three different metallicity calibrations shown in Figure 6.8 184
6.11 Evolution of the dust-to-baryonic mass ratio and star formation rate against gas fraction using the bursty SFH model 187

6.12 The DGS are more metal poor at a given gas fraction than the HiGH, HAPLESS and HRS sources, and we require a different model (Model VII) to explain their properties 188
6.13 The dust mass produced by the various dust sources in Models IV, V and VI as the galaxy evolves from gas rich to gas poor 189
6.14 Comparison of the dust-to-metal ratio for the HiGH, HRS, HAPLESS and DGS samples against metallicity 190

Chapter 1
Introduction

The interstellar medium (ISM) of a galaxy, which is defined as the baryonic matter located between the stars in a galaxy, contains vast quantities of gas; it is from this reservoir of gas that all the stars in a galaxy form, and the ISM is the place where material from stars returns at the end of the stellar lifetime. The evolution of the galaxy is therefore thought to be dominated by interactions between the stars and the ISM; the stellar cycle of birth and death slowly enriches the ISM with heavier elements which have been forged in the centre of stars. To understand the evolution of a galaxy it is necessary to study in depth the constituents of the ISM, and to detect the imprint of the interactions between the stars and the ISM which betray the history of the galaxy.

The spectral energy distribution (SED) of a galaxy, which is simply the distribution of energy emitted by the galaxy across the full spectral wavelength range, can be used to determine many physical properties, since light of different wavelengths is related to different physical processes which occur within the galaxy. For example, emission from stars is responsible for most of the ultraviolet (UV) and optical radiation from a galaxy whereas longer infrared wavelengths are generated by the coldest objects and can be used to observe the birth of stars in dense clouds. For this reason, there is significant interest in modelling the multiwavelength SED of galaxies, with the aim of maximizing the information which can be obtained. Analysis of multiwavelength SEDs is a powerful tool which can be used to infer many physical properties of large samples of galaxies.

In this thesis, I aim to investigate the physical properties of a unique sample of local galaxies from Clark et al. (2015) and De Vis et al. (2016), which will be introduced in full in Chapter 2. I investigate why these galaxies exhibit such unique

properties; they have high specific star formation rates, blue optical colours and contain large amounts of interstellar dust. To develop an understanding of the interplay between the different physical processes in these galaxies, eg star formation and the evolution of the ISM, we use a chemical evolution model to trace the build up of metals and dust over time.

An important parameter when modelling the chemical evolution of galaxies is the star formation history; the star formation history describes how the star formation rate varies over the evolution of the galaxy. Variations in the star formation history may have a strong effect on the build up of dust in the ISM of galaxies. However studies of the chemical evolution of galaxies often use a small set of fiducial star formation histories. These templates may not be representative of the individual galaxies being investigated, and may introduce a bias into the results. Multiwavelength SED modelling presents an opportunity to obtain individual star formation histories for a large number of galaxies.

The remainder of this chapter will develop in more detail the ideas described above, and will provide an overview of the current state of research in the field.

1.1 INTERSTELLAR DUST

Under favourable conditions, a fraction of the heavy elements which have been produced by stars will condense out of the gas phase, forming tiny solid particles called dust grains. Interstellar dust grains account for a small fraction of the total baryonic mass of a typical galaxy, with the dust-to-gas ratio in the Milky Way of order 0.01 (Draine et al., 2007). However, despite the low contribution to total mass, dust has a powerful effect on the host galaxy. For a typical galaxy around half of all the light that is emitted by stars is absorbed by dust grains (Lagache et al., 2005). In fact, over 50 % of light produced by stars since the big bang has been absorbed and re-radiated by dust grains (Popescu & Tuffs, 2010). These dust grains effectively reprocess the 'stolen' starlight; while individual UV and optical photons are preferentially absorbed by the dust, the grains themselves emit strong thermal radiation in the infrared. Figure 1.1 shows the wealth of information that is available from both current and previous infrared telescopes (see Section 1.2 for more details) covering $24 - 850\,\mu$m.

Dust grains do not only affect the observations we can make of a galaxy, they also play an important role in many of the physical processes which govern the evolution of the interstellar medium. As an example, dust grains are now considered very important for the production of molecular hydrogen, where they act as a catalyst which assists in the joining of two hydrogen atoms on the grain surface (Perets &

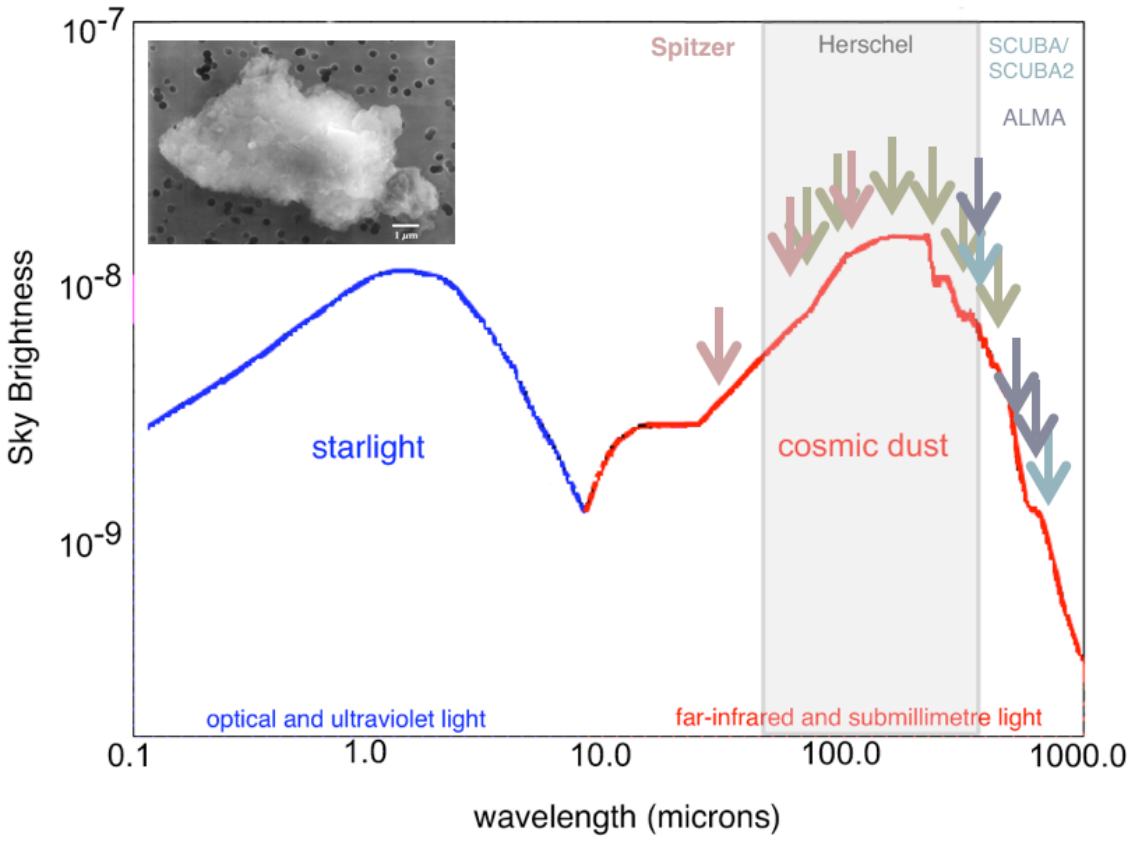

Figure 1.1 Comparison between the ultraviolet and optical light (from stars) and the far-infrared and submillimetre light (from dust grains). By combining observations from both current and previous telescopes we have impressive coverage of the cosmic dust spectral energy distribution. Figure from Haley Gomez, adapted from Dole et al. (2006).

Biham, 2006). Molecular hydrogen itself is of great importance in the process of star formation (eg Thompson et al. 2014). Therefore dust can be used as a tracer of the ISM of a galaxy, provides fuel for star formation and reveals obscured star formation (Finn et al., 2010).

Our understanding of interstellar dust, and the impact it makes on the evolution of a galaxy, has increased considerably over the last century; much of this increase has been driven by successive infrared space telescopes, which have opened a new window on the Universe. The Herschel Space Observatory (Section 1.2.3) has revolutionized our view of dust in the Universe, revealing 90 % of dust that was missed in previous studies (Devereux & Young, 1990). Yet we still know little about the origin dust in local galaxies, or even in recent cosmic history. In the section which follows we explore the history of dust, from its first discovery to the present day.

FIGURE 1.2 The dust lanes in our galaxy appear as dark regions in the night sky, where fewer stars can be observed. Image from http://www.nasa.gov.

1.1.1 HISTORY OF INTERSTELLAR DUST

One of the earliest acknowledgements of the effect of interstellar dust was made by William Herschel when he noticed that there appeared to be 'holes in the heavens', referring to the dark patches which could be seen spreading across the Milky Way, see Figure 1.2, (Herschel, 1785). At the time, it was thought that these dark patches were caused by an absence of stars in the afflicted regions of the sky. However it was not until the work of Barnard (1919) that it was realised that these dark patches were not caused by an absence of stars, but were actually caused by some obscuring bodies between the stars and the observer. This conclusion was reached from detailed study of many astrophysical photographs; for example, images of nebula showed both partial and complete obscuration of stars in the nearby vicinity.

In 1867, Wilhelim Struve performed a number count of all stars in a sphere around the Sun. He found that as the distance from the Sun increased the number of stars per unit volume decreased. There were two possible explanations for this: either the Sun was at the very centre of a cluster of stars, whose density decreased with radius, or it was an observational effect caused by the dimming of the light from more distant stars (above that of the inverse square law). Kapteyn (1909) obtained a numerical value for this 'stellar extinction' of $1.6\,\mathrm{mag\,kpc^{-1}}$. The value he obtained,

made from assumptions of uniform stellar density, later proved to be very accurate as it closely matches measurements of interstellar extinction today, with a value of $\sim 1.8\,\mathrm{mag\,kpc^{-1}}$ (Whittet, 2003).

Despite this growing body of work documenting both the presence and effect of a yet unidentified interstellar material on starlight in our galaxy, it was not until the 1930s that the concept of interstellar dust became fully established in scientific theory. Trumpler (1930) produced a study of open clusters in the Milky Way, analysing several key observational features. For a star of known spectral type, the average colour index was well known. However, there was an observed colour excess for the open clusters in our galaxy, and this colour excess (which is the difference between the intrinsic colour index of an object, and that which is observed) increased with distance. Combined with the previous observations of obscuration and stellar extinction, these new observations confirmed the presence of 'fine cosmic dust particles of various sizes' whose presence had a profound effect on the light from stars, and which provided a framework that many subsequent studies of interstellar dust have built upon.

Following the discovery that dusty particles were responsible for causing the observational effects described above, the scientific interest turned to producing theories which could explain what the dust particles were made of. Some of the earliest models were produced by Oort & van de Hulst (1946) where it was suggested that elements such as Oxygen and Carbon might freeze onto the surface of 'dust cores', forming an icy-mantle of simple molecules, such as H_2O, on the grain surface. It was also noted that in order to obtain a range of dust grain sizes some dust particles may undergo a 'fusion', possibly during a collision with another grain in a dense gas cloud. Oort and Van de Hulst produced a paper studying how these 'dirty-ice' dust particles would behave in the interstellar medium of a galaxy, estimating features such as the potential lifetime of the dust grains. At this stage however, it was not known what the condensation cores, which the ice formed upon, might be composed of.

Kamijo (1963) produced a theoretical study of the circumstellar envelope of a red-giant star. The study showed that, due to the abundance of heavy elements and relatively cool temperatures, it would certainly be possible for solid particles to condense in the atmosphere of the star. These particles, which might consist predominantly of silicates, could then be dispersed into the interstellar medium of the galaxy by strong gas flows from the star. Once in the interstellar medium, the molecules would then gradually cool through infrared emission. At this stage Kamijo suggested that these solid particles may form the nucleus of interstellar dust grains which, as suggested in the model of Van de Hulst, other elements such as Hydrogen and Oxygen may later condense onto.

The theoretically predicted silicate molecules were later detected through their emission during the late 1960s in several independent studies. For example, Knacke et al. (1969) used the infrared spectrum of a red supergiant to determine which molecules were present in its circumstellar envelope. Observations made over two nights revealed the presence of strong absorption features which closely matched the predicted absorption lines of SiO. Additional features in the spectra showed that larger molecules such as $(Mg, Fe)SiO_3$ may also be present.

The detection of these molecules lead to the creation of new more sophisticated models describing dust grain physics. Mathis et al. (1977) performed a comprehensive study of many potential molecules, with the aim of determining which were the most consistently capable of reproducing the observed extinction properties of dust in the interstellar medium. At the heart of the model were graphites, silicates, Iron, and Magnite (Fe_3O_4). Various combinations and size distributions of these primary constituents were compared against the observations. Their key findings were that, while a variety of possible interstellar dust mixtures were possible, *all* of the best fitting models contained a contribution from graphite. When combined with a mixture of silicates and matched with a power law distribution of grain sizes, these models were able to provide a close match to the observed extinction properties of interstellar dust in our galaxy.

Since this time, there have been many advancements made to our model of dust grains, and these are driven by the increase of our understanding of dust in galaxies through observations made by space telescopes (see Section 1.2.2). For example, Draine & Lee (1984) extended the model of Mathis et al. (1977), using the latest laboratory measurements of graphite. Most of the dust models which are used today still assume the same basic composition of dust grains, for example the models of Mathis (1998) or Zubko et al. (2003). In recent years there has been interest in revisiting our basic assumptions on the composition of dust grains, and to ground these models more firmly in recent laboratory results (Jones et al., 2016).

While our understanding of dust has come a long way since 1785, there are still many uncertainties in the origin of dust grains and their role in the evolution of galaxies.

1.1.2 DUST LIFE-CYCLE

Dust grains in the interstellar medium of a galaxy do not have an infinite lifetime. Depending on physical conditions, such as the radiation field strength, and the dust grain composition, there can be significant variation in destruction rates,

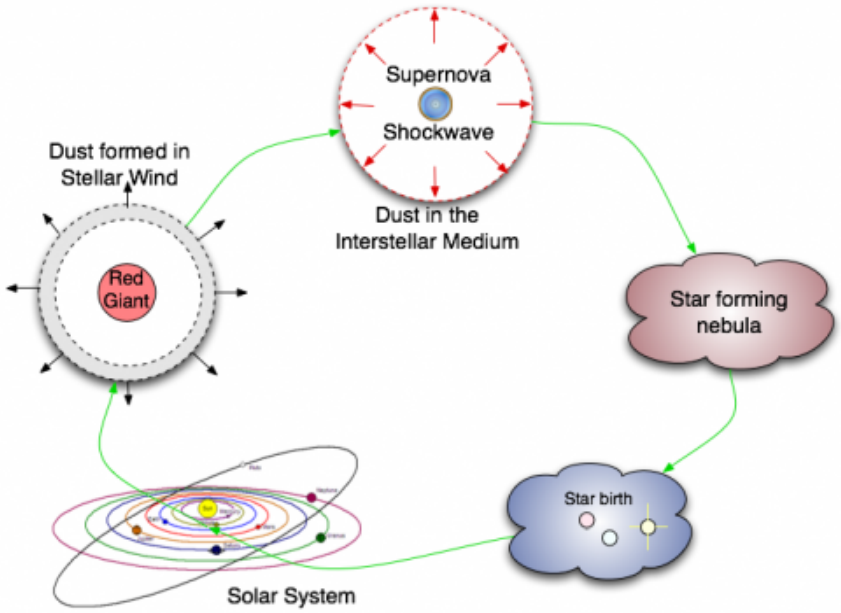

Figure 1.3 A cartoon depiction of the life cycle of dust grains in the interstellar medium. Created in the cooling outflows from evolved stars, dust grains experience a wide range of physical environments over their lifetime. Some of these dust grains are then destroyed in the production of a new generation of stars. Image from http://herschel.cf.ac.uk/science/infrared/dust; credit E. Gomez and H. Gomez.

but lifetimes are typically of the order 10^8 years (Jones & Nuth, 2011). However, the dust mass of a galaxy can remain stable over a much longer timescale. This is because the production of dust grains is not a singular event in the lifetime of the galaxy, rather dust grains enter what is known as the dust life cycle. In this section we will introduce the different stages of the dust life cycle and take a closer look at the various mechanisms which dominate during each stage of the cycle.

There is evidence that evolved low mass stars, with their metal enriched atmospheres and cooler surface temperatures, provide an environment which is favourable towards the production of dust grains (Morgan & Edmunds, 2003; Gail, 2009; Zhukovska & Henning, 2013). These evolved stars often experience significant outflows of material; through these outflows dust grains produced by stars are distributed into the local interstellar medium (Dell'Agli et al., 2015).

In the past decade, significant quantities of dust have been seen to be produced by supernova at the end of the life of high mass stars (Dunne et al., 2003, 2009; Matsuura et al., 2011; Gomez et al., 2012; Gomez, 2013; Indebetouw et al., 2014; Gall et al., 2015). The effective dust yield of supernovae is a subject of debate however, since it is thought that the powerful shocks from the supernovae may destroy a fraction

of these dust grains (Silvia et al., 2012; Temim et al., 2014; Lakićević et al., 2015), with between $\sim 11 - 16\%$ of dust grains surviving the shocks in depending on grain composition and distribution (Micelotta et al., 2016).

Once star dust grains reach the interstellar medium they are exposed to a wide range of physical environments. In a simplified picture, we can assume that there are two main phases of the interstellar medium; dense environments, such as the interior of giant molecular clouds, and diffuse environments, such as the ambient interstellar medium. The typical lifetime of a dust grain, while being relatively short compared to the lifetime of a galaxy, is longer than that of the giant molecular clouds whose lifetime is thought to be less than $\approx 10^7$ years (Blitz & Shu, 1980; Murray et al., 2010). Therefore a typical dust grain will likely experience a mixture of both dense and diffuse environments over its lifetime.

The physical conditions in the diffuse interstellar medium are particularly harsh for dust, here grains will be exposed to several different mechanisms which will, in time, lead to their gradual destruction. Powerful supernova shocks will impart considerable energy to the interstellar medium (Thornton et al., 1997), driving an increase in the rate of grain-grain collisions, and gas-grain collisions (Tielens et al., 1994). Both of these cause a reduction in the size of dust grains and can destroy dust.

Giant molecular clouds are regions of cold, dense molecular gas and are thought to be the primary regions where stars in a galaxy form (Dobbs, 2013). Dust grains assist in the fragmentation and collapse of regions of these giant molecular clouds; by radiating energy in the infrared they provide an important cooling mechanism (Chiaki et al., 2013). Dust grains inside the giant molecular clouds benefit from a more sheltered environment and will experience several constructive processes. Grain growth, a process whereby molecules condense onto the surface of dust grains forming an ice mantle, occurs readily in the depths of the giant molecular clouds and acts to increase the total dust mass (Foster et al., 2013). Dust grains will also undergo coagulation: due to the dense environment and cold temperatures, a collision between dust grains may result in the two dust grains sticking together and forming a single larger dust grain (Ossenkopf, 1993).

Often the fate of a giant molecular cloud is self deterministic; favourable conditions lead to the collapse of regions of the cloud resulting in rapid star formation. The intense radiation from massive young stars will destroy the cloud from the inside out (Matzner, 2002). Dust grains will then return to the diffuse interstellar medium of the galaxy, and begin to experience the destructive processes once more. However, it is thought that some of the dust grains which were present in the giant molecular cloud will be incorporated in the material which collapses and forms stars, and will be

removed from the interstellar medium; this is a process which is known as astration. The metals which the dust grains were formed of will then remain locked up in the star until it reaches the end of its life, at which stage new star dust grains may form in the outflows of material, and the dust life-cycle will begin once more.

1.1.3 Dust emission

Dust grains emit strongly in the far-infrared and sub-millimetre regions of the electromagnetic spectrum. We can use the radiation emitted by dust to learn about many its physical properties such as dust temperature and dust mass. We know that a body at a given temperature will emit radiation, and that if the body is a perfect emitter and absorber of radiation, then the form of the radiation will depend only upon the temperature of that body and can be modelled using the Planck function:

$$B_\lambda(T) = \frac{2hc^2}{\lambda^5} \frac{1}{e^{\frac{hc}{\lambda k_\mathrm{B} T}} - 1} \tag{1.1}$$

where h is the Planck constant, c is the speed of light, λ is the wavelength of the radiation, T is the temperature of the body and k_B is the Boltzmann constant.

Typically the thermal emission from dust grains is modelled assuming an emissivity modified blackbody, which accounts for the fact that dust grains are not perfect emitters of radiation at all wavelengths (eg Casey 2012). The modified blackbody function, sometimes referred to as a greybody function, can then be written as:

$$S_\lambda = Q(\lambda)\, B_\lambda(T) \tag{1.2}$$

where S_λ is the full spectral energy distribution produced by the dust grains and $Q(\lambda)$ is a wavelength dependent emissivity modifier. Hildebrand (1983) suggests that a simply power law can be used to represent the dependence of the dust emission on wavelength, such as $Q(\lambda) = \lambda^\beta$. In this seminal work, it was suggested that the value of β could range from $1 - 2$. However, due to an anti-correlation between the effects of β and T on the SED (Juvela et al., 2013), it is difficult to determine the value of β from observations. Despite this, there is some evidence for varying β values across a galaxy (Smith et al., 2012b; Draine et al., 2014; Tabatabaei et al., 2014).

It is possible to characterize the peak wavelength that a body of a given temperature will emit; or inversely, from an observation of the spectrum a body emits we can measure its temperature. Wien's displacement law, which can be obtained by differentiating the Planck function with respect to wavelength, provides us with this information:

$$\lambda_{\rm peak} = \frac{2.898 \times 10^{-3}}{T} \tag{1.3}$$

where $\lambda_{\rm peak}$ is the peak wavelength emitted by the body and T is the characteristic temperature. Interstellar dust grains emitting strongly in the far-infrared region of the electromagnetic spectrum have a temperature of approximately 20 K. In contrast, dust emission in the near infrared originates from dust grains of around 60 K, who have likely been heated by the radiation from nearby stars.

Finally, using this information we can also obtain an estimate of the total dust mass along a line of sight. From Hildebrand (1983):

$$M_{\rm d} = D^2 \frac{F_\lambda^{\rm dust}}{\kappa_\lambda \, B_\lambda(T)} \tag{1.4}$$

where $M_{\rm d}$ is the total dust mass, D is the distance to the galaxy, $F_\lambda^{\rm dust}$ is the flux observed at wavelength λ and κ_λ is the dust emissivity constant. The value of κ will change depending on the physical properties, such as size and condition, of the dust particles. Often dust is modelled using a two temperature black-body fit, where there is both a cold and warm component of the dust mass. In this case, $M_{\rm d}$ is given by:

$$M_{\rm d} = \frac{F_{\lambda_{\rm w}} D^2}{\kappa_\lambda \, B_\lambda(T_{\rm w})} + \frac{F_{\lambda_{\rm c}} D^2}{\kappa_\lambda \, B_\lambda(T_{\rm c})} \tag{1.5}$$

where the first term represents the warm component of the dust, and the second term represents the cold dust component.

A recent study by Clark, Schofield et al. (2016) estimated the value of the dust mass absorption coefficient at a wavelength of 500 μm, using a sub-sample of 22 galaxies drawn from the Herschel Reference Survey (HRS, Boselli et al. 2010, see Section 1.3.2 for further details). The work, following the method of James et al. (2002), is based on the assumption that the dust-to-metals ratio is constant across galaxies in the local Universe (Dwek, 1998; Leroy et al., 2011; Watson et al., 2011; Corbelli et al., 2012). There is some debate in the literature on whether the dust-to-metal ratio remains constant in low metallicity systems however (Galliano et al., 2005; Hunt et al., 2005).

The value of the dust-to-metal ratio ($\epsilon_{\rm d}$) was estimated from 12 sources in the literature (where these sources were chosen such that the dust mass had been estimated from a method independent of κ_λ, such as elemental depletion), resulting in a value of $\epsilon_{\rm d} = 0.5 \pm 0.1$. Observations of the oxygen-hydrogen abundance ratio can then be combined with the solar conversion of Asplund et al. (2009) to estimate

the metal mass fraction. With the assumption that $\epsilon_{\rm d}$ is constant, the dust mass can then be calculated from:

$$M_{\rm d} = M_{\rm g}\,\epsilon_{\rm d}\,f_{\rm Z_\odot}\,Z \tag{1.6}$$

where $M_{\rm d}$ is the dust mass, $M_{\rm g}$ is the total gas mass, $f_{\rm Z_\odot}$ is the solar metal mass fraction and Z is the metallicity of the galaxy's ISM. Substituting for $M_{\rm g} = \xi(M_{\rm HI} + M_{\rm H2})$, and equating this to Equation 1.5 for the dust mass above, yields the equation for κ:

$$\kappa_\lambda = \frac{D^2}{\xi(M_{\rm HI} + M_{\rm H2})\,\epsilon_{\rm d}\,f_{\rm Z_\odot}\,Z}\left(\frac{F_{\lambda_{\rm w}}}{B_\lambda(T_{\rm w})} + \frac{F_{\lambda_{\rm c}}}{B_\lambda(T_{\rm c})}\right) \tag{1.7}$$

where D is the distance to the source in Mpc, and ξ is a correction factor to account for the fraction of a galaxy's ISM made up of elements heavier than hydrogen (a solar metallicity galaxy has $\xi = 1.39$). To calculate the value of κ_λ using Equation 1.7, the galaxies drawn from the HRS were required to have: infrared-submillimetre flux (to fit the dust SED), 21 cm emission (to estimate $M_{\rm HI}$), $^{12}C^{16}O(1-0)$ line measurements (to measure $M_{\rm H2}$ and gas phase metallicities. A sub-sample of 22 sources from the HRS matched this criteria.

The value of $\kappa_{\rm d}$ was then calculated for each galaxy, and the uncertainty in each measurement was estimated through Monte Carlo bootstrapping. The final value of κ from this paper was then estimated from the median of the combined κ distributions, resulting in a value of $\kappa_{500} = 0.051^{+0.070}_{-0.026}\,{\rm m^2 kg^{-1}}$. This value of $\kappa_{\rm d}$ is compatible with other values in the literature (Draine, 2003; Draine et al., 2007), although it is a factor of ~ 4 lower than the value from James et al. (2002); this discrepancy was accounted for through several factors, including the use of improved observations and metallicities.

1.1.4 Dust and other Tracers of Star Formation

Star formation is a very important process that has a significant effect on the physical properties of a galaxy. It is therefore important to be able to consistently measure the star formation in different environments, and in different galaxies. However, since it is not possible to directly count each star as it is forming, the best methods of measuring the star formation rate in a galaxy depend on being able to make an observation of some feature of the galaxy which is related to, or traces, the star formation rate. The tracer must be calibrated such that the measure can be converted into a level of star formation.

The following question is posed: what are the best available tracers of star formation? Over the years, there have been many different tracers of star formation used in the literature. Many of these tracers focus on the fact that high mass stars which produce very high levels of UV light and, due to their short lifetimes, are only thought to be present if there has been recent star formation activity in a galaxy. The intensity of UV light can then be used to indicate, or trace, the level of star formation in galaxies (Wilkins et al., 2008).

However, as we have seen, dust grains are thought to absorb high fractions of the UV and optical light that is produced by stars in a galaxy (Lagache et al., 2005). In this case, some of the UV light will be missing from the observations and the star formation rate may be underestimated. An alternative method which has been considered is to use the total infrared emission as an indicator of star formation, such as in Kennicutt (1998); Elbaz et al. (2011). This method does assume that a fixed fraction of the UV photons will be absorbed by the dust in star formation regions. If this fraction changes, then a certain quantity of star formation will be missed. It also makes the assumption that the only photons which the dust grains absorb originate from high mass stars following star formation, however it is known that dust can be heated by the emission from older stellar populations (Bendo et al., 2010; Boquien et al., 2011; Bendo et al., 2012a), as seen in the nearby galaxy M31 (Groves et al., 2012).

A further alternative could be to use a monochromatic tracer of dust emission, such as the 24 μm from warm dust grains (Calzetti et al., 2010). The advantage to this method is that since the 24 μm originates from hot dust, in contrast to the longer infrared emission from cold dust grains, it should correlate more closely to the star formation rate since it will inherently contain less contamination from evolved stellar populations. However studies of star forming clouds in the Milky Way show that, for some clouds, a significant amount of the 24 μm emission does not originate from star forming regions.

Recently it has been thought that the best method of estimating the star formation rate of a galaxy could be to use a combination of tracers. In such a case, observations would benefit from the best of both methods while liming the impact of some of the negative features of each tracer. A common combination of star formation tracers is to use an infrared continuum tracer (looking at the obscured star formation), combined with a monochromatic star formation rate indicator from the optical region of the spectrum (such as H_α), which traces the gas ionised by high mass stars (Hao et al., 2011).

The above tracers are not the only method which can be used to trace the star

formation rate in a galaxy. For example, it is also possible to obtain star formation rates from full multiwavelength modelling (as described in Section 1.4.6) or from integrated spectroscopy of the galaxy (eg Winnewisser 1990).

1.2 Observing Dust

We have seen both how the thermal emission from dust grains can be used to determine physical properties relating to the dust in a galaxy, and how the total infrared emission can be used to trace the level of star formation. In this section we describe the various attempts of observing infrared radiation; from the advantages and disadvantages of both ground and space based telescopes, to a detailed overview of the Herschel Space Observatory and its related surveys.

1.2.1 Ground based Infrared Observations

Ground based observations of infrared wavelengths are made very difficult due to the presence of the atmosphere. Firstly, the gas in the atmosphere is a very good absorber of infrared radiation so little of the infrared radiation reaches ground level telescopes. Secondly, the atmosphere emits significantly at some infrared wavelengths. This sky brightness hinders observations of most of the infrared region of the spectrum. Despite these two factors there are some specific windows at which it is possible to make observations eg the K band, at $2.0 - 2.4\,\mu$m, Figure 1.4. Most of the infrared radiation is absorbed by specific molecules in the atmosphere such as H_2O and CO_2, therefore it is possible to make observations only when the conditions are good.

At higher altitude there is less atmosphere for the radiation to travel through prior to reaching the telescope. This decreases the atmospheric opacity at infrared wavelengths and improves observations that are made. The James Clerk Maxwell Telescope (JCMT), located near the summit of Mount Mauna Kea, is around 4000 m above sea level. At this altitude it is possible to observe two submillimetre (sub-mm) wavelengths from the ground, using the SCUBA-2 detector (Silvia et al., 2012). These wavelengths of $450\,\mu$m and $850\,\mu$m are sensitive to emission from cold dust grains.

Other efforts to make infrared observations of space from within our atmosphere include balloon borne telescopes eg BLAST (Pascale et al., 2008). In 2008 BLAST was equipped with a 2 m mirror and the same detector array that was designed for the SPIRE instrument on-board the Herschel Space Observatory. SOFIA (Krabbe, 2000) is a mission led by NASA to observe infrared light using a 2.5 m

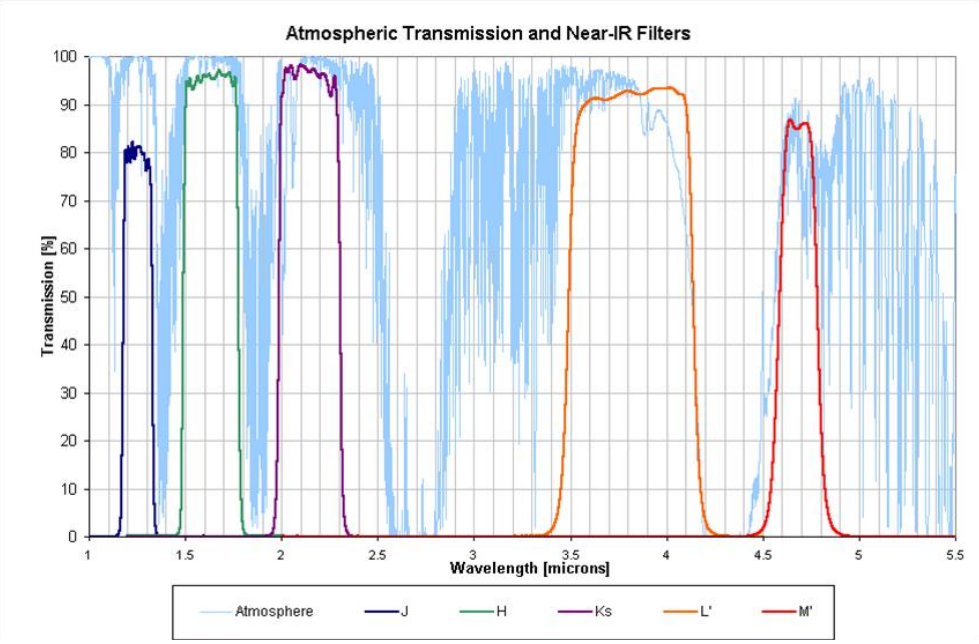

FIGURE 1.4 The low level of radiation transmitted through the atmosphere in the near infrared wavelengths. Although at some bands the opacity is 100 per cent, there are bands at which observations can be made in good conditions. Image from http://people.bu.edu.

diameter telescope carried into the upper atmosphere by a modified Boeing 747 aeroplane, above almost 99% of the water vapour. SOFIA is sensitive to emission from $0.3 - 1600\,\mu$m (Herter et al., 2012).

1.2.2 SPACE BASED INFRARED OBSERVATIONS

Space telescopes have the significant advantage of being located above our atmosphere. However being in space does introduce several new difficulties; space missions are extremely expensive, and it is often impossible to service the instrument or telescope after launch. Prior to the launch of the Herschel Space Observatory there had been three key infrared space telescopes. The scope of these missions was limited by the resolution and sensitivity that could be achieved with the technology available at the time. The first infrared space mission was the Infrared Astronomical Satellite (IRAS), launched in 1983 (Neugebauer et al., 1984). The primary mirror of IRAS measured 0.57 m, which limited the resolving power of the telescope. IRAS did perform an all sky survey from 12 to 100 μm which covered approximately 96% of the sky. The IRAS mission detected over 350, 000 new infrared sources, and also detected the presence of infrared cirrus emission. However due to limited wavelength range, it

only detected sources that were warm enough to produce significant radiation in this waveband.

Following IRAS, the Infrared Space Observatory (ISO) was launched in 1995 (Kessler et al., 1996). ISO only boasted a modest increase in the size of the mirror compared to its predecessor. However it had significant improvements in sensitivity which were largely due to improvements in infrared detector technology. ISO was also able to observe at longer wavelengths, with a wavelength range up to 240 μm. This enabled the detection of emission from colder objects that were missed by the shorter wavelength range of IRAS.

Then in 2003, the Spitzer telescope was launched into space (Werner et al., 2004). Spitzer was sensitive to shorter infrared wavelengths than ISO with a range of 3 to 180 μm but the size of the mirror was increased to 0.85 m, which offered improved resolution. As a means of further improving the sensitivity of the telescope, Spitzer was located at a greater distance from the Earth than IRAS and ISO, as the Earth is a large source of infrared emission. This relocation also reduced the amount of liquid helium which was required to cool the detectors.

1.2.3 Herschel Space Observatory

The Herschel Space Observatory (Pilbratt et al., 2010), hereafter *Herschel*, was launched on the 14$^{\text{th}}$ of May 2009, to observe the universe in the far-infrared (FIR) and sub-mm. The lifetime of the science mission of *Herschel* was limited by the amount of cryogenic coolant used to keep the on-board detectors at operational temperatures; *Herschel* carried approximately 2000 litres of liquid helium for primary cooling. On the 29$^{\text{th}}$ of April 2013 *Herschel* exhausted its supply of liquid helium. This brought an end to the observing mission of the telescope.

Herschel marked a significant advance in infrared observations. The increase in the size of the primary mirror to 3.5 m offered unprecedented resolution, and it currently remains the largest single mirror on a space-based telescope. Due to the cassegrain design of the telescope, the light from the primary mirror was reflected onto a smaller secondary mirror. The secondary mirror was 0.3 m in diameter and together the two mirrors focused the light onto the detectors. *Herschel* was sensitive to radiation with wavelengths $60-672\,\mu$m; at these sub-mm wavelengths *Herschel* was able to make observations of the previously unexplored part of the electromagnetic spectrum.

Herschel was launched with the aim of addressing four key areas of scientific interest. These objectives were stated as: studying the formation of galaxies in the

early universe, investigating the formation of stars and their interaction with the ISM, observing the chemical composition of the solar system and to study the chemistry of the universe. To achieve this *Herschel* was launched with three on-board instruments. SPIRE and PACS were primarily imaging devices, with medium resolution spectrometers. HIFI was a heterodyne spectrometer capable of producing high resolution spectra of distant objects.

The SPIRE instrument (Griffin et al., 2010) on-board *Herschel* had distinct features. Firstly as a photometer it was sensitive to three wavelength bands centred on 250, 350 and 500 μm; observations could be made simultaneously in all three photometric bands. SPIRE also contained a Fourier Transform Spectrometer (FTS) which covered a range of $194 - 671\,\mu$m. The operational temperature of SPIRE was 0.3 K, the coldest component on-board *Herschel*. The PACS detector (Poglitsch et al., 2010) covered the wavelength range of 60 to 210 μm. PACS was capable of simultaneously observing two out of its three photometric bands, which increased the observing efficiency of the telescope. The photometric bands of PACS were defined as: $60 - 85\,\mu$m, $85 - 130\,\mu$m and $130 - 210\,\mu$m.

Herschel could also be operated in parallel mode where SPIRE and PACS were deployed simultaneously enabling five photometric bands to be imaged in a single observation. This was an efficient mode to obtain multi-wavelength data sets for large areas of the sky.

1.3 HERSCHEL SURVEYS

Herschel performed many key surveys of local galaxies whilst in operation. These surveys include guaranteed time and open time key projects, ranging from nearby targeted surveys to large blind surveys; each survey presenting a unique data set and opportunity for discovery. In this thesis we will model samples of galaxies using *Herschel* data (see Chapter 2 for a introduction to our sample); here we provide an overview of the different *Herschel* surveys from which we obtain data in this thesis.

1.3.1 HERSCHEL-ATLAS

The largest extragalactic open time key project was the *Herschel*-ATLAS (H-ATLAS) survey (Eales et al., 2010), totalling 600 hours of *Herschel* observations. H-ATLAS aimed to map the largest possible area of the sky in the FIR and sub-mm wavelengths. To achieve this goal, the observations were made at the highest scan rate of the telescope. SPIRE and PACS were used in parallel mode which provided

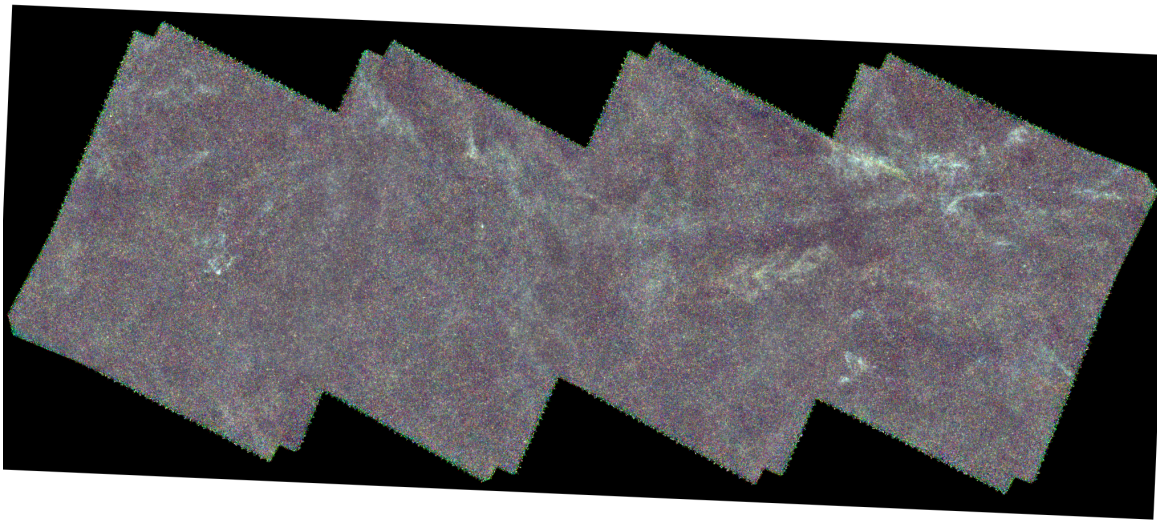

Figure 1.5 *Herschel*-SPIRE (Griffin et al., 2010) image of the GAMA 09 field (used in this thesis) from the *Herschel*-ATLAS survey Eales et al. (2010). There are three GAMA fields covered in the survey, each of RA width 12′ and DEC width 3′. The choice of fields coincident with the Galaxy And Mass Assembly (GAMA) survey (Driver et al., 2009) maximizes the ancillary data which is available (including spectroscopic redshifts).

photometric data at five different wavelength bands. All accounted for, H-ATLAS covered an area of 570 deg^2, comprised of six fields: one north galactic pole region, two south galactic pole regions and three GAMA fields (see Figure 1.5 for example of the GAMA 09 field). The observation fields were chosen towards the galactic poles to reduce the effect of dust emission from our own galaxy. All of the fields were also chosen in an attempt to maximize the complementary data that was available from other telescopes and detectors. Since this was a blind survey, it provides an unbiased flux limited view of dusty galaxies in the local universe. The large area covered by H-ATLAS provides a large number of dusty sources, and aims to address cosmic variance issues. The longer wavelength range enables the detection of dust in galaxies missed by IRAS (which was limited to 100 μm).

1.3.2 Herschel Reference Survey

The Herschel Reference Survey (HRS) was a guaranteed time project (Boselli et al., 2010) to investigate the physical properties of the interstellar medium (ISM) of local galaxies. The complete sample for HRS consists of 322 galaxies, which were all observed in the SPIRE bands. The HRS galaxies were selected using several criteria, in an attempt to ensure that the sample represents the properties of local galaxies

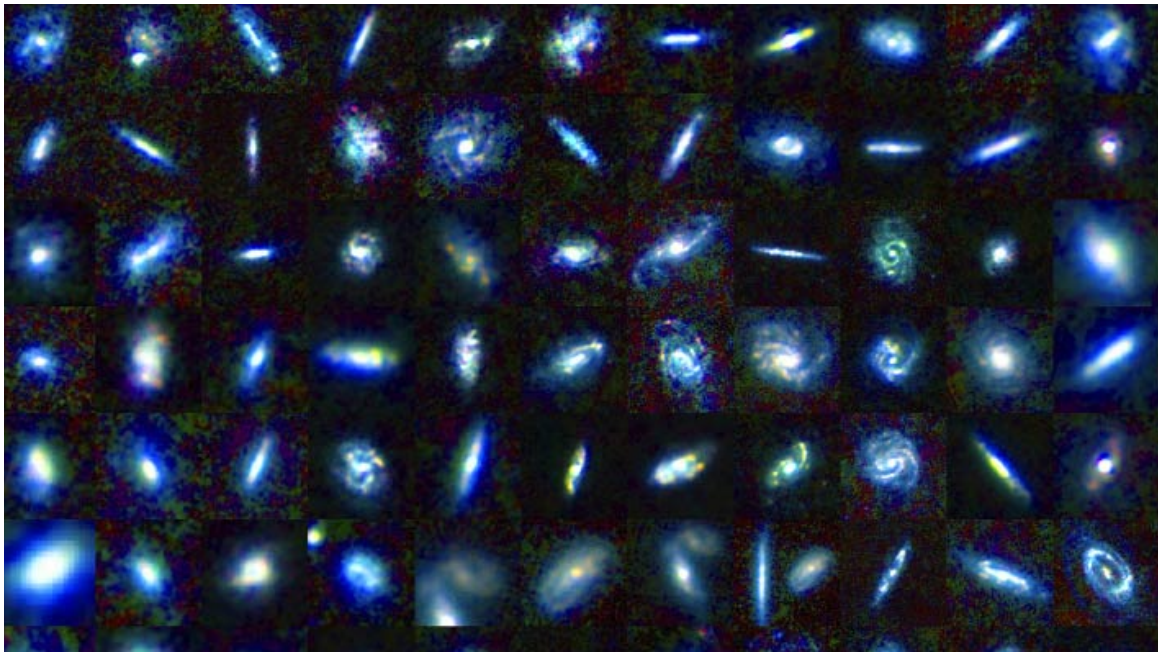

FIGURE 1.6 *Herschel* 3-colour image of 66 galaxies from the Herschel Reference Survey (Boselli et al., 2010). Credit: L ESA/Herschel/HRS-SAG2 and HeViCS Key Programmes/Sloan Digital Sky Survey/L. Cortese (Swinburne University).

in general. Firstly, the galaxies are all located in the range $15 < D < 25$ Mpc. At these distances it is possible to obtain resolved images of some of the galaxies and discern individual features. The sample was also selected by K-band flux, firstly to reduce the bias which would be inherent in an optical selection (the near-infrared is less affected by dust extinction than the optical region of the spectrum) and secondly to act as a tracer of the total stellar mass of the galaxy (which is thought to be important when studying the evolutionary properties of galaxies, see Boselli et al. 2010 for details). The sample includes galaxies of a range of luminosity and many different morphological types (example shown in Figure 1.6). As with regions of the H-ATLAS survey, the target sample are all located near the galactic poles. This is to reduce the effects of dust emission from our own galaxy, which improves the images that can be obtained.

1.3.3 DWARF GALAXY SURVEY

Another *Herschel* guaranteed time project for observing local galaxies was the Dwarf Galaxy Survey (Madden et al., 2013). In this survey, 50 dwarf galaxies were targeted. For this sample of galaxies, 48 have complete *Herschel* photometric data. The target galaxies cover a wide range of metallicity, including one of the most metal

poor galaxies known (I Zw 18, at $\sim$ 1/30 of solar metallicity Fisher et al. 2014) and were chosen to study the gas and dust properties in a range of low metallicity environments. Being a guaranteed time project, the DGS had an allocated 230 hours of observing time. Observations were again made using both the SPIRE and PACS cameras with a medium scan speed, to increase the quality of the data obtained. Combined with the *Herschel* data, this helps to build a complete picture of the low metallicity galaxies.

1.4 An overview of SED modelling

Obtaining physical properties from the multiwavelength SED is a complex and multi-stage problem. Typically, SED modelling software compares a library of templates against the observations, and the templates which produce the best match with the observations provide an indication of the physical properties of that galaxy. In Section 1.4.6 we introduce the model of da Cunha et al. (2008) which we use in this thesis to obtain the individual star formation properties of the galaxies in our sample. In this section however, we take a closer look at the process of producing the spectral libraries which are compared against the observations; a process which is known as stellar population synthesis.

1.4.1 Stellar Spectra

The resultant SED of a galaxy, is the product of the combined light from all the individual constituents of the galaxy. Stars are the ultimate source of the majority of radiation within a galaxy, and so form a good starting point in the process of stellar population synthesis. Stellar population synthesis is the creation of templates which are capable of reproducing the observed SEDs of a galaxy (Tinsley, 1978). It is necessary to understand both how stars of different mass progress through their life and the light that they will produce during each stage of their evolution. Of course the mass and metallicity of the star will strongly effect both of these processes, and so it is necessary to cover a wide grid of stellar mass and metallicity to build a complete database of stellar spectra.

Stellar libraries containing the above information can be constructed in two distinct ways. They can be obtained from complex simulations which attempt to describe a range of physical processes in the star (Gunn & Stryker, 1983). Alternatively they can be constructed from observational libraries, where individual observations of different types of stars are combined to produce a full library of the stellar spectra

(Martins et al., 2005). There are several advantages and disadvantages to using each type of method to produce the stellar libraries; in this section we will discuss the methods in more detail.

The primary advantage of using observations to construct stellar libraries is that the observations will not be limited by the current level of physical knowledge, and will not be biased by theoretical assumptions. You can observe a star of given mass and metallicity, and directly measure the stellar spectra at that stage of its life. The fundamental limit with observations comes from the fact that stars do not spend an equal fraction of their lifetime in all stellar phases. Short lived phases, such as the Asymptotic Giant Branch (AGB) phase for low to intermediate mass stars, will be poorly sampled by observations since there will not be as many examples which can be observed. Other rapid evolution phases, such as the main sequence phase of very high mass stars, will also be poorly sampled (eg Cenarro et al. 2007). In contrast the main sequence phase accounts for the majority of the lifetime of a low to intermediate mass star, and so this region of parameter space will be highly sampled. The volume of space which can be used to obtain the observations of the stars is also limited, and this relates directly to the resolving power of the telescope which is used. Therefore certain regions of the parameter space are often poorly sampled, which would lead to greater uncertainty in the modelling of the SED of these regions.

Simulations bypass the sampling restriction of observations enabling an equal coverage of the parameter space to be obtained. The parameter space coverage is limited only by the amount of computational time and power which is available to perform the simulations. The accuracy of the simulation is limited by the current theoretical understanding of the physics which governs the evolution of the stars. If crucial physics is left out, through assumptions or lack or knowledge, then the simulations will be biased. An example of this would again be the AGB phase of low to intermediate mass stars. It is known that these stars experience significant mass loss during this stage of their evolution, however it is not straightforward to calculate the exact quantities, since this depends on several physical conditions. Also, it is not clear how much dredge up these stars will experience (Stancliffe & Jeffery, 2007), this is where material is circulated between the outer layers of the star and the stellar core. The amount of dredge up depends on how far the convective envelope of the star moves inwards towards the core. The strength of dredge up will effect the chemical make up of the surface of the star (Sweigart et al., 1990), and will also alter chemical make up of the mass which is dispersed into the ISM through stellar winds.

1.4.2 Simple Stellar Populations

The next stage in the process of stellar population synthesis is to determine the spectrum that will be produced from a group of stars. All stars within this group, commonly referred to as a simple stellar population (SSP), are assumed to have formed at the same time and will therefore have the same age and initial metallicity (Maraston, 2005). Determining the fraction of stars of each mass that will have been created in a burst of star formation requires the assumption of an initial mass function (IMF).

Observations of star forming regions in our Galaxy using *Herschel* have started to provide indications on the origin of the IMF (Hill et al., 2010; Könyves et al., 2010). This is made possible because the FIR and sub-mm wavelengths which *Herschel* observes enable the inside of star forming clouds to be observed, such as the Aquila region. These observations have indicated that the IMF is directly linked to the process of star formation, and is not a subsequent effect of selection on the life of the stars. Most stars form deep inside giant molecular clouds (Krumholz, 2011), and they form when a section of the cloud becomes gravitationally bound and starts to collapse. As the star forms it passes through many different stages of evolution, from a pre-stellar core and protostar to finally a fully formed star (Ward-Thompson et al., 1994). As this formation occurs, the protostar generates significant energy due to the gravitational collapse, and heats up. The temperature of the pre-stellar core and protostar are such that they generate emission in the FIR and sub-mm. By creating a full sample of the pre-stellar cores and protostars for a star forming region, such as Aquila, it is possible to construct a Core Mass Function (CMF). Comparisons between the CMF and IMF, including an efficiency of formation factor of approximately 15%, show that the mass distribution observed in the IMF is present even in the earliest stages of star formation (Anathpindika, 2013).

The choice of stellar IMF will have a direct consequence on the properties of the galaxy which are determined from the SED modelling. In this work, we use the stellar population synthesis model of Bruzual & Charlot (2003) which assumes a Chabrier (2003) IMF. It is possible to convert properties which are determined using the Chabrier (2003) IMF, such as the star formation rate and stellar mass, to those that would have been obtained if a different IMF had been assumed following simple conversions available in the literature (Madau & Dickinson, 2014).

Armed with this information it is possible to calculate the light that will be produced by a SSP, Conroy (2013):

$$f_{\rm SSP}(t, Z) = \int_{m_{\rm low}}^{m_{\rm up}(t)} f_{\rm star}[T_{\rm eff}(M), \log g(M)|t, Z]\phi(M)\, dM \tag{1.8}$$

where $f_{\rm SSP}$ is the light produced by the SSP, t is the age of the SSP and Z is the metallicity. $f_{\rm star}$ is the spectrum of a single star as determined by the stellar libraries described in the previous section, and determines on the effective temperature of the star $T_{\rm eff}$ and metallicity of the star, Z. The integral is performed over the limits of $m_{\rm low}$ which is the lowest mass of star (typically assumed to be $0.1\,{\rm M}_{\odot}$) and $m_{\rm up}(t)$, which is the highest mass of star that has a main-sequence lifetime longer than the age of the galaxy at time t since the formation of the SSP in a burst of star formation. Finally, $\phi(M)$ is the IMF, indicating the fraction of low and high mass stars that will form in a quantity of star formation.

1.4.3 Composite Stellar Populations

Simple stellar populations, and the elements which go into constructing them, are the building blocks for composite stellar populations which ultimately form the full SED of a galaxy. There are three main differences between a simple stellar population and a composite stellar population (CSP) (Conroy, 2013). CSPs have a range of ages, which are determined by their associated star formation history. CSPs also contain stars with a range of metallicities since the average metallicity of the galaxy changes over its lifetime. Finally, CSPs include dust, and model the effect it will have on the final spectrum.

The fractional contribution of the total flux from different stellar populations is a function of wavelength. High mass stars are a powerful source of UV radiation (Maraston, 1998) and evolve on short ($\sim$Myr) timescales. Therefore, a young SSP will contribute strongly to the total UV output of a galaxy, whereas an older SSP will contribute very little at these wavelengths. The longer wavelength radiation produced by stars of lower mass, which also have longer main sequence lifetimes, will depreciate less with age. The flux contribution of SSPs is a function of age and wavelength. The fractional contribution, or weighting, of SSPs is therefore also a function of the star formation history of the galaxy (Papovich et al., 2001). However, if the rate of star formation changes over the lifetime of the galaxy, then SSPs will contain a different fraction of the stellar mass, and this will impact their contribution to the total flux.

Dust absorbs the UV and optical radiation from stars, and remit this light at longer wavelengths. Therefore, when SSPs are combined to create the CSPs which populate the stellar synthesis libraries it is necessary to determine the effect will have on the final CSP. In many stellar population synthesis codes, dust is included via

an attenuation law (eg Calzetti 2001)[1]. There are several attenuation models in the literature, and these vary due to the assumptions that are made on the geometry of dust grains. However, the effect they have on the light from the CSP is the same: redistribute a fraction of the UV and optical light produced by stars over infrared and sub-mm wavelengths.

1.4.4 Age metallicity degeneracy

It is worth noting here that there is a well known degeneracy between the age of a CSP and its metallicity (O'Connell et al., 1986; Worthey, 1994). Age will cause a stellar population to become steadily more red in colour, since the young massive blue stars will die and only the older low mass stars, which are intrinsically more red, will remain. Metallicity has two affects on the SED of a galaxy. Increasing metallicity results in a cooler main sequence, through lower effective temperatures. A cooler main sequence will be more red in colour. Also, for a fixed effective temperature a higher metallicity will result in stronger absorption lines, which will also cause a reddening of the spectra. Worthey (1994) studied the age metallicity degeneracy, using a set of SPS models. They found that for young stellar populations it was possible to disentangle the affects of age and metallicity. However, for ages $> 5\,\mathrm{Gyr}$, the two processes were degenerate.

Bell & de Jong (2000) showed that it is possible to break the age metallicity degeneracy when using full broadband SED modelling. More specifically, the optical-NIR colours of CSPs can be used to separate age and metallicity effects. They found that using a combination of optical and near-infrared colours, it was possible to estimate the stellar metallicity of galaxies from photometric data. This has been tested against spectroscopically derived age and metallicity (Eminian et al., 2008). The caveat to this is that the metallicities which are derived from broadband SED modelling depend directly on the models which are used. Therefore in principle it is possible to separate age and metallicity, however two separate models will disagree in the precise values obtained.

1.4.5 The Star Formation History of Galaxies

In this section, we review various methods which can be used to determine the SFH of individual galaxies. Standard models such as these may provide an accurate

[1] The attenuation law describes the combined extinction and scattering that will be experienced as a function of wavelength

representation of the SFH in some galaxies. However, standard SFHs are not directly related to the observations of a specific galaxy.

There are several techniques that can be used to recover the SFH of a galaxy from observations and the method that is chosen largely depends on the data that is available for a given galaxy. One of the most robust methods of recovering the SFH is to analyse resolved stellar populations within the target galaxy with colour-magnitude diagrams, although even this many not be free of ambiguity (Lilly & Fritze-v. Alvensleben, 2005). While this is the ideal method to obtain the star formation history it is somewhat limited in scope, since telescopes have a finite resolving power. Only galaxies within our local neighbourhood can be analysed in this manner and these galaxies do not form a representative sample of all galaxies within the universe (van den Bergh, 2000).

An example of using resolved stellar populations to recover the SFH of a galaxy would be the study of M31 (Brown et al., 2003). Observations were made to obtain the colour-magnitude diagram of M31 with the aim of determining the luminosity distribution of AGB stars; such observations would indicate the age distribution of the stellar population. Combining this information with an assumed stellar Initial Mass Function (IMF), such as Chabrier (2003), enables the complete SFH of the galaxy to be reassembled. Investigations of the SFH of M31 suggest that the galaxy experienced a significant merger event; evidence for a large merger event has also been suggested from numerical simulations of the galaxy (Fardal et al., 2008).

The SFH of the Large Magellanic Cloud (LMC) has also been the subject of investigation by means of colour-magnitude diagrams. Dolphin (2000) perform the study for two independent fields within the LMC, their results show that star formation began ~ 12 Gyrs ago. Both fields experienced similar SFHs, with a significant increase in star formation approximately 2.5 Gyrs ago; the SFH of the fields show some deviation within the last 200 Myr. Zhukovska & Henning (2013) used the SFH of the LMC to investigate the production of dust over the entire history of the LMC, finding that AGB stars are the major stellar dust source after the first 200 Myr (before which stellar dust production was dominated by high-mass stars).

Despite the success of resolved star fields in the recovery of the SFH of a galaxy, it is clear if studies of the chemical evolution of large representative sample of galaxies are to be completed then alternative techniques to recover the SFH are required. When the stellar populations cannot be individually resolved it is still possible to compare the spectrum of a galaxy against a series of stellar population templates to reconstruct the formation history.

Cid Fernandes et al. (2009) and González Delgado et al. (2014) use optical

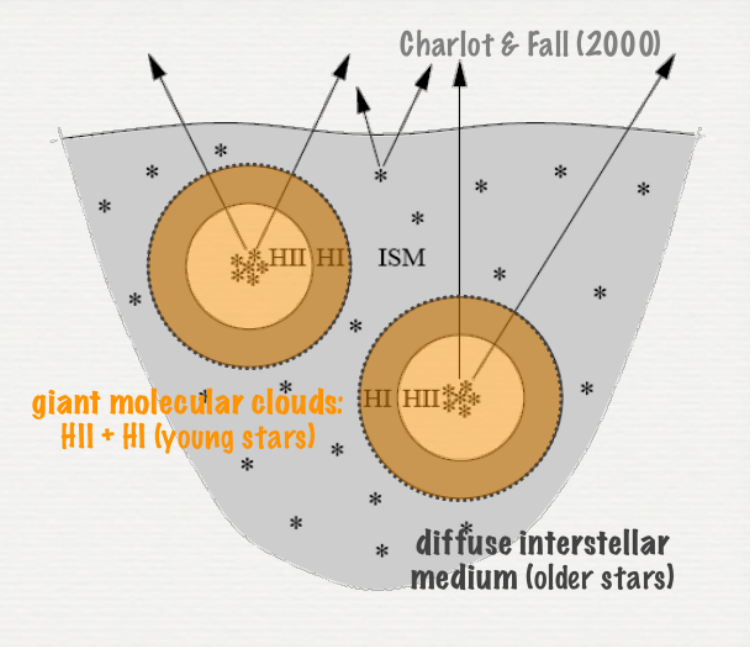

Figure 1.7 A cartoon depiction of the attenuation experienced by stars of different ages in the MAGPHYS model. The attenuation is a time dependent model; young stars formed in stellar birth clouds will experience higher attenuation by dust grains than older stars located in the diffuse interstellar medium. Figure from a presentation by E. da Cunha 2010.

spectra to obtain the SFH for a large sample of galaxies, using this to estimate the age and metallicity gradients of 200 galaxies. Vast numbers of optical spectra are now becoming available, this is primarily due to all sky surveys such as the Sloan Digital Sky Survey (SDSS). The analysis of the optical spectra is often completed through comparison with spectra generated through stellar population synthesis codes such as Bruzual & Charlot (2003).

Different software has been designed to analyse the spectra of galaxies in this manner, examples of which are the models of STARLIGHT (Cid Fernandes et al., 2009) and MOPED (Reichardt et al., 2001). Operationally the codes vary in the numerical techniques which they employ, and this effects the speed and resolution to which they work. In essence the underlying method employed in both codes is the same: use the spectrum of a galaxy to infer information about the unresolved stellar populations and hence, by comparison with a set of SSPs, reconstruct the SFH of the galaxy.

1.4.6 MAGPHYS

The full panchromatic SED of a galaxy contains vital information about the key components of the galaxy; namely the stars, gas and dust. Understanding what physical processes are responsible for the specific parts of the SED is therefore, as previously mentioned, of great importance in the study of the formation and evolution of a galaxy. There are multiple methods by which the SED of a galaxy can be modelled, and potentially the most powerful of these techniques is full radiation transfer calculations for a galaxy; in such a code the path of the light, which is generated by a stellar population, through a dusty ISM is calculated. Use of radiative transfer codes are limited though, because the complexity of the simulations rises rapidly as more factors are included into the model. The computational time is considerable for even a single simulation, therefore this method is currently unsuitable for the study of a large sample of galaxies.

The method that is implemented in this report is to analyse the SEDs of galaxies using the MAGPHYS model of da Cunha et al. (2008); MAGPHYS employs an energy balance criteria to self consistently model the emission of a galaxy from UV to sub-mm wavelengths. The energy balance is achieved by declaring that the energy which is attenuated from stellar emission, as it passes through the galaxy, will be fully re-emitted at infra-red and sub-mm wavelengths by dust. This section outlines the workings of the model, and discuss how the model is used for the work later in this thesis.

MAGPHYS requires a set of photometric observations of a galaxy as the input, these should range from the UV to sub-mm wavelengths. Initially the attenuation of the stellar emission due to dust in the target galaxy is calculated using the prescription presented in Charlot & Fall (2000):

$$L_\lambda = \int_0^t dt' \, \psi(t - t') \, S_\lambda(t') \, e^{-\tau_\lambda(t')} \tag{1.9}$$

where L_λ is the luminosity per unit wavelength emerging at time t from a galaxy illuminated by an internal stellar population, for wavelength λ. $\psi(t - t')$ gives the stars that were formed at a time $t - t'$, since ψ is the star formation history. $S_\lambda(t')$ gives the flux that is emitted by the stellar population of age t'. The exponential is the term which is responsible for the absorption of the radiation. τ_λ is the effective optical depth that is seen by stars in the galaxy, this is a time varying term because of where stars form; when a star forms it is located in a stellar birth cloud, so the optical depth is higher. After a set time the radiation from the newly formed star disperses the birth cloud. Therefore newly formed stars are more strongly attenuated

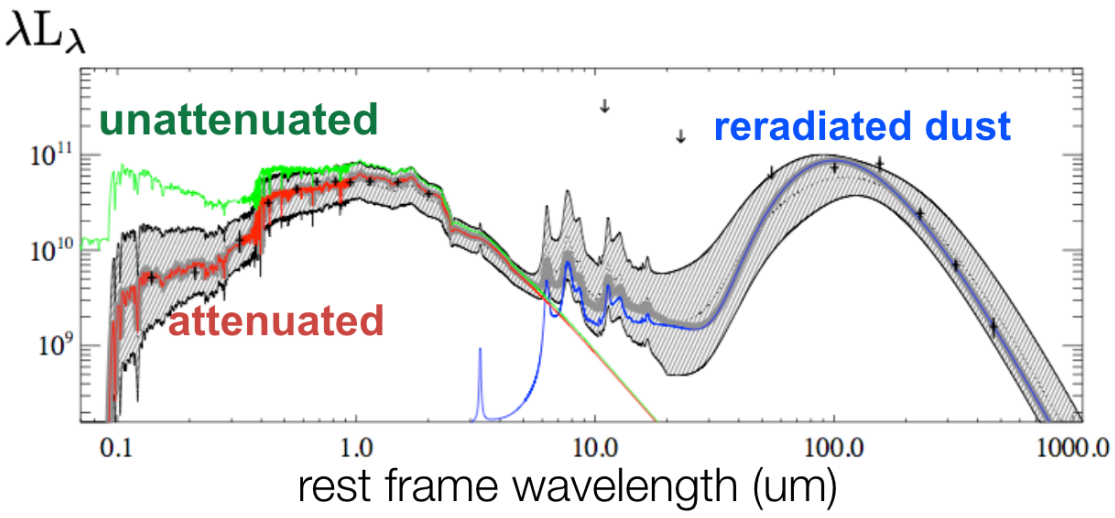

Figure 1.8 Cartoon depiction of the SED of a galaxy, as modelled by MAGPHYS. The unattenuated light from all stars in the galaxy (in the case that there was no dust in the galaxy) is shown in green. The attenuated light (red line) shows the FUV and optical light that we would observe, as a fraction of the radiation has been absorbed by dust grains (following the model of Charlot & Fall 2000). The blue line shows how this energy is re-radiated in the infrared and sub-mm wavelengths (following the dust model of da Cunha et al. 2008).

in this model than older stellar populations (see Figure 1.7).

Once the attenuated radiation has been calculated it is possible to recover the amount of energy that has been absorbed and hence the total infra-red luminosity can be calculated from the energy balance criteria. To understand the form of the infrared emission from a galaxy it is necessary to redistribute the total infrared luminosity over the full range of infrared wavelengths; this is achieved by having a complete model of the different dust components in the galaxy. In the MAGPHYS model the infra-red emission is contributed to three main sources, these are: polycyclic aromatic hydrocarbons (PAHs); small dust grains and, finally, large dust grains. PAHs are generally considered to be the molecules which are responsible for strong emission features in the near infra-red part of the SED. These molecules are transiently excited by the absorption of UV photons from stellar radiation. The PAH molecule then de-excitates producing strong line emission features at 2.2 μm.

In the mid-infrared region of the SED there is also continuum emission, this is contributed to the emission from small dust grains; these small dust grains have a very low heat capacity and therefore get heated to high temperature by the absorption of single UV photons. These dust grains emit as a modified blackbody, and hence produce continuum emission. The final part of the model are larger dust grains which

are in thermal equilibrium with the interstellar radiation field. In the stellar birth clouds the grains are modelled as a blackbody of temperature $T_W^{BC} = 30 - 60\,K$; this is because in birth clouds the dust is heated by young protostars which are forming in the cloud. In the interstellar medium, away from the heating effect of protostars in the birth clouds, there is also dust of a colder temperature. Hence in the interstellar medium there is a two component model of dust dust is modelled, having temperatures $T_W^{ISM} = 30 - 60\,K$ and $T_C^{ISM} = 15 - 25\,K$. The spectral index $\beta = 1.5$ for warm dust, and 2.0 for the colder dust.

Figure 1.8 shows how the elements of the model described above work to reproduce the full UV-FIR SED of a galaxy. Using this simple but effective model for the infra-red emission from dust in the galaxy, combined with the self consistent energy balance criteria and the stellar synthesis code of Bruzual & Charlot (2003), it is possible to create a complete set of templates for the SEDs of galaxies. These templates can be used to rapidly produce accurate fits for a large sample of galaxies.

1.5 Chemical Evolution Modelling

In previous sections we have seen how multiwavelength SED modelling with MAGPHYS presents the opportunity to obtain individual star formation properties for an entire sample of galaxies. In this thesis we aim to determine how the star formation properties, such as the star formation history, affect the chemical evolution of the galaxies. We wish to determine for example whether galaxies which have experienced more recent bursts of star formation exhibit different dust properties to galaxies in the sample which have undergone more quiescent periods of star formation. To investigate these effects we must turn to the subject of chemical evolution models; these models provide a framework where it is possible to untangle the different dust sources that are present in a galaxy by matching the predicted properties of a model galaxy to the observed properties of the galaxies in the sample.

Chemical evolution models tie together many of the different topics which have been introduced in this chapter so far, from star formation histories, stellar IMFs and stellar mass loss to dust grain growth and destruction, to create a cohesive picture of how the properties of a galaxy will change throughout its evolution. In this section we take a brief look at the various stages of modelling the chemical evolution of a galaxy.

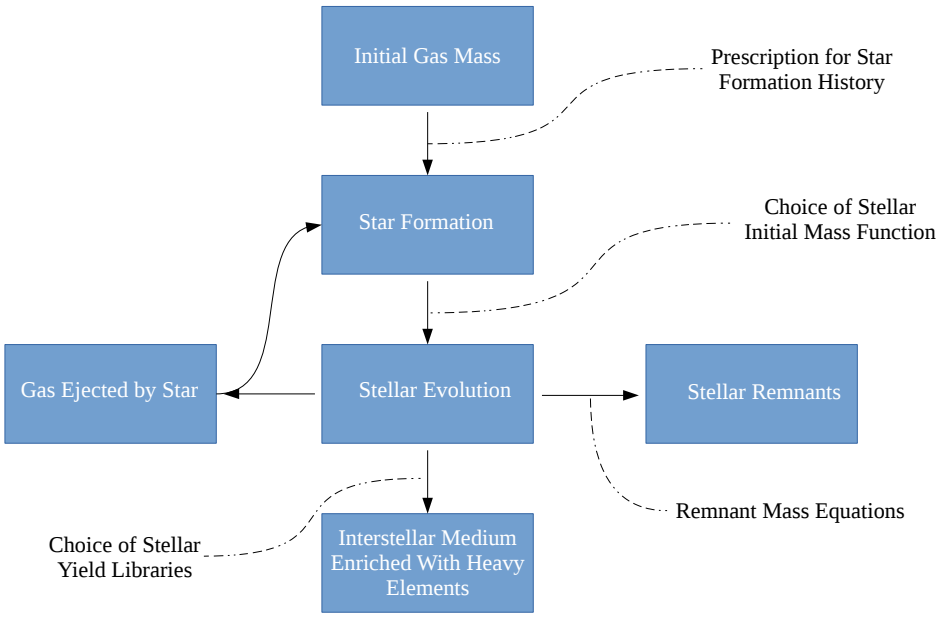

Figure 1.9 Simple flow-chart demonstrating the different stages a galaxy progresses through in a chemical evolution model. This also highlights how our choices of input libraries and equations can affect the calculations. Note that this model does not account for mergers or interactions of galaxies.

1.5.1 Simple Picture for the Evolution of a Galaxy

The basic aims of chemical evolution modelling are quite simple; use a theoretical framework to produce predictions for observational parameters which can be used to explain the distribution and abundance of chemical elements in a galaxy. To provide such a framework, we must have a general model which explains how a galaxy will evolve. Figure 1.9 shows a diagram of the evolutionary path that galaxies are assumed to follow in this work. In this model, we make the assumption that the life of a galaxy starts as a cloud of primordial gas, which is composed from elements which were formed in the big bang. According to standard big bang physics, such a primordial gas cloud should be composed primarily of hydrogen and helium with trace amounts of other light elements, such as lithium, also being present (Fumagalli et al., 2011).

As time progresses the infantile galaxy will experience some level of star formation. These stars will form out of the initial cloud of gas, and so overtime the gas fraction of the galaxy will decrease. The amount of star formation which occurs at

any given time can be described by the star formation history of the galaxy. In a given quantity of star formation the amount of high and low mass stars which form will depend of the stellar IMF which is assumed for the galaxy. Due to the variation in lifetime between high and low mass stars, the choice of IMF will have a direct effect on the rate of chemical enrichment in the galaxy.

Once stars have formed they will progress through their lifetime gradually fusing the initial gas into heavier elements. When the stars reach the end of their lifetime, some fraction of the initial stellar mass will be returned to the interstellar medium of the galaxy, although it will now be enriched with the heavy elements produced by the star. The mass which is returned to the interstellar medium is then available for production of a second generation of stars, and by this process of recycling of gas between stars and the interstellar medium the galaxy will steadily become enriched with an increasing number of heavy elements.

The cycle of star formation is not completely efficient since not all the initial gas in a volume of star formation will be returned to the interstellar medium of the galaxy. Firstly, we must consider that very low mass stars have very long main sequence lifetimes and will act as a gas sink, locking up the gas from the interstellar medium on very long timescales. Secondly, as we can see from Figure 1.9, some of the mass which is used in a volume of star formation will end up in stellar remnants. These stellar remnants, such as white dwarfs, neutron stars and black holes, permanently remove the gas from the interstellar medium of the the galaxy. Even if we assume a closed system, where there are no fresh inflows or outflows of gas into the galaxy, we will find that due to star formation the gas fraction of the galaxy will decrease with time.

As the metallicity of the galaxy increases due to stellar activity, it is thought that the dust mass of the galaxy will also increase. To predict the amount of dust which will be present in the interstellar medium of the galaxy it is necessary to consider the interplay between the different dust sources and dust sinks in the galaxy. Dust formation in the outflows of evolved stars and grain growth in the interstellar medium of the galaxy will increase the dust mass. However dust astration in star formation and dust destruction in the diffuse regions of the galaxy will act to decrease the dust mass.

The complexity of the above picture for galaxy evolution can be increased by including additional physical processes, such as inflows and outflows of gas from the galaxy to the intergalactic medium. Also, the results will vary depending on the choice of input libraries. How much metals and dust are stars of different mass thought to produce over their lifetime? What fraction of the initial gas mass will be locked up in

stellar remnants? The equations for the chemical evolution model, the impact which our choice of input libraries has on the results which are obtained and the updates we have made to the model since its previous incarnations in Morgan & Edmunds (2003); Rowlands et al. (2014) are explored in full in Chapters 4 and 5.

1.6 Aims of the Thesis

In this section we present the key science questions that we aim to answer during the remainder of the thesis. We return to these questions, and our solutions to them, in Chapter 7.

1. Can we use SED modelling to constrain the SFH of the galaxies in our sample?
2. Are the dust properties of these galaxies related to features in their SFH?
3. What is the relative balance of dust sources to the dust budget in nearby galaxies?
4. Is the dust-to-metal ratio constant in all galaxies, and if not, what drives the change?

1.7 Overview of Thesis Structure

In this chapter, I have aimed to introduce the key concepts which are relevant to understanding the research that is presented in the following chapters of this thesis. By providing an overview of the current state of research in the field, I have also aimed to provide the motivations to understand why this research is of interest and how it contributes to our understanding of dusty galaxies in the local universe.

The remainder of the thesis is structured as follows. In Chapter 2, I introduce in detail the samples of nearby galaxies, observed with *Herschel*, originally introduced in Clark et al. (2015) and De Vis et al. (2016). These intriguing galaxies, with high specific star formation rates, blue optical colours and lots of dust, form the main sample of galaxies which I investigate in this thesis. Here I present an analysis of the challenges faced when modelling the SED of these galaxies, providing an in depth account of the adaptations which are needed to obtain reliable fits to the observations. I also explain the method used to attempt to constrain the individual star formation histories of these galaxies (see Schofield et. al. in prep, De Vis et al. 2016, de Vis, Schofield et al submitted).

In Chapter 3, I then analyse the star formation histories of the galaxy samples. Here I explore how star formation histories of the galaxies relate to their other physical properties such as dust mass. I also explore the difference between the median star formation history of the two galaxy samples, and investigate whether this can explain the key differences between these samples (see Schofield et. al. in prep). I then investigate how well the star formation parameters obtained from the multiwavelength modelling relate to those obtain from other methods. I analyse the available optical spectra of the galaxies, and use tracers, such as the emission line strengths, as an independent measure of the star formation activities in these galaxies.

Chapters 4 and 5 provide a detailed account of the features I have helped to introduce, test and update in the chemical evolution model; the code, which was previously used in Morgan & Edmunds (2003); Rowlands et al. (2014) has also been converted to Python, and is available for download from GITHUB [2]. I also explore the effect that the choice of both the star formation history and the stellar initial mass function has on the evolution of a galaxy.

In Chapter 6, which is based on de Vis, Schofield et al submitted, I then use the chemical evolution model to investigate the contribution of different dust sources by compiling a large sample of ~ 400 *Herschel* sources, which cover a wider range of properties than studied before. I explore variations in the dust to metal ratio in these galaxies, and compare our results to the properties of other *Herschel* surveys. I also investigate how the use of different star formation histories enables us to reproduce the observed properties of galaxies in the local Universe over a wide range of metallicities and gas fractions.

[2] https://github.com/zemogle/chemevol

Chapter 2
Investigating Nearby Galaxies Using MAGPHYS: Limitations of the Model

2.1 Introduction

The galaxy samples we use in this thesis are obtained from the dust-selected sample in Clark et al. (2015) and the HI-selected sample in De Vis et al. (2016), where Spectral Energy Distribution (SED) fitting of $\sim 69\%$ of this sample is already published in the latter study. Here we employ the SED fitting routine MAGPHYS on the entire sample in order to investigate the star formation properties of dusty and non-dusty galaxies in the local universe. For each galaxy, we obtain a best fit SED, probability distributions of physical parameters and the best fit star formation history. We then analyse the best method to place a statistical constraint on the best fit star formation history of each galaxy. We find that although MAGPHYS describes galaxies at high-redshift and infrared bright galaxies well (eg da Cunha et al. 2008, 2015) MAGPHYS lacks information in regions of parameter space that fit the youngest and most star forming galaxies in our sample.

2.2 The Galaxy Samples

We use the H-ATLAS Phase-1 Limited-Extent Spatial Survey (HAPLESS) sample from Clark et al. (2015), which provides a dust-selected sample of 42 local galaxies ($15 < D < 46$ Mpc) from the the H-ATLAS Phase 1 internal data release

(Valiante et al., 2016; Bourne et al., 2016). Descriptions of the H-ATLAS data reduction can be found in Ibar et al. (2010) for PACS, and Pascale et al. (2011) and (Valiante et al., 2016) for SPIRE. Photometry in the SPIRE bands was performed upon maps calibrated for extended-source measurements (see Clark et al., 2015 for more details). We combine the dust selected blind sample from H-ATLAS (GAMA fields) with a HI-selected sample from the same area of sky (HIGH, De Vis et al. 2016). The HAPLESS sample is a blind, volume limited sample ($z < 0.01$) of 48 galaxies detected at $> 5\,\sigma$ at 250 μm. The blind HI-selected sample, HIGH, is extracted from the same H-ATLAS area and includes 40 unconfused HI sources. HIGH is not volume limited, but still represents a local sample of galaxies with $z < 0.035$.

The Phase 1 data release is coincident with the equatorial fields of the Galaxy And Mass Assembly (GAMA, Driver et al. 2009) redshift survey. There is a wealth of ancillary data for the HIGH and HAPLESS galaxy samples, ranging from the Far Ultraviolet (FUV) to Far Infrared (FIR), making them well suited to multi-wavelength SED fitting techniques. The GALEX satellite provides both FUV and Near Ultraviolet (NUV) data for the sample (Morrissey et al., 2007; Liske et al. 2016; Andrae et al., *in prep.*). SDSS DR7 (Abazajian et al., 2009) is used to obtain optical data in u, g, r and i bands. The VISTA VIKING survey (Sutherland, 2012) provides Near Infrared (NIR) data for the sample and Mid Infrared (MIR) observations are obtained from WISE (Wright et al., 2010; Cluver et al., 2014). We followed the method of Sanders et al. (2003) to obtain the IRAS 60 μm observations for the HAPLESS and HIGH samples using the Scan Processing and Integration tool (SCANPI). We discuss this in more detail in Section 2.3.2. Combined with the H-ATLAS data, these observations form a complete catalogue from the FUV to FIR wavelengths.

The HI Parkes All Sky Survey (HIPASS; Barnes et al. 2001) provides 21 cm coverage of the equatorial H-ATLAS and GAMA fields, and therefore provides the basic HI properties of our sample. The Arecibo Legacy Fast ALFA Survey (ALFALFA; Giovanelli et al. 2005) is both higher resolution and more sensitive than HIPASS, but does not provide full coverage of our sample. Therefore we use the HIPASS HI properties supplemented with ALFALFA where available.

The full photometry for the HAPLESS sample is presented in Clark et al. (2015) and for the HIGH galaxies in De Vis et al. (2016). All sources have reliable SDSS counterparts (R $\geq$ 0.8, Smith et al. 2011) and science quality redshifts (nQ $\geq$ 3, Driver et al. 2011) from GAMA [1]. Key properties, including redshift and morphology, of the HAPLESS galaxies are presented in Table 2.1, and the HIGH galaxies in Table 2.2. In this thesis, we focus on obtaining the global SFH properties of these

[1] A science quality redshift is defined as a probability of the redshift 'being correct' (p_z) of $p_z > 0.9$.

galaxies and explore how this may relate to their dust properties. Galaxy properties were calculated using the SED modelling tool MAGPHYS for all HAPLESS and HIGH galaxies.

There are several key advantages to using these samples rather than the 'benchmark' *Herschel* surveys of nearby galaxies (eg the HRS, Boselli et al. 2010). Firstly the blind 250 μm selection revealed an enigmatic population of very blue, dusty-and-gas-rich galaxies, dubbed 'Blue And Dusty Gas Rich Sources' (hereafter BADGRS). Surprisingly, these galaxies have high specific dust masses ($M_{\rm d}/M_*$) and cold (~ 15 K) dust temperatures, contrary to what might naively have been expected from their blue colours and high specific star formation rates. Clark et al. (2015) defined this population as having FUV-$Ks < 3.5$. The BADGRS are low to intermediate stellar mass ($10^8 - 10^{10}$ M$_\odot$) objects with irregular or flocculent morphologies and, in some cases, extended UV disks. Secondly, the two samples are highly complementary, and together they cover a wide range of gas fractions (see Chapter 6 and De Vis, Schofield et al *submitted* for details). While the blind dust selection of HAPLESS selects dusty galaxies which are located at a range of gas fractions, the blind HI selection in HIGH locates both dust-rich and dust-poor galaxies at the highest gas fractions. The range of gas fractions which we sample enables us to investigate the star formation properties of local galaxies at all stages of their evolution.

As described above, I did not perform the aperture photometry for these galaxies. Full details of the aperture photometry for these sources can be found in Clark et al. (2015) and De Vis et al. (2016) for HAPLESS and HIGH respectively. However, it should be noted that there are several galaxies in the HIGH and HAPLESS sample where there is a background of confusing sources near the source galaxy visible in *Herschel* wavelengths (HAPLESS 17 or HIGH 2 for example, see Figure 3.9 and 3.10 respectively). If unaccounted for these confusing sources would lead to a discrepancy in the value of the flux which is measured for these galaxies. Individually detected bright sources located within the source aperture are masked prior to performing aperture photometry, and therefore the flux from these galaxies does not contribute to the flux measured for the source. Furthermore, aperture photometry is performed on background subtracted maps, where the background is estimated through a plethora of randomly placed background apertures. The randomly placed apertures contain the same level of confused background sources as the source aperture, and will also contain the same variation of confused background sources. Therefore the flux and associated uncertainties produced will encompass uncertainty caused by the confused background sources.

Common name	HAPLESS	z	Distance Mpc	FUV-*Ks* MAGS	Morphology	R_{25} arcsec
UGC 06877	1	0.0038	19.9	3.08	-1	30.7
PGC 037392	2	0.0042	26.7	2.04	-	10.1
UGC 09215	3	0.0046	25.6	2.14	6	64.8
UM 452	4	0.0047	29.3	3.17	11	20.0
PGC 052652	5	0.0047	25.7	3.59	-	27.1
NGC 4030	6	0.0048	29.4	4.51	3	129.0
NGC 5496	7	0.0049	27.4	2.66	6	123.0
UGC 07000	8	0.0049	30.0	2.41	9	35.0
UGC 09299	9	0.0052	28.3	1.36	9	37.3
NGC 5740	10	0.0052	28.1	4.39	3	85.9
UGC 07394	11	0.0053	32.6	3.74	7	53.3
PGC 051719	12	0.0053	29.0	3.08	-	19.5
SDSS J145022.84+025730.5	13	0.0053	28.6	3.14		11.7
NGC 5584	14	0.0055	30.2	2.7	6	94.3
SDSS J144515.80-000934.3	15	0.0055	29.2	3.74		17.4
UGC 09348	16	0.0056	30.4	4.26	8	42.5
UM 456	17	0.0057	33.4	1.56	-	19.4
NGC 5733	18	0.0057	30.1	2.21	9	23.7
UGC 06780	19	0.0057	33.6	-99.9	8	101.0
NGC 5719	20	0.0058	30.7	7.00	1	113.0
NGC 5746	21	0.0058	30.9	-99.9	1	209.0
NGC 5738	22	0.0058	31.2	7.12	-2	22.2
NGC 5690	23	0.0058	31.6	4.96	3	85.1
UM 456A	24	0.0058	35.5	1.82	-	8.61
NGC 5750	25	0.0059	31.1	5.85	1	95.9
NGC 5705	26	0.0059	31.2	2.39	7	74.7
UGC 09482	27	0.0060	32.3	2.90	8	35.2
NGC 5691	28	0.0063	33.4	4.00	3	67.3
NGC 5713	29	0.0063	33.6	4.56	3	92.2
UGC 09470	30	0.0063	33.6	2.24	9	33.0
UGC 06903	31	0.0064	37.7	2.95	6	64.0
CGCG 019-084	32	0.0065	34.6	3.60	-	17.0
UM 491	33	0.0067	39.7	1.58	-	11.7
UGC 07531	34	0.0068	39.4	1.16	9	33.3
UGC 07396	35	0.0071	41.3	2.78	8	34.8
CGCG 014-014	36	0.0072	41.9	2.33	8	18.9
UGC 06879	37	0.0080	45.6	4.09	4	60.9
CGCG 019-003	38	0.0081	43.0	2.70	-	13.2
UGC 04684	39	0.0086	41.5	2.34	7	35.6
NGC 5725	40	0.0054	30.2	2.61	9	31.9
UGC 06578	41	0.0037	17.3	0.64	-	25.7
MGC 0066574	42	0.0062	33.4	2.48	-	4.34

TABLE 2.1 Table displaying key properties of the 42 HAPLESS galaxies, from Clark et al. (2015). Morphology is obtained from EFIGI (Baillard et al., 2011). Most of the sample are late type galaxies (with Morphology classification > 0), however HAPLESS 1 and 22 are identified as early type galaxies. A value of -99.9 in the FUV-*Ks* column indicates that the photometry was unavailable for one of the wavebands.

Common name	HIGH	Distance Mpc	z	FUV-*Ks* MAGS	Semi-major-axis arcsec
UGC06970	1	30.31	0.005	3.38	59.32
NGC4030b	2	38.36	0.0065	2.45	59.29
UGC07053	3	30.13	0.0048	1.63	69.18
UGC07332	4	13.91	0.0032	1.86	88.95
FGC1412	5	11.32	0.0030	1.94	42.78
CGCG014-010	6	11.84	0.0031	1.79	49.40
UGC04996	7	57.25	0.012	2.37	53.24
NGC4202	8	93.20	0.019	4.94	53.24
SDSSJ084258.35+003838.5	9	158.93	0.035	2.78	26.62
2MASXJ14265308+0057462	10	120.35	0.026	3.39	34.86
SDSSJ143353.30+012905.6	11	32.99	0.0061	2.59	49.40
IC1011	12	117.95	0.026	3.30	41.02
IC1010	13	118.19	0.026	3.78	59.32
UGC04673	14	59.73	0.013	1.64	41.02
UGC09432	15	28.53	0.0051	1.56	56.00
UM 501	16	39.49	0.0068	0.72	25.59

Table 2.2 Table displaying key properties of the 16 HiGH galaxies from De Vis et al. (2016). A value of -99.9 in the FUV-*Ks* column indicates that the photometry was unavailable for one of the wavebands.

2.3 Spectral Energy Distribution With MAGPHYS

In this chapter we use the multiwavelength SED modelling software MAGPHYS to analyse the HiGH and HAPLESS sample of galaxies. The version of MAGPHYS that we use has been modified from the standard version of da Cunha et al. (2008) (described in Chapter 1, Section 1.4.6), here we provide a summary of the key changes.

1. We have modified the way that MAGPHYS treats very low signal-to-noise fluxes. Some of the measured fluxes for HiGH and HAPLESS in the FIR are negative, but have errors which are consistent with zero or positive fluxes (at 1σ). By including these fluxes in the fitting process, we can place additional constraint on the data.

2. We have extended the number of galaxy parameters that MAGPHYS outputs statistical information for, such that we can include these additional parameters

in our analysis. These include the 'time since last burst' of star formation ($t_{\rm burst}$) and the 'light weighted mean age' of a stellar population ($\rm age_r$). Further analysis of these parameters is presented in Section 2.7.

3. We have changed the code such that the best-fit star formation history (SFH) selected by MAGPHYS as the best fit model to the data is included in the output for each galaxy. We describe the MAGPHYS SFHs and our attempts to improve upon using the best-fit in Section 2.4.2.

During the remainder of this chapter, we make additional changes to the input libraries for MAGPHYS, to improve the quality of SED fits obtained. A full description of the final changes that we made are provided in the following sections.

2.3.1 SED Modelling Results with MAGPHYS (A First Attempt)

The best-fit multi-wavelength SED was recovered for each galaxy in the HiGH and HAPLESS sample, example fits (for HAPLESS 3 and 14) are shown in Figure 2.1. The galaxies generally show a good fit, with low reduced χ^2 values. An unidentified MIR-FIR 'bump' is observed in the SEDs of many of the galaxies, centred around 60 μm. The 'bump' indicates that the model could be unconstrained in this wavelength range, due to a lack of photometry, or could potentially suggest the need for more warm dust. We investigate this further in Section 2.3.2.

Figure 2.2 shows an example of the physical parameters that are obtained for the galaxies (see caption for full description). MAGPHYS outputs a probability distribution function (PDF) for many physical parameters. The peak of the PDF gives the best-fit value for the parameter, the width of the PDF gives the uncertainty of the value. The red and blue lines on the PDFs indicate the mean and median values of the distribution respectively. The dust mass and SFR of the galaxy in this example (HAPLESS 3) are well constrained parameters, since they have a narrow distribution, however the temperature of the different dust components is less well constrained by the model. These PDFs were obtained for each galaxy within the sample. In many cases, the cold dust component does not show a peak within the range of the PDF (eg HAPLESS 3), and appears to rise at the lower end of the distribution (at the coldest temperatures). This feature can be highlighted by the stacking the cold dust PDF for all our galaxies within the sample (Figure 2.3). The stack was created by splitting each PDF into bins across the range of the prior. The value of the stacked PDF was then taken as the median value of the parameter obtained for every galaxy in each

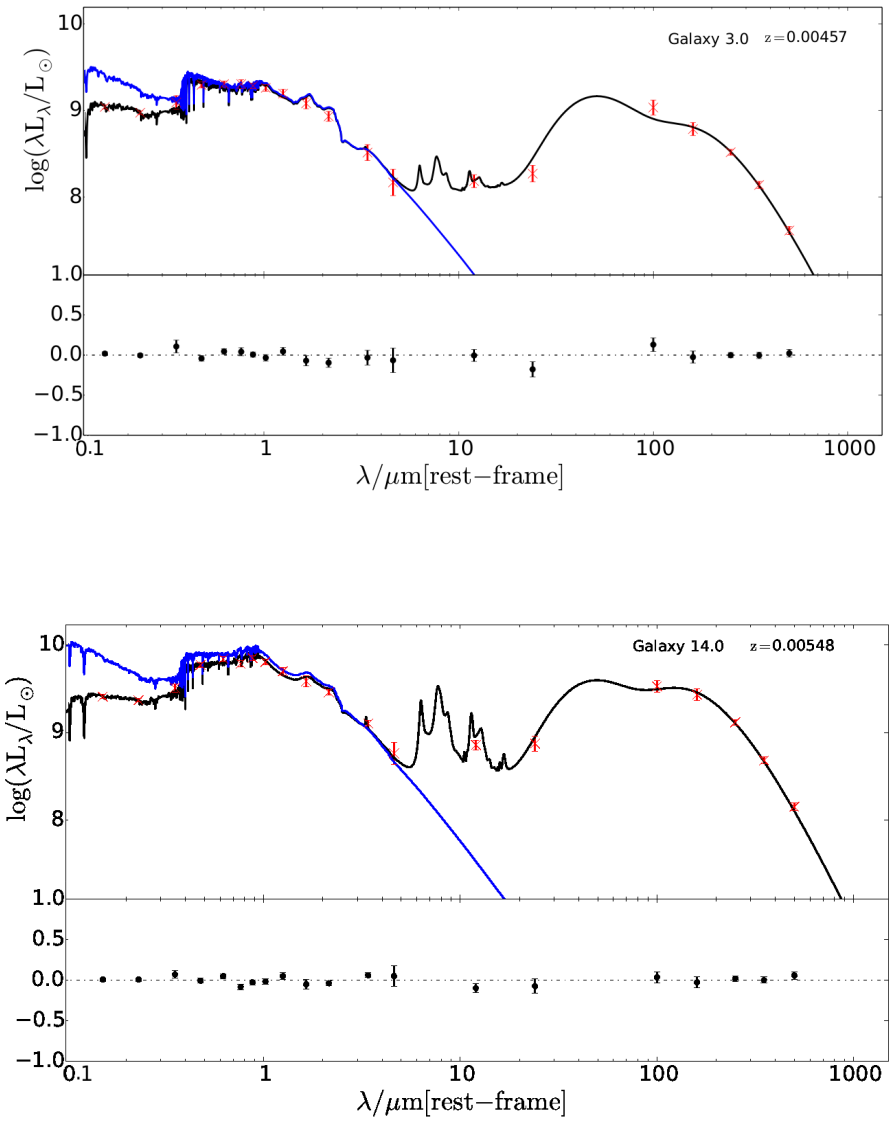

Figure 2.1 Example MAGPHYS Spectral Energy Distributions (SEDs) for two galaxies (HAPLESS 3 and 14) from our HiGH and HAPLESS samples (Tables 2.1 and 2.2). This run is using default parameters for MAGPHYS and UV-FIR data from H-ATLAS. The blue line shows the recovered stellar emission from the galaxy if there was no absorption from dust. The black line shows the SED model that best-fits the photometric data points, which are shown in red with corresponding error bars. The bottom section of each plot shows the residuals of the fit. In these examples, MAGPHYS is unconstrained in the FIR region of the SED which results in the potentially non-physical 'bump' feature, around 60 μm.

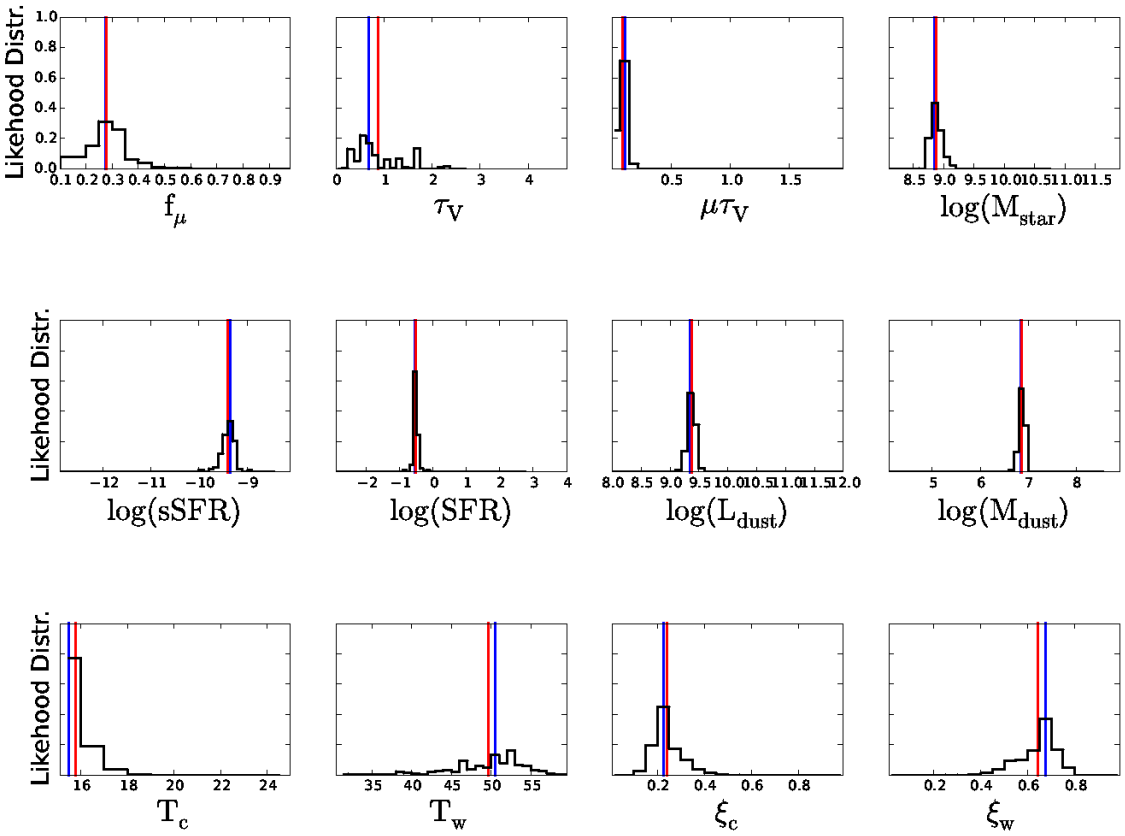

FIGURE 2.2 A selection of probability density functions for the parameters that are output from MAGPHYS for a single galaxy (in this example, HAPLESS 3). From the top, left to right, these parameters are: f_μ, fraction of the total dust luminosity which is contributed from the ambient ISM; $\tau_{\rm V}$, total V-band optical depth that is seen by stars which are forming in stellar birth clouds; $\mu\tau_{\rm V}$, fraction of $\tau_{\rm V}$ which is caused by the ambient ISM; $\log(M_{\rm star})$, log of the stellar mass of the galaxy; log(SSFR), the log of the specific star formation rate of the galaxy; log(SFR), the log of the star formation rate of the galaxy; $\log(L_{\rm dust})$, log of the total stellar luminosity that has been absorbed by dust; $\log(M_{\rm dust})$, the log of the total dust mass of the galaxy; $T_{\rm c}$, the temperature of the cold dust component in the galaxy; $T_{\rm w}$, the temperature of the warm dust component in the galaxy; $\xi_{\rm c}$, fractional contribution of the cold dust to the total dust luminosity and $\xi_{\rm w}$, fractional contribution of the warm dust to the total dust luminosity. The maximum of the likelihood distribution is related to the best-fit model for the galaxy, the width of the distribution can be used as uncertainties in the parameters true value. The vertical red and blue lines are the mean and median values of the distributions respectively. In this example, certain parameters such as $\log(M_{\rm dust})$ have narrow distributions and are therefore well constrained by the model. However, in this example parameters such as $T_{\rm w}$ are poorly constrained by the SED fitting model, with wide and flat distributions.

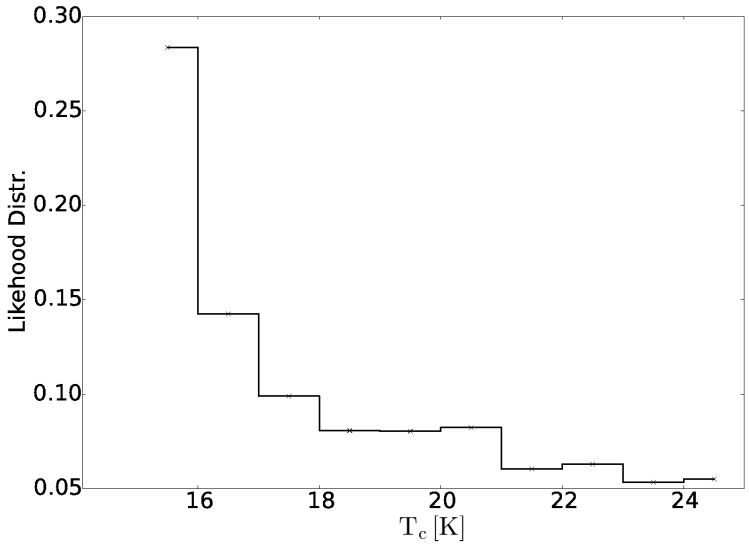

Figure 2.3 Shows the stacked probability distribution function of cold dust for the entire HAPLESS sample of 42 galaxies, obtained from MAGPHYS da Cunha et al. 2008. The standard model priors range in temperature from 15 K to 25 K. The continual increase in likelihood at low temperatures indicates that the standard priors are unable to successfully model the dust for our galaxy sample. Therefore it is necessary to extend the priors account for colder dust in these galaxies (first hinted at in Clark et al. 2015).

temperature bin. The clear rise of the PDF at low temperatures indicates that the standard cold temperature priors used in MAGPHYS, which range from 15 K to 25 K, are unable to accurately reproduce the cold dust component of the galaxies within the sample. We explore this further in Section 2.3.3.

We also modified the MAGPHYS code, such that for each galaxy the best-fit SFH would be returned. Figure 2.4 shows the best-fit SFHs for a selection of galaxies within the sample. Many of the galaxies in the sample display an increase in star formation recently, also many galaxies exhibit 'bursty' star formation (we return to the analysis of the SFHs in Section 2.4). We investigate how well a galaxy with a burst in the best-fit SFH can be modelled with a SFH that contains no burst by inspecting a full range of top fitting models for each galxay (see Section 2.6.2 for full details). It is the UV photometric observations that drive fits with recent bursts; following a recent burst of star formation the UV emission of a galaxy will be higher, due to the relative increase in the number of short lived high mass stars.

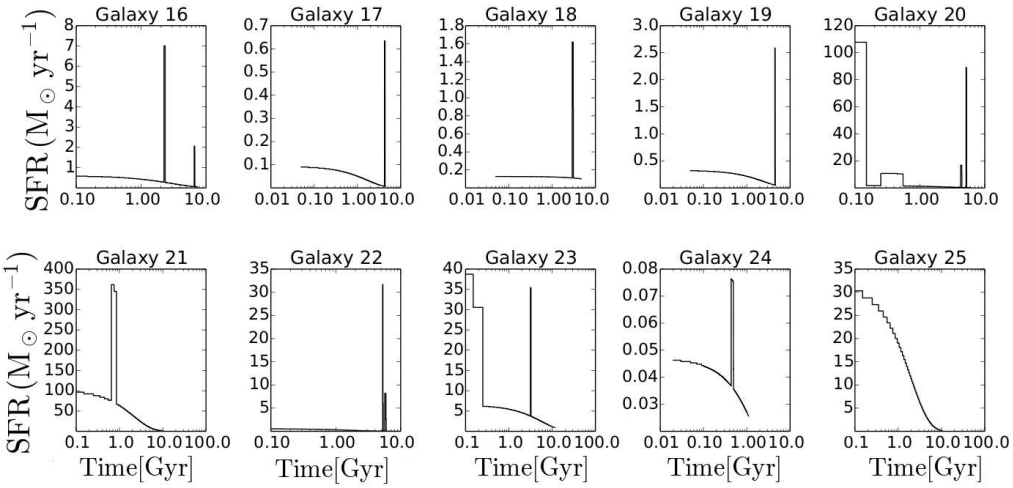

FIGURE 2.4 These are the best-fit star formation histories obtained from MAGPHYS for a selection of galaxies from our sample. Many of the galaxies in our sample exhibit bursts of star formation, with much of the star formation occurring recently.

2.3.2 INCLUDING IRAS 60 μm DATA FOR THE HAPLESS SAMPLE: CONSTRAINING THE MAGPHYS FIT

As mentioned in the previous section, the potentially non-physical bumpy feature which can be observed in the SEDs of many of the galaxies within the local galaxy sample collected here could either be due to lack of data in the MIR region of the SED, or because of some real physical processes in the galaxies. Therefore we obtained extra photometry data to attempt to constrain the model in this region. The Infrared Photometry Satellite (IRAS) telescope made all sky observations at 60 μm, and should have data which would fill the wavelength gap in the SED. We obtained IRAS photometry for HAPLESS using the online resource SCANPI[2], which enables photometric data to be extracted from IRAS maps. Before the data could be included in the galaxy sample, it was necessary to check that the IRAS 60 μm data was calibrated compared to the *Herschel* PACS photometry of our sample, to test its reliability. To achieve this, we also obtained the IRAS 100 μm photometric data from SCANPI and compared this with the PACS 100 μm photometry.

From Figure 2.5 we can see that the two data sets correspond well with each other, especially for brighter sources. There is more scatter for the faint sources, but this is probably due to the resolution (2′ at 100 μm) and sensitivity limit of IRAS (1 Jy at 100 μm, Neugebauer & Habing 1983). Since the errors increase at

[2] http://irsa.ipac.caltech.edu/applications/Scanpi/

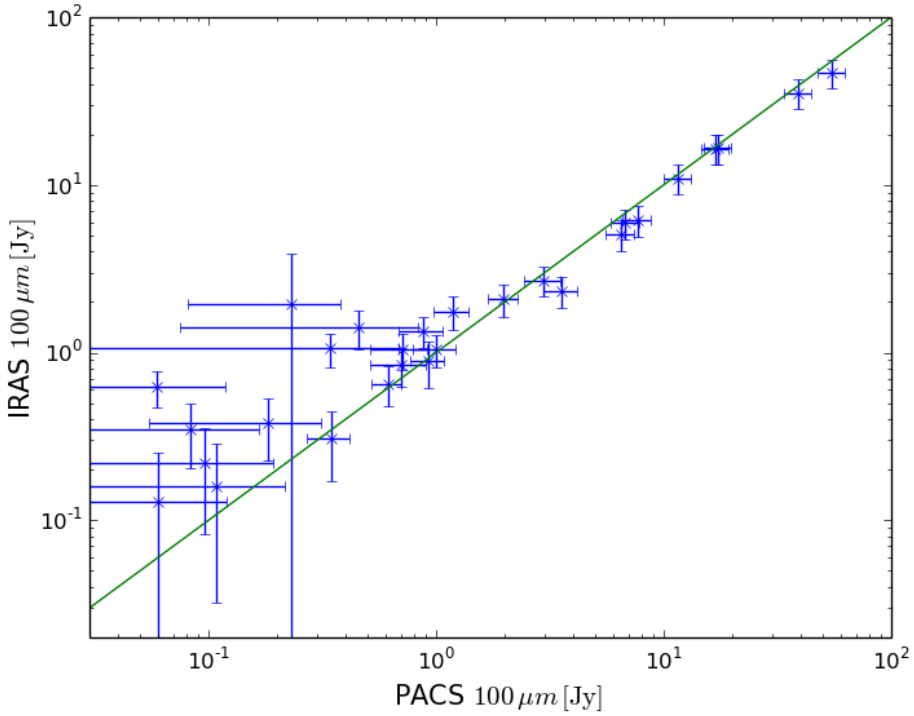

Figure 2.5 The comparison between the IRAS 100 μm flux values obtained from SCANPI with the PACS 100 μm flux for the HAPLESS sample of galaxies. There is a tight correlation between the two data sets at high flux values, although a systematic offset does become somewhat apparent at low flux values. This indicates that the difference is primarily due to difference in sensitivity and resolution of the two telescopes.

the lower flux end of the graph also, the data points still tend to fit on the one-one relationship. Despite the telescopes using different filters and having different resolutions and sensitivities, the data for these galaxies show good agreement. We therefore decided to use the IRAS 60 μm photometry to constrain the MIR 'bumpy' region of the SED. The IRAS flux for HAPLESS (60 and 100μm) is shown in Table 2.3 along with the associated error measurements, which were also obtained from SCANPI. The fluxes for the HiGH sample were provided by De Vis et al (priv. comm., PhD Thesis 2016).

Following the inclusion of the IRAS 60 μm photometry, we recalculated the SEDs for the galaxies using MAGPHYS, to see what effect the extra data in the MIR would have on the resultant fits. We stacked the best-fit SEDs with and without IRAS photometry by normalising each SED (one for each galaxy) to its mean value between 0.01 and 1000 μm, to ensure that each galaxy had equal weighting in the stack. Next we calculated the median of the sample, in each wavelength bin, to produce the

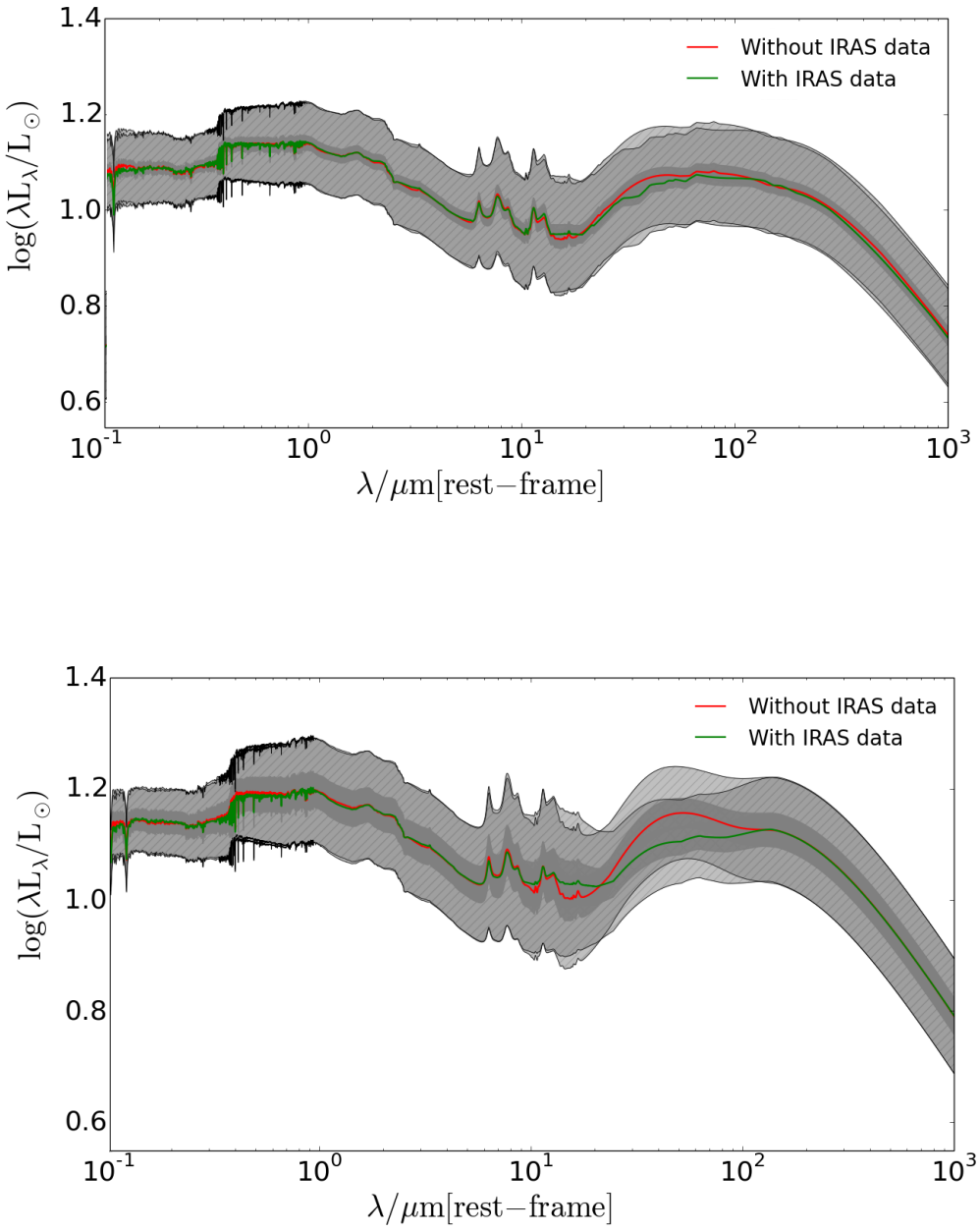

FIGURE 2.6 *Top:* Comparison between the stacked SED for the HAPLESS sample of galaxies with and without the IRAS 60 μm data. The stacked SED including IRAS data is shown in green, and the original stack (without this data) is shown in red. The light grey shaded region shows the 1σ spread of the stack, the dark grey unshaded region shows $1\sigma/\sqrt{N}$. The IRAS data has very little effect on the stacked SED of the full HAPLESS sample of galaxies. *Bottom:* The same as above except now we only include the sub-sample of 18 galaxies that had an appreciable change in their best-fit SFH selected by MAGPHYS before and after including IRAS fluxes. Including IRAS data for these sources does significantly effect the shape of the stacked SED, going some way to removing the 'bump' in the MIR (red).

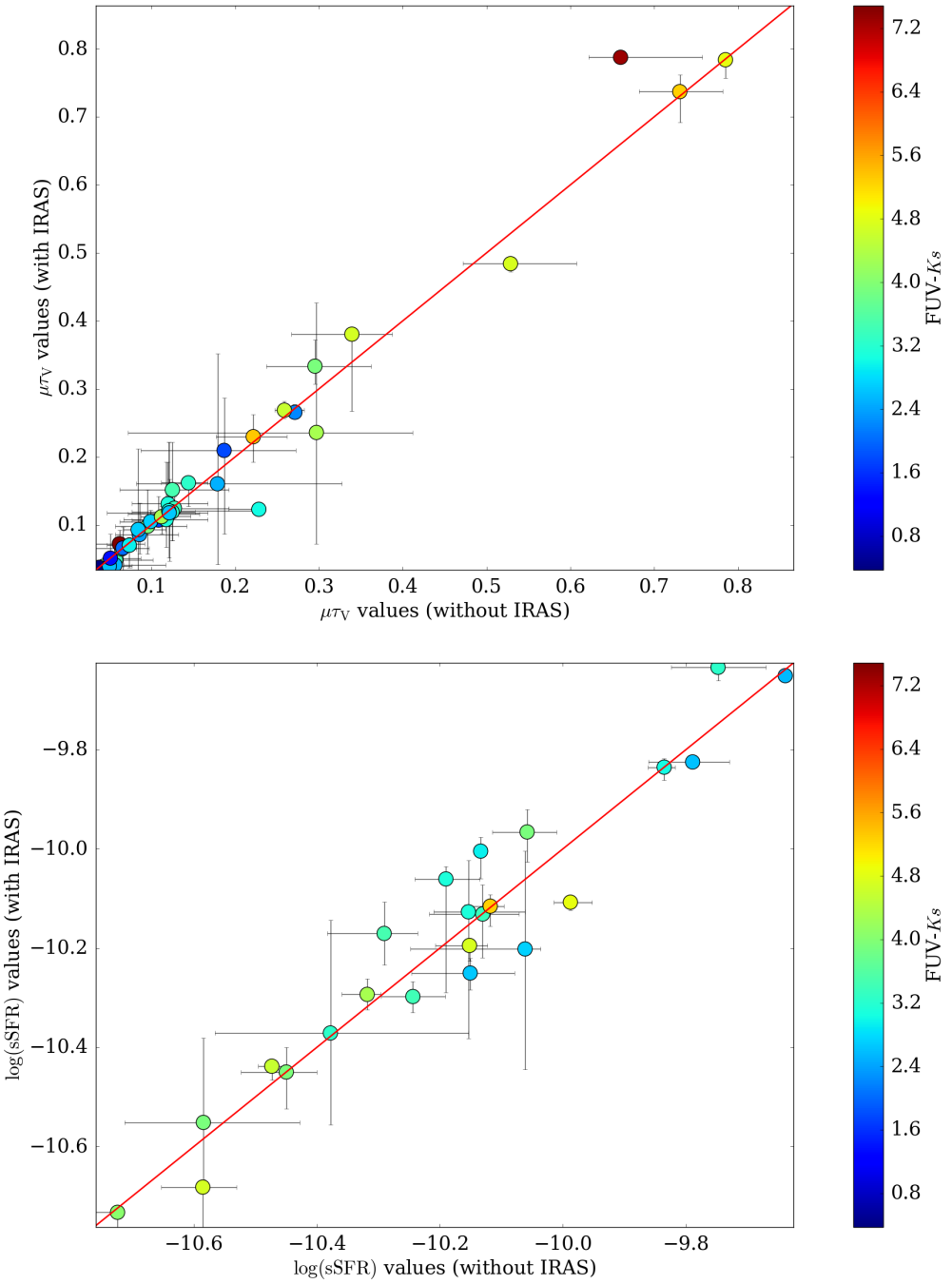

Figure 2.7 *Top:* Comparison of the parameter $\mu\tau_V$ (optical depth) for the HAPLESS sample of galaxies fit with MAGPHYS, with and without IRAS 60 μm data. There is very little scatter introduced by the new photometric data. The data points are coloured by FUV-Ks so that galaxies which are more blue (FUV-$Ks < 3.5$) have a higher fraction of the optical depth being contributed by birth clouds, due to their higher levels of star formation. *Bottom:* Plot of log($sSFR$) (Specific Star Formation Rate, SFR/M_s) for the HAPLESS sample of galaxies, again it seems the extra IRAS data has no systematic effect on the value of the physical parameters. The plot does agree with the plot for $\mu\tau_V$ in that the more blue galaxies have a higher star formation rate activity.

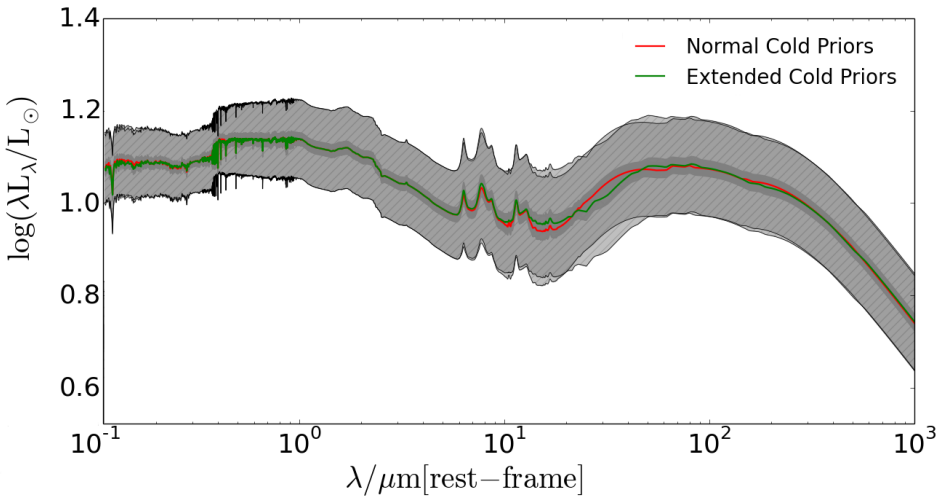

FIGURE 2.8 The stacked SED for the HAPLESS sample of galaxies (obtained from MAGPHYS using both the standard and extended cold dust priors). Extending the cold priors does not cause any significant change to the overall shape of the stacked SED, although small differences are seen in the UV and MIR. Extending the cold dust temperature priors had no effect on the star formation history of the sample.

stacked SED. This was done for the complete set of galaxies, both with and without the additional IRAS data, and is shown in Figure 2.6 (top). On inspection there does not appear to be a significant effect on the fitted SEDs of the full sample of galaxies due to adding the IRAS data, with the stacked SEDs looking very similar. However when we included IRAS photometry, 18 galaxies returned significantly different best-fit SFHs. Now we only consider the stacked SED of these 18 galaxies. The differences between the stacked SEDs (before and after including IRAS photometry) are seen in Figure 2.6 (bottom). The galaxies where we see a significant change in their SFH correspond to those galaxies whose SED was poorly constrained in the MIR initially, and exhibited the 'bumpy' feature at 60 μm. For these galaxies, including the IRAS data does improve the fit of the model to the photometry, and shows that the 'bumpy' feature was an artefact due to the lack of data rather than a 'physical' feature in the dust SED.

To investigate whether the addition of the IRAS data also affected the physical properties of the galaxies, we compared the values of the parameters, for each galaxy, from the two computational runs of MAGPHYS. Many of the physical parameters remain unchanged, see eg Figure 2.7.

HAPLESS	IRAS 60 μm (Jy)	Error (Jy)	IRAS 100 μm (Jy)	Error (Jy)
1	1.31	0.27	1.76	0.4
2	0.12	0.08	0.3	0.17
3	1.27	0.26	2.7	0.55
4	0.08	0.05	0.92	0.23
5	0.17	0.19	0.53	1.19
6	18.78	3.76	46.7	9.34
7	0.55	0.12	2.08	0.46
8	0.35	0.08	1.04	0.25
9	0.21	0.06	0.62	0.15
10	2.73	0.55	5.96	1.21
11	0.0	0.06	-99.9	101.0
12	0.2	0.05	0.31	0.14
13	0.1	0.05	0.16	0.13
14	2.34	0.47	5.09	1.05
15	0.03	0.04	0.18	0.13
16	0.46	0.1	1.35	0.29
17	0.24	0.06	0.35	0.15
18	0.35	0.08	0.65	0.17
19	0.08	0.05	0.37	0.16
20	8.09	1.62	16.62	3.33
21	2.35	0.47	10.92	2.19
22	0.0	0.06	0.13	0.12
23	7.25	1.45	16.47	3.3
24	0.0	0.06	-99.9	101.88
25	0.55	0.12	2.33	0.48
26	0.5	0.12	1.42	0.38
27	0.11	0.15	-0.1	0.41
28	3.77	0.76	6.21	1.27
29	19.56	3.91	35.35	7.07
30	0.17	0.05	0.38	0.15
31	0.34	0.08	1.06	0.24
32	0.43	0.09	1.04	0.23
33	0.08	0.05	0.27	0.14
34	0.0	0.06	-99.9	101.88
35	0.15	0.06	0.22	0.14
36	0.12	0.07	0.26	0.17
37	0.26	0.07	0.84	0.22
38	0.0	0.06	-99.9	101.88
39	0.35	0.09	0.89	0.27
40	0.43	0.09	0.93	0.26
41	0.37	0.09	0.54	0.18
42	0.0	0.06	-99.0	101.88

Table 2.3 Table displaying the IRAS 60 and 100 μm flux measurements obtained for the HAPLESS galaxies. A value of -99.9 indicates that there is no photometry available for the source at this wavelength. The HIGH values, not shown here, were obtained from De Vis et al (priv. comm., PhD Thesis 2016).

2.3.3 EXTENDING THE COLD DUST PRIORS

With the effect of including IRAS data explored, we also tested the effect of the cold dust temperature prior on the results from SED fitting. The standard version of MAGPHYS (da Cunha et al., 2008) had cold dust temperatures that range from 15-25 K. This assumption seems sensible given that average dust temperatures in nearby galaxies range from 20-30 K (e.g. Dunne et al. 2000; Smith et al. 2012c; Boselli et al. 2010; Rémy-Ruyer et al. 2013). However as we saw in Figure 2.3, some galaxies did not have well constrained cold dust temperatures, with the sample of galaxies having resultant dust temperatures from MAGPHYS that are peaking at temps < 20 K. As first noted in Clark et al. (2015), the HIGH and HAPLESS galaxies therefore have colder dust temperatures than found on average in other *Herschel* surveys in the literature (e.g. DGS Madden et al. 2013, HRS Boselli et al. 2010, KINGFISH Kennicutt et al. 2011). Here we explore this by stacking the SEDs with the standard MAGPHYS cold dust temperature priors and after changing the priors so that galaxies with dust temperatures of < 15 K can be accepted by the MAGPHYS routine. We therefore extend the cold dust temperature priors from $10-30$ K, and re-run the MAGPHYS code to compare with the original fits. It is necessary to be careful when increasing the temperature range, since the dust mass of a galaxy is very sensitive to the colder dust component temperatures. Also, dust temperatures of $<\approx 10$ K are unexpected for interstellar dust grains, because of heating from stars (Wesson, 1974). For this run we removed the IRAS 60 μm data, to isolate the effect that extending the cold dust temperature priors had on the MAGPHYS fits.

Once we refit our galaxies using the new cold dust priors, we produced the stacked SED for the sample of galaxies (following Figure 2.6 from Section 2.3.2, note here we only show HAPLESS galaxies in this example). Figure 2.8 shows the comparison between the fits; the addition of colder dust temperatures has only a small effect on the overall shape of the stacked SED, and does not help to constrain the best-fit SED. Also comparison of the SFHs of the galaxies show that, as expected, they are unchanged after the addition of the extended cold dust temperature priors. Therefore the limited range of the temperature prior in the original MAGPHYS code has little effect on the overall fit and SFH of the HAPLESS sample, (although it may have a significant effect on the dust masses derived for individual galaxies).

Figure 2.9 shows the stacked PDF for the cold dust component of the galaxies, with the new cold priors. The distribution now clearly shows a peak within the temperature range, which indicates that the cold temperatures have been better constrained by allowing a wider parameter space. Any galaxy with a cold dust temperature below

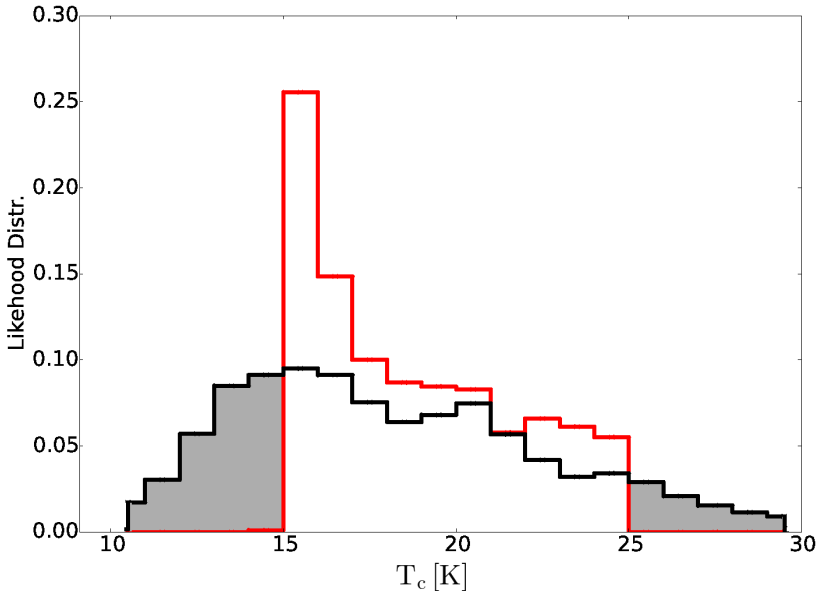

Figure 2.9 The stacked PDFs of the cold dust temperature, obtained from the SED fitting to the sample. The red line is the stack for the galaxies obtained using the standard priors for the galaxies, which range from 15 K to 25 K. The black line shows the stacked PDF obtained for the same galaxies, but now using extended priors, which range from 10 K to 30 K (with the extended region shaded grey).

15 K was previously being placed in the 16 K bin of the distribution, contributing to the rise in the PDF in Figure 2.3. Now the galaxies are free to occupy lower temperatures, and indeed they extend down to temperatures of ~ 11 K. While the peak of the cold dust temperature distribution remains at the same temperature, the entire distribution has changed. This indicates that a high bias would be introduced by missing the cold dust in these galaxies.

The change in temperature of the cold dust component may have an effect on the other physical properties of the galaxies. To investigate this, we compared the physical parameters from the first run against the values obtained using the extended cold dust priors. The plot of $\log(M_{\rm dust})$ (Figure 2.10, showing HAPLESS sources as an example) shows that, in general, the dust mass remains the same. However for the coldest objects, which can be seen as the darkest blue points in this image, the dust mass has increased significantly. This is because dust mass is very sensitive to the cold dust component; to produce the same dust luminosity ($L_{\rm FIR}$), with a lower dust temperature, requires a higher dust mass Dunne & Eales (2001).

Using the original cold dust temperature priors, the sample had a median dust mass of 1.93×10^6 M$_\odot$, with a range of 3.42×10^4 M$_\odot$ to 7.24×10^7 M$_\odot$. However, when

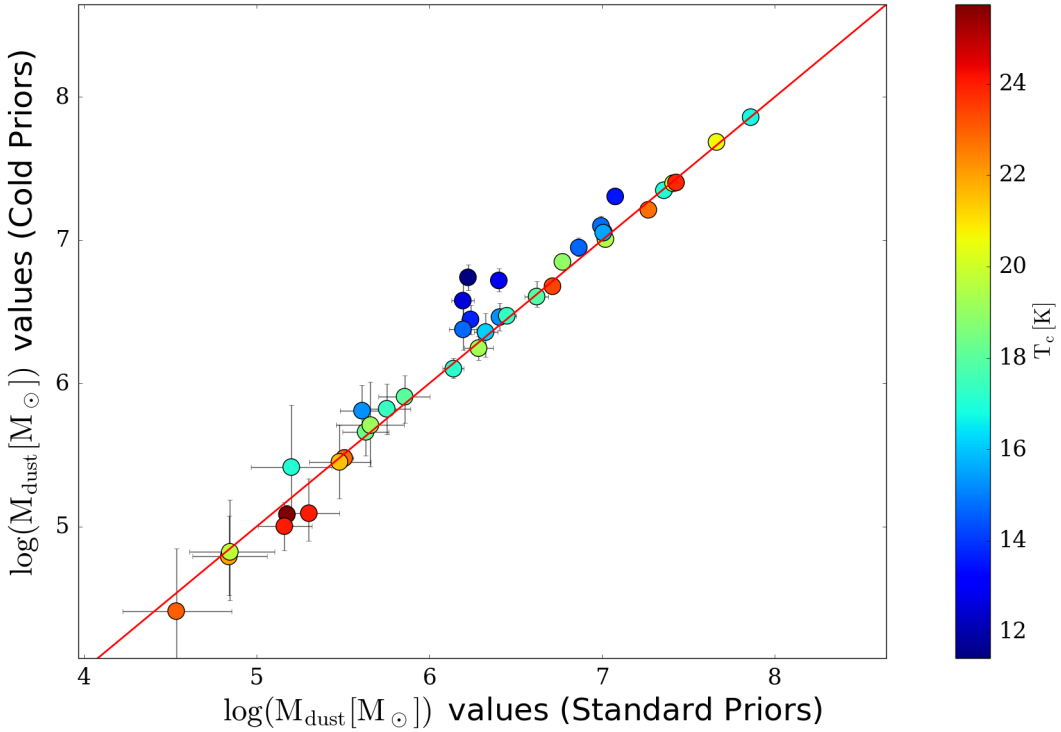

FIGURE 2.10 Variation in the dust mass when the cold dust prior has been extended (here we only show HAPLESS sources as an example). The coldest galaxies in the sample show an increase in dust mass as expected; hence when using the normal temperature priors the dust mass of these gas rich galaxies has been underestimated.

we extend the cold dust priors, we obtain a median dust mass of $2.80 \times 10^6\,M_\odot$ and a range of $2.52 \times 10^4\,M_\odot$ to $7.20 \times 10^7\,M_\odot$. Therefore using the extended cold priors has slightly increased the average dust mass of the sample, as we would expect if the dust temperature of some galaxies decreases. The largest increase in dust mass was for HAPLESS 11; using the original priors, this sources had a dust temperature of 15 K and a dust mass of $1.75 \times 10^6\,M_\odot$. When the extended priors were used the dust temperature fell to 11 K and the dust mass increased by a factor of 3.5 to $5.93 \times 10^6\,M_\odot$.

2.4 How to constrain the Star Formation History from MAGPHYS

As described in Chapter 1, the SFH of a galaxy is a key parameter to understanding the growth and evolution of that galaxy. Therefore, it is important to constrain this parameter as accurately as possible for each galaxy in the sample. The

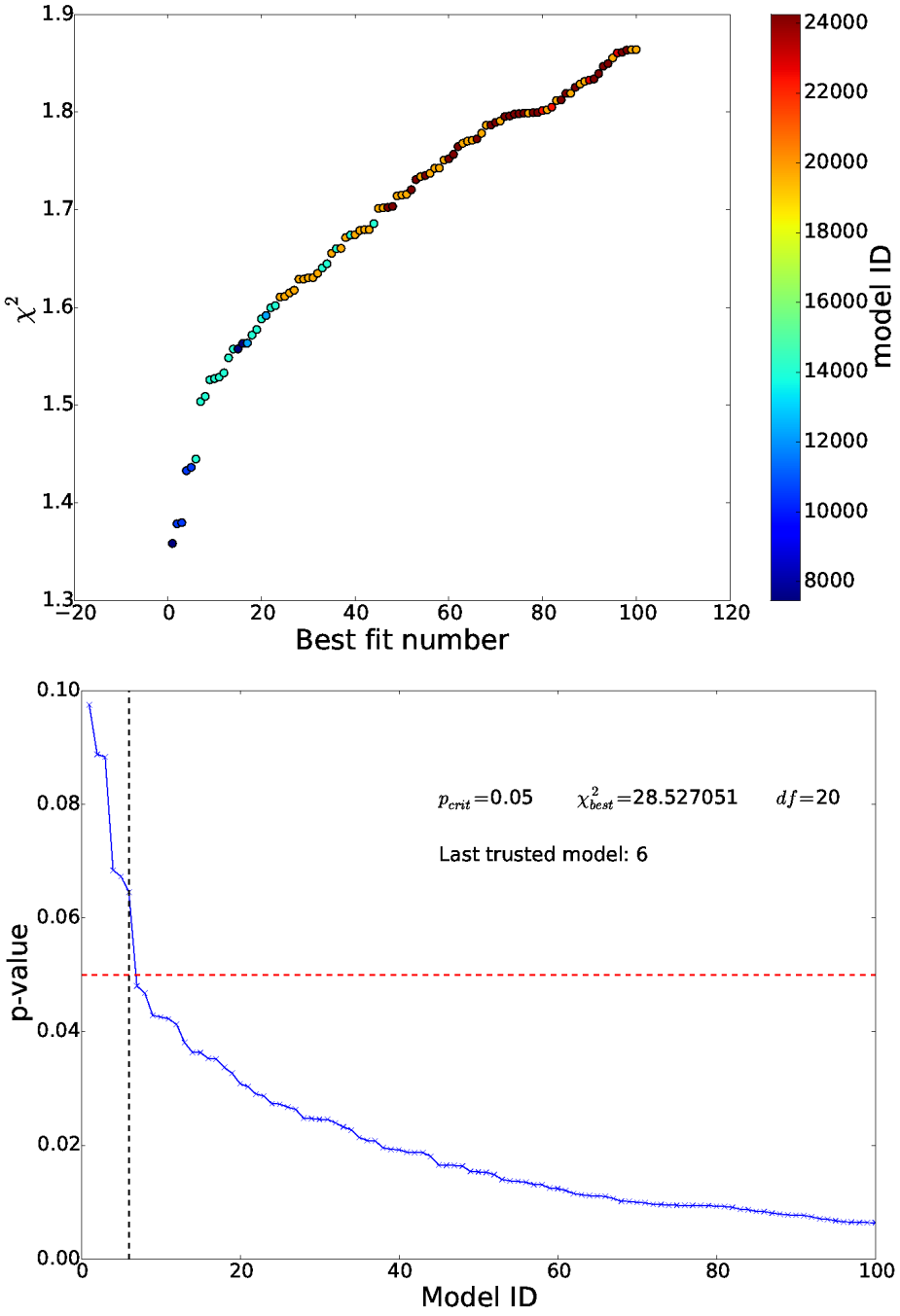

Figure 2.11 *Top:* An example of the distribution of χ^2 values for the top 100 best-fit models for a single galaxy from the sample (HAPLESS 10). This plot shows that there is a continual rise in χ^2 over this range of models, as expected. However for the 100 best-fit models there is a much smaller range of star formations histories; this is good because it can be used to limit the uncertainty in the star formation history of the galaxy. *Bottom:* Choosing a confidence level of $p = 0.05$, it is possible to restrict which models produce an accurate fit to the data for a single galaxy. In this case it can be seen that the top 6 best-fit SFH models produce a reliable fit to the data, these are the models which should have the strongest weighting when producing a stacked SFH for this galaxy.

addition of the IRAS 60 μm photometry (Section 2.3.2) caused the SFH of a significant number of galaxies within the sample to change. We showed this was mainly for the galaxies which exhibited a 'bump' in the galaxy SED (and hence were unconstrained in the MIR). In this section, we consider ways to expand the information obtained from MAGPHYS about the SFH, such that we can constrain the SFH and estimate the uncertainty in the value which we obtain.

2.4.1 Inspecting the Probability Distribution

To derive a best-fit SFH, MAGPHYS has an associated SFH corresponding to the stellar population responsible for producing the observed SED within each template. The individual SFHs in these libraries are based on an underlying exponentially declining star formation rate, with bursts of star formation superimposed at random times throughout the history of the galaxy. Any given SFH can be smooth or have a single, or multiple, burst(s) of star formation, although the standard MAGPHYS library is populated such that 50% of the templates have experienced a burst in the last 2 Gyr. As with the other parameters, the best-fit SFH can be extracted for each galaxy in the sample (though this is not a standard MAGPHYS output) and is directly related to the optical of template with the lowest χ^2 value. Unlike with the other parameters output by MAGPHYS, there is no PDF for the SFH, as such it is difficult to estimate an uncertainty in the SFH output by MAGPHYS.

To understand how robust the SFH of the galaxy returned by MAGPHYS we therefore need to consider more than the best-fit model for each galaxy. Ideally we would produce a PDF of the SFH, as MAGPHYS does for the other parameters, such as $M_{\rm d}$ or M_*. We modified the MAGPHYS code, such that the SFH for the top 100 best-fit models was output for each galaxy, along with the χ^2 value for each of these models. Inspecting the variation of χ^2 over the top 100 models, along with the corresponding SFH, indicates how unique the best-fit template is for each galaxy. This also enables us to see if there is large variation in the range of SFH models which can fit a given set of photometry.

Figure 2.11 shows an example of the χ^2 values returned by MAGPHYS for the top 100 best-fit models of a single galaxy (HAPLESS 10). We can see there is a sharp rise of χ^2 values initially for this galaxy, followed by a steady increase across the top 100 models. The data points are coloured according to the SFH template which they relate to in the optical library. Although there are 100 best-fit models below a χ^2 value of 38 that fit the galaxy photometry, these models only consist of 6 independent optical templates and therefore only 6 unique SFH templates. This suggests that only

a few SFHs from the MAGPHYS libraries are consistent with the observed photometry of this source.

To understand how the χ^2 values relate to the probability of the SFH providing a reasonable fit to the data, we use a Pearson's χ^2 test. This test is used to state, to a given pre-determined confidence level, whether there is enough information to prove or disprove a null hypothesis. In this case, the null hypothesis is that the model provides a reasonable fit to the data; here we choose a confidence level of $p = 0.05$. $p-$values smaller than this value would disprove the null hypothesis, which is to say that there would be a statistically significant variation between the model and our data.

Figure 2.11 shows the $p-$values that have been calculated for the top 100 models for the same galaxy described above. With the chosen cut-off value of 0.05, we can see that only 6 models out the top 100 lie above the cut-off and are likely all "good" fits, or at least consistent with the photometry. These should therefore have stronger weighting if we were to combine all the good model SFHs output by MAGPHYS for each galaxy.

2.4.2 Creating a Stacked SFH for each Galaxy

Having inspected the χ^2 distribution of example SFHs from MAGPHYS, we now wish to consider a method to combine the individual SFHs obtained from MAGPHYS, and their corresponding χ^2 values, to create a single 'stacked' SFH for each galaxy. Smith & Hayward (2015) marginalize over all 50000 SFH models contained in the MAGPHYS optical library to construct a 'PDF' equivalent for the SFH of the galaxy. They test the method against simulations of both isolated disk galaxies and major mergers, generated from a combination of smooth particle hydrodynamic models and radiative transfer code, and find that the 'true' SFH is recovered well using this method, especially for an isolated disk model. SFHs were less well recovered for complex mergers, although this was thought to be due to limitations in the template libraries included in MAGPHYS, rather than fundamental limitations of the method. None of the HIGH or HAPLESS galaxies show evidence of undergoing major mergers, therefore we have confidence we can obtain reliable SFHs for these galaxies. In this chapter, we use a method similar to Smith & Hayward (2015) to create a stacked SFH for each of our galaxies.

Prior to creating a stack of a sample of SFHs, it is first necessary to normalise each SFH to the median stellar mass of the sample, insuring that each SFH contributes equally to the stack. Following this, it is necessary to extend each SFH file so that the

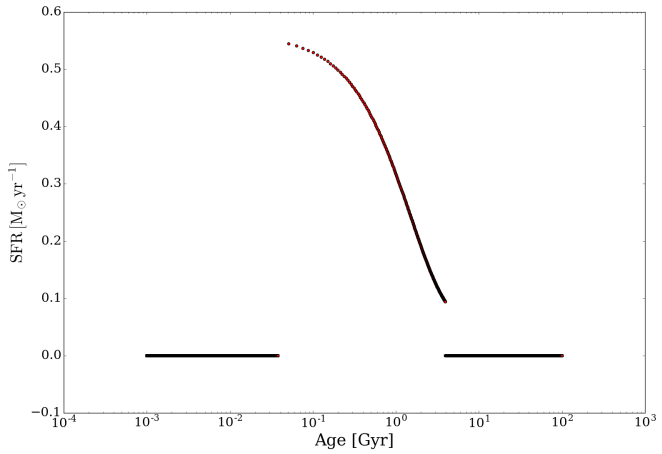

FIGURE 2.12 This figure shows the SFH of a single galaxy after it has been normalised to the median stellar mass of the sample. The SFH has been extended to a standard length and then re-sampled at an array of time steps distributed across the full range of the SFH. The re-sampled SFH is shown as the red data points, and the resolution of the re-sampling can be changed to any chosen level.

same time period is covered by all galaxies within the sample. If a given SFH does not contain information on the SFR at a given time, the SFR is set a zero at this point, in this manner no data is added to the SFH file. Next, a function is fit to the SFH data such that the SFR can be re-sampled at a standard array of time steps, which are distributed uniformly in log space over the full range of time (see Figure 2.12).

Next, we calculate the probability of each SFH template with respect to the galaxy being modelled, directly from the χ^2 value:

$$p = e^{-0.5\,\chi^2} \tag{2.1}$$

then we normalise the templates such that:

$$\sum_{i=1}^{50000} p_i = 1 \tag{2.2}$$

once the normalised probability has been calculated for each SFH template, we can use the values as a weighting factor, such that models with a high probability contribute strongly to the stack when compared to models with a lower associated probability. We then calculate the weighted mean, or expected value of the SFH from the individual templates:

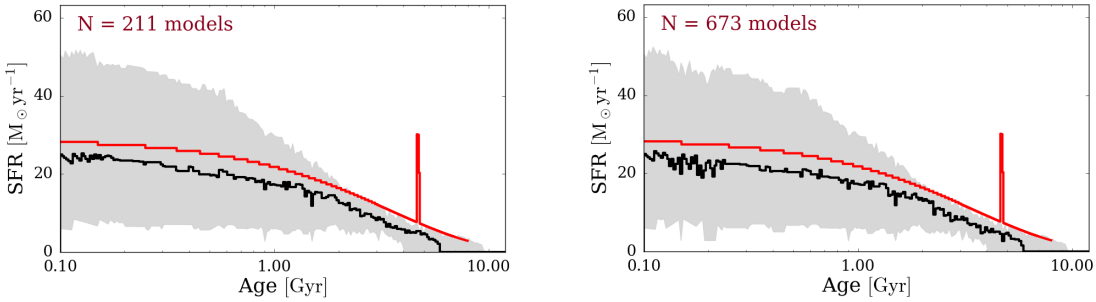

Figure 2.13 The median fit SFHs obtained from magphys for HAPLESS 6 and the associated uncertainties using our method. The median SFH is shown as the black line, and the 16$^{\text{th}}$ and 84$^{\text{th}}$ percentiles of the distribution are shown by the grey shaded region. For comparison we also plot the best-fit SFH model output by magphys in red. *Left:* Here we show the results of the stacked SFH if we go to a probability level of 97 %, which includes 211 independent SFH models. The best-fit history is included within the error margins calculated, and in this case shows good agreement with the median SFH, however the burst is not reproduced. *Right:* Same calculation, but this time to a probability level of 99 %, which include 673 independent models of the SFH for each galaxy.

$$E(x) = \sum_{i=1}^{n} x_i P(x_i) \tag{2.3}$$

where $E(x)$ is the expected value, calculated from all individual values of x multiplied by their associated probability. In this case, $E(x)$ provides the most likely value of the SFH in every time bin.

From Section 2.4.1, we know that the χ^2 distribution of the SFH templates rises steeply with increasing number of models. Therefore, we consider that it may not be necessary to calculate the stacked SFH using the complete 50000 libraries, rather it may only be necessary to consider the models which have a high probability for each galaxy. Figure 2.13 shows the expected value of the SFH of HAPLESS 6, calculated to different cumulative probability levels. Firstly we have include all models up to a cumulative probability level of 0.97 (which includes 211 independent SFH templates). We have then repeated the calculation for HAPLESS 6, up to a cumulative probability level of 0.99 (a total of 673 independent SFH templates). We find that there is little variation between the stacked SFH of HAPLESS 6 in the two cases for both the expected value (shown by the black line) and the corresponding uncertainty (shown in grey, which is calculated from the 16$^{\text{th}}$ and 84$^{\text{th}}$ percentiles of the stack) has little variation. Since limiting the cumulative probability level limits the number of templates calculated for each galaxy, it significantly decreases the computation time, and enables the stacked SFHs of the full sample of galaxies to be calculated.

We therefore choose to use the expected value calculation to obtain the stacked SFH of the sample, where we calculate the stack to a fixed level of $p = 0.97$. Using the stacked SFH model for each galaxy enables us to estimate the uncertainty in the value of the SFH which is obtained, which we can not do by considering the best-fit SFH template alone. However, bursts that feature in the best-fit SFH for our galaxies often appear 'washed out' in the stacked SFH, we explore this further in Section 2.6.

2.5 FINAL SED FITS- MAGPHYS PARAMETERS

In 2.14 we present the best-fit SED of the galaxies with the median likelihood SFH, obtained following the method described in Section 2.4.1, along with the corresponding uncertainty and the best-fit SFH. Figure 2.14 also shows the best optical spectra available for the galaxies, although these are not discussed further until Chapter 3. We used the MAGPHYS model of da Cunha et al. (2008), with the Bruzual & Charlot (2003) optical library. The cold dust priors are extended to $10 - 30\,\mathrm{K}$ (see Section 2.3.3), and we include the additional IRAS $60\,\mu$m (Table 2.3) to further constrain the fits. We follow da Cunha et al. (2015) and include an additional 10 % calibration error on the photometry. Some of the best-fit parameters for HAPLESS and HIGH are shown in Tables 2.4 and 2.5 respectively. Of the 58 galaxies in the combined HAPLESS and HiGH sample, we find that the best-fit SFH is comfortably contained within the uncertainty margins for most models. There are a small number of galaxies (~ 5), HAPLESS 1 for example, where the best-fit SFH appears elevated above the stack. This is because the best-fit and median stacked SFH are normalised to produce the same stellar mass, although they are not normalised to the same time duration. Therefore if there is significant variation in the time duration of the top SFH templates which can contribute to the galaxy, best-fit and stacked SFH may have different timescales. In this case there will be a small offset in the star formation rate, such that the same stellar mass is produced over the full duration of the histories. We explore the quality of these fits further in Sections 2.6 and 2.7. As a sanity check on the galaxy parameters from MAGPHYS, De Vis et al. (2016) and Clark et al. (2015) compare the MAGPHYS stellar masses to standard stellar-mass measurement techniques (eg using optical colours and K band luminosity). They found the stellar masses for HAPLESS and HiGH sources to be consistent across methods. Indeed, MAGPHYS-derived stellar masses have been shown to be in agreement with other methods on even larger optical samples of galaxies, see the extensive review in Taylor et al. (2011).

HAPLESS	$\log(M_{star}[M_\odot])$	$\log(SFR[M_\odot/(yrs)])$	T_C[K]	$\log(M_{dust}[M_\odot])$
1	8.79	-0.92	26.61	5.32
2	7.95	-2.35	16.47	5.71
3	9.12	-0.47	18.53	6.74
4	8.83	-1.63	19.59	5.27
5	8.41	-1.19	14.13	5.73
6	10.73	0.50	21.73	7.68
7	9.41	-0.61	16.53	7.03
8	8.76	-1.41	18.99	6.16
9	8.41	-2.00	15.43	6.49
10	10.25	-0.26	20.41	6.96
11	8.80	-1.80	11.61	6.68
12	8.59	-1.48	17.03	6.15
13	8.06	-2.16	13.61	5.58
14	9.89	-0.41	17.78	7.36
15	8.60	-1.97	14.82	5.37
16	9.30	-1.18	17.03	6.57
17	8.09	-1.11	17.34	5.20
18	8.67	-0.82	15.98	6.35
19	8.75	-1.16	13.05	6.72
20	10.65	-0.32	21.25	7.30
21	11.17	-0.09	16.63	7.94
22	9.58	-2.32	19.71	5.03
23	10.19	0.11	20.67	7.45
24	7.39	-1.92	16.70	5.29
25	10.39	-0.68	18.65	6.92
26	9.65	-1.24	14.10	7.24
27	8.67	-1.49	13.47	6.13
28	9.71	-0.21	24.25	6.70
29	10.29	0.55	23.89	7.45
30	8.74	-1.10	15.04	6.37
31	9.75	-0.82	16.50	6.95
32	8.89	-1.04	18.78	6.22
33	8.17	-1.06	18.36	5.61
34	8.33	-1.62	10.82	6.81
35	8.77	-1.07	13.61	6.62
36	8.25	-1.72	11.51	6.53
37	10.03	-0.66	14.80	7.18
38	8.36	-1.48	13.73	6.05
39	9.54	-0.46	17.97	7.70
40	8.98	-0.83	19.32	6.16
41	7.88	-1.29	13.89	5.93
42	7.62	-2.37	10.68	6.33

Table 2.4 Table displaying best fit parameters I have derived using magphys for the 42 HAPLESS galaxies.

HIGH	$\log(M_{star}[M_\odot])$	$\log(SFR[M_\odot/(yrs)])$	$T_C[K]$	$\log(M_{dust}[M_\odot])$
1	9.51	-0.81	13.74	6.71
2	8.73	-0.96	20.71	5.74
3	8.37	-1.25	25.22	4.83
4	8.44	-1.71	26.81	3.88
5	6.82	-2.35	10.10	5.32
6	7.33	-2.90	29.68	2.96
7	9.07	-0.21	12.52	7.37
8	10.30	0.09	19.76	7.50
9	9.77	-0.02	14.82	7.39
10	9.54	-0.08	18.28	7.19
11	7.60	-2.37	24.82	4.49
12	10.20	0.56	23.50	7.36
13	10.84	0.48	16.19	7.88
14	8.95	-0.97	12.45	7.40
15	8.19	-2.31	28.78	3.88
16	7.90	-1.09	14.00	5.85

TABLE 2.5 Table displaying best fit parameters I have derived using MAGPHYS for the 16 HIGH galaxies.

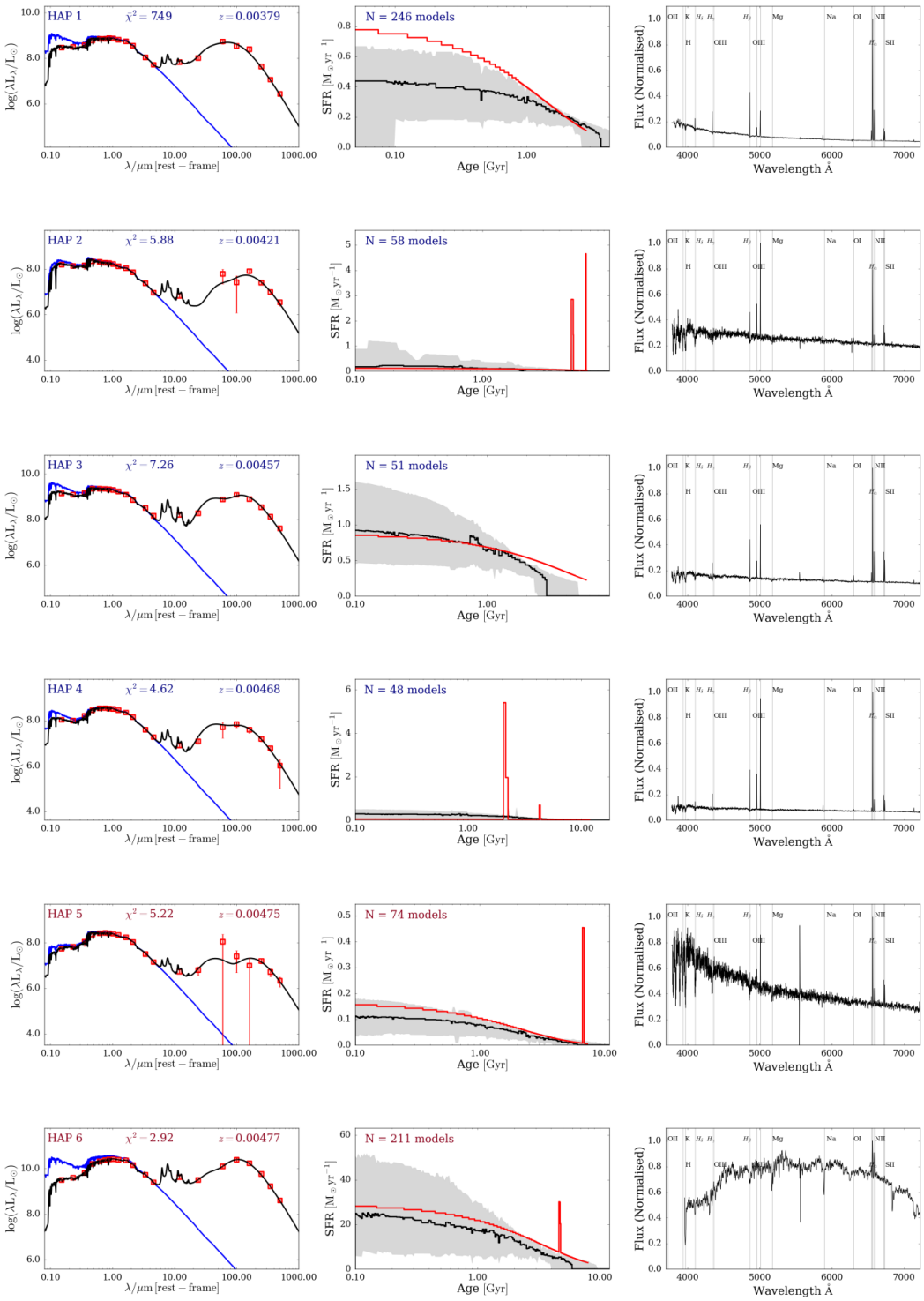

Figure 2.14 *Left:* The best fit SED from magphys for each galaxy (black line). The blue line shows the un-attenuated light from the intrinsic stellar population. Blue text indicates that the galaxy belongs to the BADGRS sub-population, while red text indicates the galaxy is a non-BADGR. *Middle:* The best fit SFH from magphys is shown in red, with the median of the stacked SFH shown by the black line. The grey region shows the estimated uncertainty in the SFH. *Left:* The galaxy spectrum, normalised (normalised to an arbitrary flux) with key emission and absorption lines highlighted (see Chapter 3 for further details).

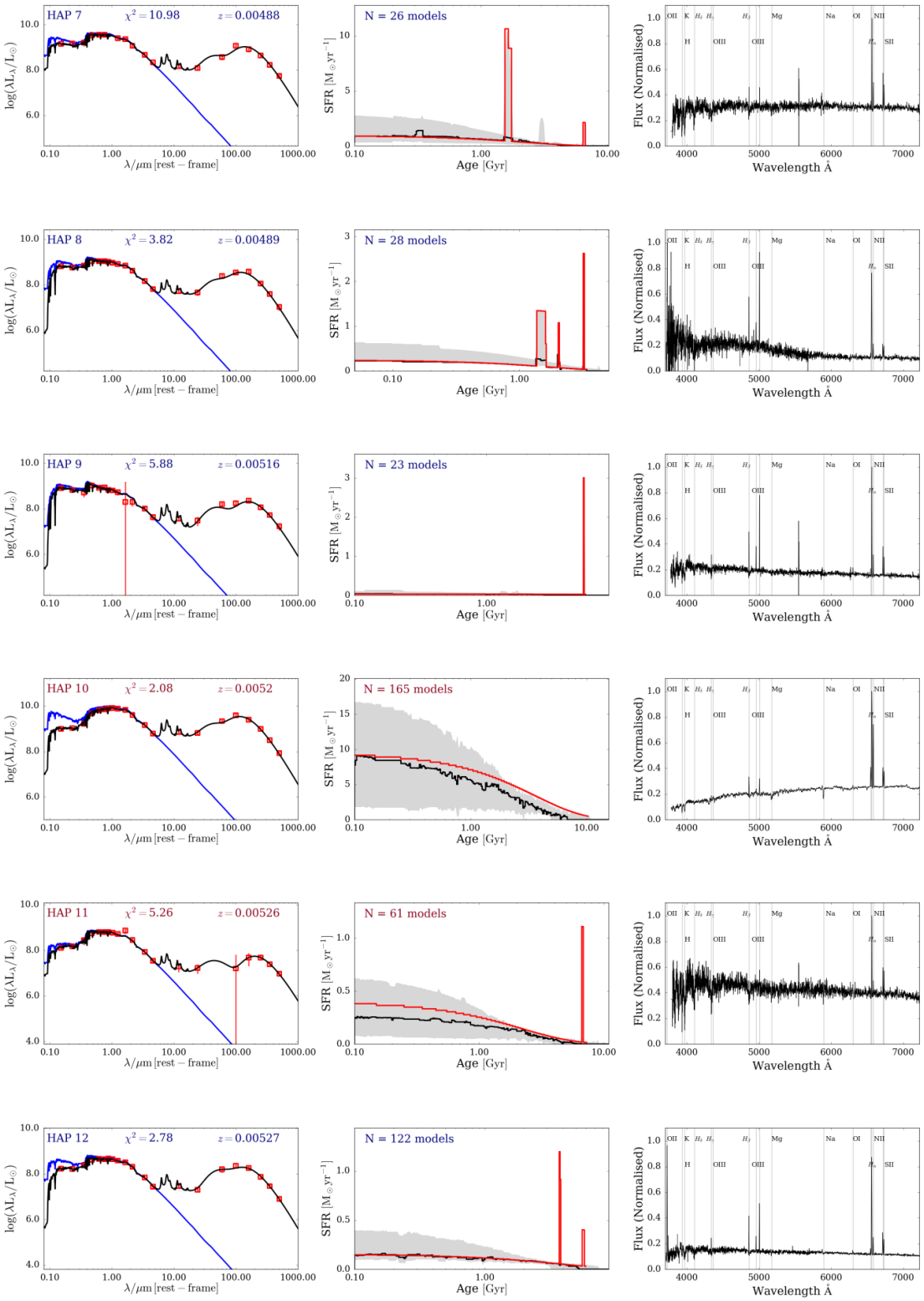

FIGURE 2.14 *Continued Figure*

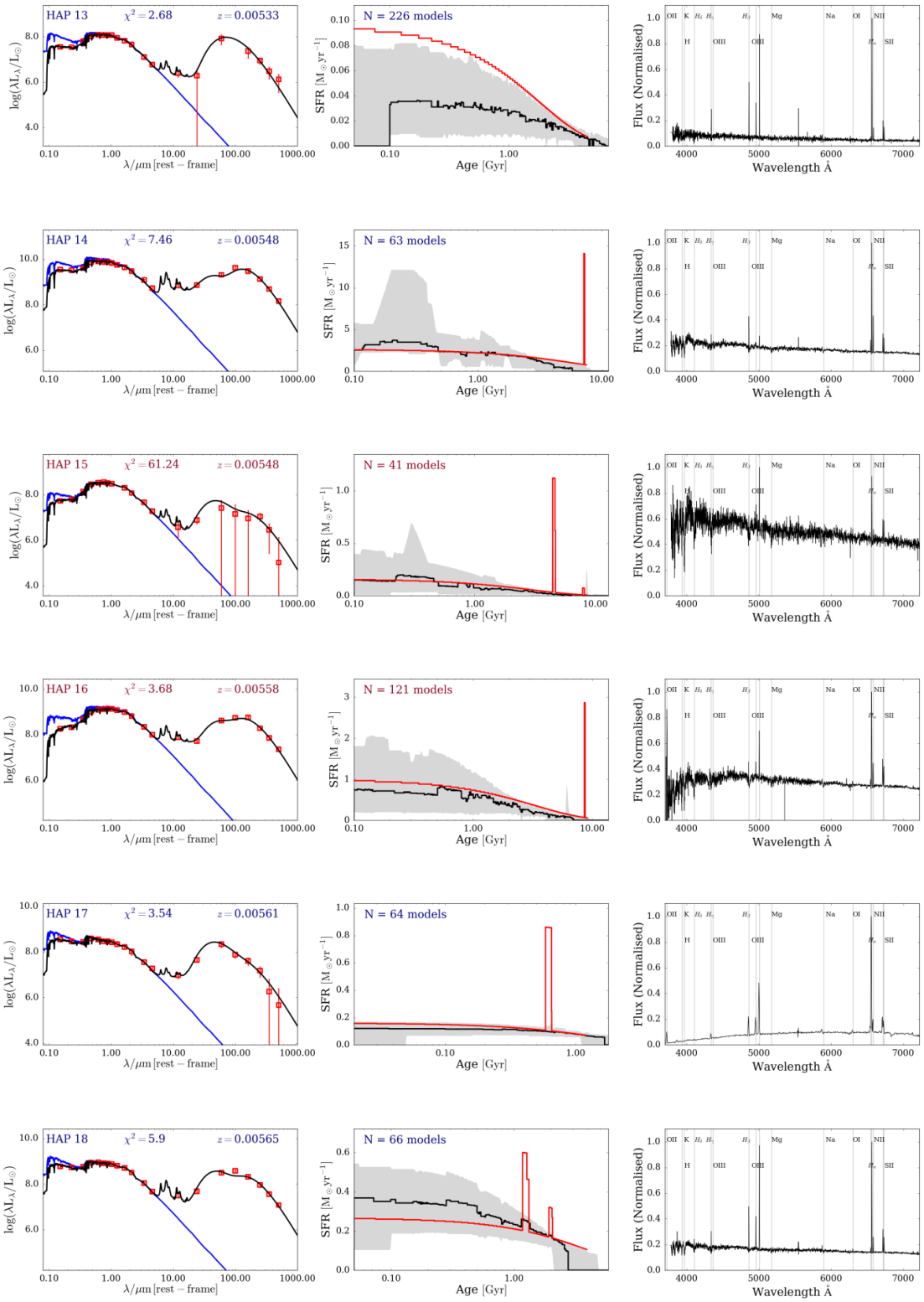

Figure 2.14 *Continued Figure*

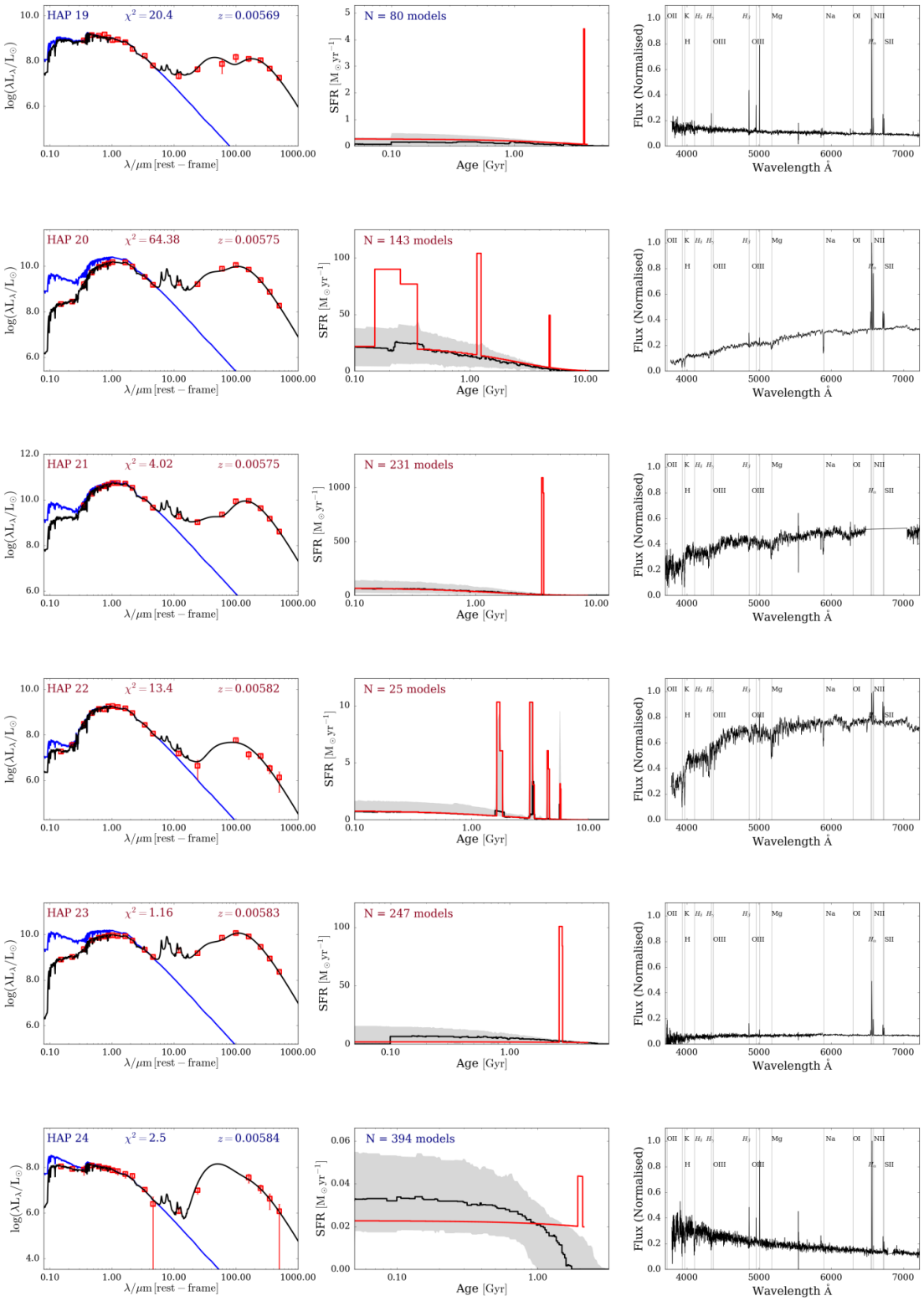

FIGURE 2.14 *Continued Figure*

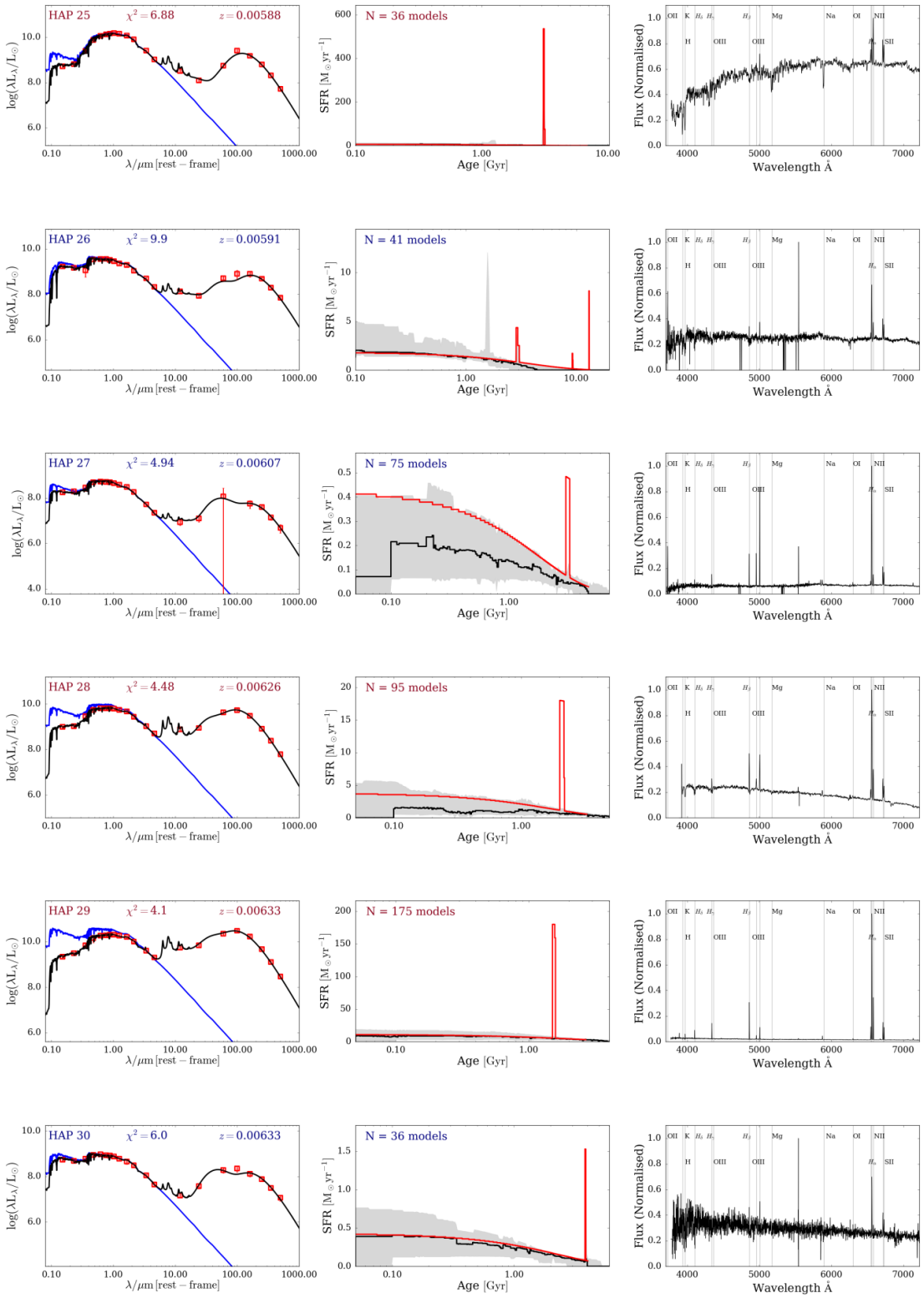

Figure 2.14 *Continued Figure*

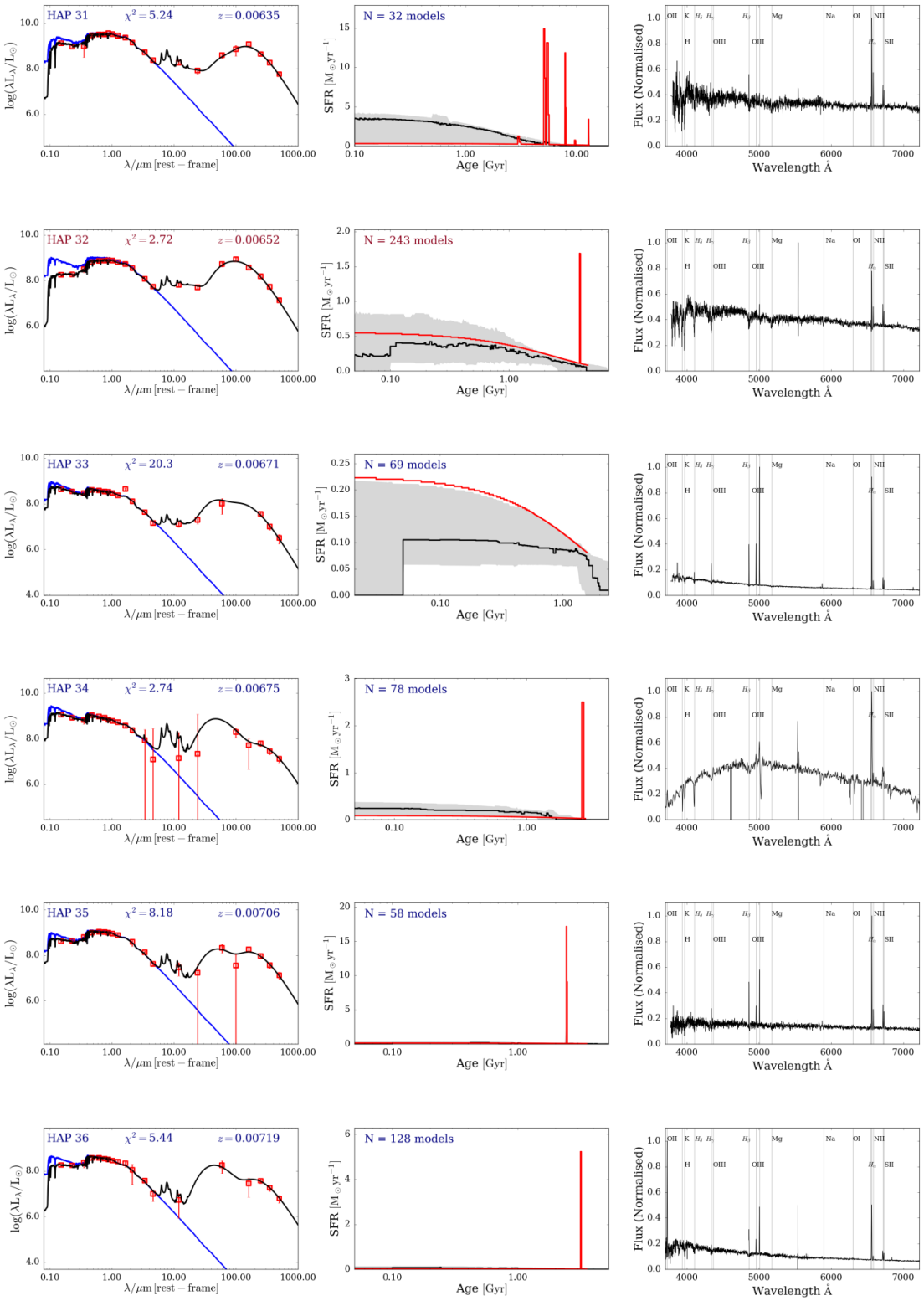

FIGURE 2.14 *Continued Figure*

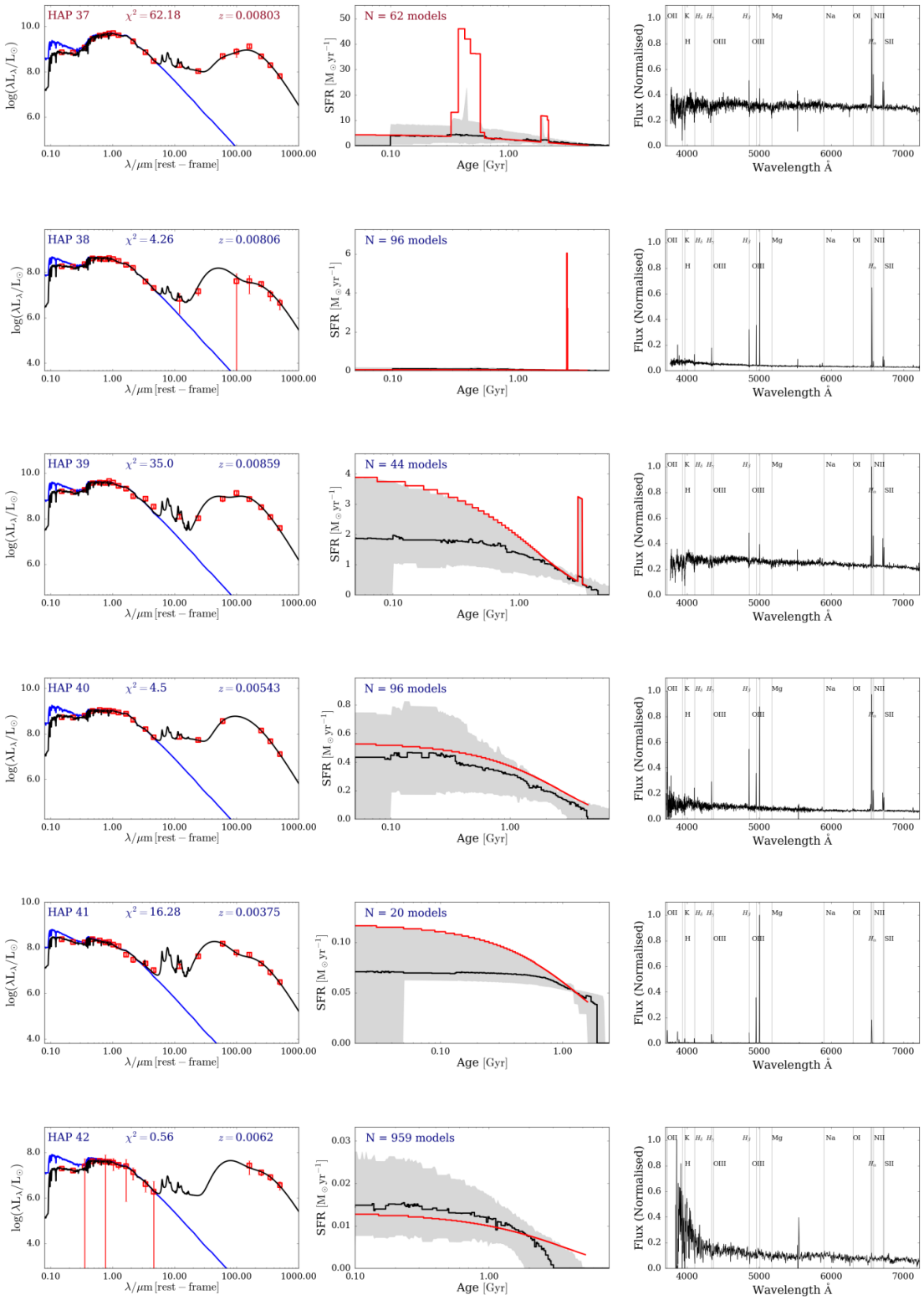

Figure 2.14 *Continued Figure*

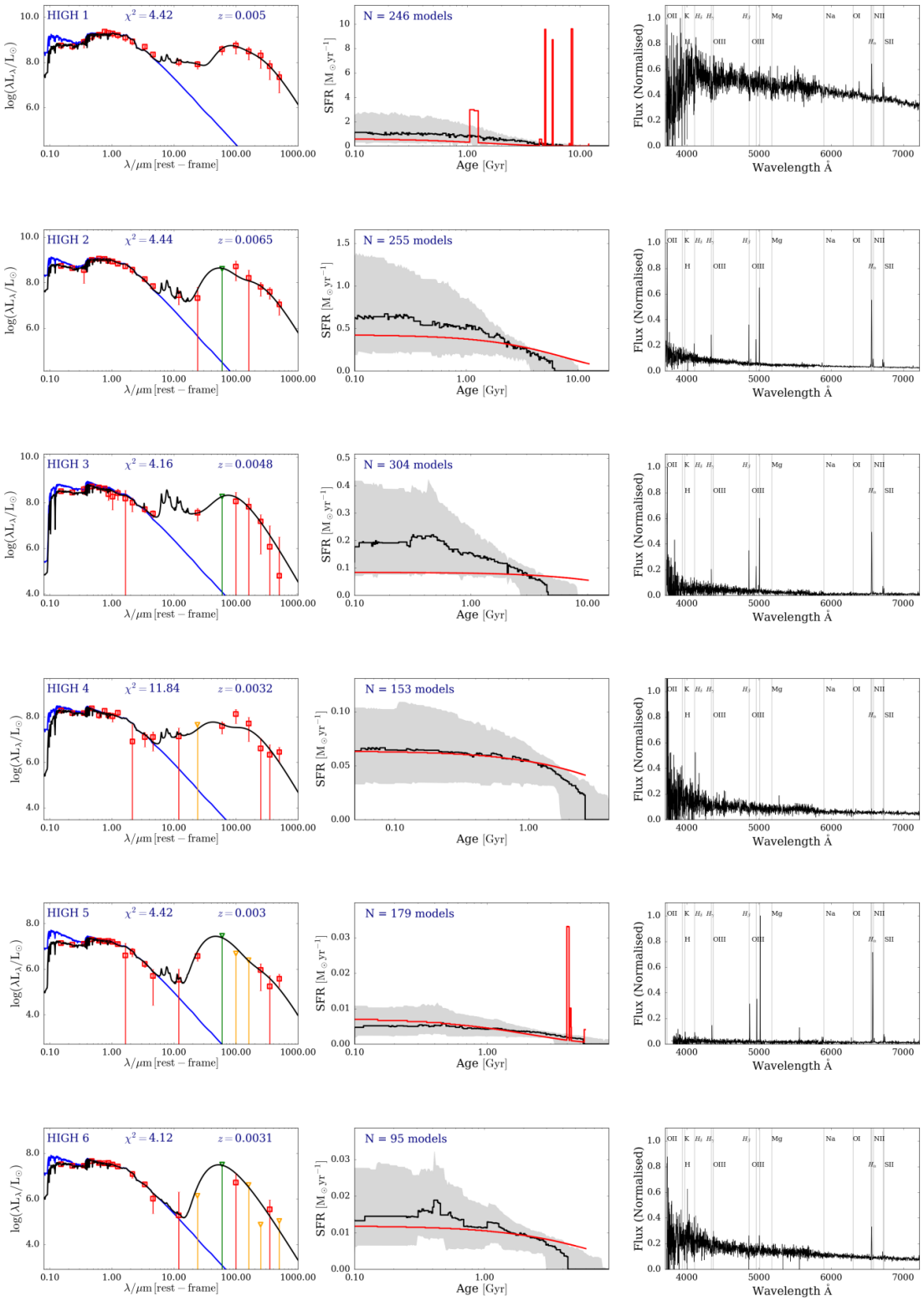

FIGURE 2.14 *Continued Figure*

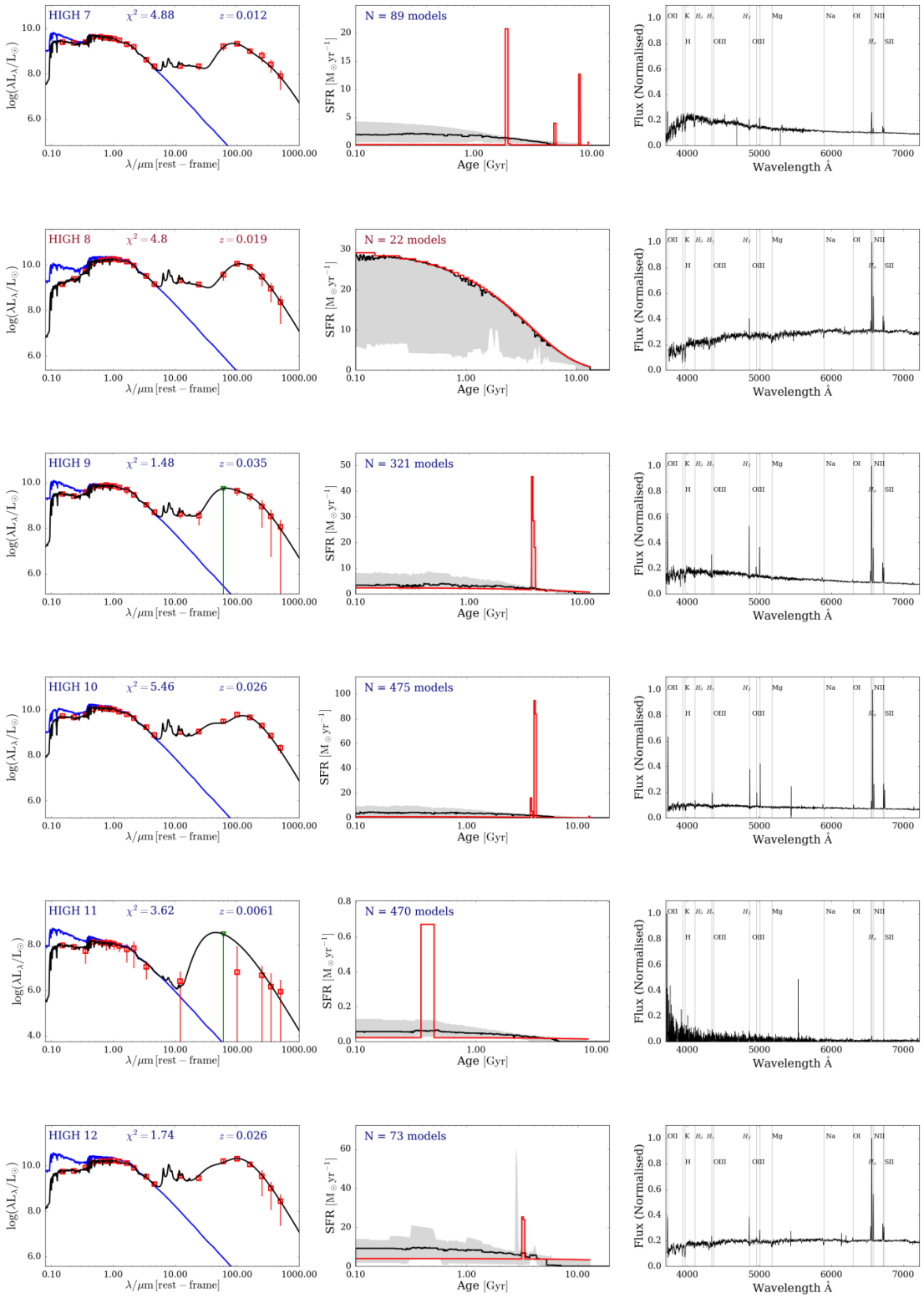

Figure 2.14 *Continued Figure*

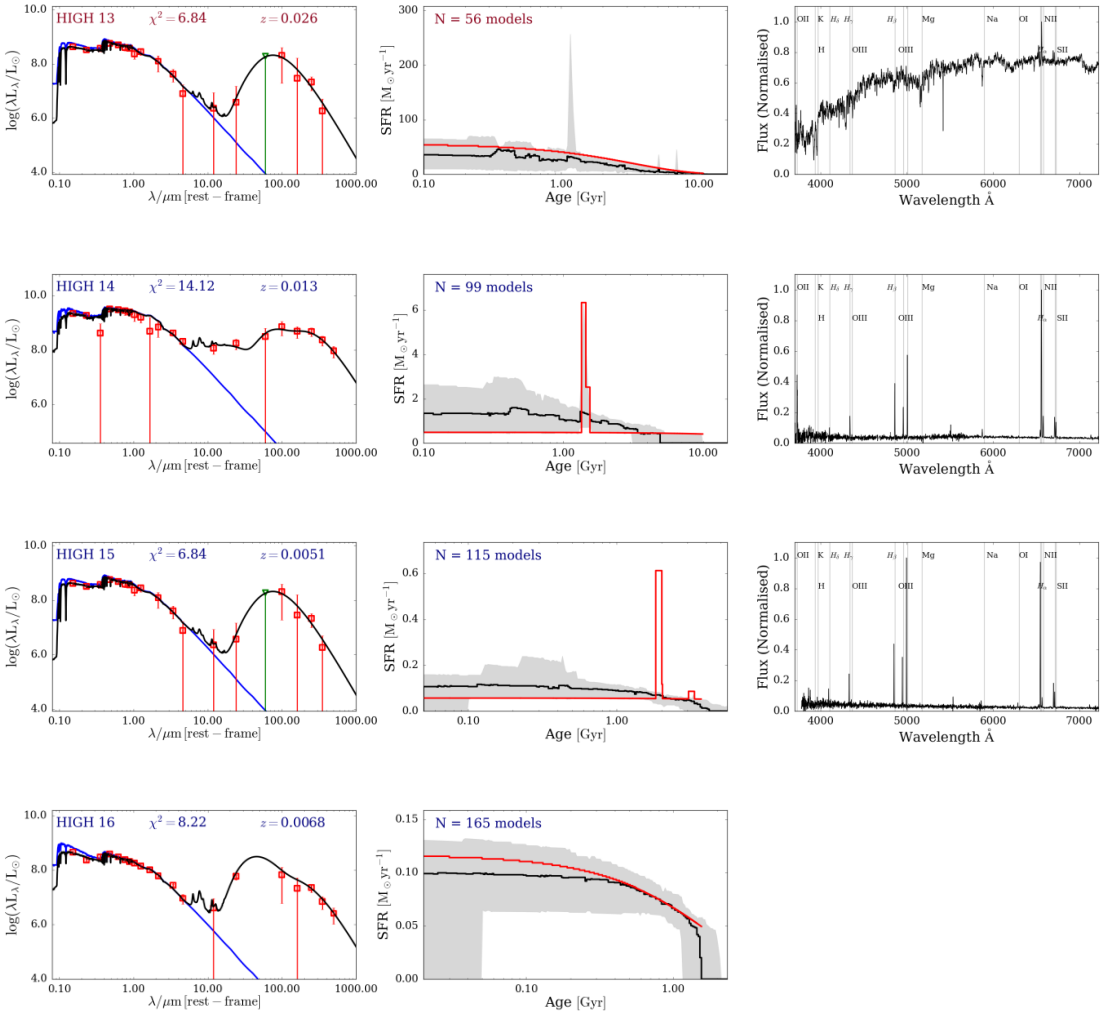

FIGURE 2.14 *Continued Figure*

2.6 Star Formation Rates in MAGPHYS

The MAGPHYS fits, shown in Figure 2.14, highlight the issue that the median star formation history rarely retains any information on whether there was a burst of star formation in a galaxy: any bursts seen in the best fit simply get washed out. We thought this could be because each individual burst is very localized. While the bursts may be located in a similar region of the star formation history, if they do not exactly overlap then they will not produce a significant cumulative contribution to the stacked star formation history.

Furthermore, close inspection of the MAGPHYS fits obtained in Section 2.5 showed that some of the sources have a best-fit star formation history which is consistent with the galaxy experiencing a burst of star formation $\sim 10^8$ years ago. This can causes a potential problem for MAGPHYS since an equally good fit can be obtained for galaxies where the burst falls just inside or just outside the last 10^8 years. This consequently affects the star formation rate values output by MAGPHYS. Each galaxy template in the library is created with a stellar population synthesis code and has an intrinsic star formation history, the current star formation rate is then estimated for the template by integrating over the last 10^8 years of the star formation history of the galaxy:

$$\mathrm{SFR}_8 = \frac{1}{10^8} \int_0^{10^8} \psi(t)\, dt \tag{2.4}$$

where $\psi(t)$ is the value of the star formation history at a time t. In this way, MAGPHYS SFRs are obtained by effectively averaging the SFR over the last 10^8 years. The star formation rate output by MAGPHYS for a galaxy template will therefore change significantly if the burst is located just within the last 10^8 years, compared to if the burst ended just before the last 10^8 years. This dichotomy manifests itself as a bimodal SFR PDF for 15 galaxies in our sample. All these galaxies are blue and gas rich sources (the BADGRS).

While SED modelling based on photometric data can give us an indication of whether there has recently been a burst of star formation in a galaxy, there is not enough information available to say with certainty whether the burst of star formation occurred just inside, or just outside, the window which we wish to estimate the star formation rate over. In Section 2.6.1 we explore a potential solution to these problems.

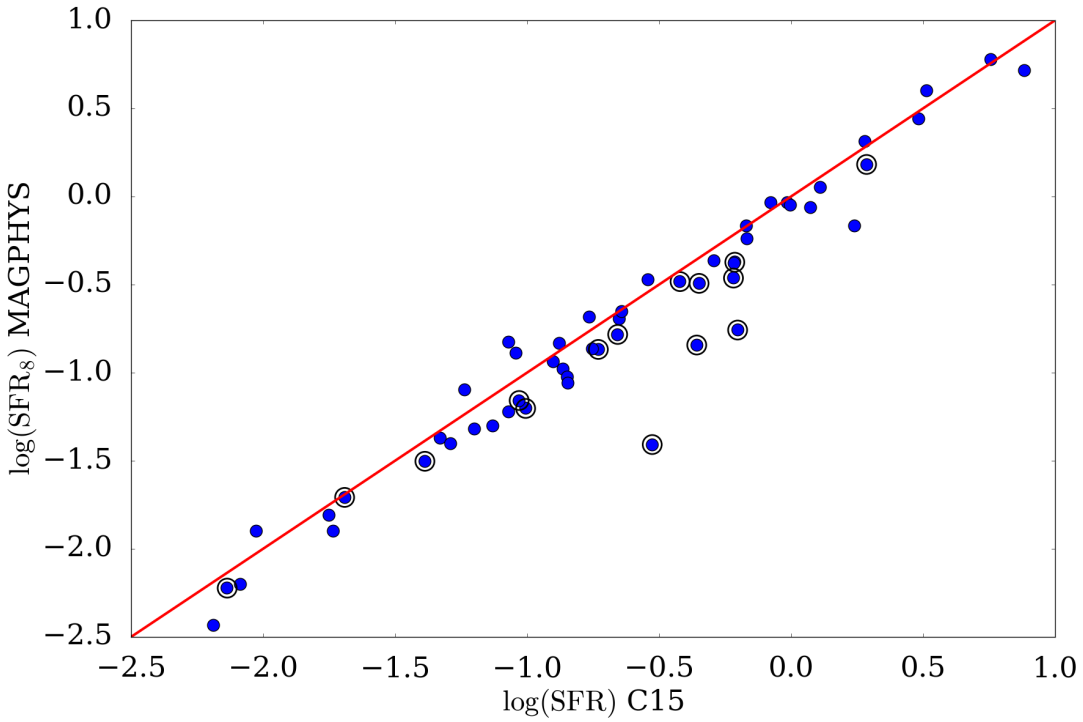

FIGURE 2.15 Comparison between the star formation rate measured by MAGPHYS, against the star formation rate measured in Clark et al. (2015) for the HAPLESS sources. Many of the galaxies which are strongly offset from the 1:1 relationship (red line) have bimodal star formation rate PDFs output from MAGPHYS (black circle).

2.6.1 SMOOTHED STAR FORMATION RATES

For the HAPLESS sources, we can use the star formation rate (SFR) estimated in Clark et al. (2015) as a 'sanity check' on the value the SFR measured by MAGPHYS (see Figure 2.15). The SFR from Clark et al. (2015) was measured using a combination of GALEX FUV and WISE 22 μm tracers. De Vis et al. (2016) showed that the SFR measured by Clark et al. (2015) from 22 μm is likely an overestimate, because dust heating from an older stellar population had not been fully accounted for. However De Vis et al. (2016) showed this produced an average offset of a factor of 1.07 (excluding the bimodal sources), and that the SFRs could be scaled by this factor to enable direct comparison between the methods. We also note that the method used to estimate the SFR in Clark et al. (2015) assumes a constant SFR over the last $\sim 10^8$ years (Lee et al., 2009), and for bursty galaxies is therefore likely to provide an underestimation of the SFR when compared to MAGPHYS, since MAGPHYS is able to account for bursts (provided that the burst is completely contained within the last 10^8 years). There are several sources which are further offset from the 1:1 relationship; these are the galaxies with a bimodal SFR PDF output by MAGPHYS.

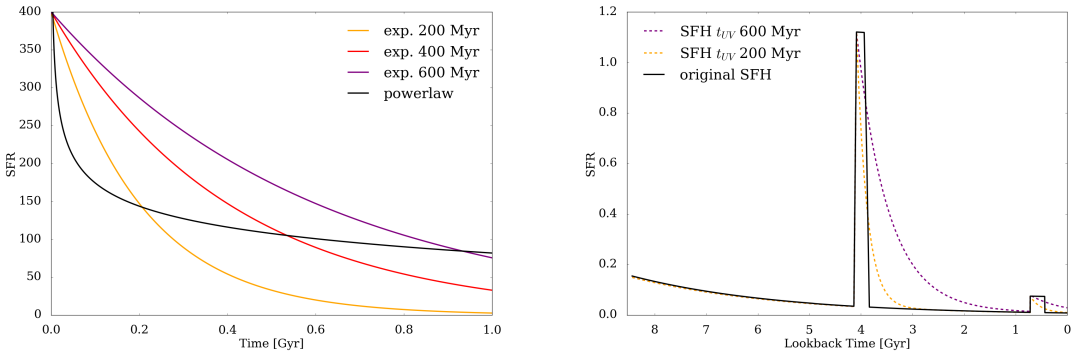

Figure 2.16 *Left:* The range of decay timescales following a burst of star formation (see Miller & Percival 1998; Bruzual & Charlot 2003; Madau & Dickinson 2014) that are used in this work. Shorter timescales are more representative of a top-heavy initial mass function, due to the increased fraction of high mass stars. *Right:* Smoothing the HAPLESS 15 best-fit star formation history model (shown as 'original SFH') by the UV decay timescales of 600 and 200 Myr (yellow and purple curves respectively). Instead of having sharp edges, the bursts slowly decay back to the underlying star formation rate.

The bimodal SFR PDFs, and the resulting offset in the SFRs output by MAGPHYS, are thought to be caused by the dependence of MAGPHYS on the *precise* location of the burst in the star formation history of the galaxy. This has such a large affect because the burst assumed by MAGPHYS is discrete, whereas we know that a burst of star formation would likely effect the galaxy over large timescales. To address the problem, we decide to create a smoothed version of the star formation history for each galaxy, where a range of smoothing timescales are chosen (see Figure 2.16). Each burst of star formation will no longer have sharp boundaries, but will instead gradually decay to the underlying ambient SFR. In this manner, bursts of star formation which lie just outside the last $\sim 10^8$ years will still 'contribute' to the MAGPHYS SFR, where the strength of their contribution will fade the further from the 10^8 year window they are located. Additionally, by smoothing the bursts they will become more extended (less discreet) and may have a stronger cumulative effect in the stacked star formation history of the galaxy.

In MAGPHYS, each star formation history is constructed of two components: a continuous exponentially declining base level of star formation and a series of bursts superimposed at random times (see Section 2.4.1 for further details). To create the smoothed star formation history, it is first necessary to separate the continuous and burst component of the star formation history. We achieve this by first calculating the exponentially declining continuous component using the decay timescale parameter γ for each galaxy, combined with the equation for exponential decay:

$$\psi(t) = A \times \exp^{-\gamma t} \tag{2.5}$$

where A is a scaling factor relating to the initial rate of star formation in the galaxy. The underlying continuous SFR can then be subtracted from the original star formation history to isolate the bursts.

With the bursts of star formation separated from the underlying continuous star formation component, we can then perform the smoothing function. The level of UV radiation will decay at a given timescale following a burst of star formation, although there will be some variation depending on the initial mass function (Miller & Percival, 1998; Bruzual & Charlot, 2003; Madau & Dickinson, 2014). Figure 2.16 demonstrates this for two different star formation histories, where the discrete bursts used in MAGPHYS have been replaced with an exponential decay function relating to the two extremes of values found in the literature. We can now calculate a new value of the SFR averaged over the last 10^8 years for the smoothed histories, using Equation 2.4.

2.6.2 RESULTS FROM SMOOTHING THE STAR FORMATION HISTORIES

Figure 2.17 shows the effect smoothing the bursts has on our estimate of SFR. We compare the MAGPHYS SFR vs Clark et al. (2015) SFR, where the red line shows a 1:1 relationship (only the bimodal sources are shown on this plot, ie the circled sources in Figure 2.15). Best fit and median values for each galaxy are shown as yellow and black markers respectively. Despite the bimodal nature of the PDF for 15 sources, the median SFR compares well with Clark et al. (2015) for the majority of the sources (only 3-4 sources are significantly offset from the 1:1 relationship).

The purple marker for each galaxy shows the effect smoothing the burst by 300 Myr has on our estimate of the SFR. Smoothing the bursts effectively applies a scaling factor to the SFR, increasing the SFR derived from the star formation history. However, there does not seem to be a consistent smoothing which we can apply to our sample. In effect these 3-4 sources would require individual scaling factors, and therefore smoothing the burst does not easily resolve the bimodal SFRs and underestimated values from MAGPHYS.

While it does not seem possible to use a simple smoothing factor to improve the MAGPHYS estimate of the current SFR for the bimodal sources, it could still be used to improve the stacked star formation history for each galaxy. However, Figure 2.18 shows that even when smoothing the bursts, the median stacked star formation history

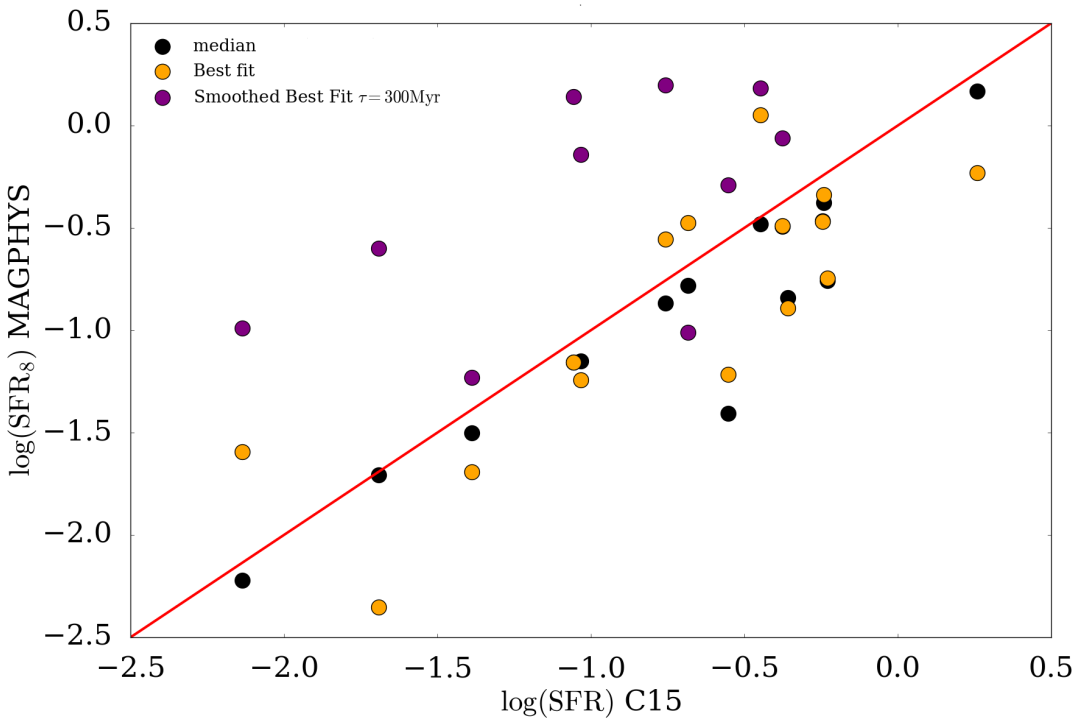

Figure 2.17 Comparison of the star formation rate (SFR) estimated by MAGPHYS against the SFR measured in Clark et al. (2015) for the sources with a bimodal SFR PDF. Despite having a bimodal PDF, the median SFR (shown in black) compares well against the Clark et al. (2015) value for all but four sources. The best fit value (shown in yellow) is further offset from the 1:1 relationship (red line) for all sources. Smoothed SFRs (shown here in purple for the 300 Myr timescale) improve upon the best fit and median for the most offset sources. However, there does not seem to be a consistent smoothing timescale we can apply to all galaxies in the sample to match the Clark et al. (2015) value.

(black line) does not provide any additional information on the location of the bursts in the star formation history. The 84$^{\text{th}}$ percentile of the stack shows some more bursty features, but the burst seen in the best-fit is still washed out in the median SFH. This trend is seen in all galaxies in our sample.

Figure 2.19 indicates why smoothing the star formation history bursts may have little effect on the median stacked star formation history that is obtained for each galaxy. Here we show (for the same galaxy as in Figure 2.18) the best fit star formation history (now plotted against lookback time) overlaid on a histogram showing the number of bursts at each time in the star formation history (for the top 211 star formation history models that are considered 'good fits' to the photometry). Firstly, we can see that even for a galaxy which has strong evidence for a burst in the best-fit star formation history, there are a large number of models which have no burst (76/211$\sim$36%). The properties of the galaxy can be explained almost equally as well

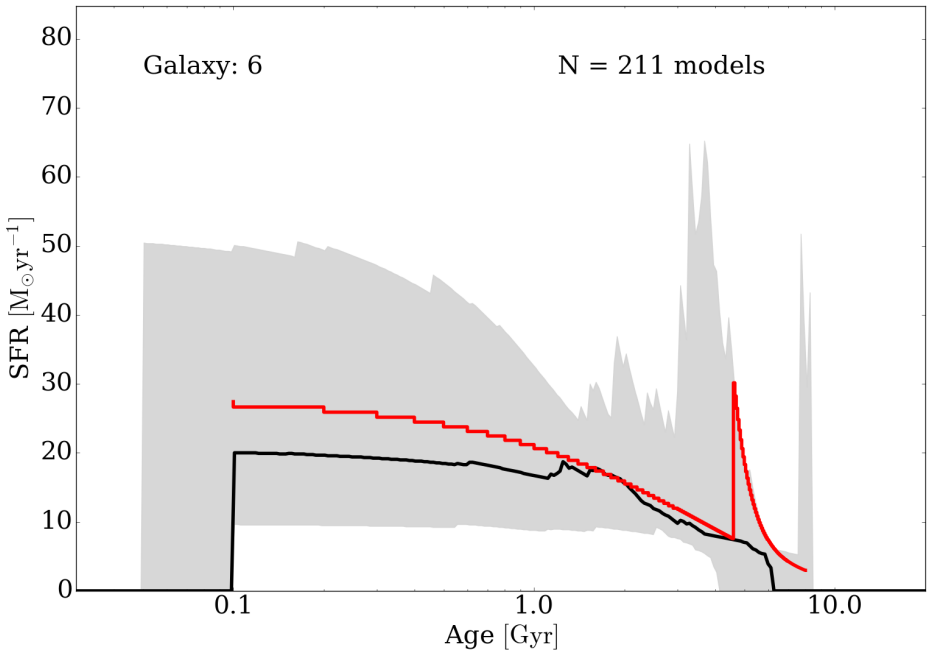

FIGURE 2.18 The stacked star formation history (shown here for HAPLESS 6) obtained using the method described in Section 2.4.2 after the smoothing function has been applied to the individual star formation histories. The burst in the best fit (shown in red) has been extended by the smoothing, and now some indication of this burst is shown in the 84$^{\text{th}}$ percentile of the stack (shown in grey). However, the burst does not appear in the median star formation history (black line) for this galaxy.

by models with no burst as they can be by models which contain a burst. Secondly, even amongst the top star formation histories which contain a burst, there seems to be very little localization of the burst (shown here for the most recent 4 Gyr). The bursts seem almost equally distributed in time (with some statistical fluctuations), and this remains the case even if the bursts are weighted by quality of fit.

2.7 INVESTIGATING THE MAGPHYS PARAMETER SPACE

Since the SFRs we obtained for the galaxies displayed the bimodal nature described above, there was often a large discrepancy between the best fit and median model. For a well constrained parameter, with a narrow distribution, it would be expected that the best fit and median model were more closely related. As previously described, the MAGPHYS fits are obtained by comparing the observations of the

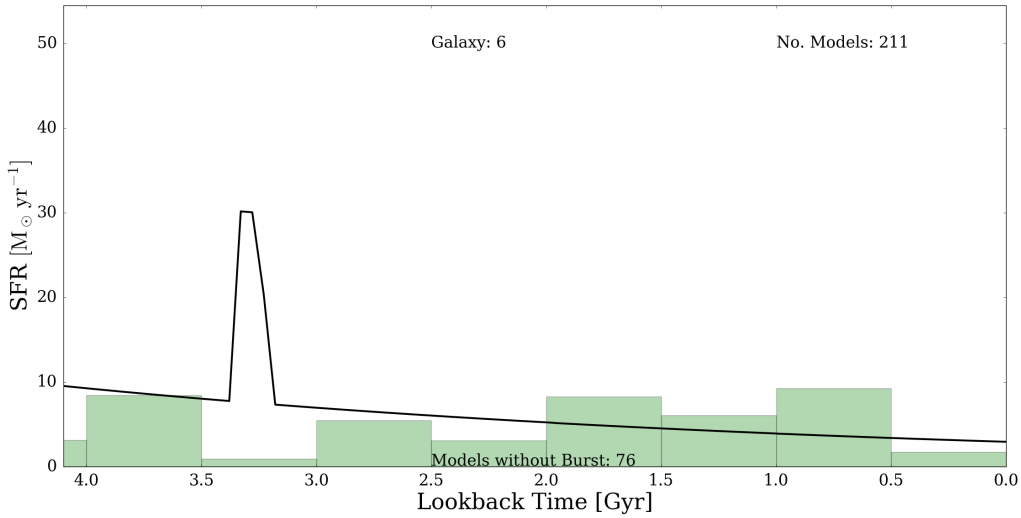

FIGURE 2.19 The best-fit star formation history for HAPLESS 6 (shown in black) plotted against lookback time. This is overlaid on a histogram of the location of bursts of star formation for the top 211 models for this galaxy (where the histogram is shown in green). While the burst appears strongly in the best-fit star formation history, there does not appear to be a consistent location of the burst across the range of best fitting models for this galaxy (ie all models MAGPHYS returns that are a 'good fit' using the criteria described in Section 2.4.2). A large fraction of best fit models do not contain any burst.

galaxies against a library of galaxy templates and noting, for each combination of optical and infrared templates which satisfy the energy balance criteria, how closely the model templates match the observations. The distribution of galaxy templates in the library, which in turn depends on the parameter priors used to produce the templates, limit the type of galaxy which the model can be used on. If the library does not contain a sufficient number of models which are appropriate for the type of galaxy which is being modelled then this will limit the quality of fit which can be obtained. Therefore we decided to investigate where the best fit and the median models for the galaxies with bimodal SFRs were located in the MAGPHYS parameter space, to see if this gave any further indication what was the cause of the bimodal SFRs or which of the values, mean or median, were more reliable.

We chose to focus on the parameters which related most closely to the SFR of the galaxy, namely the specific SFR average over the last 10^8 years (ssfr_8), time since last burst of star formation (t_{burst}) and the light weighted mean age of the (age_r). Figure 2.20 compares the full library templates for galaxy parameters used in MAGPHYS to the individual fits obtained for the HIGH and HAPLESS sample. Due to the high density of templates in certain regions of the parameter space, we indicate

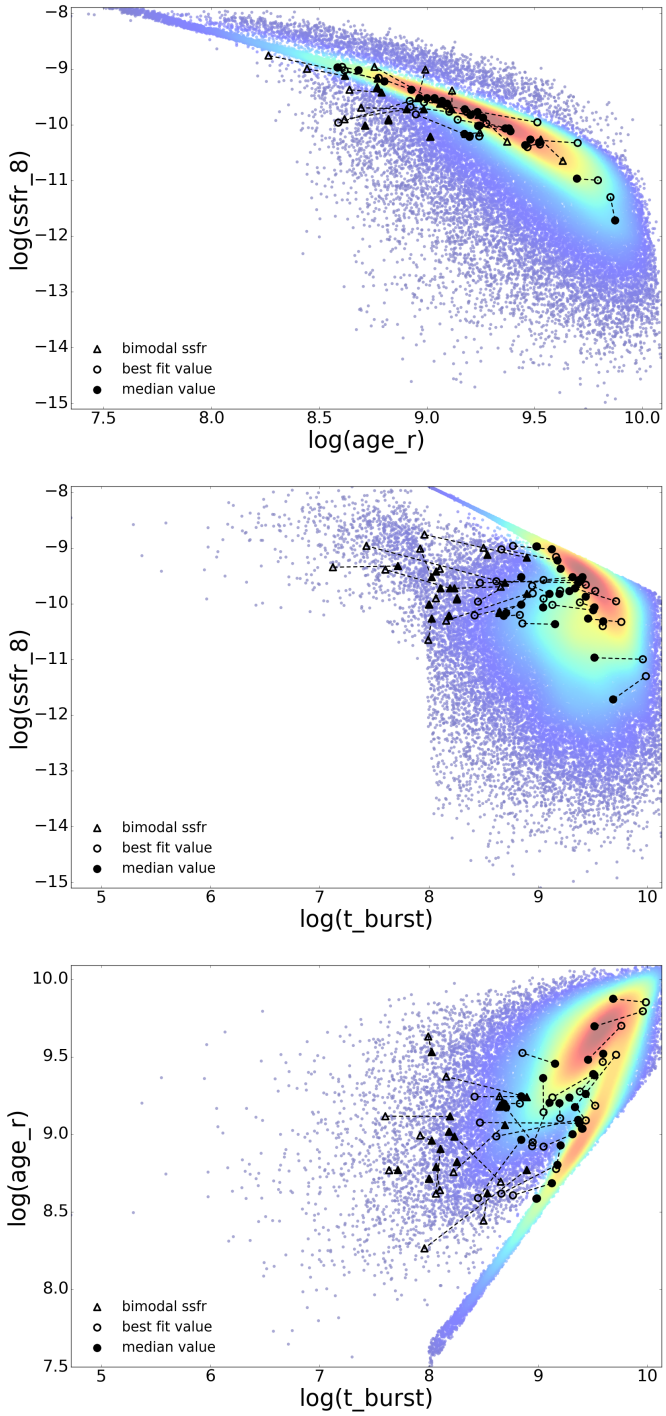

FIGURE 2.20 Distribution of all the models in the MAGPHYS libraries, across the full range of parameter space, shown here for three MAGPHYS parameters: specific star formation rate (ssfr_8), time since last burst (t_{burst}) and light weighted mean age (age_r). The density of models is indicated by a colour map, where regions of higher density are shown in red, and the lowest density regions are shown in blue. The individual galaxy fits for the full HiGH and HAPLESS sample are also shown for comparison. Sources with bimodal SFR PDFs are shown as a triangle, and the normal sources are shown as a circle. Best fit models (empty markers) are connected to the corresponding median fit for that galaxy (filled markers) with a dotted line.

the density of the templates across the parameter space using a colour map. The area of the parameter space with the highest density of models is shown in red and the lower density regions are shown in blue.

From the plot of $ssfr_8$ against age_r we can see that the galaxy templates in the MAGPHYS library are not evenly distributed across the parameter space, rather there is a locus of models centred around higher light weighted ages ($\log(age_r) \approx 9.0$) and moderately high specific star formation rates ($\log(ssfr_8) \approx -10$). For values of $\log(age_r) < 8.5$ and $\log(ssfr_8) < -12$ the density of galaxy templates in the library decreases substantially. The highest density of models are also located at longer values of time since last burst ($t_{burst} > 9.5$). Galaxies that have bimodal SFRs output by MAGPHYS are marked with triangles. We show how the best-fit and median parameter compare in these plots. We find that there are two noticeable features of the galaxies which exhibit bimodal SFRs. Firstly, the median fit for bimodal galaxies is often located in a region of higher template density than the best fit model. This is because the median value is obtained from the PDF and will be weighted towards higher density regions. Therefore if the parameter space is more sparsely sampled this will bias the median value output by MAGPHYS away from the best fit parameter. Secondly, many of the bimodal galaxies seem to be located in more sparse regions of the parameter space than the models who have well constrained SFRs. This indicates that although MAGPHYS provides a good fit to nearby galaxies that have lower gas fractions and are stellar dominated (eg M31 Viaene et al. 2016; HRS galaxies De Vis et al. 2016; and ULIRGS da Cunha et al. 2015) the MAGPHYS libraries do not contain enough models with young stellar ages and short time since last burst of star formation to satisfactorily model the unique properties of the recently detected BADGRS. These galaxies make up $\sim 35\%$ of the dust mass in the local Universe (Clark et al., 2015) and yet MAGPHYS is unable to constrain their star formation properties. Again, as with Section 2.6, this suggests that when deriving anything related to star formation properties for blue gas rich galaxies, the best-fit values from MAGPHYS are more appropriate than the median values.

2.7.1 USING OTHER MODEL LIBRARIES

The original MAGPHYS libraries, which were created with the Bruzual & Charlot (2003) stellar synthesis codes, seem limited in their compatibility with the youngest and more bursty galaxies in the HIGH and HAPLESS samples (see Section 2.7). Here we compare other MAGPHYS libraries available in the literature against the HIGH and HAPLESS samples. New extended libraries were created for use on Submillimetre

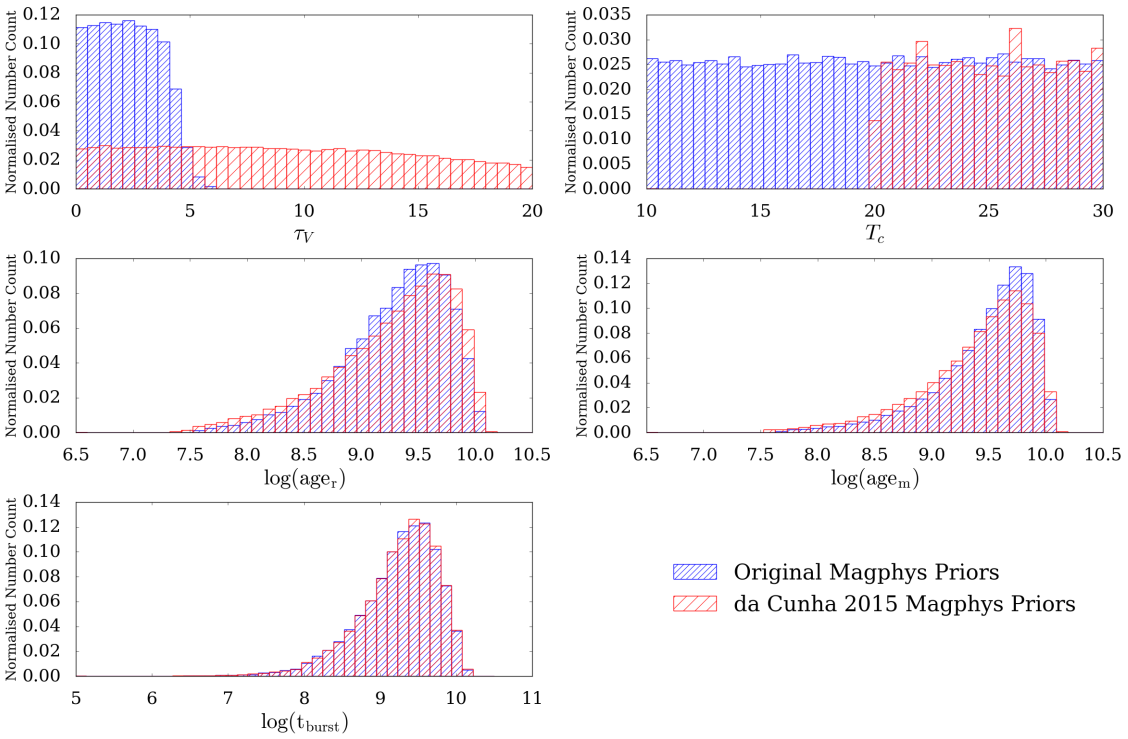

FIGURE 2.21 Comparison of a selection of the parameters from the original MAGPHYS library against the extended library used in da Cunha et al. (2015) to model high redshift galaxies; these are the parameters for which the original library was shown to have lower density of models relating to the HIGH and HAPLESS sample (see Section 2.7). The parameters are: optical depth (τ_V), cold dust temperature (T_c), light weighted mean age (age$_r$), mass weighted mean age (age$_m$) and time since last burst ($t_{\rm burst}$).

Galaxies (SMGs), since these galaxies were also noted to have physical properties outside the range of the standard library. da Cunha et al. (2015) describes in full the changes which been made to the standard MAGPHYS priors, namely an increase in the number of young, bursty and star forming templates in the library. It is worth noting that to avoid biasing the results, a large number of models were also included which have the opposite properties: older stellar ages and lower star forming rates. Due to the similarity of our sample to the properties of the SMGs (highly star forming and gas rich), it was worth comparing our sample in detail against this library. There are however two important differences between the SMGs and the BADGRS in our sample; our galaxies are local galaxies which are thought to have low optical depths, due to their very blue colour, while the SMG priors are designed for high redshift, optically thick galaxies.

Figure 2.21 shows the comparison of the standard MAGPHYS libraries against

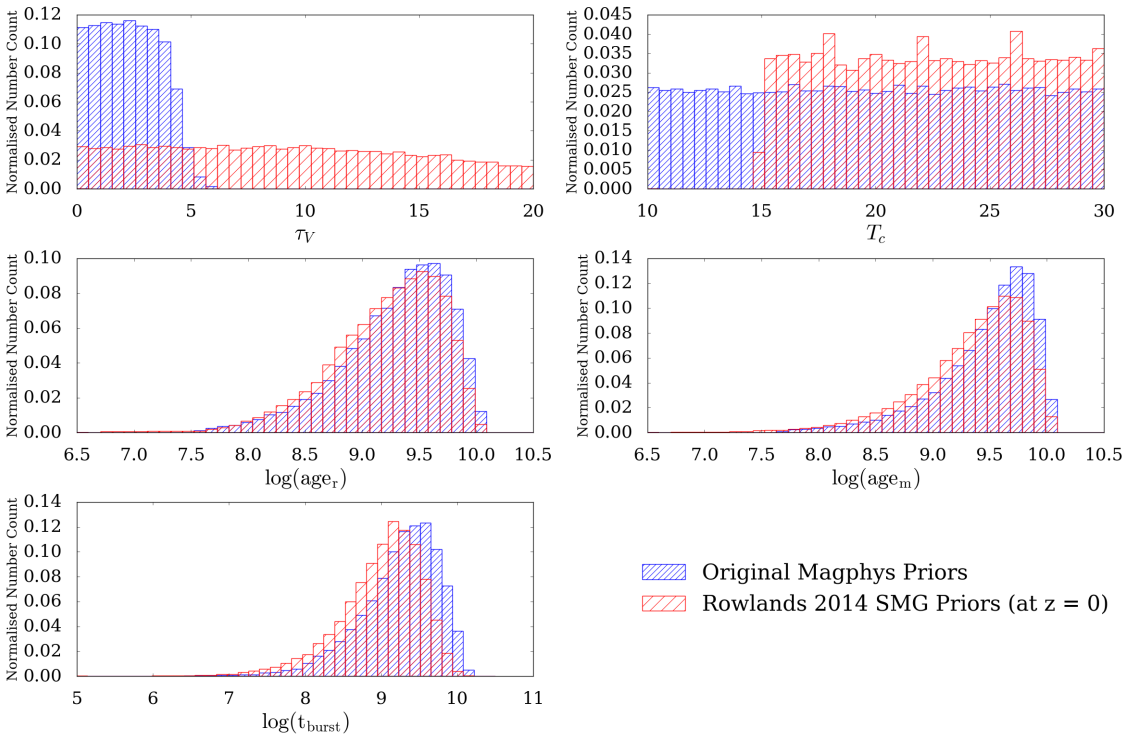

FIGURE 2.22 Comparison of a selection of the parameters from the original MAGPHYS library against the library used in Rowlands et al. (2014), similar to Figure 2.21. The parameters are: optical depth (τ_V), cold dust temperature (T_c), light weighted mean age (age$_r$), mass weighted mean age (age$_m$) and time since last burst (t_{burst}).

the SMG libraries of da Cunha et al. (2015). We have shown here the comparison of the parameters which were found to be most incompatible with the properties of the HIGH and HAPLESS galaxies in the standard libraries (stellar ages and time since last burst of star formation). We also show the comparison for other parameters which have significantly changed between the different versions of the MAGPHYS libraries. We can see that the high redshift library of da Cunha et al. (2015) includes many models which have a higher optical depth, with τ_V now ranging from 0-20 in contrast to 0-8 in the original library of da Cunha et al. (2008). The cold dust temperature in the da Cunha et al. (2015) libraries have a range from 20-30 K, while in the Section 2.3.3 we have seen that the MAGPHYS fits for the HIGH and HAPLESS sample can be improved when extending the cold dust temperature down to values as low as 10 K. Therefore, it seems that the dust properties of the HIGH and HAPLESS sample are different to the dust properties of the SMGs targeted by the da Cunha et al. (2015) libraries.

When looking at the parameters which relate to the age of the stellar populations in the galaxies, we can see that there are a selection of templates in the da Cunha et al. (2015) library with lower intrinsic stellar ages, as indicated by the lower mass- and light-weighted ages. However, the shift in the age distribution of the templates in the library is small when compared to the difference in optical depth and dust temperature. Finally, when comparing the time since last burst for the galaxy templates, we find little difference between the two distributions. It would seem that while the SMG library of da Cunha et al. (2015) does contain some models which extend to younger stellar ages, switching to this library for the HiGH and HAPLESS sample would not be advantageous, due to the intrinsic differences SMGs and the samples used in this work.

There was also a second extended MAGPHYS library available in the literature, which had been used in Rowlands et al. (2014) which had been again designed for use with SMGs located at lower redshifts ($z \sim 2$), and therefore could potentially be even more well suited to the HiGH and HAPLESS sample. In Figure 2.22, we now compare the same parameters from the original MAGPHYS library against the Rowlands et al. (2014) SMG MAGPHYS library. Again, we find that the range of optical depths in the Rowlands et al. (2014) library is substantially extended to high optical depths, limiting the number of galaxy templates in the library which are directly applicable to the HiGH and HAPLESS sample. The cold dust temperature ranges from 15-30 K in the Rowlands et al. (2014) library and again fails to reach cold dust temperatures as low as thought to be present in the HiGH and HAPLESS galaxies.

We can see a substantial increase in the number of models with younger mass and light weighted ages, and there is also a shift towards galaxy templates with a shorter 'time since last burst' in the Rowlands et al. (2014) library. Both of these adaptations would increase the number of templates which occupy the same region of the parameter space as the HiGH and HAPLESS galaxies, and hence could improve the quality of the fits obtained. However the Rowlands et al. (2014) library has been computed using the spectral synthesis code of Charlot & Bruzual 2007 (CB07); there are known issues with modelling of the 'Thermally Pulsing'-AGB stars in the CB07 library, and it is recommended in MAGPHYS documentation to return to the library of Bruzual & Charlot (2003). Therefore neither the library of Rowlands et al. (2014) or da Cunha et al. (2015) would offer any advantages to the modelling of the HiGH and HAPLESS samples. This highlights the need for new libraries to be created that extend down to $\log(t_{\rm burst}) < 8.5$ and $\log(\mathrm{age}_r) < 9.5$ with $-11 < \log(\mathrm{ssfr}_8) < -8$. This work is beyond the scope of this thesis.

2.8 Conclusion

In this chapter we have introduced the dust-selected sample from (Clark et al., 2015) (selected at 250 μm from the GAMA fields, see section 2.2 for further details) and HI-selected sample from (De Vis et al., 2016) (HI-detections in the same GAMA fields, see section 2.2 for further details) which are used in this thesis. We described the changes we initially made to the SED fitting model of da Cunha et al. (2008) in order to fit the spectral energy distribution (SED) of this sample of galaxies. We showed that to obtain good fits for the galaxies in the sample, it was necessary to obtain additional photometry (eg from IRAS) to constrain the mid-infrared SED.

The unique physical properties of the Blue And Dusty Gas Rich Sources (BADGRS, galaxies in our sample having FUV-$Ks < 3.5$) caused problems for the standard library of galaxy templates used in MAGPHYS. We have shown that we have to use an extended cold dust temperature prior ($10 - 30$ K) when modelling these galaxies, and suggested a method to create a 'PDF' for the individual SFH of each galaxy. MAGPHYS has difficulty measuring the star formation rate in the BADGRS (resulting in an underestimate of SFR, and a bimodal PDF, suggesting the SFH is also not constrained), and we have shown that this is likely to be due to the method used to measure the star formation rate becoming unreliable if the galaxy had recently experienced a burst of star formation. We suggest a method of smoothing the MAGPHYS bursts to resolve this issue, but there is no single smoothing factor for the sample. Therefore this method is unlikely to be useful for large samples of galaxies. We also demonstrated that neither the standard library templates, nor additional libraries in the literature (eg Rowlands et al. 2014; da Cunha et al. 2015) contain a high enough density of models with young stellar ages and low time since last burst to satisfactorily represent the BADGRS in our sample. Therefore our sample really highlights the limitations of the MAGPHYS routine. We recommend that if galaxies are located in a sparsely populated region of the parameter space the *best-fit* values are used for those galaxies, since the median value output by MAGPHYS is likely biased due to lack of models to choose from in that region of parameter space. Additionally, creating a median SFH for a galaxy washes out any information on burst location compared to the best-fit SFH model. Finally, for the bimodal sources, the best-fit value SFR either shows good agreement with, or improves upon, the median SFR when compared to the SFR estimated using the FUV and 22 μm (itself likely to be underestimated for bursty galaxies), with the exception of two galaxies. In the next chapter we move away from looking at individual galaxies, and instead attempt to constrain star formation properties of the sub-populations within the combined

HiGH and HAPLESS sample.

Chapter 3
The Average Star Formation Properties of Dust Rich and Blue Galaxies in the Local Universe

3.1 Introduction

The star formation history plays an important role in the evolution of a galaxy, influencing the build up of stars, metals and dust in the interstellar medium (Annibali et al., 2013; Michałowski et al., 2014; Casey et al., 2014; González Delgado et al., 2014). Multiwavelength spectral energy distribution modelling presents a unique opportunity to investigate the the star formation histories of large numbers of galaxies, with initial work showing good agreement to star formation properties derived from more classical methods (Schawinski et al., 2007; Walcher et al., 2008; Wild et al., 2009; Rowlands et al., 2012). In this chapter we use the MAGPHYS fits obtained in Chapter 2 to investigate the average star formation properties of the HiGH and HAPLESS samples, when they are first split by colour (into BADGRS and non-BADGRS) and then by dust (into dust-rich and dust-poor, defined in Section 3.3.1). To achieve this, we investigate the average Spectral Energy Distributions (SEDs), Star Formation Histories (SFHs), and physical properties of each sub-sample to characteristic key differences between their star formation properties.

We base our analysis in this chapter on the *best-fit* values obtained from MAGPHYS for the HiGH and HAPLESS galaxies. We use the best-fit values because many of the galaxies in the sample have been shown to be located on the extremities of the MAGPHYS parameter space, where the template density in the input libraries is lower (see Chapter 2, Section 2.7). As such, the median value output by MAGPHYS for

certain parameters can be incorrectly biased towards regions of higher template density, away from the best-fitting value for that galaxy. Additionally, by comparing the differences *between* sub-samples of galaxies we can identify whether there are differences in the star formation properties of galaxies as a population (ie on average), as measured by MAGPHYS, without worrying if the values obtained from MAGPHYS for individual galaxies are correct.

Following this, we also attempt to verify the differences between the star formation properties of the BADGRS and non-BADGRS, and dust-rich/dust-poor galaxies by comparing the results obtained from MAGPHYS SED modelling against the star formation properties derived from the optical spectra of the sample. This enables us to determine if multiwavelength SED modelling using MAGPHYS presents a reliable method of obtaining general star formation properties for HIGH and HAPLESS.

3.2 SAMPLE SPLIT: BADGRS VS NON-BADGRS

In this section, we compare the properties of the BADGRS (ie the blue and gas rich sources, defined as galaxies with FUV-$Ks < 3.5$, see Clark et al. 2015) and non-BADGRS, as derived from SED modelling using MAGPHYS. We choose to investigate the differences between the average properties of the BADGRS and non-BADGRS for the following reasons. We know that the BADGRS are optically blue (by definition) and we also know that optically blue galaxies tend to be both younger and more actively star forming than 'red and dead' galaxies (Leslie et al., 2016; Guo et al., 2016). By comparing the average values of the sub-samples we can 'test' whether the SEDs and star formation properties derived by MAGPHYS produce sensible results for our sample of 58 galaxies. In Section 3.3 we will next investigate whether there are intrinsic differences between the same properties of the dust-rich and dust-poor galaxies in our sample.

3.2.1 AVERAGE SPECTRAL ENERGY DISTRIBUTIONS: BADGRS AND NON-BADGRS

To determine whether there are any variations in the best-fit SEDs of the BADGRS and non-BADGRS as derived by MAGPHYS, we create a stacked SED for these two sub-samples following the method of Smith et al. (2012a). Firstly we normalise each best-fit SED to its mean value between 0.01 and 1000 μm, so that the stacked SED of each sub-sample is not dominated by the more luminous galaxies. Then we

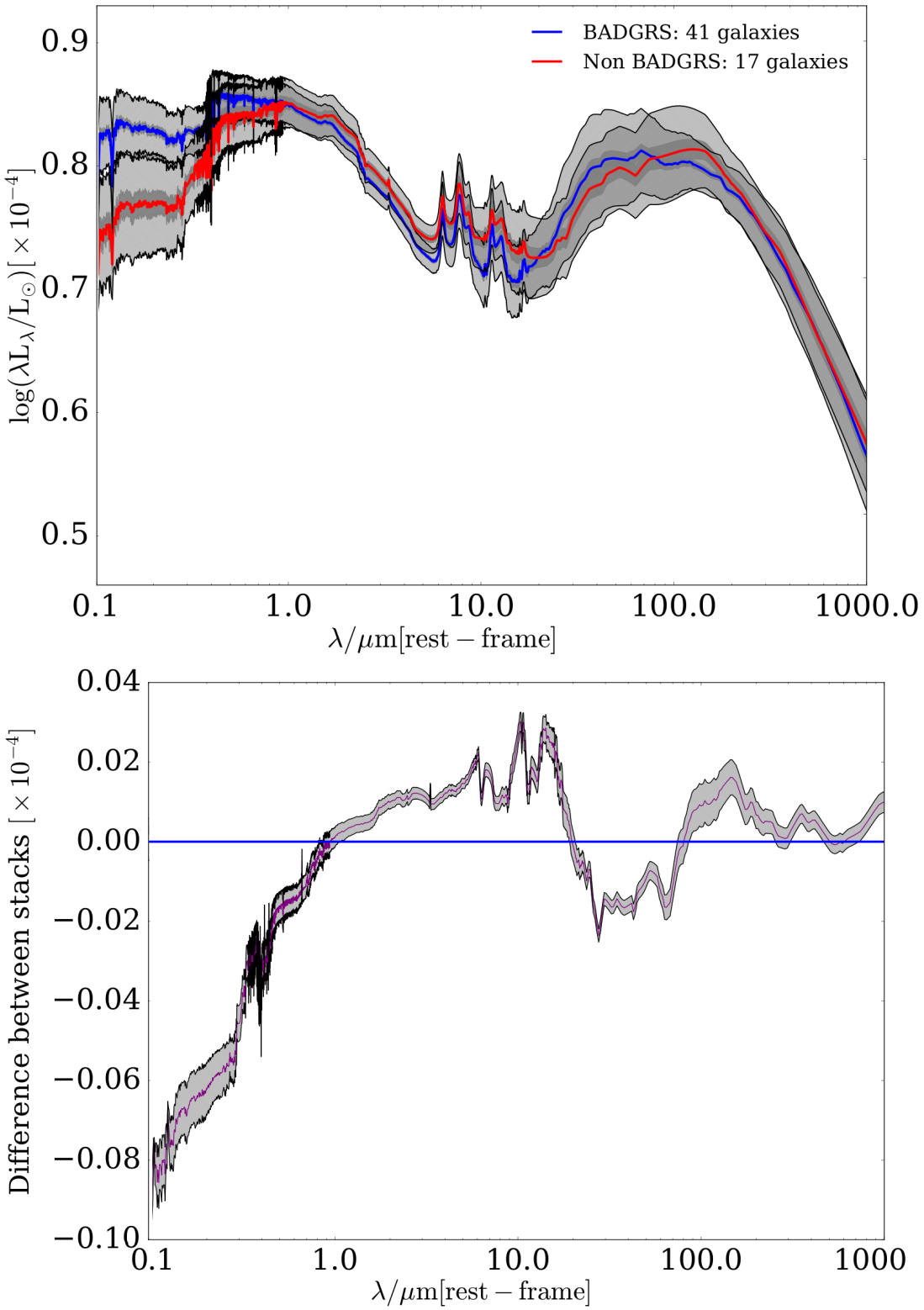

Figure 3.1 *Top:* The stacked best-fit SEDs of the combined HiGH and HAPLESS sample obtained from MAGPHYS and separated into BADGRS and non-BADGRS sub-samples defined by their FUV-*Ks* colour. The blue line shows the median of the stacked SED for the BADGRS, while the red line shows the median SED for the non-BADGRS. The 1σ spread for each population is shown in light grey, dark grey shows $\sigma/\sqrt{N}$. *Bottom:* The delta stack: the difference between the median non-BADGRS and the median BADGRS SEDs. The non-BADGRS have less emission at UV wavelengths, compared to the BADGRS.

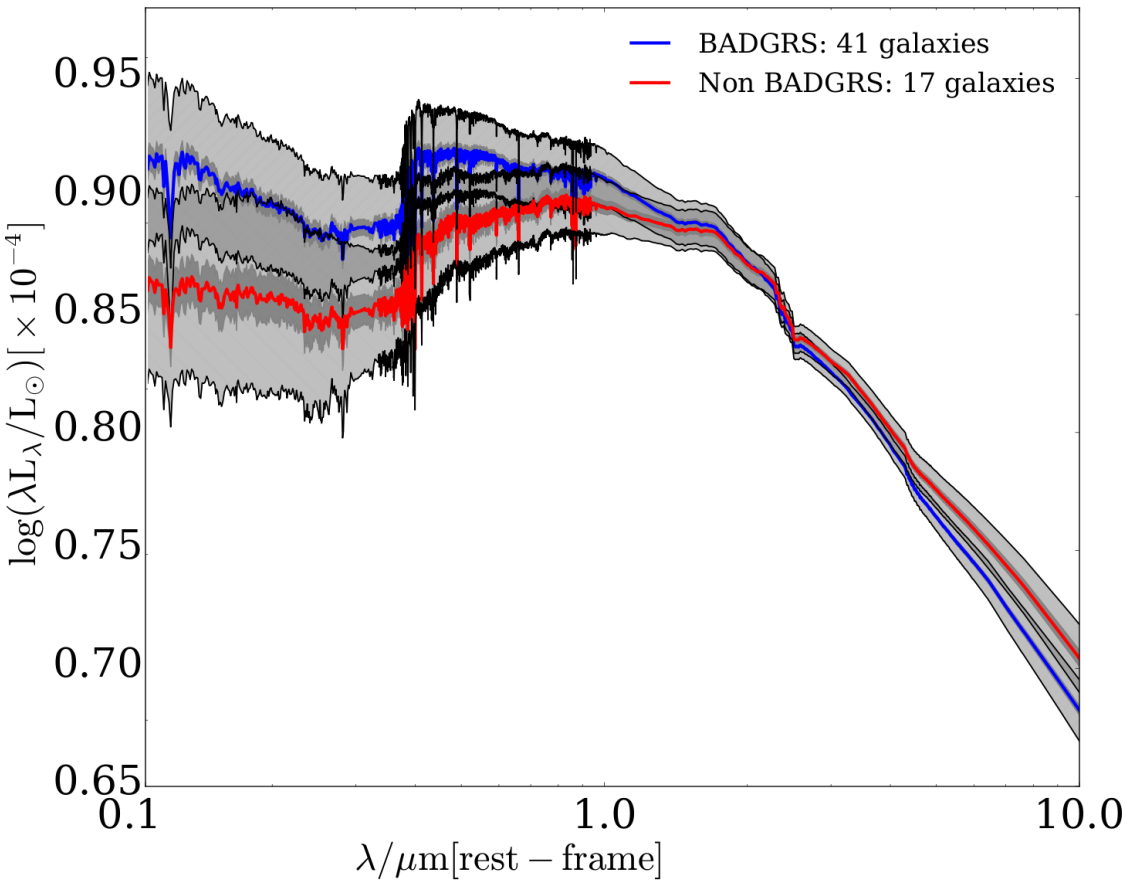

FIGURE 3.2 The recovered stellar emission of the sample from MAGPHYS: the light that would have been emitted if it had not been attenuated by dust.The BADGRs have an intrinsic excess of emission at short wavelengths, compared to the non-BADGRS, which could be attributed to a younger stellar population.

re-sample the galaxies onto an equal size wavelength grid. Finally, for each wavelength bin we calculate the median and 1σ uncertainty for the ensemble of galaxies.

Figure 3.1 (top) shows the comparison of the stacked best-fit SEDs for the two populations of galaxies. For ease of comparison, we also plot the difference between the median BADGRS and the median non-BADGRS SED (Figure 3.1, bottom). We find that the median SED for the non-BADGRS has significantly less emission at wavelengths shorter than 0.8 μm compared to the median BADGRS SED; as expected, the BADGRS appear more optically blue. We also see that the BADGRS potentially have more emission in the MIR region of the SED from dust than the non-BADGRS.

In Figure 3.2, we compare the SEDs of the recovered unattenuated starlight from MAGPHYS (i.e. the stellar emission if there was no dust attenuation). As expected due to the red colour, the non-BADGRS have intrinsically less stellar emission in the UV-optical regions of the SED. These results could be interpreted as the BADGRS

having experienced enhanced star formation recently, which would have the effect of increasing the relative number of short-lived, blue, massive stars in these galaxies. Alternatively, a different dust extinction law for the BADGRS population could account for the variations seen in Figure 3.2 although we leave this for future work.

3.2.2 Average Star Formation Histories: BADGRS and non-BADGRS

To investigate whether there are any differences between the SFHs of the BADGRS and non-BADGRS populations as measured by MAGPHYS, we created a stacked SFH (of the best-fit SFHs only) for each population. We did this since it is difficult to accurately obtain unique individual histories from SED modelling (see Chapter 2), and so by comparing the SFHs of the populations as a whole, we can more easily investigate the average properties of a population of galaxies. Additionally, we have shown that using the median SFH is likely to 'wash out' any bursty features (Chapter 2, Figure 2.14).

To create the stacked SFHs, we followed in part the method of Rodríguez-Muñoz et al. (2015). First, the individual SFHs were normalised to the median stellar mass of the sample, such that each galaxy produces the same number of stars. This was done so that all galaxies contribute equally to the stacked SFHs, independent of their stellar mass. The individual best-fit SFHs were then uniformly re-sampled in time, to enable direct comparison between the sub-samples. The individual SFHs were then aligned such that they had the same end time (ie today). The median value in each time bin was calculated separately for both the BADGRS and non-BADGRS, with uncertainty given by the $\sigma/\sqrt{\mathrm{N}}$ spread of the data in Figure 3.3. The BADGRS appear to be forming stars more recently than the non-BADGRS population, with a median SFH timescale ~ 3 Gyr shorter than the non-BADGRS (shown by the solid blue and red lines for the BADGRS and non-BADGRS respectively). It is worth noting that in Figure 3.3, the stacked SFHs are displayed such that they have the same end time. Therefore we can see that during the first ~ 2 Gyr the stacked BADGRS SFH is more dominated by bursty features than the stacked SFH of the non-BADGRS.

Next, we compare the average Probability Distribution Functions (PDFs) of star formation parameters for the BADGRS and non-BADGRS output by MAGPHYS. First we discuss the 'r-band light weighted mean age of the stellar population' (age_r); this is the average age of all stellar populations in the galaxy, weighted by their current contribution to the total luminosity. To calculate the stacked PDF for this parameter for BADGRS and non-BADGRS, we first take the best-fit value of the

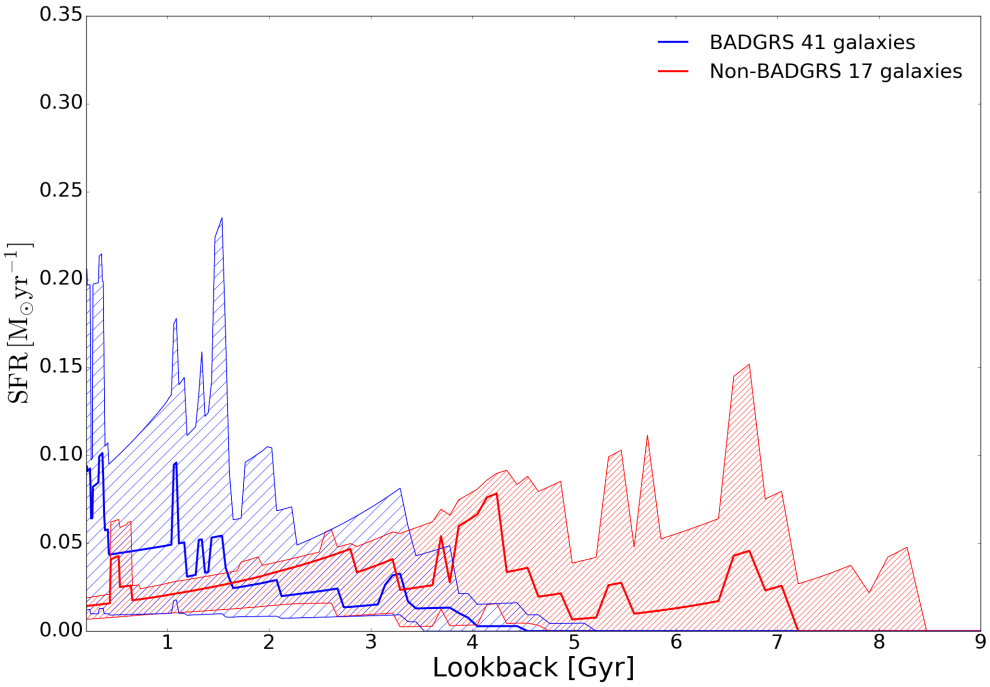

FIGURE 3.3 The stacked best-fit SFH of the HIGH and HAPLESS galaxies for the BADGRS and non-BADGR galaxies obtained from MAGPHYS. The solid line shows the median SFR at each time for the two populations, and the shaded region indicates the 16$^{\text{th}}$ and 84$^{\text{th}}$ percentiles of the stack. The median BADGRS SFH (solid blue line) is ~ 3 Gyr shorter than the median non-BADGRS SFH (solid red line), indicating that these galaxies are at an earlier stage of their evolution and have more recently experienced a burst of star formation.

PDFs output by MAGPHYS for each individual galaxy. We then create a histogram of the value of each parameter for the BADGRS and non-BADGRS sub-samples (Figure 3.4) and measure the mean value for each sub-sample. To estimate the uncertainty on this value, we randomly perturb the value in each bin of the histogram by a value between $\pm\sqrt{N}$ and re-sample the mean of the resultant distribution for 10^4 iterations. The error on the mean for each sub-sample is then estimated from the $1\,\sigma$ width of the resultant distribution. Figure 3.4 shows that the BADGRS subset are, on average, younger than the non-BADGRs, with an age$_r$ of (1.89 ± 0.14) Gyr compared to (5.32 ± 0.21) Gyr for the non-BADGRS galaxies. A two-tailed K-S test shows that the BADGRS and non-BADGRS are sampled from populations with different age$_r$ distributions ($p = 0.00041$) assuming 95% critical $p-$value.

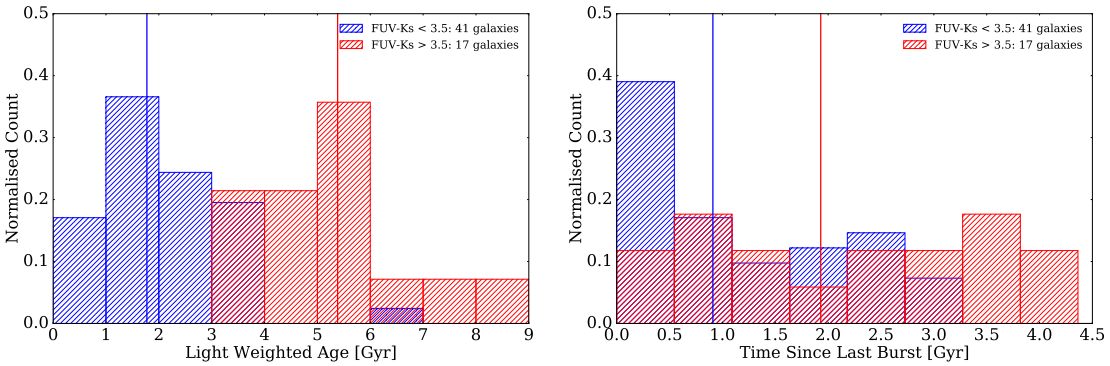

Figure 3.4 *Left:* Histogram showing the comparison between the 'light weighted mean age' parameter (age_r) for the BADGRS and non-BADGRS, as measured by MAGPHYS. The BADGRS have a significantly lower age_r than the non-BADGRS. *Right:* Similar plot, showing the time since last burst for the BADGRS and non-BADGRS. It seems, on average, that the BADGRS have more recently experienced a significant burst of star formation than the non-BADGRS.

The differences between the BADGRS and non-BADGRS star formation properties are further corroborated by comparing the time since last burst ($t_{\rm burst}$) parameter from MAGPHYS for the two populations (Figure 3.4). This shows that the BADGRS have more recently experienced a burst of star formation with a $t_{\rm burst}$ of (0.91 ± 0.15) Gyr in contrast to (1.93 ± 0.27) Gyr for the non-BADGRS. Again, the two-tailed K-S test shows that the two populations have statistically different $t_{\rm burst}$ distributions ($p-$value of 0.038).

In summary (and as expected) we find that the BADGRS have bluer SEDs (both intrinsic and attenuated by dust), have evidence of recent bursts in the stacked SFHs and $t_{\rm burst}$ parameter, and have younger stellar populations.

3.3 Sample Split: Dust-Rich vs Dust-Poor

Following Section 3.2 we have confidence that we can use the best-fit values output by MAGPHYS to further investigate the average differences between subpopulations of galaxies in our sample. One unresolved issue from Clark et al. (2015) and De Vis et al. (2016) is that some of the BADGRS were dust rich, while others were dust poor. Here we wish to determine if their dust properties are a result of their past or current SFH (note that in Chapter 6 we will explore other potential explanations, including different dust sources and IMFs).

3.3.1 DEFINING A DUST RICH GALAXY

We compare the $M_{\rm d}/M_{\rm HI}$ (dust-to-gas mass ratio) and $M_{\rm d}/M_{\rm s}$ (dust-to-stellar mass ratio) of our sample in Figure 3.5 (for more details of the sample properties see Chapter 2). We have chosen to define how dust-rich or dust-poor a galaxy is from mass ratios, because we do not want to split the sample by absolute dust mass. Rather we wish to define how dust-rich or dust-poor a galaxy is compared to its gas and stellar content.

From Figure 3.5, we can see that there are three distinct regions of the plot that the HIGH and HAPLESS galaxies occupy. In region 'A', the galaxies have a relatively high dust mass compared to their atomic hydrogen gas mass. These galaxies have high $M_{\rm s}$ and are thought to be at the later stages of their evolution (due to their lower gas content) ie, they have converted much of their initial gas into stars (these sources are the more typical 'grand design' spirals present in stellar mass selected samples such as the HRS). These galaxies have a lot of dust relative to their atomic gas, but are relatively dust-poor when comparing the dust mass to the stellar mass. In region 'B', the galaxies can be defined as dust-poor compared to both their stellar mass and gas mass. These galaxies are likely to be in an unevolved state, they have not yet converted much of their initial gas into stars, and also have not created much dust (such high gas fraction sources are a feature of the blind HI-selected sample HIGH). Finally, in region 'C' the galaxies have high dust content compared to both the gas mass and stellar mass. These galaxies seem to have created a large amount of dust given the amount of gas that they have converted into stars, again suggesting an early stage of evolution (these sources are seen in the blind dust-selected sample, HAPLESS). Here we wish to investigate whether these differences relate to different star formation properties. Therefore we define the dust-rich sample as galaxies that have $\log(M_{\rm d}/M_{\rm HI}) > -3.6$ and $\log(M_{\rm d}/M_{\rm s}) > -2.6$.

Of the 58 galaxies that are in the combined HIGH and HAPLESS sample, there are 11 galaxies that do not have any HI measurements. We cannot classify these sources as dust-rich or dust-poor from Figure 3.5. Therefore in the following sections we compare the star formation properties of the 47 galaxies split into 16 dust-rich galaxies and 31 dust-poor galaxies.

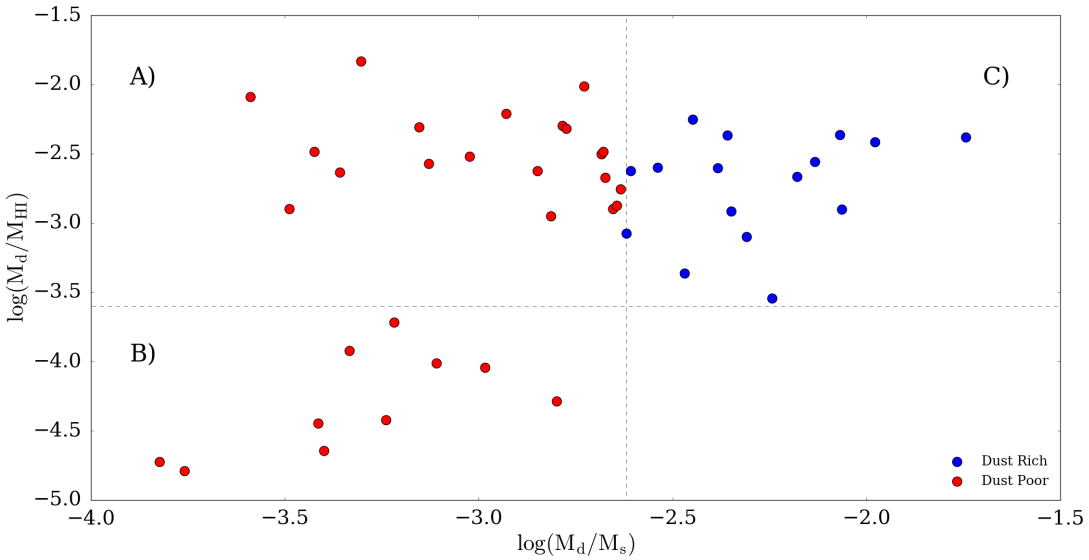

Figure 3.5 Comparison of $\log(M_{\rm d}/M_{\rm HI})$ against $\log(M_{\rm d}/M_{\rm s})$ for the HiGH and HAPLESS sources. There are 11 galaxies that do not have HI measurements, and so can not be classified in this scheme. We define dust-rich galaxies (shown in blue, region 'C') as galaxies with both $\log(M_{\rm d}/M_{\rm HI}) > -3.6$ and $\log(M_d/M_{\rm s}) > -2.6$. We note that there can be considered two classes of dust-poor galaxies: evolved galaxies that are dust-poor in $M_{\rm d}/M_{\rm s}$, but not in $M_{\rm d}/M$HI, due to the large number of stars they have formed (region 'A'); and unevolved galaxies that are dust-poor in $M_{\rm d}/M_{\rm HI}$ (region 'B').

3.3.2 Average Spectral Energy Distributions: dust-rich and dust-poor

In this section, we compare the stacked best-fit SED for the dust-rich and dust-poor sub-samples. We use the same method as described in Section 3.2.1 with results in Figure 3.6. We can see that there are key differences between the stacked SED of the dust-rich and dust-poor sub-samples. Firstly, the dust-rich galaxies appear bluer than the dust-poor galaxies; they have enhanced UV and optical emission, although the difference is not as striking as in Figure 3.1 (where we compared the BADGRS and non-BADGRS). Secondly the dust-rich galaxies are less luminous in the MIR and FIR regions of the SED than the dust-poor galaxies. There is also an indication that the FIR peak is wider for the dust-rich galaxies than for the dust-poor galaxies. This is subject to the caveat that this region of the SED can be affected by limited photometry (see Chapter 2 Section 2.3.2).

Figure 3.6 (bottom) shows the comparison between the stacked un-attenuated SED of the dust-rich and dust-poor sub-samples. In contrast to Figure 3.2, there seems to be little difference between the intrinsic light from the stellar populations

of the dust-rich and dust-poor galaxies. This is an indication that the differences which we can see between the stacked SEDs of the dust-rich and dust-poor sub-samples (described above) are due to different dust properties of the galaxies and not differences between their stellar populations.

3.3.3 AVERAGE STAR FORMATION HISTORIES: DUST-RICH AND DUST-POOR

Here we compare the stacked best-fit SFH of the dust-rich/dust-poor galaxies in HIGH and HAPLESS following the method described in Section 3.2.2. We can see that there appears to be no significant differences between the best-fit SFHs output by MAGPHYS for the two populations, with both stacked SFHs showing some 'bursty' features and having the same time duration. In contrast to Figure 3.3, there are very few galaxies with SFH longer than 4.5 Gyr in the dust-poor and dust-rich populations. The absence of the longer duration SFHs is due to the fact that we are missing the reddest, low gas fraction sources due to lack of HI detection. These galaxies could not be classified on dust-rich/dust-poor following the method outlined in Section 3.3.1, and are shown as a third 'unclassified' sample in Figure 3.7. These galaxies are excluded from further analysis in this Section since we are specifically investigating the difference between dust-rich and dust-poor galaxies in the sample. At first glance there seems to be little difference in the average SFHs of the dust-rich and dust-poor sub-samples.

Next, we create a histogram of the best-fit values of age_r and t_{burst} in Figure 3.8. Again there appears to be little variation between the age of the dust-rich/dust-poor galaxies: the dust rich galaxies have $\mathrm{age}_r = (1.69 \pm 0.39)$ Gyr compared to the dust-poor galaxies, which have $\mathrm{age}_r = (2.23 \pm 0.27)$ Gyr. A K-S test shows that there is no statistical variation between the light weighted mean age of the two sub-samples, with a $p-$value of 0.056. This seems to be in agreement with the stacked SFH of the galaxies from MAGPHYS in Figure 3.7.

We also compare the time since last burst histogram for the dust-rich/dust-poor sub-samples. The dust-rich galaxies have a mean value of $t_{\mathrm{burst}} = (0.61 \pm 0.16)$ Gyr, compared to a value of $t_{\mathrm{burst}} = (1.37 \pm 0.22)$ Gyr for the dust-poor galaxies. A K-S test shows there to be some statistical variation between the two sub-samples, with a $p-$value of 0.027. In summary, there appears to be little difference in the average star formation properties (and SFHs) of the dust-rich and dust-poor galaxies (although there is slight evidence that there have been more bursts in the last Gyr for dust-rich sources compared to dust-poor galaxies). However these findings, and

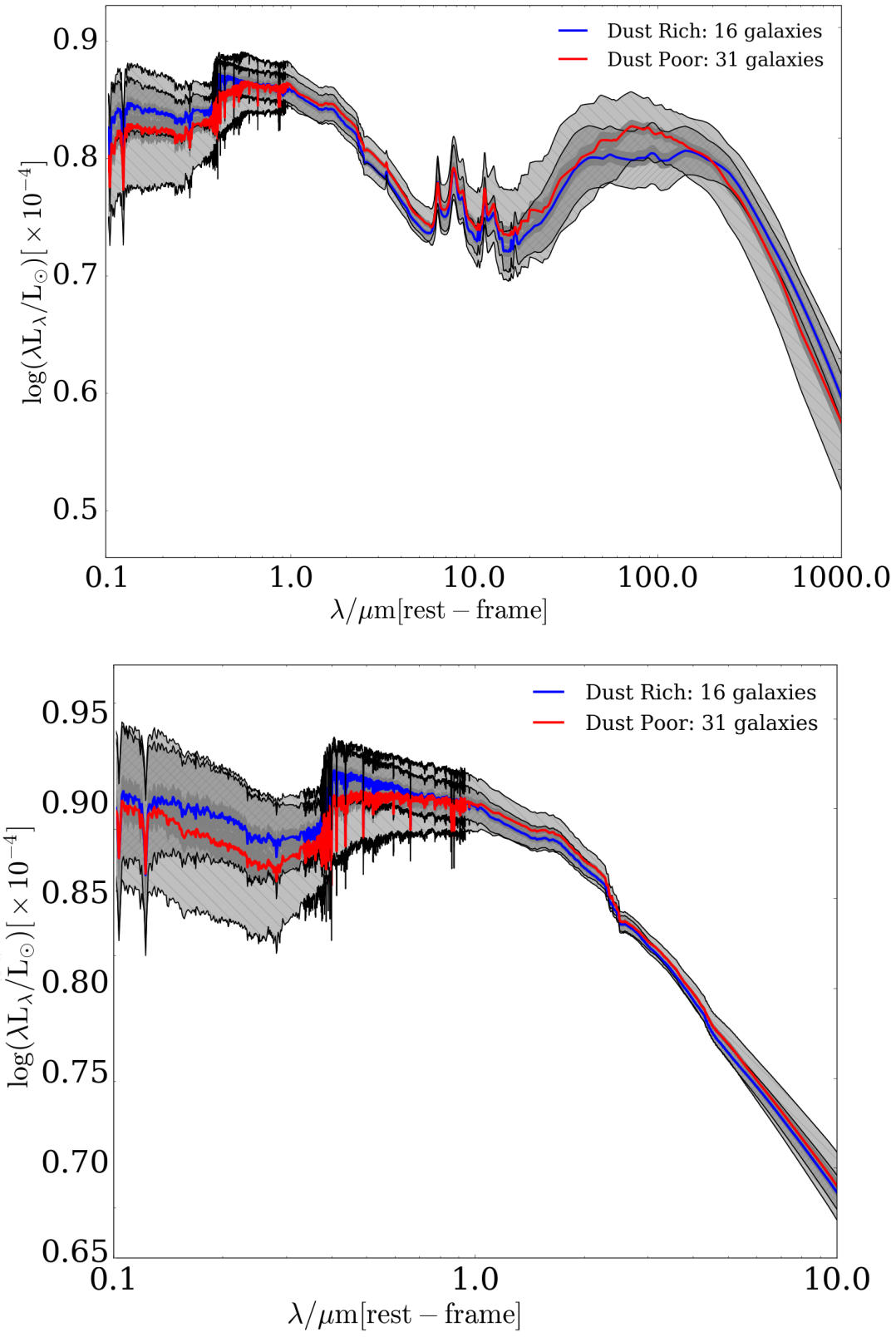

Figure 3.6 *Top:* Comparison of the stacked best-fit SEDs (created using the method described in Section 3.2.1) for the dust-rich and dust-poor galaxy sub-samples. The dust-rich galaxies (shown in blue) appear both bluer in the optical and less luminous in the mid-FIR. *Bottom:* Comparison of the un-attenuated SED for the dust-rich/dust-poor galaxy sub-samples. We can see that the intrinsic light from the stars is similar for the two sub-samples, so key differences seen in the stacked SED (above) could be due to the different dust properties of the two sub-samples.

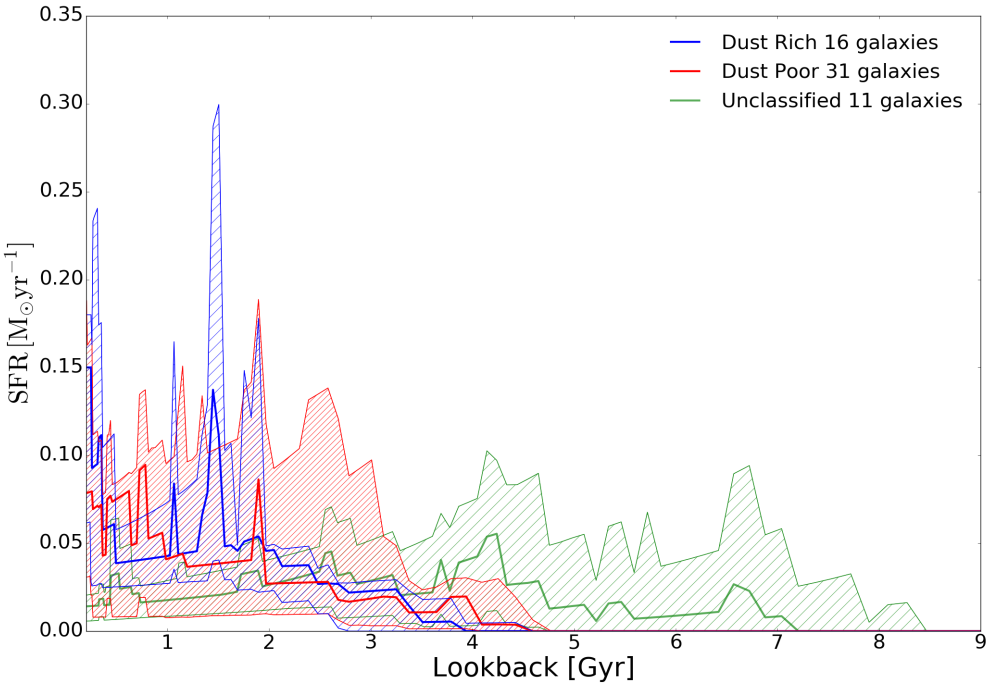

FIGURE 3.7 Stacked best fit SFHs for the two galaxy sub-samples, dust-rich (shown in blue) and dust-poor (shown in red), created using the method described in Section 3.2.2. We can see that these populations have similar length stacked SFHs. We are missing the oldest, reddest galaxies that were seen in the long tail of the distribution in Figure 3.3, due to lack of gas information (shown for reference here in green).

the results from the comparison of the BADGRS and non-BADGRS in Section 3.2, are subject to the following caveats:

1. There are a low number of sources in the sub-samples (this is particularly true for the dust-rich galaxies) and these low numbers may be affecting the comparison of the star formation properties.

2. We are comparing the best-fit values of the parameters only, since the median parameters for some of the galaxies in our sample are likely biased due to the galaxies occupying sparsely sampled regions of MAGPHYS parameter space.

3. The lack of HI measurements for some galaxies prevents us from including our full sample in the dust-rich and dust-poor comparison (this preferentially excludes the reddest galaxies in our sample, region A of Figure 3.5).

4. MAGPHYS star formation properties are based on broadband photometry, and are not based on spectra. Therefore they may be biased by uncertainties in the

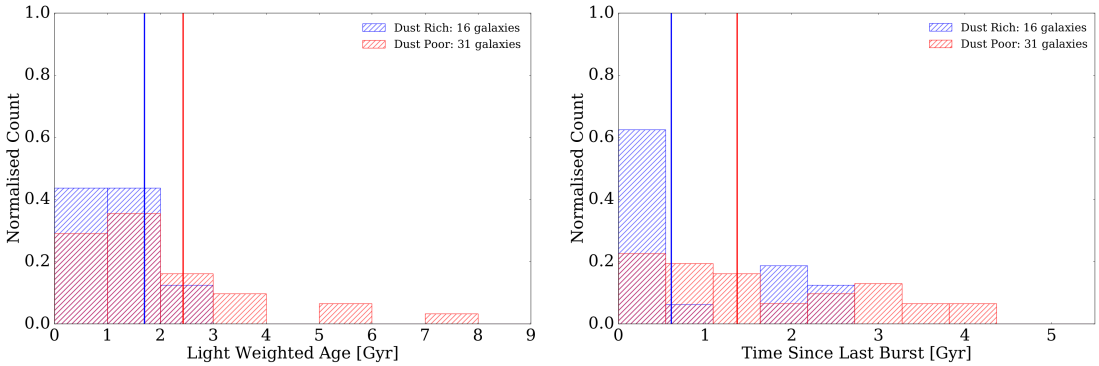

Figure 3.8 *Left:* Histogram showing the comparison of the best-fit 'light weighted mean ages' for the dust-rich and dust-poor galaxy sub-samples. In agreement with Figure 3.7, we see that these galaxies have a similar age distribution (although there are a few sources in the dust-poor sub-sample with higher ages). *Right:* Histogram showing 'time since last burst' for the two sub-samples. We see that there is some evidence that the dust rich galaxies have more recently experienced significant bursts of star formation than the dust-poor galaxies.

process of SED modelling; the choice of IMF and stellar population models for example.

3.4 What can we learn from optical spectra of our sample

In the previous section, we saw how we can use MAGPHYS to analyse the average star formation properties of the combined HiGH (De Vis et al., 2016) and HAPLESS (Clark et al., 2015) galaxy sample. We found that when the sample was either split into dust-rich and dust-poor galaxies or by colour (BADGRS: FUV-Ks < 3.5) there were significant differences between the star formation histories of the different sub-populations of galaxies. For example, the results obtained from MAGPHYS indicated that the BADGRS were both younger and had experienced a significant burst of star formation more recently than the non-BADGRS. In this section we aim to verify these findings using spectroscopic data of our sources. This will enable us to determine whether multiwavelength SED modelling from MAGPHYS presents a reliable method of obtaining general star formation properties for populations of galaxies.

3.4.1 OPTICAL SPECTRA AS A TOOL TO LEARN ABOUT STAR FORMATION

There are many physical properties which can be determined from the optical spectrum of a galaxy. For example we can learn about the stellar mass and star formation activity of the galaxy (eg Hopkins et al. 2003; Shivaei et al. 2015). We are able to derive these values because the optical spectrum of a galaxy is produced by the light from all the individual stars within a galaxy, and physical events, such as a recent starburst, will leave an imprint on the resultant spectrum.

There are specific spectral features which can be used as tracers or indicators of the general star formation properties that a galaxy has experienced. For example, Kauffmann et al. (2003) take a large sample of $\approx 120,000$ galaxies from SDSS and use the relative strengths of specific features in the spectra to distinguish recent bursts of star formation from older quiescent star formation activity. They use both the 4000-Angstrom break and H_δ line absorption (which is part of the Balmer series) tracers of the current star formation activity of these galaxies. The 4000-Angstrom break is caused by a collection of absorption lines from the metals in the atmospheres of stars, which absorb high energy radiation. The feature is enhanced when there is a reduction in the number of high mass stars in a galaxy, since these stars produce high levels of radiation in this region of the spectrum. The Balmer series of hydrogen emission lines will be stronger in galaxies which are experiencing enhanced levels of star formation, since high energy photons are required to excite these lines.

When analysing the spectral features of the galaxies, it is necessary to consider whether all the emission and absorption lines are produced by the stellar population, or by a secondary source such as Active Galactic Nuclei (AGN). AGN, which are thought to be powered by the accretion of matter onto a black hole in the centre of a galaxy, result in excess emission across many regions of the electromagnetic spectrum. In optical spectra this is often seen as the presence of both broad and narrow emission lines, although there is some variation between different classes of AGN objects (Cohen, 1983). If the presence of an AGN is not accounted for, and it is assumed that all the emission in the optical spectra has been produced by stars, then the measured star formation activity of the galaxy may be unreliable. Therefore we remove any spectra dominated by AGN activity from further analysis (see Section 3.4.3).

3.4.2 The Optical Spectra of HIGH and HAPLESS

In this section, we describe the optical spectra which are available in the literature for the HIGH and HAPLESS samples. Fibre optical spectra from the Sloan Digital Sky Survey (SDSS, York et al. 2000; Ahn et al. 2012) are available for the majority of our sources. We supplement these with optical spectra from the Galaxy and Mass Assembly survey (GAMA, Driver et al. 2009; Hopkins et al. 2013), which uses the AAOmega spectrograph (Saunders et al., 2004; Sharp et al., 2006). Both sets of spectra cover a similar wavelength range ($3800-9200$ Å and $3750-8850$ Å for SDSS and GAMA respectively), and have comparable resolution ($R \sim 1500-2500$ and $R \sim 1000-1600$ again for SDSS and GAMA respectively). The individual spectra are shown next to the SED and median SFH from MAGPHYS for all our sources in Figure 2.14. No spectrum was available for HIGH 16 so this galaxy is also not included in any of the following analysis.

The available spectra only cover the central region of the galaxies, however the BADGRS show only a weak bulge contribution (Clark et al., 2015). The galaxies in our sample also display high levels of flocculence. Due to these facts, the central region of the galaxy is more likely to be representative of the galaxy as a whole, than it would be for a galaxy which exhibited strong radial metallicity gradients.

For many galaxies in our sample only one spectrum was available, however 14 galaxies in the sample had two or more associated spectra listed in GAMA. For galaxies where multiple spectra were available, we chose to use only the most central spectrum. We did this to ensure that we are comparing the same region in each galaxy across the entire HIGH and HAPLESS sample. Finally it is worth noting that by having only the one fibre spectrum for each galaxy we could underestimate the emission features of a galaxy, if the region covered by the fibre happens not to contain any HII regions.

Figure 3.9 shows for each galaxy in the HAPLESS sample, the region covered by the optical fibres alongside the GALEX FUV, SDSS *gri* three-colour, VIKING K_s-band and *Herschel* 250 μm galaxy cutouts from Clark et al. (2015). The location of the fibre on the galaxy is shown by the crosshairs on top of the SDSS 5 band colour image (produced by GAMA). Figure 3.10 shows the same images for the 16 HIGH galaxies from De Vis et al. (2016). These show that for all galaxies in the combined HIGH and HAPLESS sample, the region covered by the optical fibre (crosshairs) is at the centre of the galaxy. Therefore comparison of the spectra of the sub-populations of galaxies should indicate any relative difference in their star formation properties, although any absolute values should be treated with caution

since the fibre covers such a small area of the galaxy.

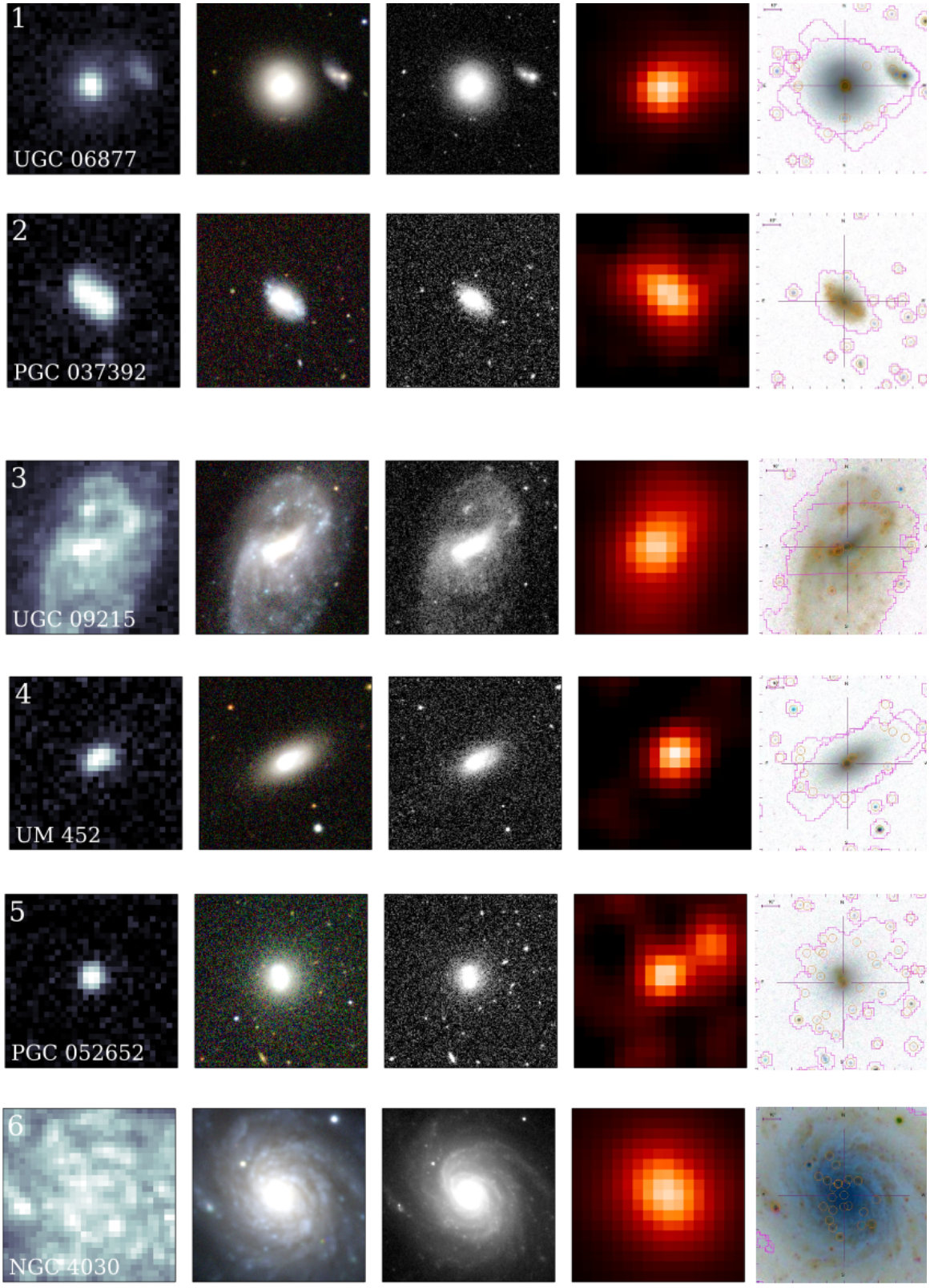

Figure 3.9 The HAPLESS galaxies shown in (from left to right) GALEX FUV, SDSS 3-colour optical, VIKING NIR and *Herschel* FIR (from Clark et al. 2015). The final cutout in each row shows the region covered in the fibre optical spectra superimposed on a 5 colour band SDSS image (obtained from GAMA single object viewer). The pink contours show segmap boundaries- this is where sextractor identified the pixels belong to the target object.

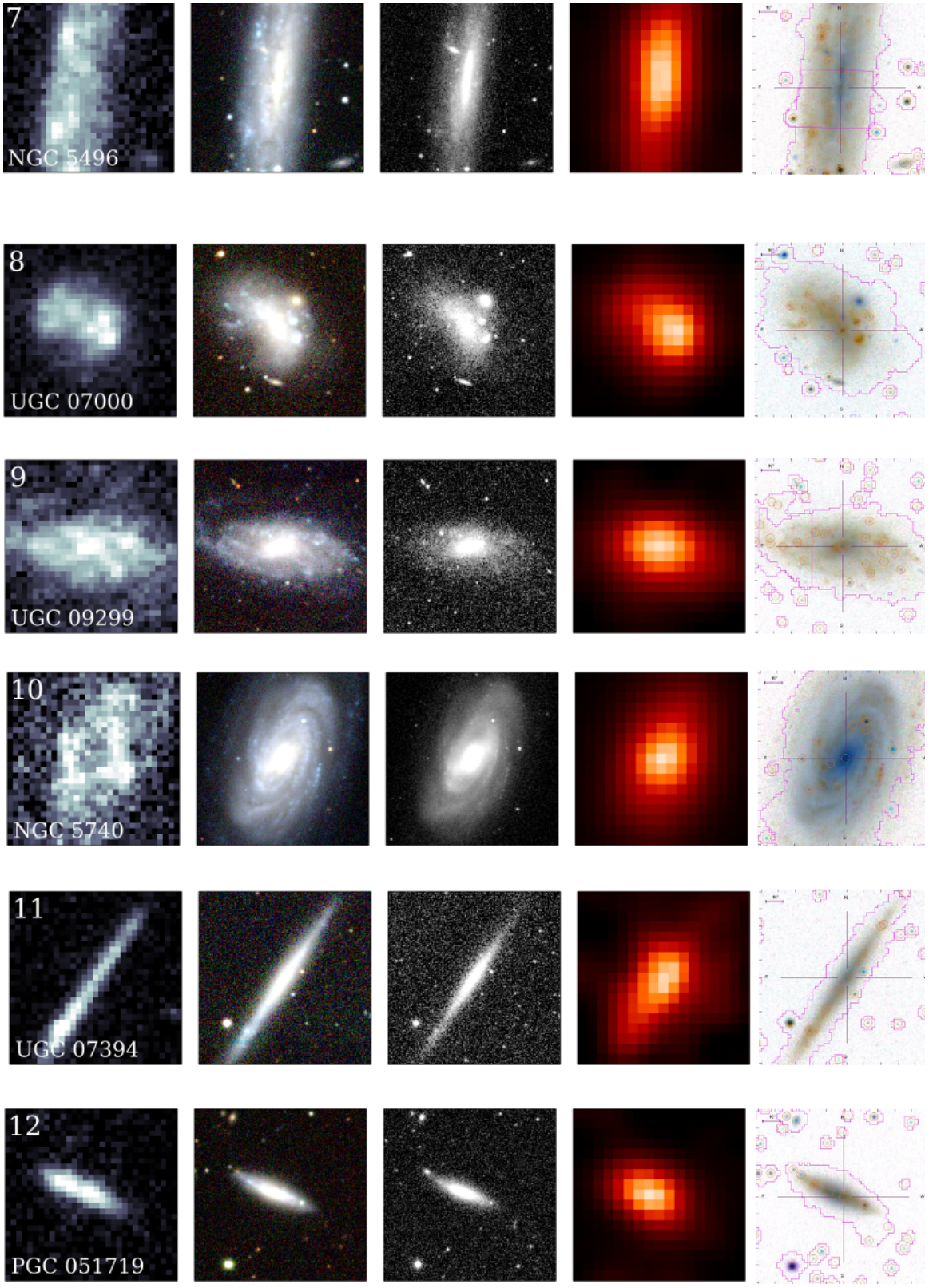

FIGURE 3.9 *Continued Figure*

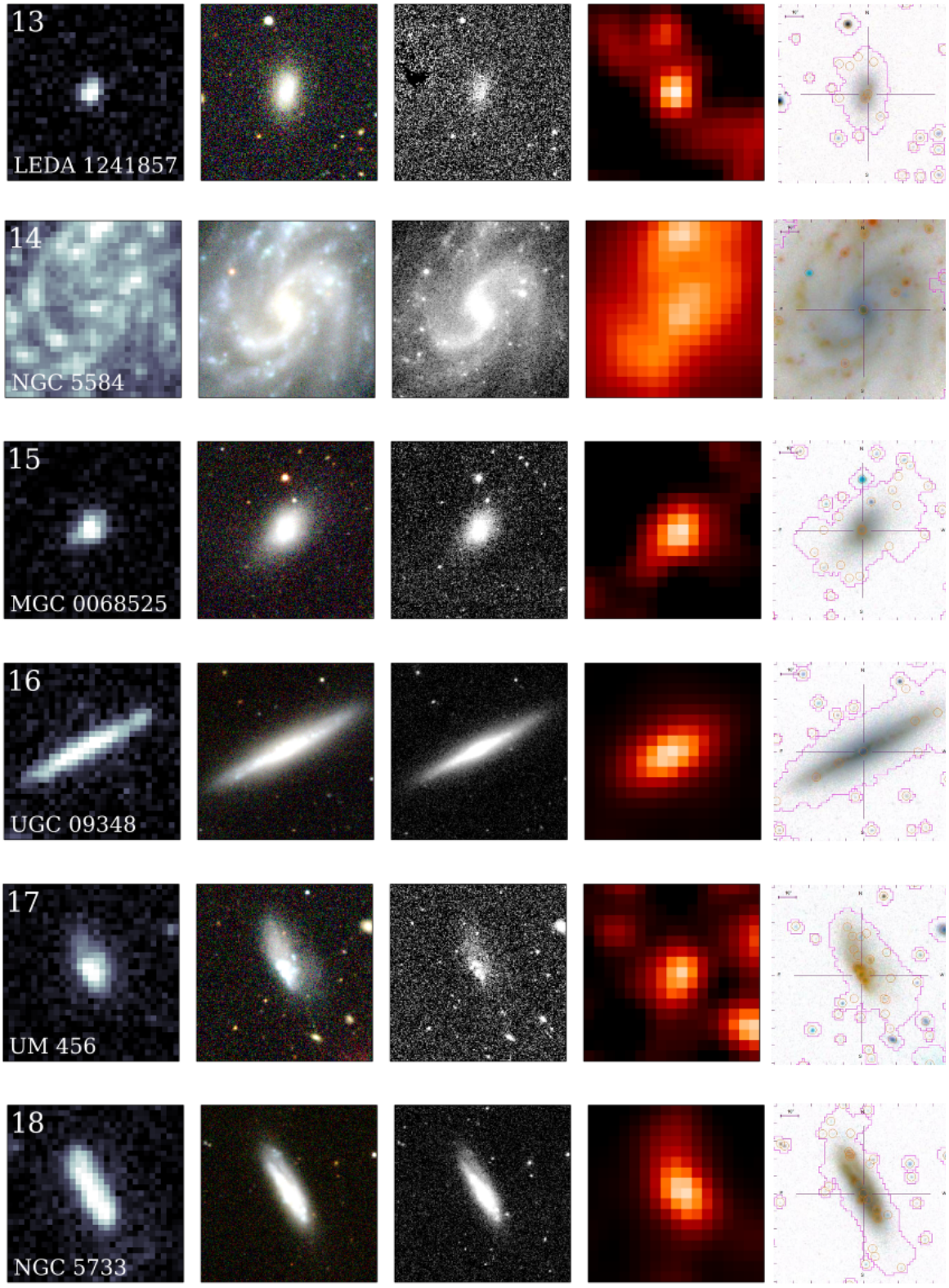

Figure 3.9 *Continued Figure*

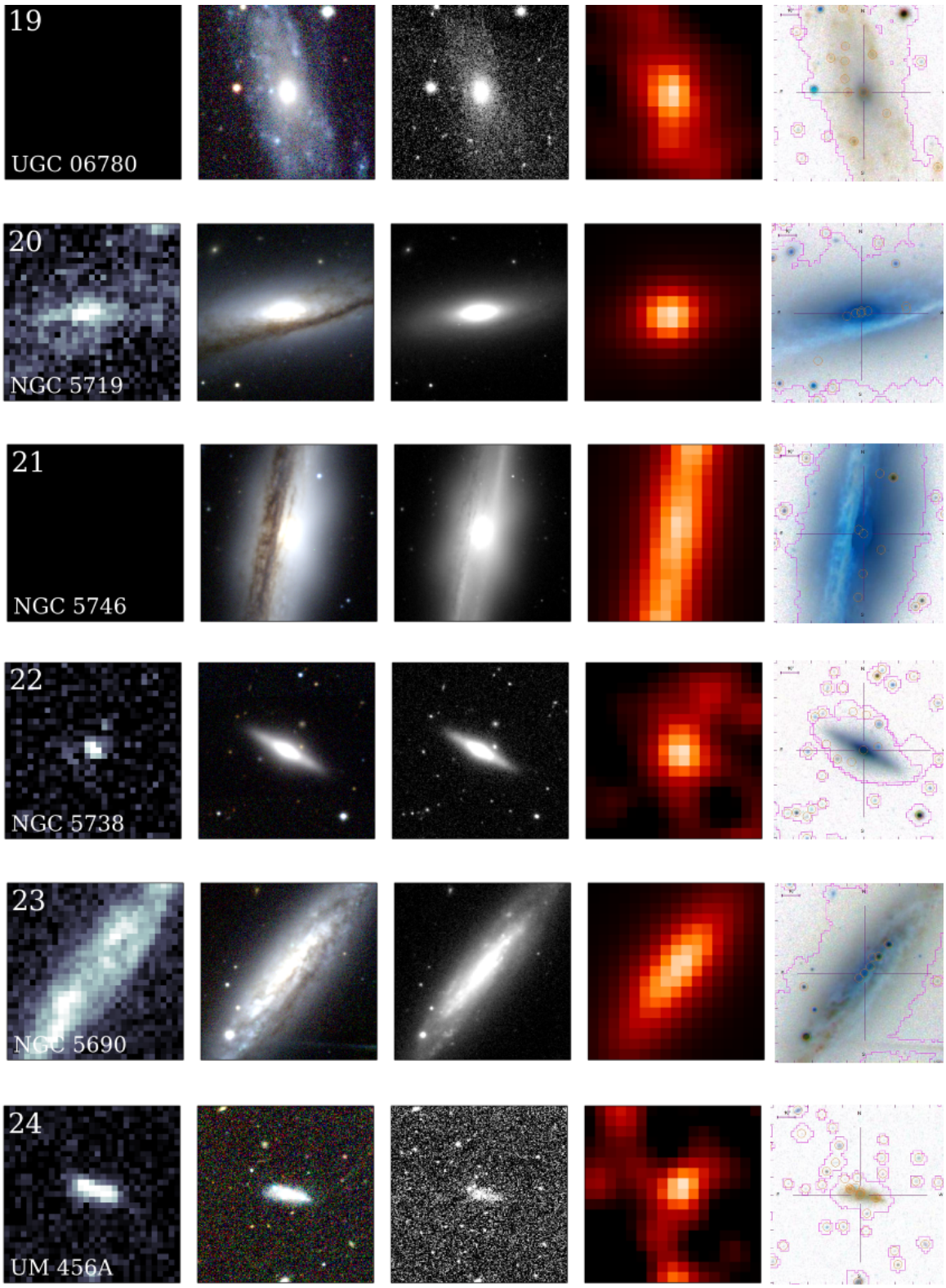

FIGURE 3.9 *Continued Figure*

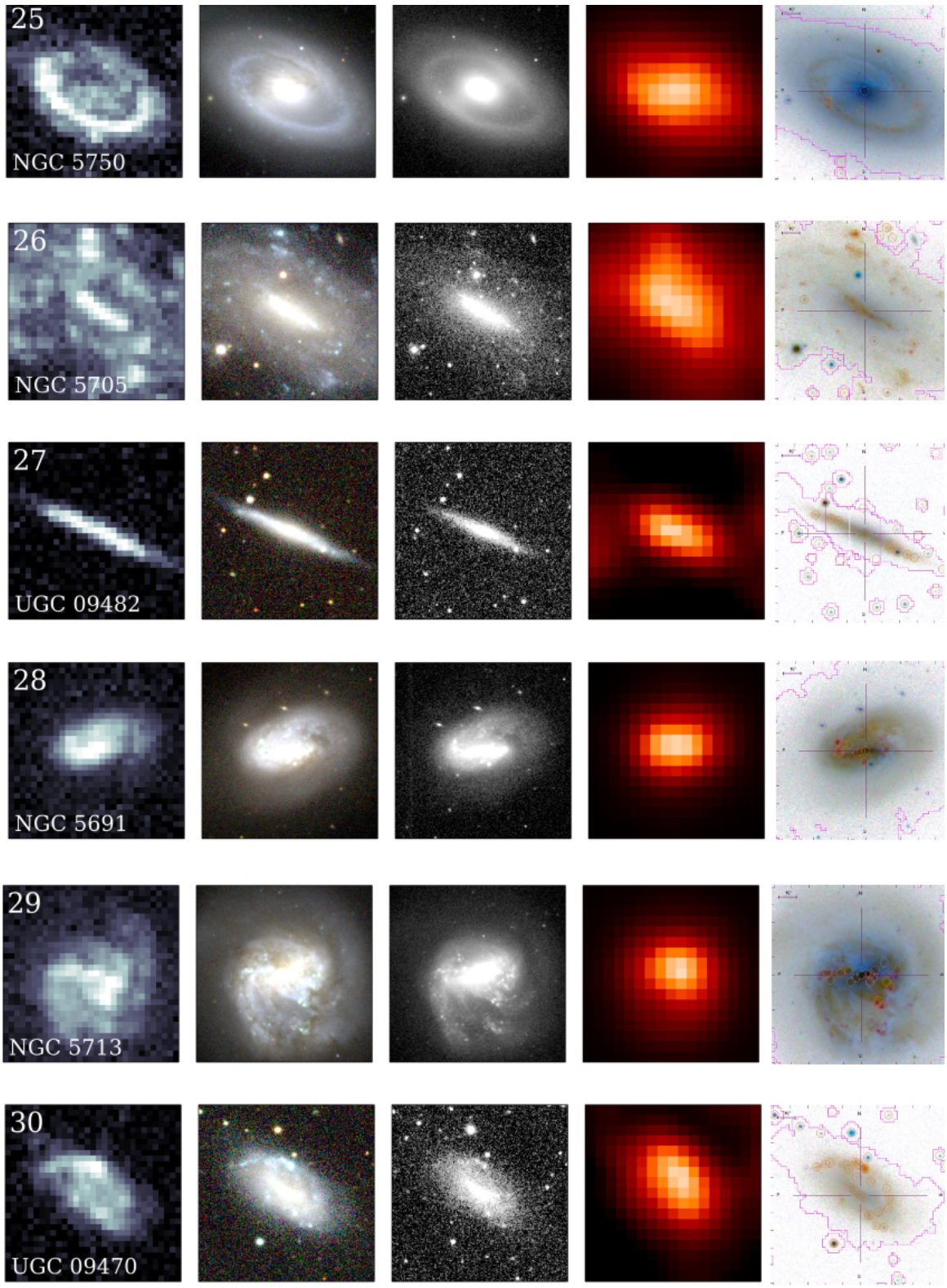

Figure 3.9 *Continued Figure*

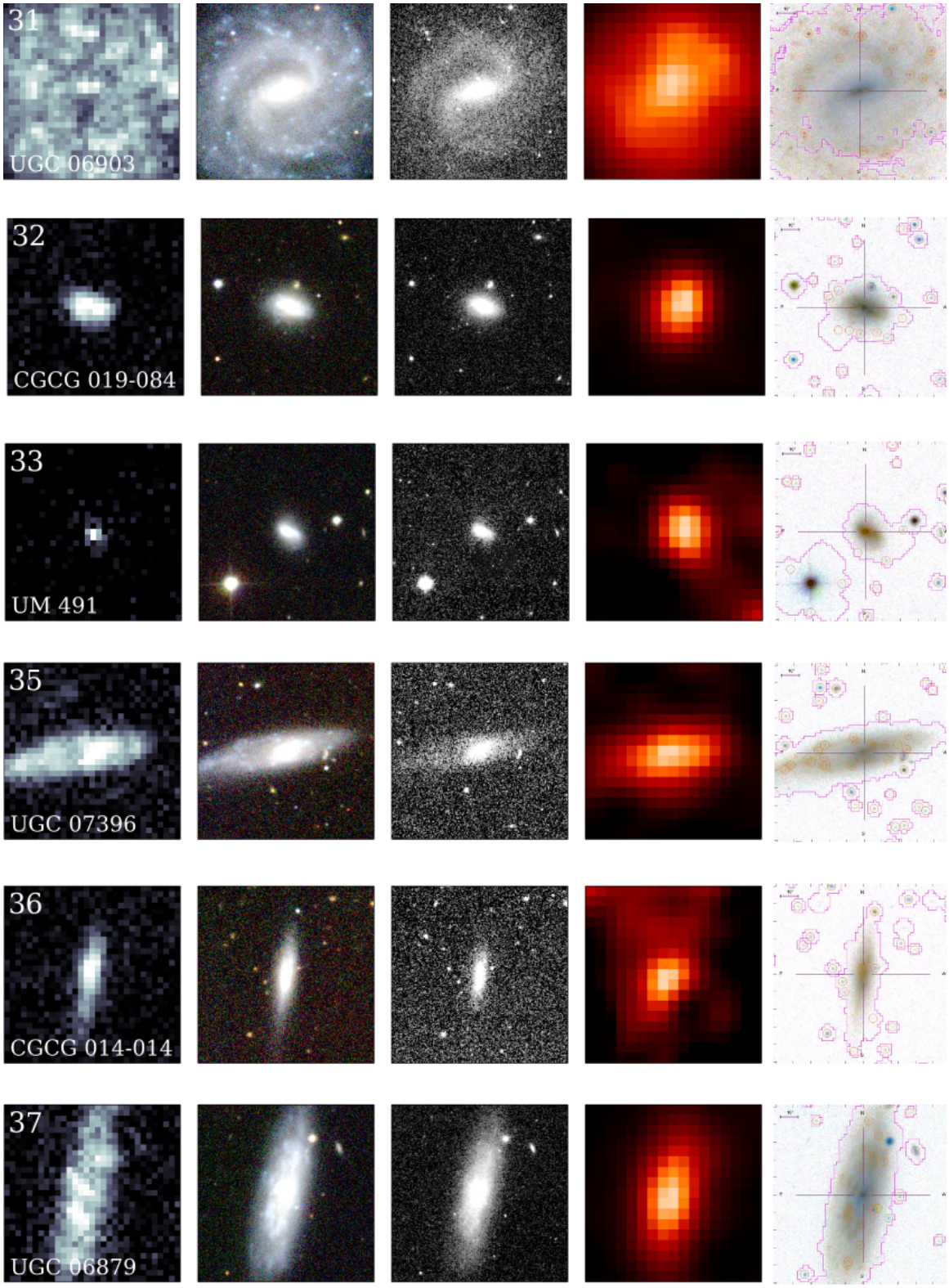

FIGURE 3.9 *Continued Figure*

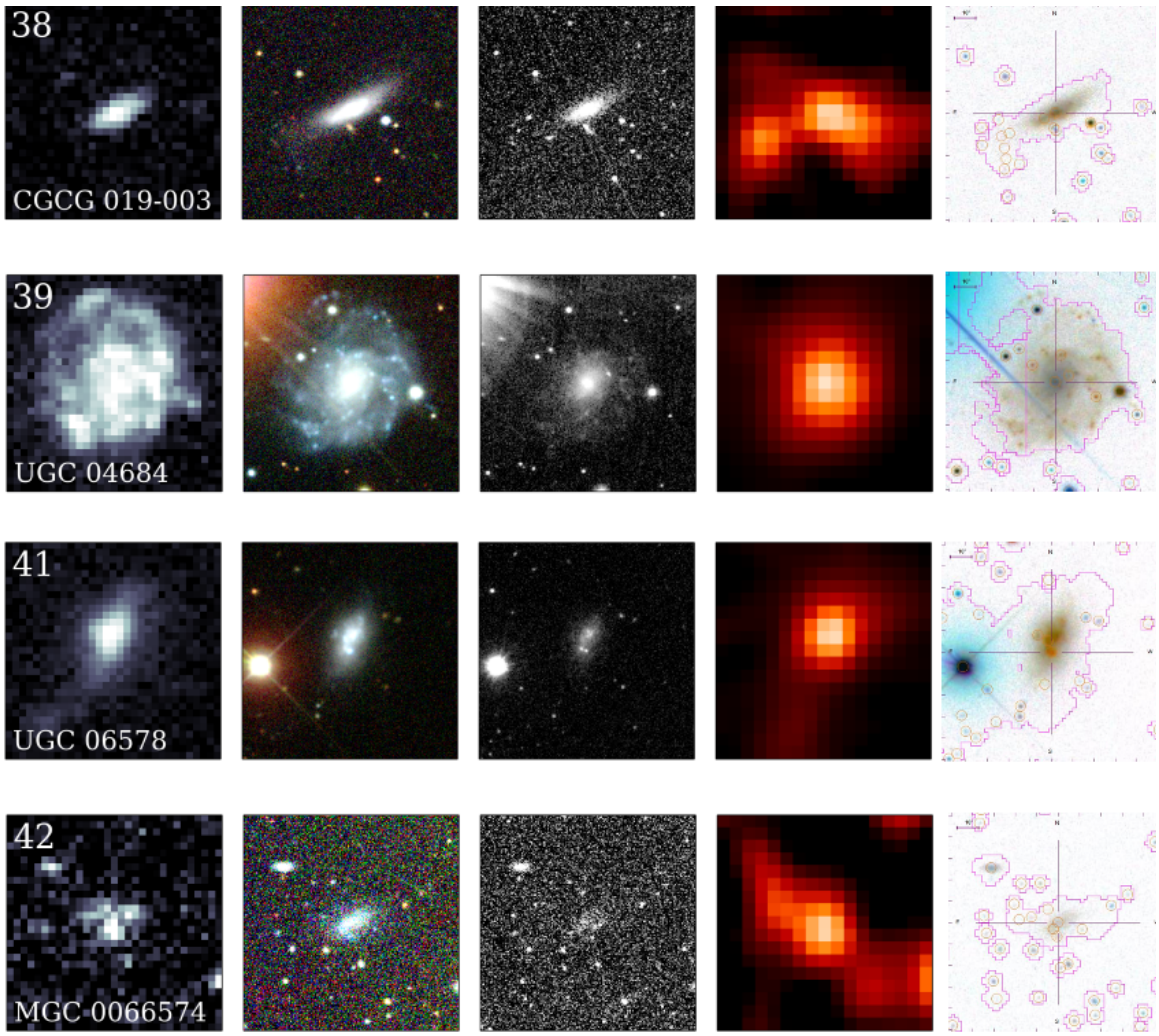

Figure 3.9 *Continued Figure*

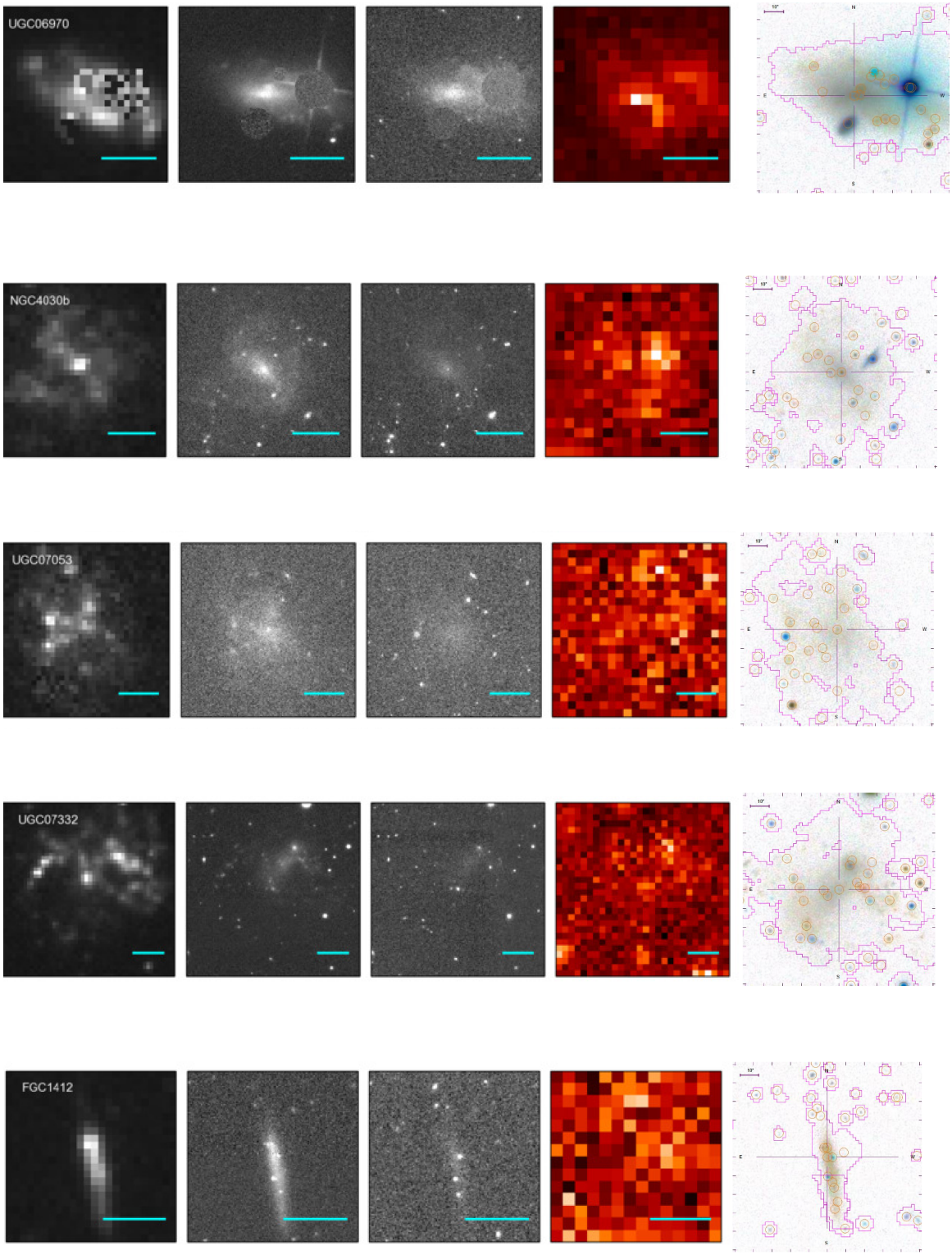

FIGURE 3.10 Same as Figure 3.9, but for the galaxies from the HIGH sample. The GALEX FUV, SDSS 3-colour optical, VIKING NIR and *Herschel* FIR images are from De Vis et al. (2016). No spectrum was available for HIGH 16.

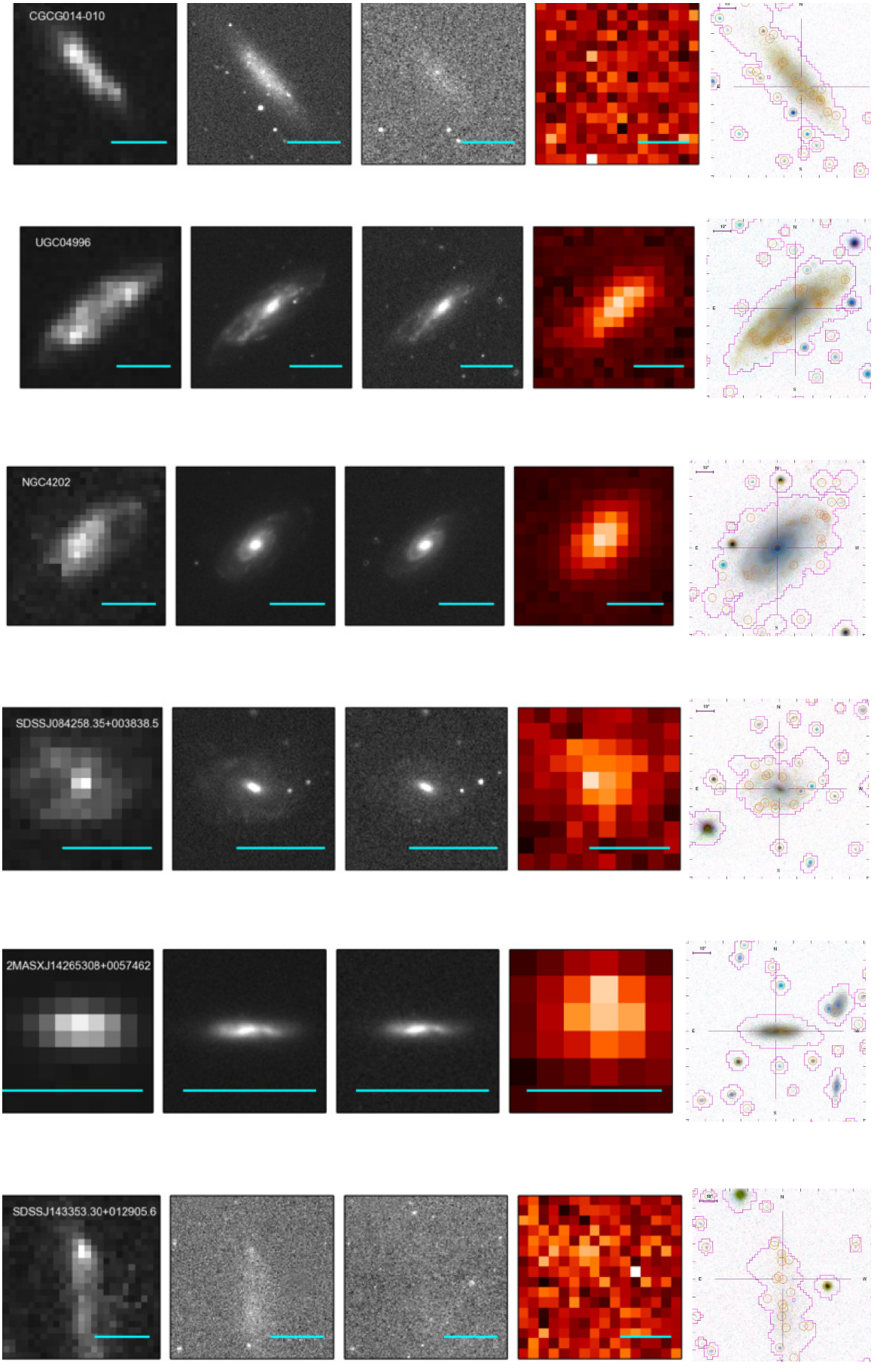

Figure 3.10 *Continued Figure*

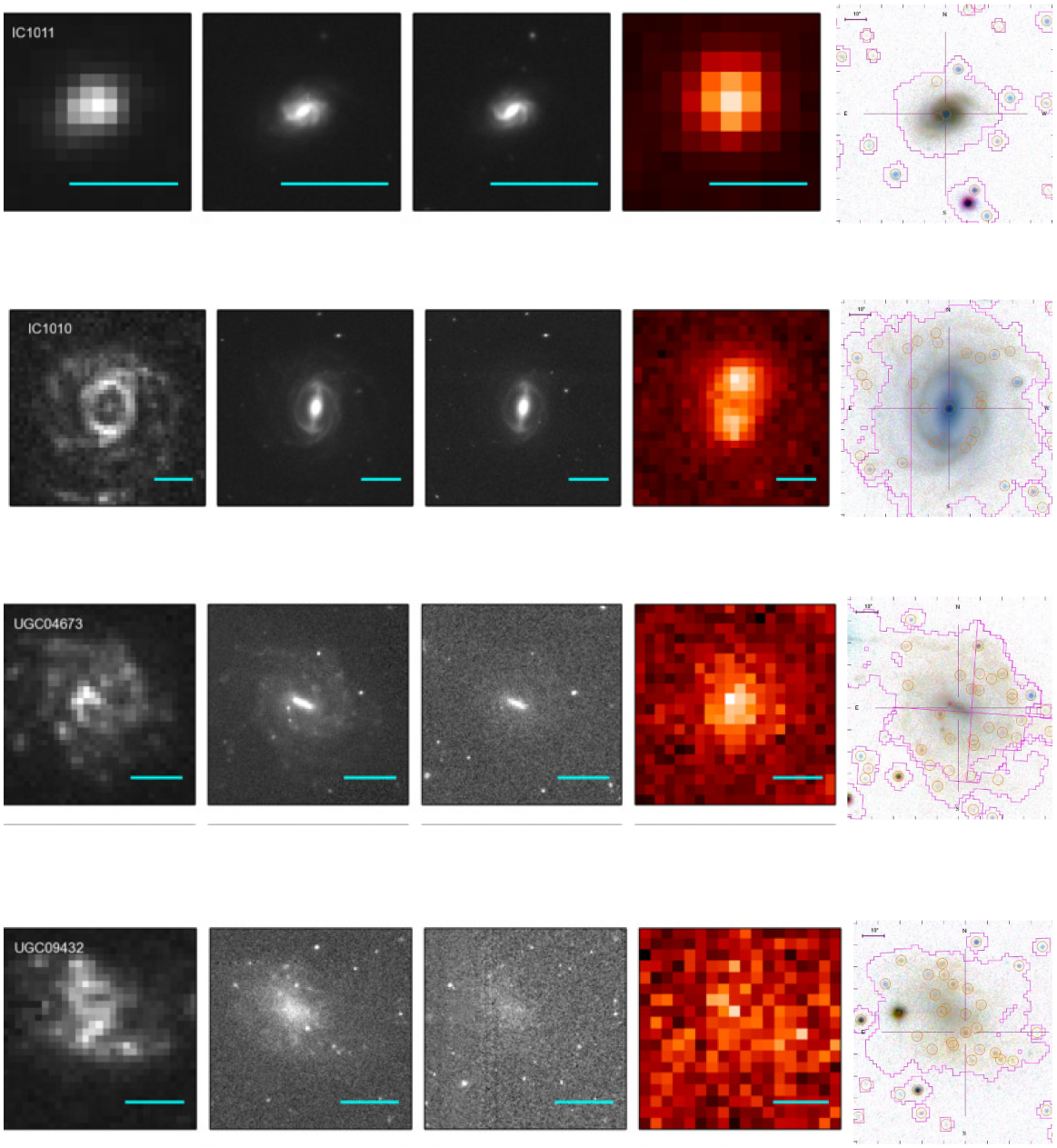

FIGURE 3.10 *Continued Figure*

3.4.3 Removing AGN from our Sample

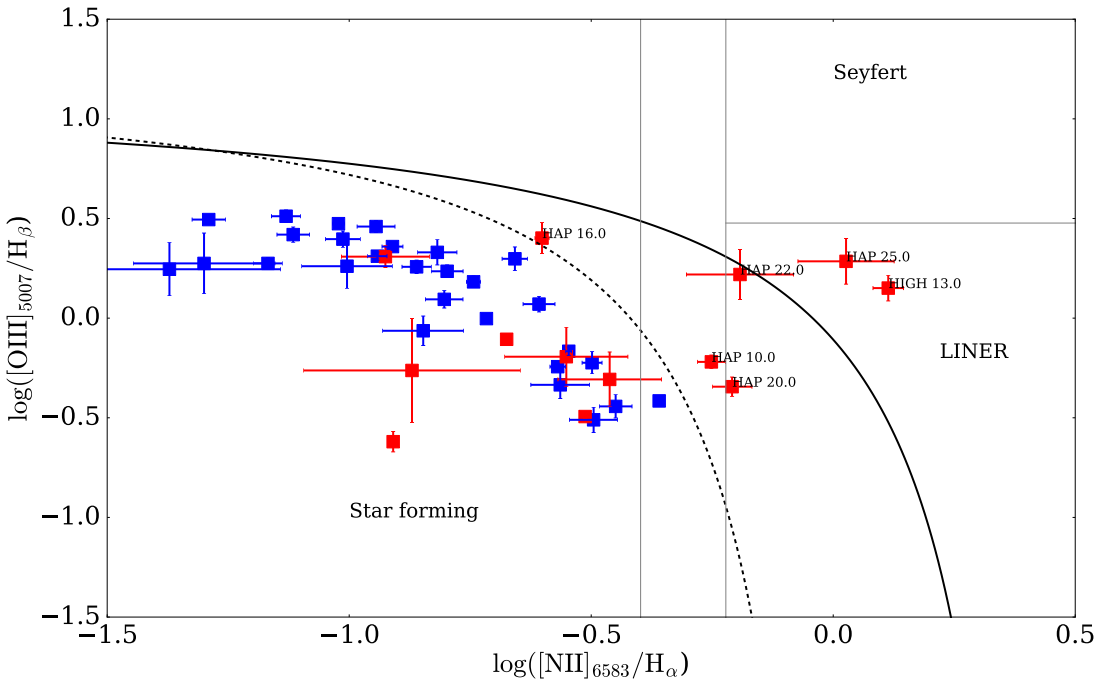

Figure 3.11 Baldwin et al. (1981) (BPT) style diagram to identify spectra dominated by AGN emission. The Decarli et al. (2007) scheme (shown as the straight black lines) marks the classification boundaries between star-forming, LINER, Seyfert and composite galaxies. The curved black dashed line and the curved solid black line show the separation between star forming and AGN dominated galaxies from Kauffmann et al. (2003) and Kewley et al. (2001) respectively. We find that of the 45 HAPLESS and HIGH galaxies with available emission line measurements, 6 are consistent with line emission origination from AGN.

In this section we investigate the line ratios for the HIGH and HAPLESS sample to determine whether star formation or AGN activity is the dominant source of ionization in our sample. Any spectrum which is found to be dominated by AGN emission will subsequently be removed from our analysis.

The Baldwin et al. (1981) (BPT) diagram is an empirical diagnostic tool which we can use to determine whether the emission originates from star formation or AGN. Specific line ratios can be used to identify the source of the emission, since the various emission lines are affected differently by changes to the physical environment (such as temperature, or radiation field strength). BPT style diagrams can still be used today to separate starburst galaxies from AGN dominated galaxies. The method has remained the same, however the classification boundaries have been revised to take account of both advancements in sample size and stellar modelling (Kewley et al.,

2001; Kauffmann et al., 2003; Decarli et al., 2007).

Using line measurements we can compare $\log([O_{III}]/H_\beta)$ against $\log([N_{II}]/H_\alpha)$, where we separate the galaxies into AGN and star-forming using the empirical line from Kauffmann et al. (2003), which is based on observations of 22,623 galaxies from the SDSS. The flux of the emission lines and strength of the absorption features in these galaxies are available in the OSSY database (Oh et al. 2011, for the SDSS spectra) and the SpecLineSFR catalogue (Hopkins et al. 2013, for GAMA sources). These emission line measurements are available for 45 of the 57 galaxies with spectra in our sample (where the SNR was too low for the emission lines in the remaining galaxies). We find that of the 45 galaxies which have available emission line measurements, only six galaxies fall into the parameter space indicating their emission is dominated by AGN. All six of these galaxies are from the non-BADGRS sub-sample, and are removed from further analysis.

3.4.4 CREATING A STACKED OPTICAL SPECTRUM

Figures 3.12 and 3.13 shows the spectrum for every galaxy in our sample (where each spectrum has been normalised to a maximum flux of 1) with prominent emission and absorption lines indicated. While we can not see the variation of the continuum emission on this scale, we can see that the BADGRS (3.12) typically display stronger emission lines than the non-BADGRS (3.13). Specifically, the H_β and O_{III} emission lines appear enhanced in the BADGRS, while some absorption lines including Na are stronger for the non-BADGRS. The implication of these spectral features on the star formation properties of the two sub-samples is discussed in more detail below.

To further investigate whether there are significant differences between the optical spectra of different galaxy sub-samples (BADGRS/non-BADGRS and dust-rich/dust-poor) introduced in the previous chapter, we choose to create a representative stacked optical spectrum for each of the sub-populations. We follow the method of Rowlands et al. (2012) to create the stacked spectra. Firstly we correct the individual spectra to their rest wavelength, then we re-sample each galaxy to the same wavelength grid. Next, we normalise each galaxy spectrum by the median flux value across the full wavelength range. The median flux value of the ensemble of galaxies is then calculated in each wavelength bin, to create the median spectrum for each sub-population of galaxies. Finally, we smooth the stacked spectrum of each sub-sample by a boxcar function of width 5Å to remove high frequency noise. This process was completed for both the BADGRS and non-BADGRS, and the dust-rich and dust-poor sub-samples.

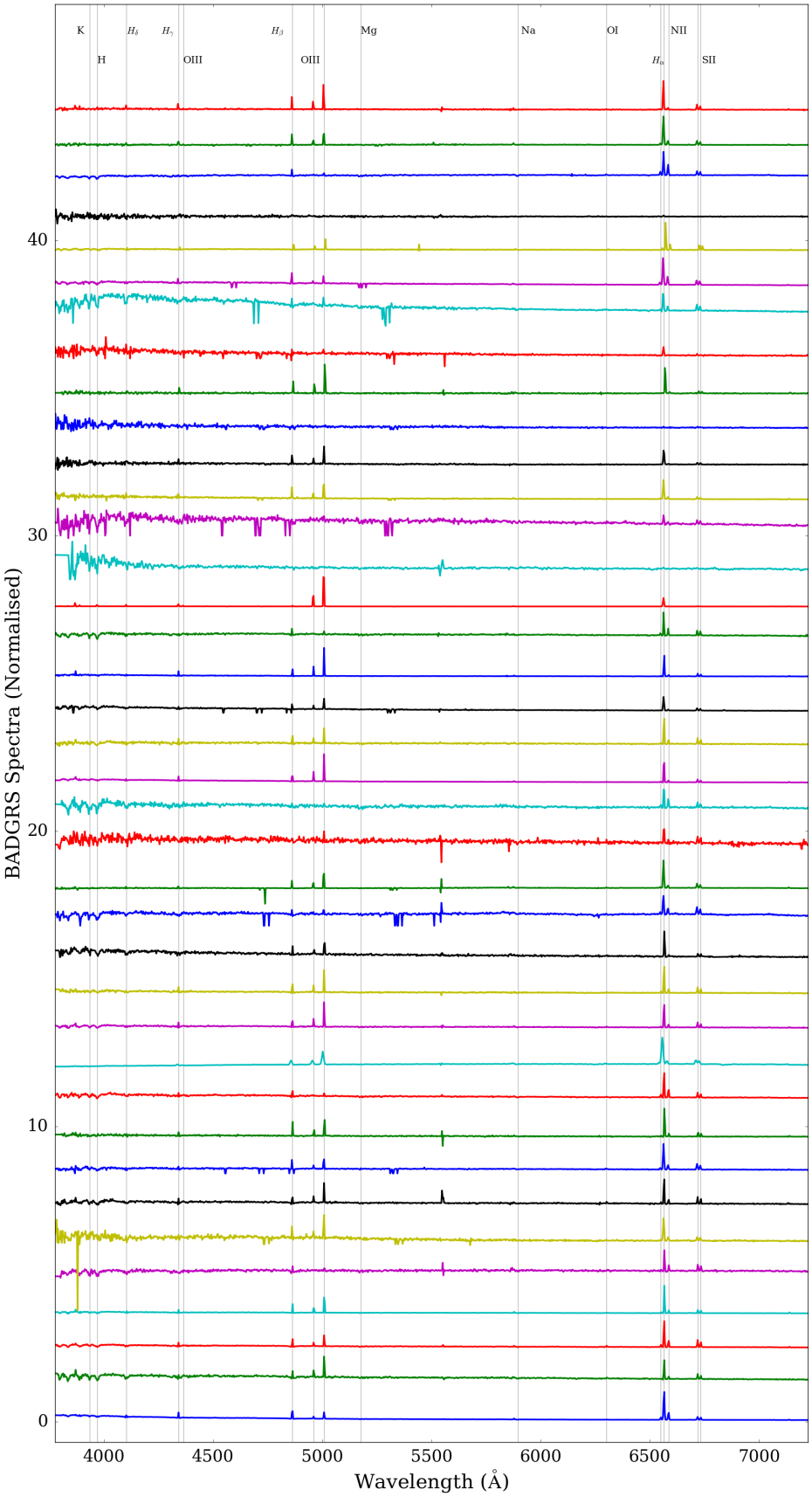

Figure 3.12 Individual spectra of the BADGRS from SDSS and GAMA. Galaxies have been normalised and offset for clarity (the absolute flux is arbitrary).

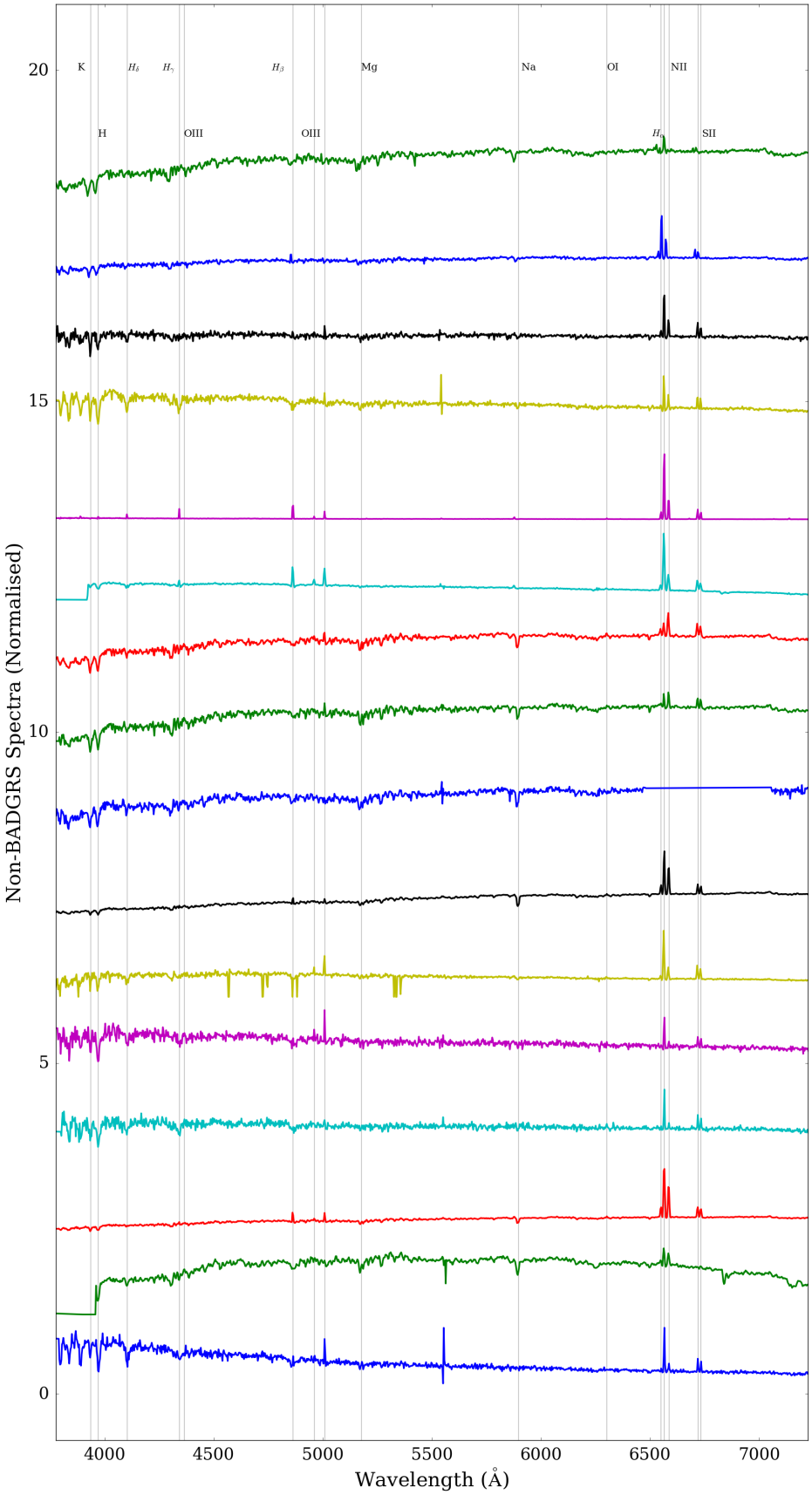

FIGURE 3.13 Individual spectra of the non-BADGRS from SDSS and GAMA. Galaxies have been normalised and offset for clarity (the absolute flux is arbitrary).

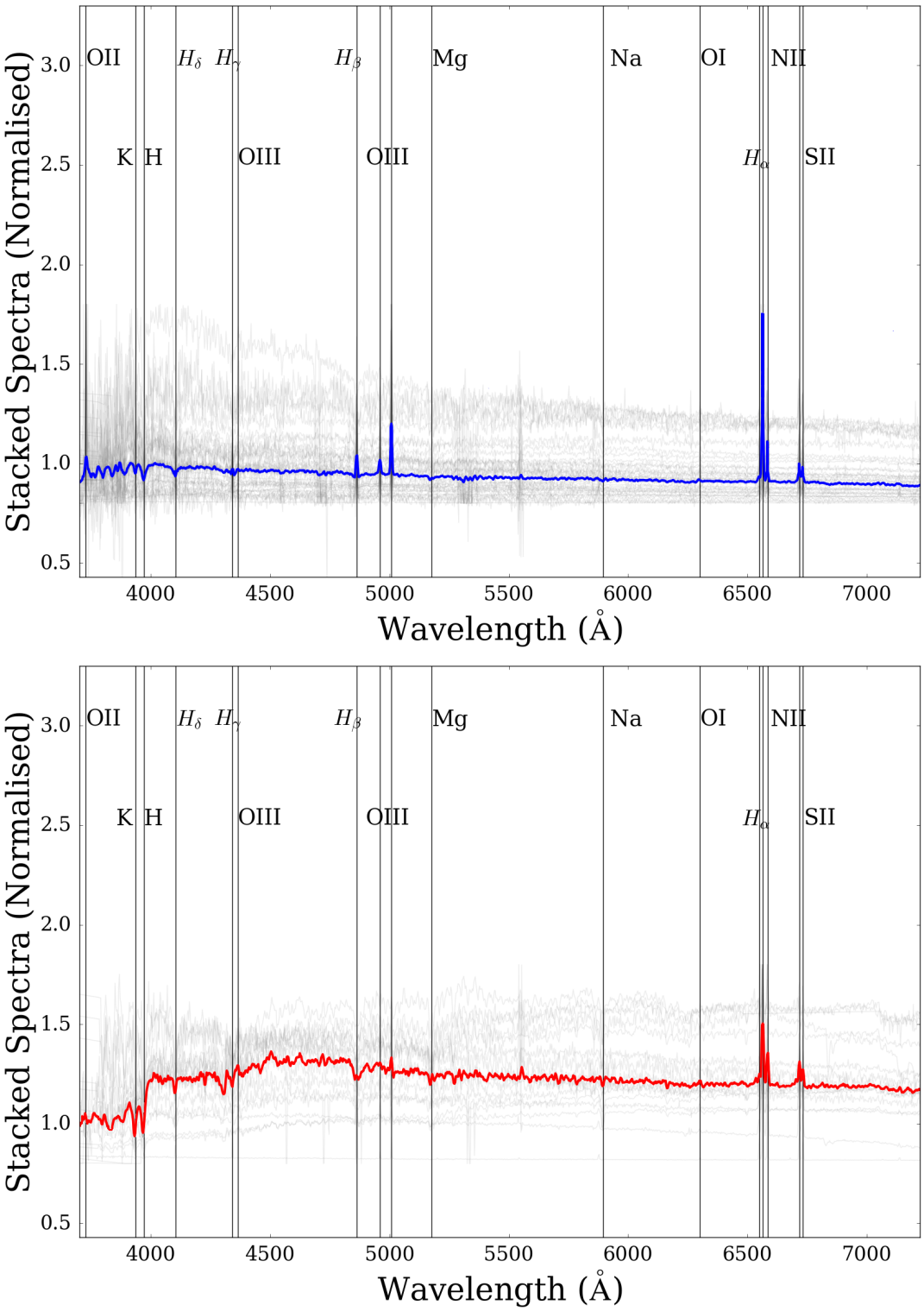

Figure 3.14 The stacked spectra for 40 BADGRS (top) and 11 non-BADGRS (bottom). 6 galaxies have been excluded from the non-BADGRS sample due to AGN activity (see Figure 3.11) and no spectrum was available for HiGH 16. The median of the stack for each sub-population is shown by the solid coloured line (BADGRS in blue, and red for non-BADGRS). The location of emission and absorption features are indicated on the plot by the vertical black lines. The individual galaxy spectra (normalised by their median flux) are shown in grey.

Figure 3.14 shows the resultant stacked spectra for the BADGRS and non-BADGRS (defined as BADGRS have $FUV - Ks < 3.5$). It is clear that there are several key differences between the stacked spectra for the two sub-samples of galaxies. Firstly, we can see that the BADGRS continuum emission is much bluer than that of the non-BADGRS (as expected since these sources are bluer by definition), indicating that the BADGRS contain more young stars than the non-BADGRS. The BADGRS also show enhanced emission lines such as H_α, the OIII emission lines at 5000 Å and H_β. These emission lines indicate that the BADGRS are currently undergoing active star formation, or alternatively they could contain significant AGN activity (see Section 3.4.3). In contrast, the stacked spectrum of the non-BADGRS is lacking many of these prominent emission lines; they have a weaker H_α and OIII is absent. In addition we find that the non-BADGRS display some stronger absorption features, such as Na and Mg, which are indicators of an older, metal-rich galaxy (eg Whitaker et al. 2013). Finally, a strong 4000 Å break is seen in the non-BADGRS stacked spectrum, which could also indicate that these galaxies harbour an older stellar population and have less recently experienced significant star formation. The stacked spectral features are therefore all in agreement with the results derived from MAGPHYS, specifically those indicating that the BADGRS have undergone more recent star formation than the non-BADGRS.

To verify that the stacked spectra are not being dominated by a small number of galaxies with prominent emission or absorption features, we re-calculate the stacked spectrum for both the BADGRS and non-BADGRS using a randomly selected sample containing 60% of the galaxies. By repeating this process we can ascertain if the stack is being dominated by a small sample of galaxies. We find that the spectral features described above are robust to the re-sampling, suggesting the intrinsic differences between the BADGRS and non-BADGRS are real.

Figure 3.15 shows a comparison between the stacked optical spectrum for the dust-rich and dust-poor samples of galaxies. The dust-sample is shown in blue, while the dust-poor sample is shown in red. Again, there are some prominent differences between the stacked spectra of the two sub-samples. We find that the dust-rich galaxies have enhanced star formation features when compared to the dust-poor galaxies, including enhanced OIII and H_β emission lines. The 4000 Å break appears slightly weaker in the stacked spectrum of the dust-poor sub-sample than it appears in the stacked spectrum of the non-BADGRS. The stacked dust-rich and dust-poor spectra would suggest that the HIGH and HAPLESS galaxies which are experiencing the most active star formation are also the most dusty galaxies in the sample.

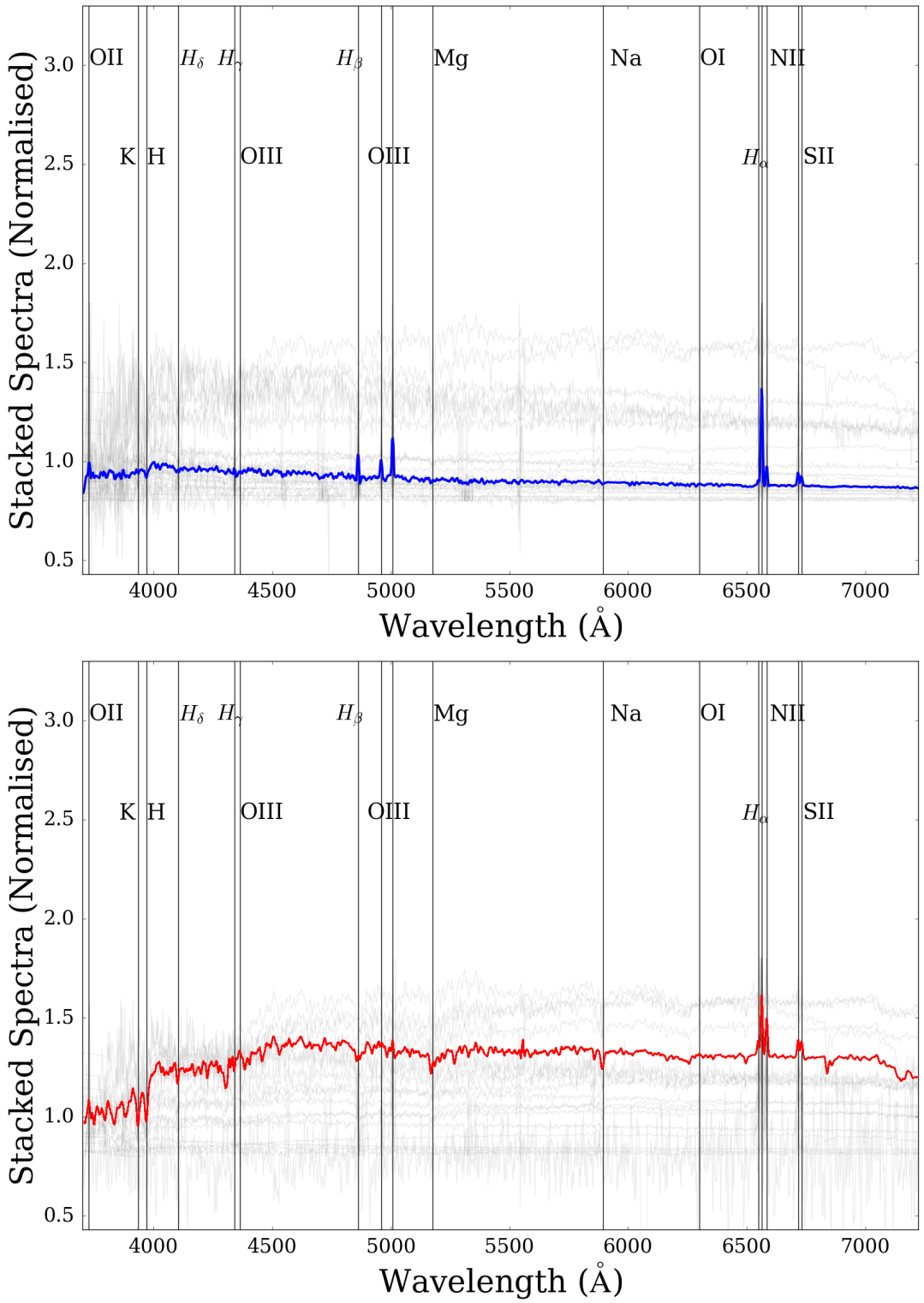

Figure 3.15 Stacked optical spectra for HiGH and HAPLESS (similar to Figure 3.14), but where the galaxies have been split into the dust-rich and dust-poor sub-samples. The 16 dust-rich galaxies (shown in blue) exhibit much stronger emission features than the 27 dust-poor (red) sub-sample.

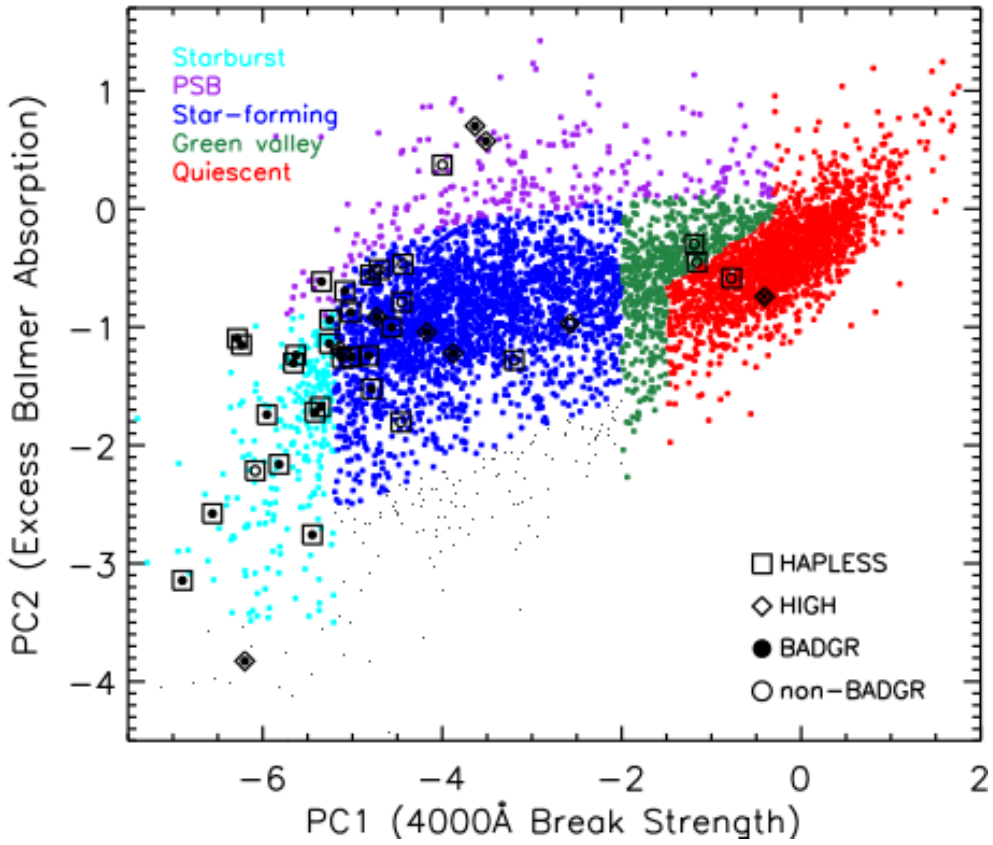

FIGURE 3.16 Principle Component Analysis of the strength of the 4000 Å break against the strength of the Balmer absorption lines in our galaxies. The coloured points indicate the different regions of galaxy classification in this space (ie starburst, post-starburst, quiescent etc). We find that the BADGRS (shown by a filled square or diamond for HAPLESS and HIGH respectively) have on average lower PC1 values compared to the non-BADGRS (shown by an unfilled square or diamond respectively). Approximately 60% of the BADGRS are classified as starburst galaxies, while only one of the non-BADGRS (HAPLESS 5) is identified as such. These findings are in agreement with the results from MAGPHYS.

3.4.5 ADVANCED ANALYSIS OF THE SPECTRA

In Figure 3.16 we show the distribution of two spectral indices (PC1 and PC2) which parametrise star formation features for galaxies in the GAMA survey. We restrict our analysis here to galaxy spectra with a signal to noise ratio (SNR) of > 3.5 at ~ 4200Å (see Rowlands et al. 2016) (20 spectra in our sample fail to meet this cut, and 6 are removed because they are dominated by AGN activity)[1]. Following the method outlined in (Wild et al., 2007), these two spectral indices are based on a Principal Component Analysis (PCA) of the 3175–4150Å region of the spectra.

[1] Note that the Principal Component Analysis plot shown in this thesis (Figure 3.16) was created by Kate Rowlands.

Principle Component Analysis is a statistical technique that can be used to analyse a complex set of data. Correlations and variance within a data set are reduced to a small number of parameters. These parameters (or principle components) can then be used to identify key features within the data and are placed in order of the amount of variance within the data that they can account for. The principle components are not single parameters, but rather a collection of spectral features. These describe the strength of the 4000Å break and anti-correlated Balmer absorption (PC1), and excess Balmer absorption over that expected for the given 4000Å break strength (PC2). Nebular emission lines and regions of bad sky-line subtraction are masked before performing the PCA. Galaxies which show no evidence of recent or current star formation form the 'red-sequence' which lies on the right of Figure 3.16, with strong 4000Å break strength from the old stars. Galaxies that are forming stars have younger mean stellar ages and therefore weaker 4000Å break strengths and form the 'blue-sequence'. A small number of galaxies are undergoing a 'starburst' i.e. there has been a sharp increase in the galaxy's star-formation rate (SFR) over a short timescale ($\sim 10^7$ years). These galaxies are identified by their unusually weak Balmer absorption lines, strong UV–blue continua, and weak 4000Å breaks i.e. spectra dominated by light from O/B stars. These objects lie in the lower left of Figure 3.16. As the starburst ages to a few 10^8 years, the Balmer absorption lines increase in strength as the galaxy passes into the post-starburst phase (Dressler & Gunn, 1983; Couch & Sharples, 1987). A post-starburst galaxy is defined as a galaxy whose spectrum exhibits the spectral features of a K-type star, while also showing the strong Balmer absorption features of a typical A-type star Dressler et al. (1999). These features would only occur in a galaxy that had been rapidly forming stars in the last 1.5 Gyr, and whose star formation rate had recently significantly declined. These objects lie to the top of Figure 3.16.

We use Figure 3.16 to investigate the recent SFH of the HAPLESS galaxies (see also Table 3.1). The majority of the BADGRS/non-BADGRS lie in the starburst and star-forming regions of Figure 3.16. On average the the BADGRS sample has a higher fraction of galaxies with low PC1 values compared to the non-BADGRS, and so there are more BADGRS in the starburst region. The evidence from the PCA that the BADGRS have younger stellar populations (ie they are located in the lower left-hand-side of Figure 3.16 compared to the non-BADGRS) agrees well with the stacked spectra which show bluer stellar continuum than the non-BADGRS.

When splitting into the dust-rich and dust-poor sub-samples, we find that many of the dust-rich galaxies also occupy the more actively star forming regions of the plot. Of the 10 dust-rich galaxies classified using PCA, all are classified as

star-forming or starburst galaxies. All the quiescent, green valley and post-starburst galaxies in our sample are found in the dust-poor sample.

3.5 CONCLUSION

In this chapter we have investigated the differences in the star formation properties of sub-samples of galaxies within the combined HIGH and HAPLESS sample. Initially we split the sample by colour into BADGRS and non-BADGRS (where BADGRS have FUV-Ks < 3.5, Clark et al. 2015), and used the individual best-fit values obtained from MAGPHYS in Chapter 2 to create average SEDs, SFHs and PDFs for each sub-sample. The BADGRS are younger, with a 'light weighted mean age' of (1.89 ± 0.14) Gyr compared to the non-BADGRS (5.32 ± 0.21) Gyr. Additionally, the BADGRS have experienced a burst of star formation more recently (0.91 ± 0.15) Gyr than the non-BADGRS (1.93 ± 0.27) Gyr. Following this, we split the sample into dust-rich and dust-poor sub-samples, where the dust-rich galaxies are defined as having $\log(M_{\rm d}/M_{\rm HI}) > -3.6$ and $\log(M_{\rm d}/M_{\rm s}) > -2.6$. The average SEDs, SFHs and PDFs for these sub-samples show that while there is no evidence for the dust-rich and dust-poor galaxies having different median ages, the dust-rich galaxies have experienced a burst of star formation more recently (0.62 ± 0.16) Gyr than the dust poor galaxies (1.37 ± 0.22) Gyr.

We then used the optical spectra available in the literature, and via GAMA, to investigate the star-forming properties of the HIGH and HAPLESS galaxies. We obtained optical fibre spectra for each galaxy in the HIGH and HAPLESS sample from SDSS and GAMA, with the exception of HIGH 16, for which no spectrum was available. Then we used a BPT style diagram to determine whether the excitation mechanism causing the emission features in the spectra was consistent with star formation or AGN activity. Any spectrum dominated by AGN emission was removed from the analysis. Following the method of Rowlands et al. (2012), we created a stacked spectrum for each of the galaxy sub-samples. Both the BADGRS and dust-rich sub-samples exhibit stronger emission features compared to the non-BADGRS and dust-poor sub-sample, consistent with recent bursts of star formation. A PCA analysis was carried out to explore this further. This showed that most of the BADGRS are indeed starburst or blue star forming galaxies. Of the dust-poor and dust-rich sub-samples, we find that all of the galaxies identified as green valley, quiescent or post-starburst are located in the dust-poor sub-sample. These findings seem to agree with the results from MAGPHYS and would indicate that there are indeed intrinsic differences in the level of star formation (and the time since recent bursts of star

ID	BADGR	Dust-Rich	PCA-Type
1	✓	✗	starburst
2	✓	✓	starburst
3	✓	✓	starburst
4	✓	✗	starburst
5	✗	✗	starburst
6	✗	✗	-
7	✓	✓	starburst
8	✓	✗	-
9	✓	✓	star-forming
10	*	*	*
11	✗	✓	star-forming
12	✓	-	post-starburst
13	*	*	*
14	✓	✓	star-forming
15	✗	-	star-forming
16	*	*	*
17	✓	✗	-
18	✓	-	starburst
19	✓	✓	starburst
20	*	*	*
21	✗	✗	-
22	*	*	*
23	✗	✗	green valley
24	✓	✗	starburst
25	*	*	*
26	✓	✓	-
27	✓	✓	starburst
28	✗	✗	-
29	✗	✗	-
30	✓	✗	star-forming
31	✓	✗	star-forming
32	✗	-	star-forming
33	✓	✓	starburst
34	✓	✓	-
35	✓	✓	star-forming
36	✓	-	starburst
37	✗	-	star-forming
38	✓	-	starburst
39	✓	✗	star-forming
40	✓	✗	-
41	✓	✓	-
42	✓	-	-
43	✓	✗	post-starburst
44	✓	✗	-
45	✓	✗	post-starburst
46	✓	✗	-
47	✓	✗	-
48	✓	✗	-
49	✓	✓	-
50	✗	✗	star-forming
51	✓	✗	star-forming
52	✓	✓	-
53	✓	✗	-
54	✓	✗	star-forming
55	✗	✗	-
56	✓	✓	-
57	✓	✗	quiescent
58	✓	✗	-

Table 3.1 The ID and PCA classification of each galaxy in HIGH and HAPLESS. Galaxies that belong to the BADGRS or dust-rich sub-sample are shown by a tick. A '*' marker indicates that the spectrum of that galaxy was dominated by AGN emission. A '-' in the 'Dust-Rich' column indicates that the galaxy has no gas information and could not be identified as either dust-rich or dust-poor. A '-' marker in the 'PCA-type' column indicates that the galaxy could not be classified using the PCA because it had SNR<3.5 in the 4000 Å break region.

formation) between the galaxies in the different sub-samples. This suggests that there may be a direct link between features in the SFH (eg recent bursts of star formation) and the dust content of the galaxy.

Chapter 4
The Chemical Model I: Introduction, Libraries and Tests

4.1 Introduction

Galaxies are complex dynamical systems which are driven by both the conversion of gas into stars, and inflows and outflows of gas from the intergalactic medium. Stars are responsible for the production of the majority of heavy elements in the universe, and are important factories for dust grains. The build up of dust and metals in a galaxy over time is linked to the star formation history. This can be modelled by combining key elements such as stellar yields and initial mass functions, within a mathematical framework for galactic evolution. In this chapter, we introduce the chemical evolution model used in this thesis, starting with an analytical approximation (Tinsley, 1980; Dwek, 1987). We introduce an updated version of the full chemical model and code from Morgan & Edmunds (2003); Rowlands et al. (2014).

We have made several changes to the chemical evolution model since it was used in Rowlands et al. (2014). These changes include updating several of the input libraries, validating and testing the equations and prescriptions used and correcting software issues in their version. These changes are highlighted and explored in the relevant sections of this chapter. The full chemical evolution code, written in Python, is freely available to download from GITHUB [1]. The results from this code have been published in Clark et al. (2015), De Vis et al. (2016) and De Vis, Schofield et al 2016 and will be used to explore nearby galaxies in the final chapters of this thesis.

[1] https://github.com/zemogle/chemevol

4.2 MODELLING DUST, GAS AND STARS USING AN ANALYTIC APPROACH

Modelling the chemical evolution of a galaxy in full requires a complex model, and can be quite computationally expensive. However by making some basic assumptions it is possible to create a model which can be solved analytically. Here we follow the formulation and derivation as outlined in the literature by Tinsley (1980), Edmunds (2001) and Dunne et al. (2011). The analytical model can provide insight into the general evolution of the gas and dust properties of a galaxy over time. Here we outline the key assumptions which we make in order to describe the evolution of a galaxy analytically:

1. The galaxy evolves as a closed box system, such that there are no inflows or outflows, and therefore the total mass of the system is a conserved quantity.

2. The galaxy starts its life as a single massive cloud of gravitationally bound gas, which has a negligible metal content, so is primordial in its chemistry.

3. All stars over a given mass have a zero lifetime, so their metal and dust yields are produced instantaneously following their formation, and low mass stars have a lifetime longer than that of the galaxy, so do not contribute to enrichment. This is know as the Instantaneous Recycling Approximation.

4. The evolution of the galaxy occurs in a single zone, which is well mixed, such that the enrichment of the galaxy metal and dust content is the same everywhere and can be described by a single parameter.

The first assumption (a closed box) allows us to write an equation of the conservation of mass of the galaxy over time:

$$\frac{dM_{\rm tot}}{dt} = 0 \tag{4.1}$$

where $M_{\rm tot}$ is the total mass of all components of the galaxy. Equation 4.1 is a simplification of the physical evolution of a galaxy, since galaxies are rarely thought to evolve in complete isolation. It is an assumption which can be relaxed to allow for the outflow of gas from a galaxy due to feedback of star formation, or the inflow of gas clouds from the intergalactic medium into the stellar disk of the galaxy. Nonetheless, it is a good starting point for the derivation of the analytical model of chemical

evolution. We know that over time the galaxy will form stars, and therefore at any time in the life of the galaxy the total baryonic mass can be described as:

$$M_{\rm bary} = M_{\rm star} + M_{\rm gas} \tag{4.2}$$

where $M_{\rm star}$ is the stellar mass of the galaxy, including both living and stellar remnants, with an initial value of zero (second assumption). $M_{\rm gas}$ is the gas mass of the galaxy. The relative mass of other components, such as metal or dust is negligible in comparison (combined metal and dust mass is of the order $\approx 1\,\%$ of total mass). Since stars are forming from the gas we would expect, in a very broad sense, the gas mass of the galaxy to decrease over time, while the stellar mass of the galaxy increases. The change in gas mass is linked to the amount of stars which the galaxy forms, and the time-scale on which these stars form; these processes are described by the star formation history of the galaxy, ψ. Therefore we can describe the evolution of the gas content of the galaxy with the equation:

$$\frac{dM_{gas}}{dt} = -\psi(t) + E(t) \tag{4.3}$$

$\psi(t)$ is the star formation rate at time t and accounts for the gas which is removed from the interstellar medium due to the formation of stars. $E(t)$ is the ejected mass of gas from dying stars which is returned to the interstellar medium. In full, this term can be written as:

$$E(t) = \int_{m_{\rm t}}^{m_{\rm u}} \left[m - m_{\rm r}(m)\right] \psi(t - \tau_{\rm m})\, \phi(m)\, dm \tag{4.4}$$

$m_{\rm t}$, the lower mass limit of the integral, corresponds to the mass of star whose lifetime is equal to the age of the galaxy, such that they are the lowest mass star which could be dying at any given time. The upper limit is obtained from stellar theory, and is typically assumed to be approximately $100\,{\rm M}_\odot$. $m_{\rm r}(m)$ gives the mass of stellar remnant produced when a star of mass m dies. Hence the first term inside the integral gives the total mass of gas returned to the interstellar medium at the end of the lifetime of a star mass m. $\psi(t - \tau_{\rm m})$ is the star formation rate at the time which the star of mass m formed. Finally, $\phi(m)$ is the stellar initial mass function, and describes the fraction of stars formed with a given mass m. Here we are interested in obtaining an analytic model, and therefore must invoke the third assumption.

Under the Instantaneous Recycling Approximation, it is assumed that stars fall into two categories based on their mass. Low mass stars, which have lifetimes comparable to the lifetime of the host galaxy, can be approximated to an infinite

lifetime (they act as sinks which lock up gas and dust away from the ISM). High mass stars, whose lifetime is insignificant compared to the lifetime of the galaxy, have zero lifetime and return their yield of enriched gas to the ISM as soon as they form. Therefore, $\psi(t - \tau_{\rm m})$ simplifies to $\psi(t)$. Equation 4.4 becomes:

$$E(t) = \psi(t) \int_{m_{\rm t}}^{m_{\rm u}} [m - m_{\rm r}(m)]\, \phi(m)\, dm. \tag{4.5}$$

Instantaneous recycling may appear to be a simplistic approximation, however it has been shown to provide reasonably accurate results, provided the gas fraction (defined as $f_{\rm g} = \frac{M_{\rm g}}{M_{\rm tot}}$) of the galaxy does not fall too low, typically below a gas fraction of 0.10 (Prantzos & Aubert, 1995). In this regime the large amounts of gas, returned from the death of low mass stars, have a significant effect on the final gas fraction of the galaxy. The approximation also breaks down at very early times in the evolution of a galaxy ($< 500\,$Myr), where the lifetime of high mass stars becomes comparable to the age of the galaxy, causing the metallicity to increase too rapidly in the model. For a given Initial Mass Function, which has a fixed ratio of high to low mass stars, and fixed assumptions of the remnant mass, the integral in Equation 4.5 can be computed as a constant numerical value, denoted R. Therefore $E(t)$ becomes:

$$E(t) = \psi(t)\, R \tag{4.6}$$

Substituting $E(t)$ into the Equation 4.3 gives:

$$\frac{dM_{\rm gas}}{dt} = -\psi(t) + \psi(t)\, R = -\psi(t)(1 - R) = \alpha\, \psi(t) \tag{4.7}$$

where $\alpha = (1 - R)$, and is known as the locked up fraction. When investigating the evolution of a galaxy, we are also concerned with the production of metals and dust over time. Any increase of the metal or dust content of the galaxy will be intrinsically linked to the number of stars in the galaxy, and their subsequent evolution. From assumption four, we assume that the metal yield from all stars contributes immediately to the composition of the ISM. Hence we can write an equation that governs the metal content of the galaxy:

$$\frac{d(Z M_{\rm gas})}{dt} = -Z\, \psi(t) + E_z(t) \tag{4.8}$$

here, Z is the mass fraction of metals so $Z M_{\rm gas}$ gives the mass of metals in the galaxy. $E_{\rm z}(t)$ gives the mass of metals which are injected into the ISM in a given time period from the dead stars. With the Instantaneous Recycling Approximation, the metal fraction of the galaxy can be shown to have the analytical solution of:

$$Z = p \ln(1/f) \tag{4.9}$$

where p is the effective yield of heavy elements from star formation, and f is the gas fraction of the galaxy. Since the gas fraction at a given time is a function of the star formation history, the metal fraction of the galaxy will also depend on the star formation history. It would be simple to include pre-enrichment of the initial gas reservoir by including an extra term:

$$Z = Z_{\rm i} + p\, ln(1/f) \tag{4.10}$$

where $Z_{\rm i}$ is the initial metallicity of the gas cloud from which the galaxy formed. Pre-enrichment of the gas may be a necessary part of the solution to explain the metal fraction of the globular clusters of our own galaxy (Bailin & Harris, 2009), in which case observations have shown that $Z_{\rm i} = 0.1 - 0.2\,{\rm Z}_{\odot}$. Finally, the evolution of the dust mass of the galaxy is very similar to the increase of the metal fraction of the galaxy, at least in its most simple form. If we make the assumption that there is no dust grain destruction, and that stars provide the only source of dust in the galaxy, then it is possible to write the dust mass evolution as:

$$y = \chi\, p \ln(1/f) \tag{4.11}$$

here y is the dust mass fraction of the interstellar medium and χ is a parameter to describe the fraction of metals in dust grains ($\approx 0.2 - 0.5$, Morgan & Edmunds 2003; Dunne et al. 2011). This is a simplification, because we know that dust grains can be destroyed by shocks in the ISM, different fractions of dust may be produced in supernovae and Low and Intermediate Mass Stars (LIMS) (which can be parametrised by using χ_1 and χ_2) and also grain growth in the interstellar medium may be an important consideration for the production of dust (Mattsson et al., 2014).

Despite these limitations, the above equations can be used to form an analytic model for describing the chemical evolution of a galaxy over time. Figure 4.1 shows the results using the simple model to model the evolution of a galaxy with a smoothly declining star formation history, where there is a burst of star formation approximately 1-2 Gyr after the formation of the galaxy. The burst of star formation is seen to be responsible for rapidly depleting the gas reservoir of the galaxy. The stellar mass of the galaxy increases rapidly at this time, and then returns to the steady increase. The burst has an interesting effect on the dust mass of the galaxy, with the amount of dust created in the burst depending strongly on the values of χ_1 and χ_2

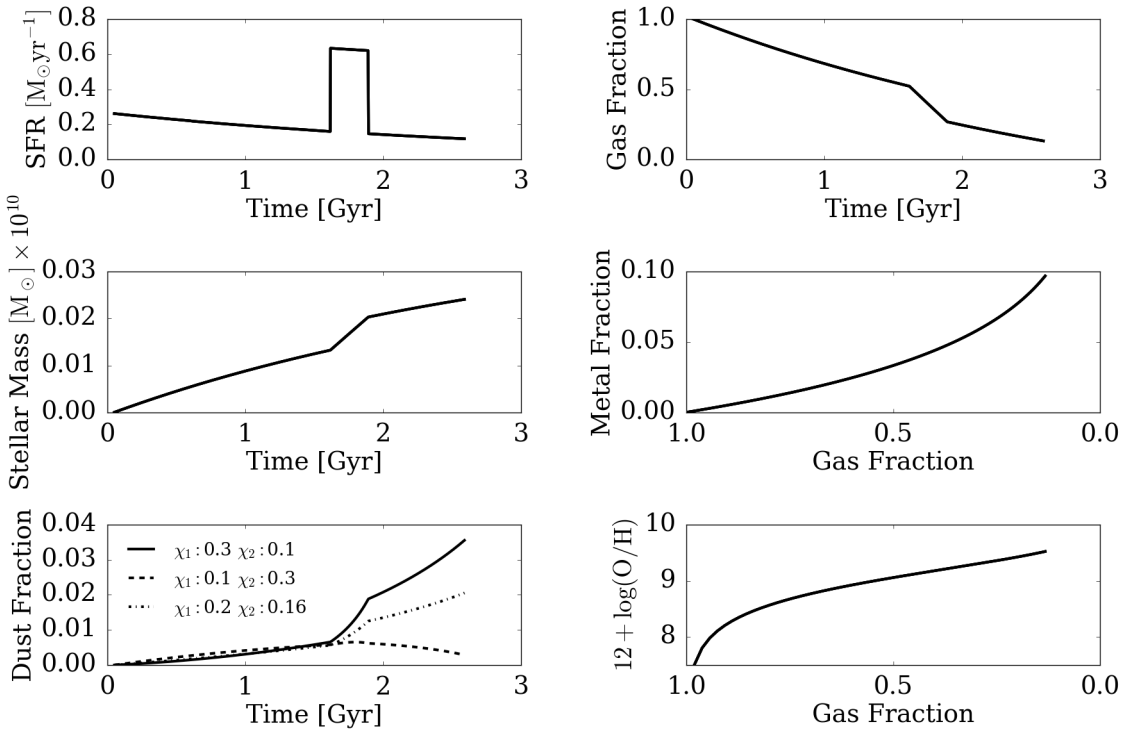

FIGURE 4.1 The analytic solutions for a test galaxy. *Top left:* The SFH which is assumed for the test galaxy. *Top right:* The evolution of the gas fraction over time. *Middle left:* The increase in the stellar mass of the galaxy as it evolves. *Middle right:* The build up of metals in the galaxy. *Bottom left:* The evolution of the dust fraction of the galaxy. *Bottom right:* The gas phase metallicity against gas fraction.

which are chosen. When the dust source is dominated by supernovae, we find that the burst rapidly increases the dust content of the galaxy (solid black line). However, if LIMS are the dominant dust source (dashed black line) we find that there is no increase in dust mass of the galaxy due to the burst and there is actually a slight decline in the dust fraction. Using the values of χ_1 and χ_2 from Morgan & Edmunds (2003), we find that there is a moderate increase in the dust mass of the galaxy during the burst of star formation. This shows that both the choice of dust source, and the star formation history, can have an effect on the evolution of the dust mass in a galaxy. Finally, the bottom right panel of Figure 4.1 shows the evolution of the gas phase metallicity of the galaxy, which is the observable quantity for metallicity. This has been calculated from the metal fraction, using (from Hayward et al. 2013):

$$12 + \log\left(\frac{O}{H}\right) = 12 + \log\left(\frac{Z}{29.2}\right) \tag{4.12}$$

this equation is calibrated for solar metallicity, using the observed oxygen abundance of Asplund et al. (2009):

$$12 + \log\left(\frac{O}{H}\right)_{\odot} = 8.69 \tag{4.13}$$

and a solar metal mass fraction of $Z_{\odot} = 0.014$. There is a non-linear relationship between the total mass of metals and the oxygen mass in a galaxy (Vincenzo et al., 2016) with a dependence on the gas metallicity. Since Equation 4.12 has been calibrated for solar metallicity it will become a less accurate conversion for metallicity values which are significantly higher or lower than the solar metallicity value. For the analytical model, where we only trace the total metal mass, this is the only conversion we can apply to obtain the oxygen abundance. However for the full chemical model introduced in the following section, it is possible to directly trace both the oxygen mass and total metal mass. In this case, we can obtain the oxygen abundance using the equation:

$$12 + \log\left(\frac{O}{H}\right) = 12 + \log\left(\frac{\text{oxygen mass}/16}{\text{gas mass}/1.32}\right) \tag{4.14}$$

where we have divided the oxygen mass by a factor of 16 to obtain the number of oxygen atoms. The gas mass, which is a mixture of hydrogen and helium, must be divided by a factor of 1.32 to obtain the number of hydrogen atoms in the galaxy. Directly tracing the oxygen mass enables us to more accurately calculate the oxygen abundance at the full range of metallicities which are being modelled.

This simple model of chemical evolution is useful to gain an understanding of the general evolution of a galaxy. Improvements to the model can be made by relaxing the assumptions that lead to the analytical solutions, these will allow the model to be useful in a wider range of regimes. For example, the assumptions that are made in the analytical model causes the model to break down at low gas fractions. A consequence of using a more complex model is that the results must be computed numerically, which increases the time needed to model each galaxy. However by being more physically motivated, this should provide an improved set of results for galaxy properties, this is why we next move on to the full time-dependent chemical model.

4.3 The Chemical Evolution Model

One of the largest assumptions in the construction of the analytic model was the Instantaneous Recycling Approximation. Relaxing this condition means the stars in the model will have finite lifetimes, and their effective yield will only be produced when the star reaches the end of its evolution. Hence there will be a delay between

variations in the star formation history of the galaxy and the corresponding metal and dust production. The closed box model, in which the mass of the galaxy remains constant over its lifetime, can also be relaxed to allow for inflows and outflows of material from the galaxy. Also more detailed dust production can be accounted for, such as allowing dust destruction and grain growth in the ISM.

We begin with the same equation for the total baryonic mass of the galaxy as presented in the previous section:

$$M_{\rm bary} = M_{\rm star} + M_{\rm gas}.$$

This equation does make the assumption that the dust mass of the galaxy is negligible in comparison to the gas and stellar mass of the galaxy. This is a reasonable assumption to make, even for galaxies with very high dust fractions such as Sub-millimetre Galaxies (SMGS), where the dust-to-stellar mass ratio can be increased by a factor of 30 (Santini et al., 2010). Since we are no longer assuming that the galaxy evolves in a closed box model, the equation that governs the gas mass of the galaxy becomes:

$$\frac{dM_{\rm gas}}{dt} = -\psi(t) + E(t) + I(t) - O(t) \tag{4.15}$$

in this equation $I(t)$ represents the inflow of gas in units of mass per unit time, which may be either enriched or primordial composition, into the galaxy from the intergalactic medium. $O(t)$ describes the outflow of gas from the galaxy in units of mass per unit time; this may be as a result of feedback from star formation, such as the powerful radiation from a supernova explosion (Barai et al., 2015).

$E(t)$ (from Equation 4.4) must then be evaluated at every time step in the history of the galaxy. There is again a corresponding equation for the evolution of the metal content of a galaxy, which (setting pre-enrichment to zero) can be written as:

$$\frac{d(ZM_{\rm gas})}{dt} = -Z(t)\psi(t) + E_{\rm z}(t) + I_{\rm z}(t) - O_{\rm z}(t)$$

$I_{\rm z}(t)$ describes the metals added to the ISM by inflows, while $O_{\rm z}(t)$ gives the metal mass lost through outflows. $E_{\rm z}(t)$ is the metal mass returned to the ISM by stars at every time in the evolution:

$$E_{\rm z}(t) = \int_{m_{\tau_{\rm m}}}^{m_{\rm u}} ([m - m_{\rm R}(m)]Z(t-\tau_m) + mp_{\rm z}) \times \psi(t-\tau_{\rm m})\,\phi(m)\,dm. \tag{4.16}$$

Equation 4.16 is of a similar form to the equation for the ejected gas mass,

although it contains metals from two sources. The term $[m - m_{\rm R}(m)]Z(t - \tau_{\rm m})$ describes the metals which existed prior to the formation of the star. These metals were taken from the ISM and locked up into the star when it formed, and are released back into the ISM when it dies. The second term mp_z describes the new metals which have been produced over the lifetime of the star, via core fusion and shell burning, and is the yield of a star of mass m. P_z is called the integrated mass fraction, and is given by:

$$P_z = \int_{m_1}^{m_2} mp_z(m)\,\phi(m)\,dm \tag{4.17}$$

here, m_1 and m_2 define the mass range for which the stellar yield is being calculated over, and z is the specific heavy element which we are calculating the yield over (this can be C, N, O or total metals z). $p_z(m)$ is the individual yield of a star of mass m, and is input from a library calculated from stellar evolution theory. Different libraries for metal yields are considered in Section 4.4.

Finally, we must consider the build up of dust in the galaxy. Here we follow Morgan & Edmunds (2003) and Rowlands et al. (2014). In the simple model, the dust mass of a galaxy was defined as a constant fraction of the metal mass. However this neglected any dust destruction, from powerful SNe shocks, or grain growth in the ISM. By relaxing these assumptions, we can write an equation for the mass evolution of dust as:

$$\frac{dM_{\rm d}}{dt} = E_{\rm d}(t) - \frac{M_{\rm d}}{M_{\rm g}}\psi(t) - (1-f_{\rm c})M_{\rm d}\delta_{\rm dest}(t) + f_{\rm c}\left(1 - \frac{M_{\rm d}}{M_{\rm z}}\right)M_{\rm d}\delta_{\rm grow}(t) + \frac{M_{\rm d}}{M_{\rm g}}I(t) - \frac{M_{\rm d}}{M_{\rm g}}O(t) \tag{4.18}$$

$E_{\rm d}(t)$ is the dust mass which is ejected by stars when they die and gets returned to the ISM. This includes dust grains formed from old metals, that were locked up in the star, and dust grains formed from new metals which have been produced by the star over its life. The second term in Equation 4.18, $\frac{M_{\rm d}}{M_{\rm g}}\psi(t)$, describes the astration of dust grains, this is where dust grains are removed from the ISM by star formation and the corresponding metals are locked up in the star during its life. Compared to Rowlands et al. (2014) we have added an additional term, $f_{\rm c}$, to account for the fraction of cold gas in the ISM of the galaxy. Grain growth will only occur in the fraction of gas which is cold and dense, while dust destruction will be more efficient in the warm diffuse ISM. We follow Mancini et al. (2015) and Inoue (2003) and set this factor to 0.5 as our default value. There may be a change in the fraction of cold gas as the galaxy evolves, with some evidence of a higher cold gas fraction at earlier

times (Popping et al., 2014; Nozawa et al., 2015).

Thus, the third term in Equation 4.18, $(1 - f_c)\, M_d \delta_{dest}(t)$, describes the destruction of dust grains by SNe shocks, and will be explained in more detail below. The fourth term, $f_c \left(1 - \frac{M_d}{M_z}\right) M_d$, explains the growth of dust grains in the ISM. The final two terms account for the mass of dust which may be either added or removed from the ISM due to inflows or outflows of gas. The equation for the ejected dust mass, $E_d(t)$, can be written as:

$$E_d(t) = \int_{m_{\tau m}}^{m_u} ([m - m_R(m)] Z(t - \tau_m) \delta_{lims} + m p_z \delta_{dust}) \times \psi(t - \tau_m)\, \phi(m)\, dm \quad (4.19)$$

δ_{lims} describes the fraction of the metals locked up into stars which form dust grains in LIMS winds. δ_{dust} is the condensation fraction, which is the amount of new metals produced by stars and are converted into dust grains. These can be from both high mass stars and low mass stars. Stars over $40\,M_\odot$ do not contribute to the dust mass, since they are thought to end their lives as black holes, so do not produce any yield (Maeder, 1992).

The equations presented in this section provide a framework which the Python code uses to calculate the chemical evolution of a galaxy. The code loads a user input file with values of the initial gas mass, inflow and outflow rates (as a multiple of the SFR), a user SFH file and values for the strength of dust destruction and grain growth (see Sections 4.4.4 and 4.4.5 respectively). Metal and dust yields for high and low mass stars are read from input tables (see Section 4.4 for details). Equations 4.8, 4.15 and 4.18 are then evaluated for every time step in the user SFH file (along with corresponding equations such as 4.19) to obtain the mass of gas, stars, metals and dust at every time step. These values are then stored in an output file, alongside additional secondary parameters such as gas fraction and dust-to-metal ratio.

4.4 Libraries and Inputs of the Chemical Evolution Model

Here we take a closer look at the various inputs that are required to model the evolution of a galaxy including the stellar initial mass function and stellar yields. We also describe our prescriptions to calculate stellar lifetimes, and the remnant mass stars of given mass will produce. All these individual elements combine with the equations which have been presented in Section 4.3, to produce the complete model

of chemical evolution which we use to investigate galaxy samples in later chapters.

4.4.1 Initial Mass Function

There has been considerable observational evidence for the existence of a universal stellar IMF (Bastian et al., 2010), although recently there have been new questions raised as to whether it is truly universal across all environments (Cappellari et al., 2012). The IMF describes in a given amount of star formation the mass distribution or relative number counts of the stars which will form. The proposed IMFs vary slightly in their functional form, usually at the extremes of the distribution where it is more difficult to obtain large number statistics from observations. For example, at the high mass end of the IMF, there are considerably less stars, and so the empirical limits which can be placed on the form of the IMF are rather less restrictive. At the other end of the IMF, low mass stars are much fainter and therefore hard to observe. This leads to an incomplete sample which may bias the IMF which is obtained from a set of observations eg Ward-Thompson et al. (1994).

The IMF will clearly play an important role in understanding the chemical evolution of a galaxy. If the IMF is biased towards high mass stars then there will be an increase in the rate of supernova (SNe), which will have an effect on the amount of metals that a given population of star formation will produce. An increase in the rate of SNe will also effect the amount of dust which is destroyed by SNe shock waves (Jones, 2004). On the other hand, if the IMF is biased towards creating more low mass stars in a given amount of star formation, then much of the metals and dust will be locked away in these low mass stars on longer time-scales, and therefore the chemical enrichment of the galaxy will be slower. Here we introduce the different functional forms of the IMF included in the chemical code created for this thesis, adding to the Salpeter (1955) and Miller & Scalo (1979) functional forms originally included in Morgan & Edmunds (2003). The mass function, $\phi(m)$ can be defined such that $\phi(M)dm$ is the number of stars with mass between M and $M + dm$. The total number of stars with mass between M_1 and M_2 is then given by:

$$N(M_1, M_2) = \int_{M_1}^{M_2} \phi(M) dM \tag{4.20}$$

and taking derivaties of both sides gives:

$$\frac{dN}{dM} = \phi \tag{4.21}$$

where ϕ is the number of stars dN in a mass interval dM.

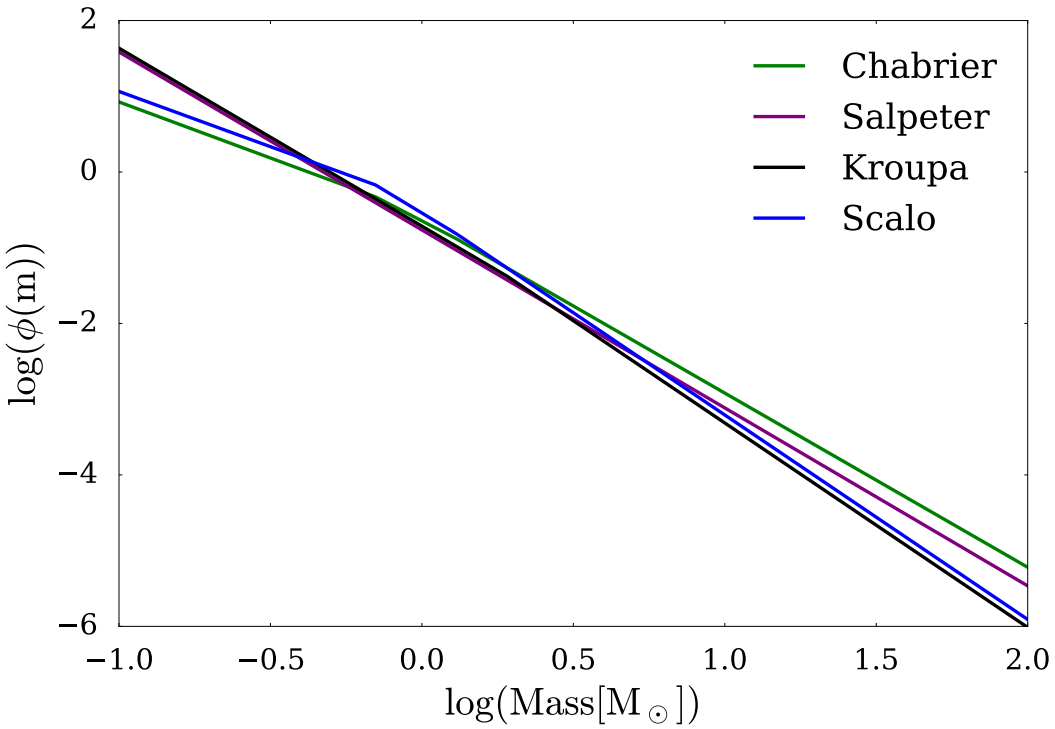

FIGURE 4.2 Comparison of different stellar IMFs which are described in the text. The Chabrier (2003) has more high mass stars when compared to the other IMFs in the literature, and is similar to the Salpeter (1955) IMF (shown in purple) in this regime.

There are many functional forms of the IMF presented in the literature at present, although variations between them are mostly found in the relative numbers of stars which are formed at the high and low mass limits of the distribution. These IMFs have been suggested as the best fit to the observed mass distribution of stars. The first functional form of IMF suggested was that of Salpeter (1955), here the IMF is presented as a single power law:

$$m\,\phi(m)_{\rm Salp} \propto m^{-1.35} \tag{4.22}$$

The number of objects decline rapidly with mass of the object, hence a large number of low mass objects are formed when using the Salpeter IMF. The IMF of Miller & Scalo (1979) offers a refinement to the Salpter model, with a flattening of the slope of the IMF for low mass objects:

$$m\,\phi(m)_{\rm Scalo} \propto \begin{cases} m^{-0.25}, & \text{if } m < 1\,{\rm M}_\odot \\ m^{-1.0}, & \text{if } 1 < m < 2\,{\rm M}_\odot \\ m^{-1.7}, & \text{if } m \geq 2\,{\rm M}_\odot \end{cases} \tag{4.23}$$

While the Scalo IMF is a broken two part power-law, Kroupa et al. (1993) suggests that this can be defined better as a three part power-law, with less high mass mass objects:

$$m\,\phi(m)_{\rm Kroupa} \propto \begin{cases} m^{-0.3}, & \text{if } m \leq 0.5\,{\rm M}_{\odot} \\ m^{-1.2}, & \text{if } 0.5 < m < 1\,{\rm M}_{\odot} \\ m^{-1.7}, & \text{if } m > 1\,{\rm M}_{\odot} \end{cases} \tag{4.24}$$

Using observations of the distribution of low mass objects in the Galactic disk, Chabrier (2001) show that the stellar IMF is shallower than predicted by either Scalo or Salpeter. A new functional form for the IMF was presented in Chabrier (2003) to fit the data:

$$m\,\phi(m)_{\rm Chabrier} = \begin{cases} 0.85\exp(-\frac{(\log({\rm m})-\log({\rm m_c}))^2}{2\sigma^2}), & \text{if } m \leq 1\,{\rm M}_{\odot} \\ 0.24\,m^{-1.3}, & \text{if } m > 1\,{\rm M}_{\odot} \end{cases} \tag{4.25}$$

For observations of more actively star forming galaxies, such as star bursts it would also seem to be appropriate to use such an IMF. Figure 4.2 shows a graphical comparison of the range of IMFs from the literature, where they are normalised according to Equation 4.26:

$$\int_{m_{\rm t}}^{m_{\rm u}} m\,\phi(m)\;dm = 1 \tag{4.26}$$

The Chabrier IMF can be seen to produce significantly more high mass stars than the other IMFs considered. Later in this thesis, we investigate the effect using a range of stellar IMFs have on the results obtained.

4.4.2 Metal and Dust Yields

There is considerable debate as to how many metals stars of given mass produce, and how many of these metals then condense into dust. Therefore the metal yields and dust condensation efficiency can strongly effect the final dust mass which a galaxy produces. In this section, we consider the different libraries which are included in in the chemical evolution model used in this work (and compare with the yields assumed in Rowlands et al. 2014). We also discuss how these metal yields compare to other theoretical calculations and observational studies.

4.4.2.1 LOW MASS STAR YIELDS: VAN DEN HOEK & GROWEGEN 1997

van den Hoek & Groenewegen (1997) present metal yields for stars of the mass range $0.1 - 8\,\mathrm{M}_{\odot}$, obtained from theoretical calculations. The work presents metal yields for both pre-AGB and AGB phases of stellar evolution. The AGB phase combines the use of evolutionary tracks from the Geneva group, with a synthetic thermally pulsing AGB model. The AGB calculations begin at the first thermal pulsation, and continue either until all the envelope mass of the star has been lost, or the Chandrasekhar mass limit is reached.

Stellar yields in these calculations are defined as:

$$mp_j(m) = \int_0^{\tau(m)} E(m,t)(Z_j(t) - Z_j(0))\,dt$$

where the integral is computed over the full range of stars which have reached the first thermal pulsation, and $\tau(m)$ is the lifetime of a star at time t. $E(m,t)$ is the stellar mass loss rate of a star of mass m at time t. $Z_j(t) - Z_j(0)$ provides the metals which have been produced over the lifetime of the star, taking into account any pre-existing metals. The calculation can be performed over different species j, and it is possible to obtain negative yields, such as in the case of hydrogen, where large amounts of the element has been fused into heavier elements by the star.

The synthetic AGB model takes into account several physical features of AGB stars at different phases of evolution. The first of these stages is the 'first dredge-up', where the convective envelope of a star moves inwards as the star transitions into the red giant phase. During this process the star loses mass, and the helium abundance increases, since helium produced in the core of the star is brought into the outer envelope. Following this, the star may undergo a second dredge up phase, depending on initial core mass. This occurs at the formation of an electron degenerate CO core, the star does not lose significant mass during this stage. The more massive stars with a core mass greater than a critical limit, which is set at $0.58\,\mathrm{M}_{\odot}$ to fit luminosity observations, undergo a third dredge up phase which can again lead to significant mass loss. The thermal pulsing phases of an AGB star can lead to significant mass loss, for example $\approx 4.8\,\mathrm{M}_{\odot}$ for a $6\,\mathrm{M}_{\odot}$ star.

These libraries have the advantage of being the only models to consistently treat the full mass range of LIMS, and include prescriptions for the super AGB mass range of $5 - 8\,\mathrm{M}_{\odot}$. This regime is thought to be of considerable importance for the total metal yield of a galaxy, given the increased mass loss and cool atmospheres driving this stage Morgan & Edmunds (2003).

To produce predictions for the amount of dust stars of different mass produce

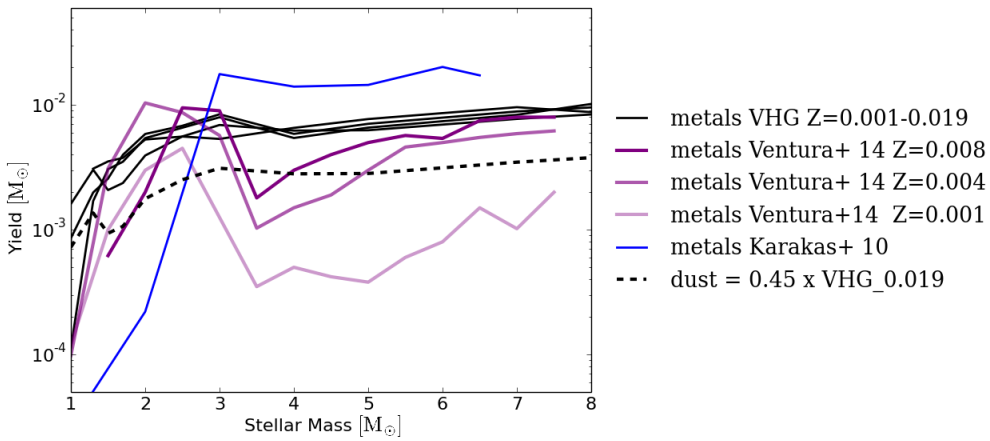

Figure 4.3 Comparison of the different mass yields of LIMS ($0.1 - 8\,M_\odot$) from various works in the literature. Metal yields from Karakas (2010) are shown by the cyan line, and van den Hoek & Groenewegen (1997) metal yields are shown by the solid black line (with corresponding dust yields shown by the dashed black line). Dust yields from the theoretical model of Ventura et al. (2014) for a range of metallicity are shown by the red, purple and blue dashed lines. We can't use Ventura et al. (2014) dust yields with van den Hoek & Groenewegen (1997) metal yields, as for a metallicity of $Z = 0.004$ or $Z = 0.008$ we would be creating more dust than metals (for a mass range of $1.5 - 3\,M_\odot$. We must choose van den Hoek & Groenewegen (1997) if we wish to cover the mass range of $5 - 8\,M_\odot$ in detail, since it is the only input file which covers the full mass range.

over their lifetime, it is also necessary to assume a dust condensation efficiency, which effectively prescribes what fraction of the metals produced by a star will form dust grains. Work by Rowlands et al. (2014) combines these metal yields with the dust condensation efficiency from Morgan & Edmunds (2003), and estimates a dust production of (1-2000)$\times 10^{-5}\,M_\odot$ per LIMS. Ladjal et al. (2010) performed a study of the circumstellar envelope produced by mass loss of AGB stars, using observations at 870 μm. This provides constraints on the amount of dust which can be produced by these stars during their evolution. They selected a sample of 9 stars, to cover a range of chemical and evolutionary phases. They estimate the mass loss and dust production over their lifetime and found that the total dust mass production ranges from 0.01-2000 $\times 10^{-5}\,M_\odot$ for the sample. These observations are in good agreement with the dust mass predictions from Rowlands et al. (2014).

More recently, Ventura et al. (2012) provides a theoretical model of the dust mass production from AGB stars. Their model includes the physical Hot Bottom Burning (HBB) phase, where nucleosynthesis occurs at the bottom of the convective envelope, which is thought to be an important feature for these stars. HBB conditions

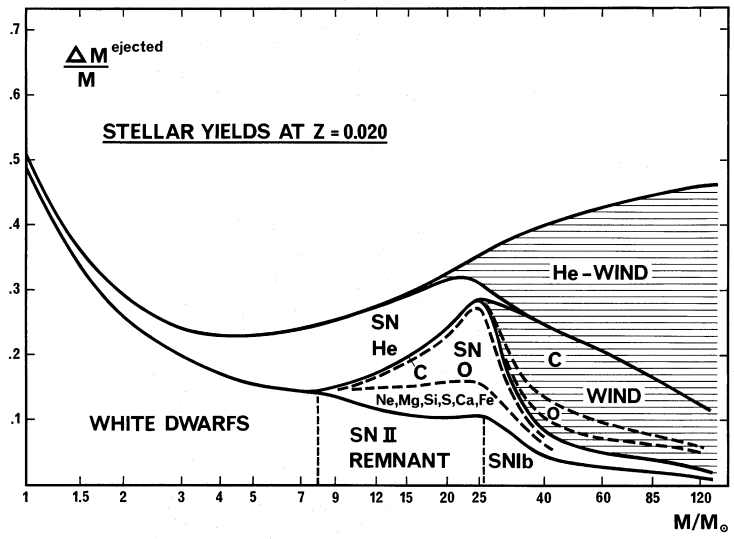

FIGURE 4.4 Figure reproduced from Maeder (1992), showing how the stellar yield varies with initial stellar mass for a fixed metallicity of $Z = 0.020$. Stellar remnants account for a considerable fraction at low stellar mass, while the effects of stellar winds become more significant for high mass stars.

are reached in all stars with an initial mass greater than $4\,M_\odot$. The dust prediction from Ventura et al. (2012) shows good agreement with the dust yields in our model.

Figure 4.3 shows the comparison between the different metal and dust yields in the literature which we could use as inputs for the chemical evolution model. We choose to remain with the van den Hoek & Groenewegen (1997) metal yields and a dust condensation efficiency factor of 0.45 from Morgan & Edmunds (2003) for the following reasons. Firstly, if we chose to use the Ventura et al. (2014) dust yields with the van den Hoek & Groenewegen (1997) metal yields, then for certain mass and metallicity ranges we would be creating more dust than metals, which is clearly unphysical. Secondly, as described above, we prefer to remain with van den Hoek & Groenewegen (1997) metal yields, since other metal libraries (such as Karakas 2010) do not cover the full mass range of LIMS.

4.4.2.2 HIGH MASS STAR YIELDS: MAEDER 1992

Maeder (1992) present metal yields for stars ranging from $1 - 120\,M_\odot$ for metallicity $Z = 0.001$ and $Z = 0.02$. We use this library for the theoretical yields of high mass stars ($> 8M_\odot$) in our model. The nucleosynthesis production of high mass stars is strongly dependent on the initial metallicity, therefore it is important to choose a library with significant metal 'resolution', if reliable stellar yields are to be obtained. The model of Maeder (1992) also includes several physical features, such as

moderate core overshooting and stellar rotation. These are required because they can affect the mass loss and amount of fuel which is available in the core, hence changing the lifetime and yields of stars.

Stars whose initial stellar mass exceeds $\sim 40\,M_\odot$ will produce, at the end of their lifetime, a black hole. The effect of black hole formation is included in the model of Maeder (1992). Decreasing the initial mass required for black hole formation strongly reduces the metal yield of high mass stars.

The consequence of stellar winds on the effective metal yields of high mass stars is also considered, see Figure 4.4. For some stars, such as Wolf Rayets stars, the stellar winds can have a significant effect in the mass loss and metal yields of the stars.

The total metal yield of high mass stars decreases with increasing initial metallicity, a feature which can be explained by considering one of the dominant processes by which a high mass star will interact with the surrounding interstellar medium. The process, which occurs during the evolution of the star, is the stellar wind. High mass stars lose a significant fraction of their mass through stellar winds, and this mass lose has an direct consequence on their evolution. Stellar winds are comprised mostly of hydrogen and helium, so significant mass loss through stellar winds will reduce the mass of hydrogen and helium which remains to be synthesized into heavy elements. Therefore, stars with strong stellar winds will have a lower metal yield. The efficiency of the stellar wind is known to increase with increasing metallicity, since stellar winds are initiated and driven by absorption of UV photons by metal lines. An increase in metals, from higher initial metallicity, will lead to a higher stellar wind. As such, stars with a higher initial metallicity will experience enhanced mass loss through stellar winds, and will suffer a decrease in metal yields as a consequence of this. We can see the difference in the metal production of high mass stars by comparing the two plots in Figure 4.4, which show the mass distribution of the various elements of a high mass star yield. We can see for the high initial metallicity stars in their model, a larger fraction of the mass is lost through stellar winds, which results in a lower final metal yield of elements such as oxygen.

Todini & Ferrara (2001) investigated the total dust grain production in the supernova of high mass stars ($12-40\,M_\odot$). The models cover a range of initial metallicity, from primordial composition to solar metallicity. To calculate the dust production, they combine a standard model for dust nucleation, with a model to describe the supernova ejecta and molecule formation. The model of dust nucleation, which describes how solid dust grains can condense out of gas phase elements, is taken from

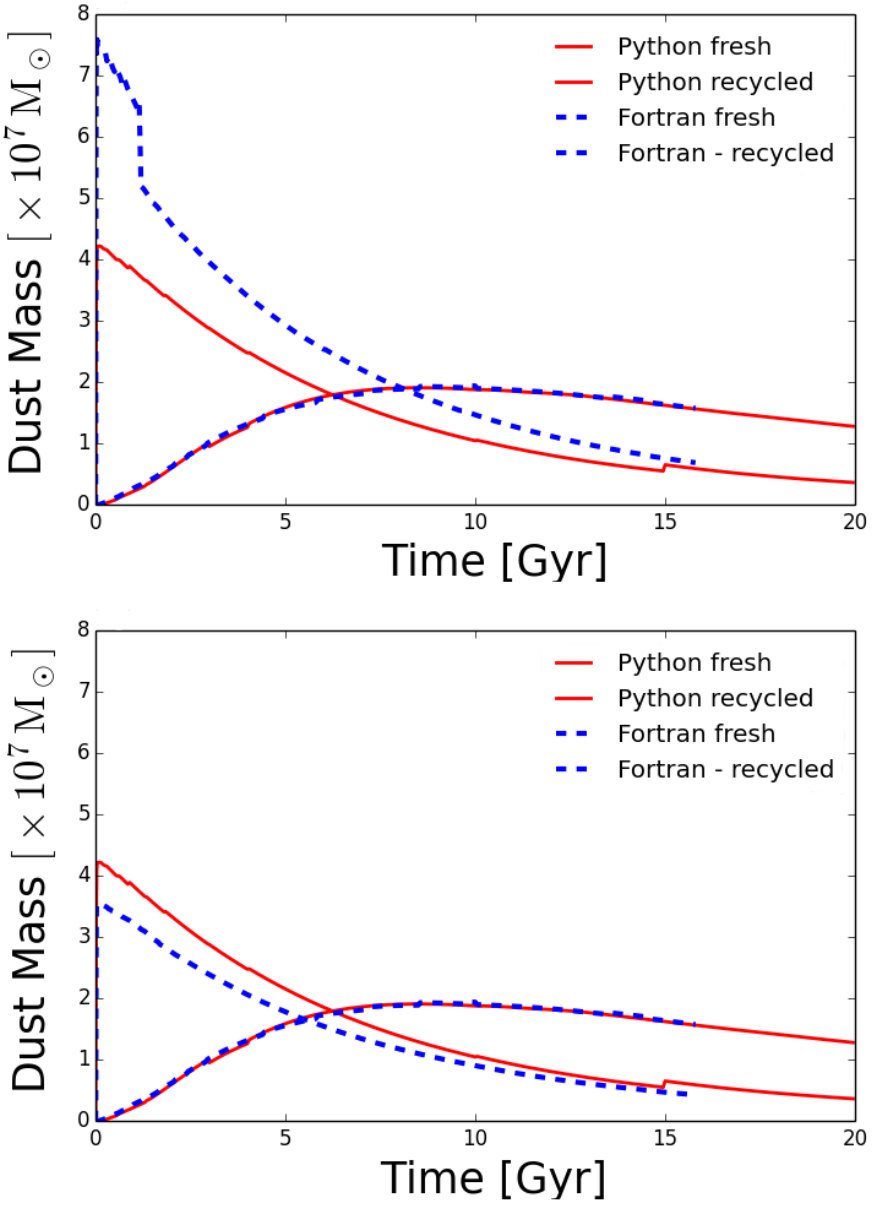

FIGURE 4.5 Comparison between the total dust production of high and low mass stars against time for this work and Rowlands et al. (2014). *Top:* Here we see the dust produced by the new Python code in red, and the dust from the old Fortran code of Rowlands et al. (2014) shown in blue. The low mass star dust yields are the same, but there are variations between the dust yields of high mass stars. In the Fortran code, we estimated a dust efficiency and applied this to the metal yields from Maeder (1992), whereas for Python the dust yields are used directly from Todini & Ferrara (2001). *Bottom:* If we use the same dust yields for both the Fortran and Python code, then there is still a small difference between the dust yields of high mass stars. Rowlands et al. (2014) interpolate between the stellar yields for a star of given mass, while we now use a nearest neighbour approach to ensure that we are not biasing the data.

Initial Mass ($M_\odot$)	Metal Yield SN ($M_\odot$)	Metal Yield Winds ($M_\odot$)	Dust Yield SN ($M_\odot$)	Dust Yield Winds ($\times 10^{-3} M_\odot$)
0.9	0.00	6.83×10^{-3}	0.00	3.07
1.0	0.00	0.16×10^{-3}	0.00	0.07
1.3	0.00	1.70×10^{-3}	0.00	0.77
1.5	0.00	3.06×10^{-3}	0.00	1.38
1.7	0.00	3.51×10^{-3}	0.00	1.58
2.0	0.00	5.43×10^{-3}	0.00	2.44
2.5	0.00	6.58×10^{-3}	0.00	2.96
3.0	0.00	7.98×10^{-3}	0.00	3.60
4.0	0.00	5.44×10^{-3}	0.00	2.45
5.0	0.00	6.59×10^{-3}	0.00	2.97
7.0	0.00	8.35×10^{-3}	0.00	3.76
8.0	0.00	10.2×10^{-3}	0.00	4.59
9.0	0.17	0.00	0.17	0.00
12.0	0.69	0.00	0.20	0.00
15.0	1.32	0.00	0.50	0.00
20.0	2.73	0.00	0.50	0.00
25.0	4.48	0.00	1.00	0.00
40.0	1.61	6.40	0.40	0.00
60.0	0.00	8.69	0.00	0.00
85.0	0.00	17.7	0.00	0.00
120.0	0.00	9.39	0.00	0.00

Table 4.1 Summary of the stellar yields for stars of mass $0.9 - 120\,M_\odot$, with initial metallicity of $Z = 0.02$, which are input to the chemical evolution model. The metal yields of low mass stars ($< 8\,M_\odot$) are obtained from van den Hoek & Groenewegen (1997), and are distributed via stellar winds. Metal yields of high mass stars ($> 8\,M_\odot$) are obtained from Maeder (1992), although no metals are produced via SNe for stars of mass $> 40\,M_\odot$, due to the formation of a black hole. However these very high mass stars $> 40\,M_\odot$ still distribute some metals via stellar winds prior to the formation of the black hole. The dust yield of low mass stars through stellar winds is obtained using a dust condensation efficiency of 0.45 from Morgan & Edmunds (2003), while the dust yield of high mass stars ($8 < M < 40\,M_\odot$) is input from Todini & Ferrara (2001).

Abraham & Hornbogen (1974). In this work the formation of solid dust grains is described as a two stage process, where initially critical clusters must form out of the gas phase. These clusters then grow by the accretion of further compounds onto the surface of the cluster to produce dust grains. There are some compounds which form by chemical reaction on the surface of the dust grain, rather than by accretion onto the dust grain, and this is accounted for following Kozasa & Hasegawa (1987). The nucleosynthetic yields of high mass stars (obtained from Woosley & Weaver 1995) and temperature evolution of the supernova ejecta (calculated assuming adiabatic expansion) are then applied to the nucleation theory to calculate the dust production of high mass stars. Todini & Ferrara (2001) compare the results of their model with the observed dust production in SN1987A (Nomoto et al., 1991), and find that they reliably reproduce the principle features of the dust production in the supernova.

Rowlands et al. (2014) applied the dust production of high mass from Todini & Ferrara (2001) to the chemical evolution model in a two-stage process. Firstly, a dust condensation efficiency was estimated for high mass stars, using the metal and dust yields of Todini & Ferrara (2001). The dust condensation efficiency was then applied to the Maeder (1992) metal yields, to obtain the dust mass which was produced by the high mass stars. We have since updated this process, so the dust yield of high mass stars are obtained directly from Todini & Ferrara (2001). Rowlands et al. (2014) also used interpolation to obtain the dust yields of stars of a given mass from the input library. We now apply a nearest neighbour technique, such that the yields for stars of all mass are read directly from the input libraries.

In Figure 4.5 (left) we compare the dust yields of high and low mass stars using our chemical evolution model (Python, shown in red) against the dust production from Rowlands et al. (2014) (Fortran, shown in blue). We find that the production of fresh dust from high mass stars is slightly reduced compared to Rowlands et al. (2014). To decouple the effect of the two modifications, we then change the Fortran model such that the dust yields also use the nearest neighbour method (this is shown in the second plot in Figure 4.5). We find directly using the dust yields of Todini & Ferrara (2001) slightly increases the dust production, compared to applying a dust condensation efficiency to the Maeder (1992) yields. Combining, these two issues, we therefore have less SNe dust by approximately a factor of 1.8 in this model compared to previous published works.

Finally, whilst rewriting the code in Python, an error in the Rowlands et al. (2014) metallicity calculation was found. Figure 4.6 (top) compares the metallicity Z (blue) and yield P_Z (red, Equation 4.17) output using the Fortran code from Rowlands et al. (2014). Here we zoom in on the metallicity mass produced by a Milky Way galaxy at 0.2-2.0 Gyr. Between 0.6-0.63 Gyr, we see a huge step-change in the yield output from the Fortran routine, which in turn manifests as a smaller step-change in metallicity from the 'fresh' metals output by stars (second term of Equation 4.16, dashed blue line). Consequently this introduces a flattening in the metallicity growth after that time (solid blue line). When we zoom out to show a longer timescale range in Figure 4.6 (bottom) and plot the mass of stars that are contributing to the metal mass/yield for each time step (shown as vertical lines), it becomes clear that this is a discontinuity in the code. Before 0.6 Gyr, stars of mass up to $\sim 35\,\mathrm{M}_\odot$ are contributing metals to the yield P_Z as they should, but after this time, only stars with $M_\mathrm{i} < 5\,\mathrm{M}_\odot$ are contributing. After careful checking, we identified that the yields from stars for a given M_i and Z used in Rowlands et al. (2014) were misread from the Maeder (1992) files. When this was corrected (Figure 4.7), the large step-change at 0.6 Gyr

disappears and the total metallicity increases approximately linearly with time (solid blue line, bottom panel) as expected as gas is turned into stars, and those stars die and eject metals into the ISM.

4.4.3 Stellar Lifetimes and Remnant Mass

Stars only release their yield of dust and heavy elements when they reach the end of their evolution. The lifetime of an individual star can be predicted, provided that the initial mass and metallicity of the star are known. Therefore it is necessary to incorporate a prescription for the lifetime of stars into the chemical model. We use the calculations of (Schaller et al., 1992), which have extensive grids for which the lifetime of a star of specific mass and metallicity can be measured from. The grids cover the mass range $0.8 - 120\,\mathrm{M}_\odot$ and metallicity $Z = 0.020 - 0.001$. These models contain extensive physical effects including stellar rotation and mass loss.

We also need to have a prescription for the mass of the stellar remnant which a star of given mass leaves behind when it dies. This is an important value, since the higher the remnant mass the more gas and metals which get locked up in stars. In both Morgan & Edmunds (2003) and Rowlands et al. (2014), the authors used the remnant mass model from Talbot & Arnett (1973):

$$m_{\mathrm{R}}(m) = \begin{cases} 0.106\,m + 0.446, & \text{if } m \leq 8.0\,\mathrm{M}_\odot \\ 1.5, & \text{if } m > 8.0\,\mathrm{M}_\odot. \end{cases} \tag{4.27}$$

We have since updated the remnant mass for the model in Ferreras & Silk (2000) which is based on mass loss models of Iben & Tutukov (1984) and Woosley & Weaver (1995):

$$m_{\mathrm{R}}(m) = \begin{cases} 0.106\,m + 0.446, & \text{if } m \leq 9.0\,\mathrm{M}_\odot \\ 1.5, & \text{if } 9.0 < m < 25.0\,\mathrm{M}_\odot \\ 0.61\,m - 13.75, & \text{if } m \geq 25.0\,\mathrm{M}_\odot. \end{cases} \tag{4.28}$$

This equation allows massive stars to contribute metals and gas to the ISM. However, stars which end up as a black hole at the end of their lives may in fact have metals and gas collapse inward, this could affect the metal enrichment from massive stars. This is indeed an assumption made often in the literature (Madau & Dickinson, 2014). Here we therefore test two cases where the black hole mass (m_{BH}) is set to $40\,\mathrm{M}_\odot$ or $60\,\mathrm{M}_\odot$, assuming that stars above this mass do not contribute metals and gas into the ISM (ie the remnant mass, $m_{\mathrm{R}}(m)$, is equal to the initial mass of the

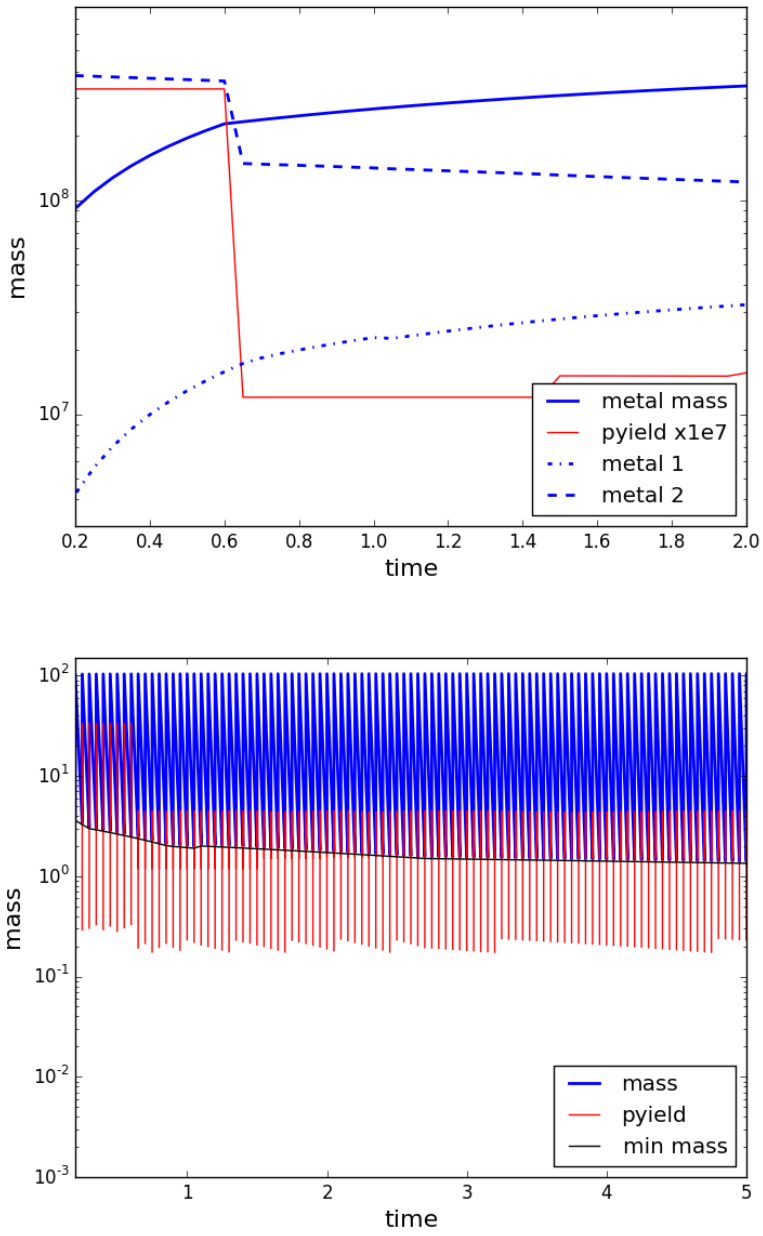

FIGURE 4.6 Comparison of the mass of a galaxy over time in Gyr (solid blue line) from the old Fortran code used in Morgan & Edmunds (2003) and Rowlands et al. (2014), using a Milky Way style SFH of Yin et al. (2009). *Top:* The recycled metals (in $M_\odot$) output from each generation of stars (dotted blue line) and the fresh metals output by stars (dashed blue line) are derived using the first and second terms of Equation 4.16 respectively. The kink seen in the freshly formed metals output by stars (and the total metals) between 0.6-0.63 Gyr is even more significant when plotting the stellar yield P_Z (from Equation 4.17, red line). (Note that the yield has been multiplied by 10^7 to compare on a similar scale to the metal mass.) *Bottom:* We now zoom out and compare the metal mass and yield over a timescale of 0-5 Gyr for the same galaxy. Here the blue and the red shows the mass of stars in each time step that are contributing to the metal mass and the yield calculation respectively. There is clearly an issue given that beyond t >0.6 Gyr there appears to be no high mass stars contributing to the yield. The black solid line displays the minimum mass of the star with lifetime equal to the age of the galaxy (and therefore contributing metals).

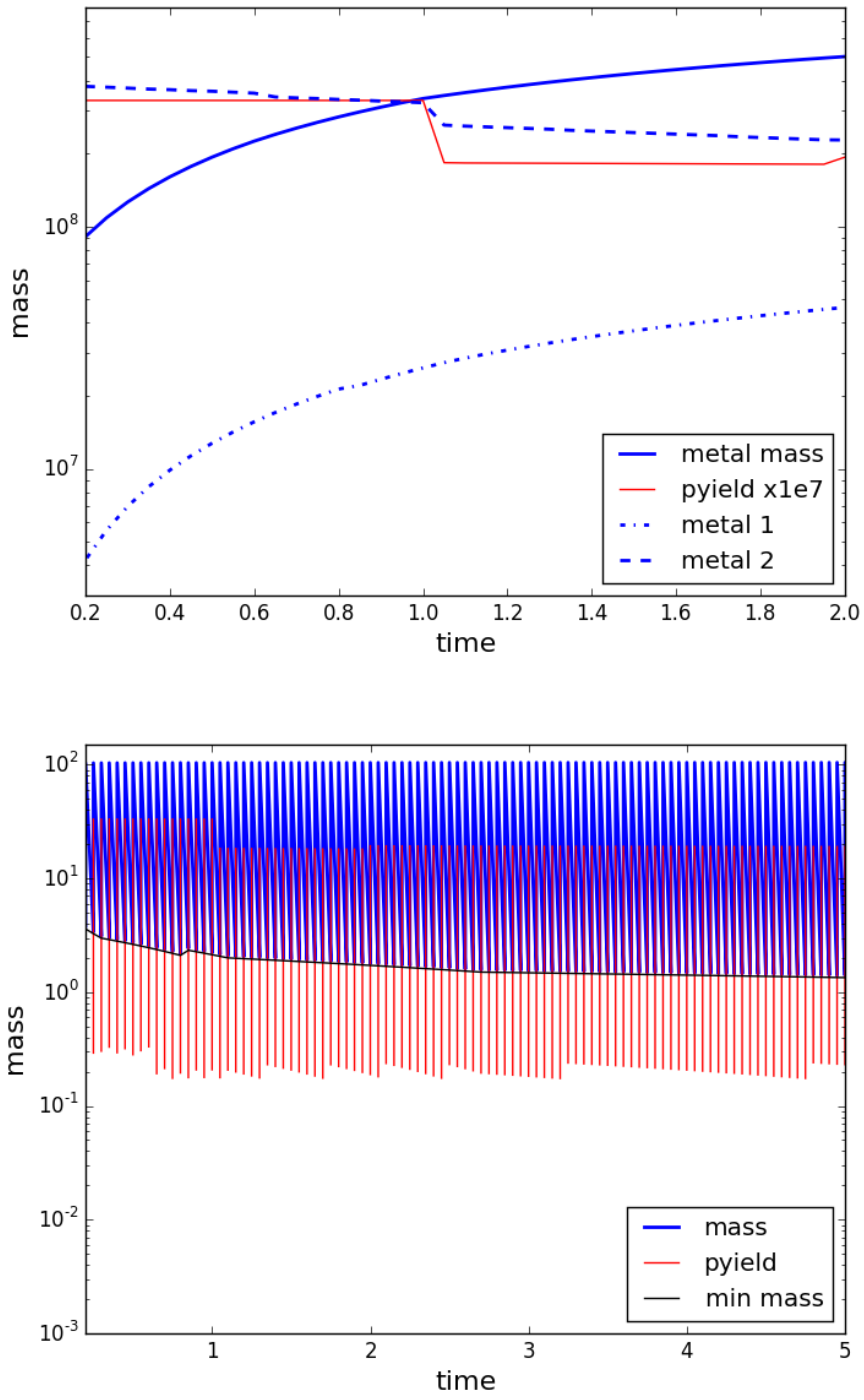

Figure 4.7 Same as Figure 4.6 but now using the correct metal yields from Maeder (1992). Note there is still a kink, this time at ∼1 Gyr, but this is due to the code changing its read out from one metal mass library to another at a different metallicities (the code switches between reading from mass outputs for $Z = 0.008$ and $Z = 0.019$). In the corrected version, the metal mass (solid blue line) no longer flattens with time, and increases roughly linearly as the gas is converted into stars and metals are ejected.

star).

Figure 4.8 compares the effect using two different remnant mass functions and two different cut off limits for $m_{\rm BH}$ on the evolution of the gas and dust mass for a Milky Way like galaxy. These models include dust sources from stars, grain growth in the ISM and destruction via SN shocks (see Section 4.3). We can see that Equation 4.27 (from Rowlands et al. 2014) releases the most gas mass back into the ISM, allowing for galaxies to have a higher gas fraction at any given time. Using Equation 4.28 (from Ferreras & Silk 2000) we find that less material is released as the stars die, and this is further compounded by assuming that all metals are swallowed up in the BH collapse above the $m_{\rm BH}$ mass. The effect on the dust mass (scaled by a factor of 10 in this figure) is small, though we start to see differences beyond 15 Gyr in this galaxy.

However Maeder (1992) points out that stars above the $m_{\rm BH}$ cut off can still contribute stellar yields to the ISM via their stellar winds, prior to the formation of the BH. This becomes more important at higher metallicity when a greater proportion of the yield is returned via winds compared to SN. In Figure 4.4, Maeder (1992) compares the yields from massive stars in both SN and winds at $Z = 0.001$ and 0.02, which allows us to separate out the contributions and ignore the SN yields above $m_{\rm BH}$. Comparing this with the Ferreras & Silk (2000) prescription for deriving the remnant mass (Equation 4.28) agrees well with that expected when just including yields from winds in Maeder (1992). We therefore choose to use Ferreras & Silk (2000) (dashed curve in Figure 4.8) with no further need to set a cut-off limit in the remnant mass function, as this prescription adequately describes mass return by stars above $m_{\rm BH}$ from stellar winds only.

4.4.4 Dust Destruction

We can now look in more detail at the remaining terms in Equation 4.18, which are $\delta_{\rm dest}$ and $\delta_{\rm grow}$. These terms are responsible for including both dust grain destruction and dust grain growth respectively. There are various prescriptions which could be chosen to describe these processes, here we describe the equations which have been implemented in the code used for this work.

It has long been suggested that the powerful shocks produced by SNe have the potential to destroy dust grains present in the ISM. Firstly, there is observational evidence presented in Shull et al. (1977). Here the authors found that high line of sight velocity clouds have a significantly lower percentage of their elements contained in dust grains, when compared to clouds with low line of sight velocities. There is also

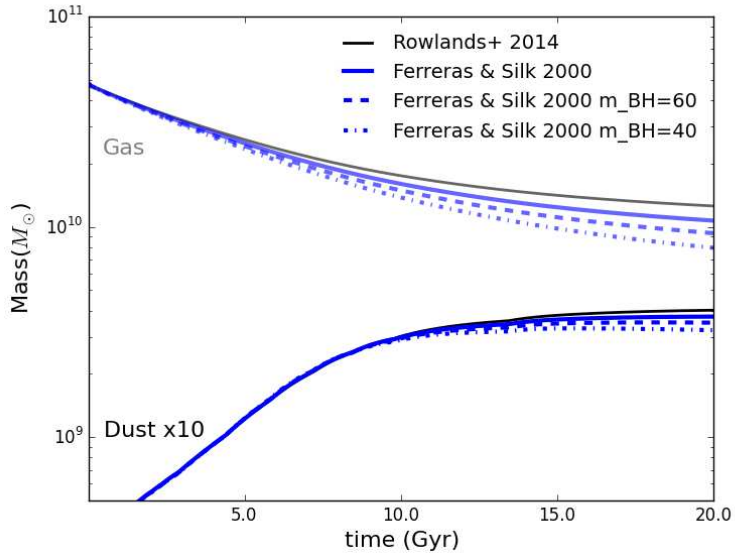

Figure 4.8 Testing the effect different remnant mass equations have on the amount of gas and dust which are produced. The model has been computed for a Milky Way like galaxy, with dust sources from stars and grain growth. We also account for dust destruction in the ISM from SN shocks. Less gas is returned to the ISM when using the Ferreras & Silk (2000) prescription for remnant mass compared to Rowlands et al. (2014). We choose to use the equation without a BH cut-off mass, since even high stars will contribute yields to the ISM via stellar winds (Maeder, 1992).

an array of theoretical studies which predict dust grain destruction by SNe (Spitzer, 1976; Barlow & Silk, 1977; Seab & Shull, 1983).

Despite this work, there is still much debate about the efficiency of shocks at destroying dust grains (Bocchio et al., 2014). A large reason for this is the number of factors which contribute to the complicated processes in the ISM. For example, dust destruction is thought to depend on both the physical composition of the ISM, as well as the velocity of shocks produced by SNe (Jones, 2004; Dwek et al., 2007). Varying size dust grains are thought to experience shocks differently, with small grains more vulnerable to destruction, while large grains are eroded by grain-grain collisions, but are perhaps not fully returned to the gas phase (Owen & Barlow, 2015).

We have updated the chemical evolution code, since it was used in Rowlands et al. (2014), to include the fraction of cold gas in the ISM (see Equation 4.18), and this has a direct consequence on the efficiency of dust destruction in our model. Destruction of dust grains from SNe is caused by the powerful shocks which are produced when the speed of the ejected material exceeds the local sound speed in the medium. If the material from the star is ejected with less than the critical velocity, then there will not be a shock and the dust destruction will be inefficient. The critical

value is set by the local sound speed, which in turn is dependent on several factors including the density of the ISM. The speed of sound increases as the density of the environment increases and therefore in the cold dense regions of the ISM the ejected SNe material must have a much higher speed for dust destruction to become efficient. In contrast, when a SNe occurs in a diffuse region of the ISM, the critical velocity for shocks is much lower. Therefore, dust grain destruction in the diffuse ISM is a much more efficient process.

In our model, we implement the dust destruction prescription of Dwek et al. (2007). Here, the dust destruction is described as a function of the rate of SNe in a galaxy. $\delta_{\rm dest}$ from Equation 4.19 is given by $\delta_{\rm dest} = \tau_{\rm dest}^{-1}$ where:

$$\tau_{\rm dest} = \frac{M_{\rm g}}{m_{\rm ISM} R_{\rm SN}(t)} \tag{4.29}$$

$\tau_{\rm dest}$ is the timescale of dust destruction, $m_{\rm ISM}$ is the mass of ISM which is swept up by each SNe explosion, and $R_{\rm SN}(t)$ is the effective rate of SNe derived from:

$$R_{\rm SN}(t) = \int_{9{\rm M}_\odot}^{40{\rm M}_\odot} \phi(m)\, \psi(t)\, dm \tag{4.30}$$

in Equation 4.30, the bottom limit of the integration is set by the boundary of low mass and high mass stars. Below this limit, the star will not end its life in a SNe and therefore will not contribute to the destruction of dust in the ISM (Prieto Katunaric, 2009). The amount of interstellar medium which is swept up by each SNe event, $m_{\rm ISM}$ is uncertain. We vary between $100 - 1000\,{\rm M}_\odot$ as suggested by Gall et al. (2011) and Dwek et al. (2011) respectively. This parameter can be adjusted to account for different efficiencies of dust destruction.

4.4.5 GRAIN GROWTH

Unlike SNe shocks, grain growth in the ISM increases the dust mass of a galaxy. Grain growth itself can be split into two distinct processes: coagulation and accretion. Coagulation is the sticking together of pre-existing dust grains in the ISM, into one larger dust grain. While coagulation changes the physical dust properties such as dust grain size, it does not cause a net increase in the mass of dust present in a galaxy. Accretion is the process of metals condensing onto dust grains in the ISM, resulting in an increase in the dust mass of a galaxy. Since Equation 4.19 models the change in dust mass, we are only interested here in the process of dust grain accretion.

Dust grain growth has been predicted to occur under suitable conditions in the ISM of a galaxy for many years. Work by Dwek & Scalo (1980) suggested that

interstellar dust grains may undergo accretion if the environment is cold and dense enough, such as within a giant molecular cloud. Direct evidence of grain growth remains hard to obtain, however there is significant indirect evidence which hints to its importance in the assembly of dust in galaxies. Recent work highlights the inadequacy of stellar sources alone to produce the observed dust mass in galaxies (Draine, 2009; Dunne et al., 2011; Gall et al., 2011; Boyer et al., 2012; Asano et al., 2013). In the absence of other potential sources of dust mass, grain growth could prove to be the missing link in understanding how galaxies obtained their dust masses.

In the model, we implement the grain growth prescription of Mattsson & Andersen (2012):

$$\tau_{\rm grow} = \tau_0 (1 - \frac{\eta_d}{Z})^{-1} \tag{4.31}$$

where $\tau_{\rm grow}$ is the timescale of dust grain growth in the ISM, $\eta_{\rm d}$ is the dust to gas ratio and Z is the metallicity. τ_0 is given by:

$$\tau_0 = \frac{\langle m_{\rm gr} \rangle d_{\rm c}}{f_{\rm s} \pi a^2 Z \Sigma_{\rm mol} \langle v_{\rm g} \rangle} \tag{4.32}$$

$\langle m_{\rm gr} \rangle$ is the mean mass of dust grains in the ISM, $d_{\rm c}$ is the size of the molecular cloud in which the process of dust grain growth is occurring. $f_{\rm s}$ is the sticking coefficient, which is the probability that upon collision an atom will stick to the dust grain. a is the typical dust grain radius, and $\Sigma_{\rm mol}$ is the surface density of the molecular gas cloud. Finally, $\langle v_{\rm g} \rangle$ is the mean thermal speed of the gas particles. Making the assumption that the typical dust grain radius does not vary significantly, and that the the mean thermal speed is roughly constant (since grain growth will only occur in specific conditions). We also assume that $\Sigma_{\rm mol} \approx \Sigma_{\rm H2}$ which traces the star formation rate of the galaxy:

$$\Sigma_{\rm H2} \propto \psi(t) \tag{4.33}$$

with these assumptions, the equation for τ_0 becomes (from Mattsson & Andersen 2012):

$$\tau_0 = \frac{M_{\rm g}}{\epsilon Z \psi(t)} \tag{4.34}$$

where ϵ is a constant, free parameter, which can be used to vary the default rate of grain growth in the calculations. There are several works in the literature which incorporate dust grain growth in their calculations when modelling the chemical evolution of a galaxy, and there is some variation around what timescale dust grain

growth should act over. Hirashita (2000) calculate dust grain growth timescales in a range of physical environments. They show that the timescale will be dependent on gas density, since a denser environment will make it easier for metals to accrete onto the surface of dust grains. In molecular clouds dust grain growth is the dominant source of dust mass. Typical dust growth timescales used in the work are in the range of $10^7 - 10^8$ years.

Asano et al. (2013) use a fiducial value of 4.0×10^5 years for the timescale of dust grain growth. This value rises up to 10^8 years for lower metallicity environments ($\sim 0.2\,Z_\odot$). The effect of metallicity evolution is included in their work, and this has a direct effect on the time at which grain growth becomes the dominant source of dust mass in the galaxy. Mattsson & Andersen (2012) investigate the effect of changing the default timescale of grain growth, stating that ϵ has a range of possible numerical values, depending on the assumptions of the physical environment in the galaxy. A value of $\epsilon \approx 2$ results in grain growth timescales of the order of a Gyr. However larger epsilon values of 2×10^4 leads to grain growth timescales which are significantly shorter at around $\tau \approx 1 \times 10^6$ years. Therefore a range of values for ϵ can be used to match the full range of grain growth timescales used in the literature.

Finally, in low metallicity environments, such as dwarf galaxies, a significant amount of time (up to 1 Gyr) may need to pass prior to grain growth becoming a significant factor in the evolution of a galaxy Zhukovska (2014). However, when the metallicity reaches a level which supports grain growth (which can be as high as $Z = 0.014$ for the Milky Way), the rate of grain growth may be enhanced. This is due primarily to an abundance of small dust grains, for which dust grain growth is known to occur more rapidly Hirashita & Kuo (2011). Typical dust grain growth timescales for these galaxies are $10^6 - 10^7$ years. We note also that there was a mistake in the original Rowlands et al. (2014) code where incorrect units were used for the grain growth timescale. This was fixed in the Python routine developed here.

4.5 CONCLUSION

In this chapter we have introduced the basic chemical evolution model which will be used to investigate samples of galaxies in later chapters. We have explored the various elements which contribute to this model. We have revised and updated several features of the code, in line with current research in the various fields and corrected mistakes in previous versions of the code. The final Python code, which is available for download for free from GITHUB [2], varies from the Fortran code used

[2] https://github.com/zemogle/chemevol

in Morgan & Edmunds (2003) and Rowlands et al. (2014), and other models in the literature used in in the following ways.

- We no longer interpolate the stellar yields from stars of a given mass, but rather choose the nearest neighbour value. We have seen that this has a small effect on the resulting stellar yields (Section 4.4.2.2).

- The dust mass yields for high mass stars ($8.5 < M_i \leq 40$) have been updated, such that they are now directly input from Todini & Ferrara (2001). Previously, Rowlands et al. (2014) used the dust masses from Todini & Ferrara (2001) to estimate a condensation efficiency for SN dust (δ_{SN}), which they then applied to the metal yields from Maeder (1992). We have shown that using the dust yields directly from Todini & Ferrara (2001) reduces the dust mass by a factor of ~ 1.8 for a Milky Way-like galaxy at early times ($< 0.8\,\mathrm{Gyr}$) compared to the method used in Rowlands et al. (2014).

- We have updated the remnant mass function to that of Ferreras & Silk (2000) (see Section 4.4.3) to account for more recent models in the literature of mass loss and stellar evolution. This produces more interstellar material compared to previous works. Secondly, we have considered that stars with initial mass $> 40\,M_\odot$ form a black hole at the end of their lives, and do not contribute any gas or metals into the ISM at this stage. However, these stars will still lose gas and metals over their lifetime in stellar winds, and this mass loss contributes to the enrichment of the ISM.

- We have corrected two errors in Rowlands et al. (2014) including (i) in the original code, high mass stars were not contributing to the metal mass at times $> 0.6\,\mathrm{Gyrs}$ and (ii) errors in the grain growth timescales.

- We also include prescriptions for dust grain growth and dust destruction, and include an additional cold gas fraction term (f_c) to the model to account for grain growth in cold dense regions of the ISM, and higher efficiency of dust destruction by SNe shocks in the warm and diffuse ISM.

In the next chapter we show how the dust mass of a galaxy evolves using fiducial galaxy models to illustrate how the dust, stars and gas properties vary over time.

Chapter 5
Chemical Model II: results from using fiducial galaxies

5.1 Introduction

We introduced the range of libraries, values and inputs which must be included with the equations presented in Chapter 4 to produce the full model of chemical evolution for the galaxies. In this chapter we turn instead to investigating what effect our various choices have on the results, such that when we use the model and compare with observed galaxy samples later on, we are already aware of the bias that our chosen inputs have on the findings.

5.2 Star Formation History

To understand more about the properties of the galaxies and to investigate their dust content, it is necessary to parametrize the star formation history such that it can be included in the chemical evolution models, here we use fiducial SFHs to test our model. The classical way of doing this is to describe the star formation history as some standard function (Morgan & Edmunds, 2003). Typically, standard models may be of the form:

1. A Milky Way type SFH, which decreases exponentially with time:

$$\psi(t) \propto \exp\left(-\frac{t}{\tau}\right) \tag{5.1}$$

2. A smooth, increasing SFH, which rises exponentially with time:

$$\psi(t) \propto \exp\left(\frac{t}{\tau}\right) \tag{5.2}$$

3. A delayed SFH, for which star formation begins rises slowly and then falls off exponentially with time (Lee, 2010). This has the form:

$$\frac{t}{\tau^2} \times \exp\left(-\frac{t}{\tau}\right) \tag{5.3}$$

4. A smooth, declining SFH, with a significant burst of star formation superimposed partway through the evolution.

In the above equations, τ is a delay constant, which is used to vary the timescale of the exponential decrease in star formation. These templates cover a diverse range of possible histories, and will help to demonstrate the effect the SFH has on the physical properties of a galaxy. This set of standard SFHs is shown in Figure 5.1. The SFHs have been normalised to create the same total stellar mass at the end of the duration, which is set to an arbitrary 3.3 Gyr.

To realistically compute the chemical evolution of these galaxies one ideally would wish to have individual SFHs that are consistent with the photometric observations of the galaxy sample (eg SED fitting) or spectral analysis (see Rowlands et al. 2014). The code which is produced here allows the user to apply a SFH file (t, SFR) when computing the evolution of a galaxy.

5.2.1 DUST PRODUCTION OF DIFFERENT INITIAL MASS FUNCTIONS

In this section, we wish to further investigate how the choice of stellar IMF can affect the amount of dust which is produced when modelling a galaxy. In Figure 5.2 we show the amount of dust produced for the range of IMFs from Section 4.4.1, using a Milky Way type SFH (Figure 5.1) with an initial gas mass of $4 \times 10^{10}\,\mathrm{M}_{\odot}$. We used a closed box, with no dust destruction or grain growth, since we are investigating the total amount of dust which can be produced from stellar sources. The Chabrier IMF produces considerably more dust than the other IMFs, with the peak mass being approximately twice the peak dust mass created by the Salpeter IMF and four times more than the Scalo IMF. This is due to the increased fraction of high mass stars which are created by the Chabrier IMF. We can also see from Figure 5.2 that the evolution of the galaxy carries on to a much later time. The reason for this is that

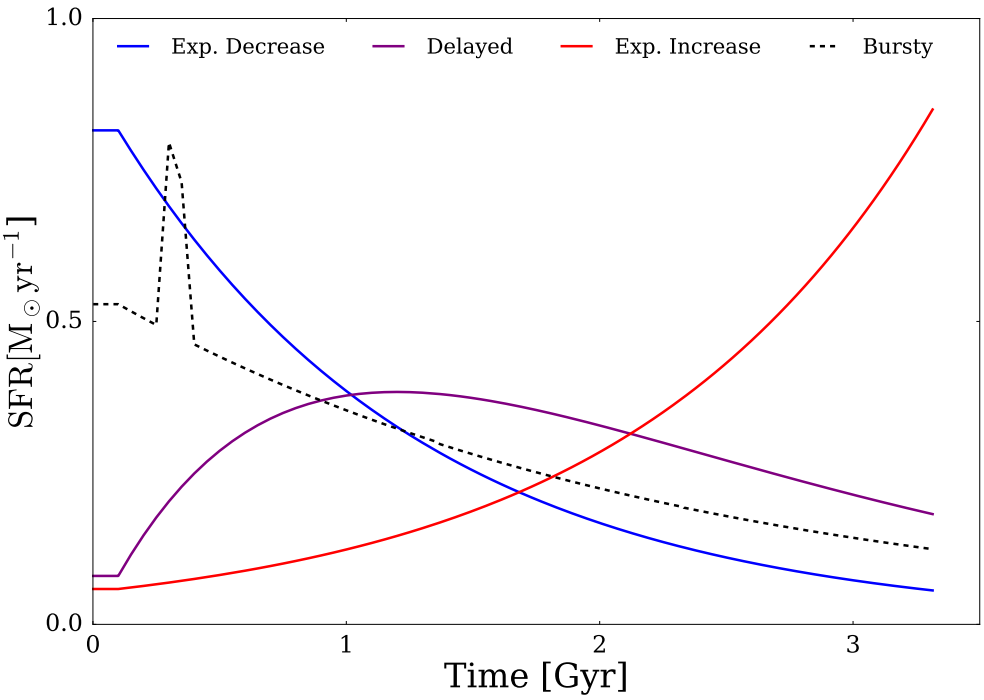

Figure 5.1 Different 'fiducial' SFHs used to investigate the effect that the SFH has on the dust and metal content of a galaxy in this chapter. The blue and red lines show an exponentially increasing and decreasing SFH respectively. The dashed black line shows a exponentially declining SFH, with a single burst of SFH superimposed. The purple line shows a delayed SFH model, the functional form of which is given in the text (Equation 5.3). The SFHs have been normalised to the same length, and to produce the same total stellar mass over their duration.

the gas return fraction is higher for the Chabrier IMF due to the increased number of high mass stars, and therefore ejected gas. Only a small fraction of the gas used for star formation is locked up in stars, due to the reduced number of low mass stars. In the Scalo IMF, more gas is locked up in low mass stars for a given quantity of star formation, so the gas fraction of the galaxy rapidly decreases.

Figure 5.2 also shows the dust mass production for the same galaxy, plotted against gas fraction. Here we can see that the maximum dust mass is reached at approximately the same gas fraction for each IMF, even though the different IMFs produce a different quantity of dust. If given a sufficiently long time to evolve, then the Chabrier IMF would also reach a zero dust mass, when the gas fraction reaches zero.

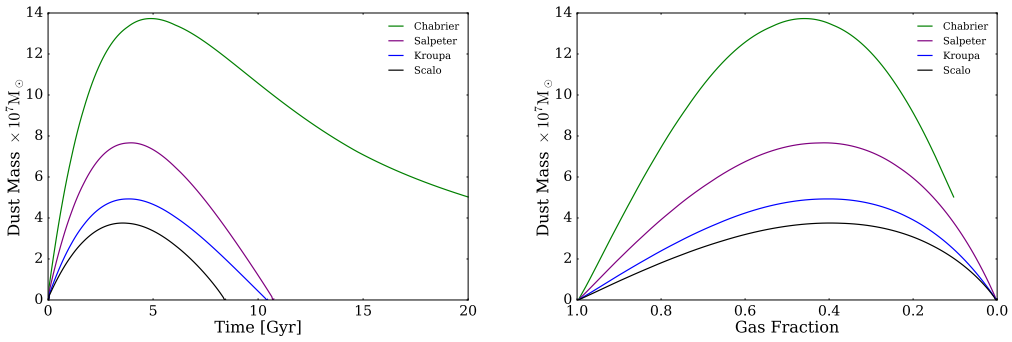

FIGURE 5.2 *Left:* The dust mass production from different stellar IMFs present in the literature (see Section 4.4.1). Variations in the dust mass production are caused by a change in the rate of SNe, which is dependent on the relative number of high mass stars produced. The models were calculated using an initial gas mass of $4 \times 10^{10}\,\mathrm{M}_{\odot}$, with a predetermined Milky Way SFH with $\tau = 6.6\,\mathrm{Gyr}$ from Yin et al. (2009). Gas depletion occurs on much shorter time-scales for the Scalo IMF (shown in black) compared to the Chabrier IMF (shown in green), since more gas is locked up in low mass stars for Scalo. The choice of IMF does not seem to effect the time at which the peak dust mass of a galaxy occurs. *Right:* Dust mass produced from different IMFs against gas fraction. Here we can see that maximum dust mass is reached around a gas fraction of 0.4 for all IMFs (although it is fractionally lower for the Kroupa and Scalo IMF). The Chabrier IMF fails to deplete all the gas reservoir prior to the end of the SFH for this galaxy. At every gas fraction, the IMFs which create fewer low mass stars have more dust than those which are biased towards low mass star production.

5.2.2 DUST PRODUCTION AND STELLAR LIFETIME

In the early stages of the evolution of a galaxy, the lifetime of LIMS may exceed the current age of the galaxy. These stars may therefore not be able to contribute to the dust budget within a galaxy at early times. This is important since many studies have found the presence of significant quantities of dust in high redshift galaxies. For example, Watson et al. (2015) found a galaxy located at $z > 7$, with $2 \times 10^{7}\,\mathrm{M}_{\odot}$ of dust. The dust budget crisis is made worse at high redshift, simply because there has been less time for the stars in the galaxy to evolve. In Figure 5.3 we show the theoretical lifetime of stars, against stellar mass in our model. The red line shows the location of an $8\,\mathrm{M}_{\odot}$ star on this plot, and this indicates the earliest time at which LIMS could start to contribute to the dust budget of a galaxy. We find that before a time of $\approx 0.04\,\mathrm{Gyr}$ since the onset of star formation in a galaxy, all the dust must be produced by high mass stars. At $z > 7$, approximately 500 million years after the first onset of star formation (Richard et al., 2011), only stars of mass $> 4\,\mathrm{M}_{\odot}$ can contribute to the dust budget (indicated by the blue line).

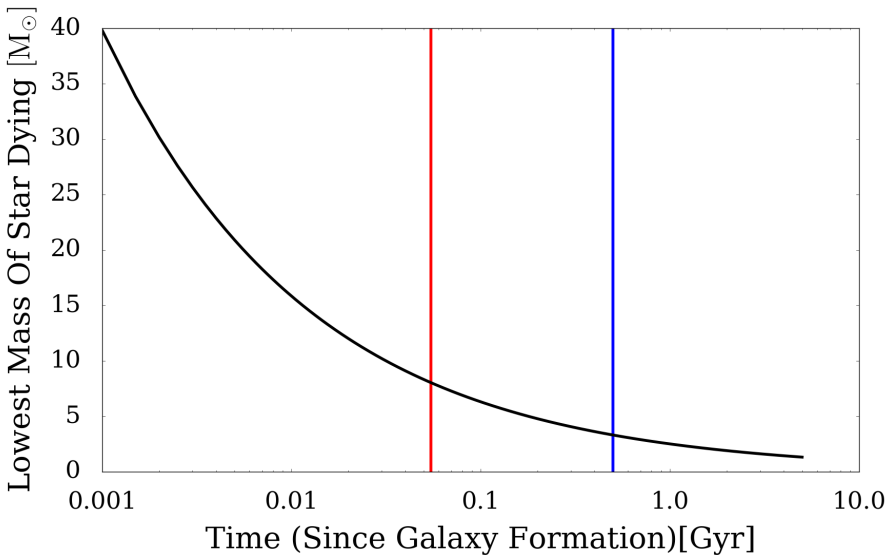

Figure 5.3 The lowest mass of star that can contribute to the dust budget over the lifetime of a galaxy. The red line indicates the lifetime of an $8\,M_\odot$ star ($\approx 0.04\,Gyr$). We assume that the first galaxies formed 200 million years after the Big Bang (Richard et al., 2011). The blue line indicates 700 million years after the Big Bang (500 million through the lifetime of the first galaxies); this is the time at which Watson et al. (2015) observed $2 \times 10^7\,M_\odot$ of dust to have formed.

5.2.3 Metal Production of Different Initial Mass Functions

Different IMFs change the balance of high mass to low mass stars which a galaxy produces, and therefore can change many aspects of the chemical evolution of a galaxy. One of these is the metal yield of the galaxy, which is how many metals the galaxy will produce over a given amount of time. High mass stars have a much higher metal yield than low mass stars, since they are able to fuse hydrogen in multiple shells around the core, and the temperatures reached are high enough to produce heavier elements. Therefore, an IMF which is top heavy will produce more metals when compared to a bottom heavy IMF. Also, a greater fraction of these metals will be located in the ISM of the galaxy, rather than being locked up in long lived low mass stars. In Figure 5.4 we compare the metal yields of the different IMFs from Section 4.4.1, plotting the gaseous metal fraction ($Z \times M_g/M_{tot}$) against gas fraction. We compare the top heavy Chabrier (2003) IMF against the bottom light Salpeter IMF. For every gas fraction, the Chabrier IMF produces more metals than Salpeter. This is an important consideration when we are choosing an IMF to use with the chemical evolution model. The analytic model shown in red (with $p = 0.048$,

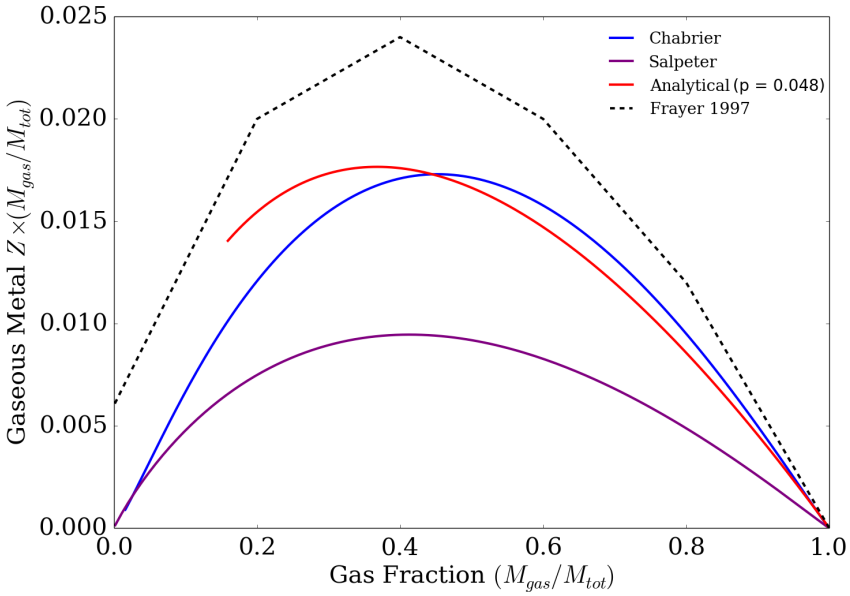

FIGURE 5.4 The gaseous metal fraction, against gas fraction, for a Milky Way type SFH. Different tracks show the metals produced by a range of stellar IMFs, and demonstrate that the highest metal mass is produced by IMFs weighted towards high mass stars, where fewer low mass stars are formed. The analytical model (red line) is simply from Equation 4.9 with $p = 0.048$.

to match the Chabrier IMF) shows good agreement with the results from the full model, although variations between the models increase at low gas fractions. As a sanity check on the evolution of metals with gas fraction, we also compare the results from our model with the results from Frayer & Brown (1997). We find generally good agreement with our model, with the maximum value of $Z \times M_{\rm g}/M_{\rm tot}$ at a gas fraction of $\sim 0.4 - 0.5$.

Figure 5.5 also demonstrates this, by comparing the evolution of metals (12 + log(O/H) against gas fraction. Here we again compare the metals produced by the Chabrier and Salpeter IMFs, but also directly compare with the analytic solutions for these IMFs. Using a p value of 0.048 we can see there is good agreement between the Chabrier IMF and the corresponding analytic solution, although variations can be seen at low gas fractions. This is the region where the assumptions which form the bases of the simple model start to deviate from more detailed calculations (see Section 4.2 for details). The analytic model with a p value of 0.010 corresponds to a model with a small return fraction, so more mass remains locked up in low mass stars. This value is more appropriate for describing a Salpeter IMF, and we can see that it produces significantly less metal than the other IMFs.

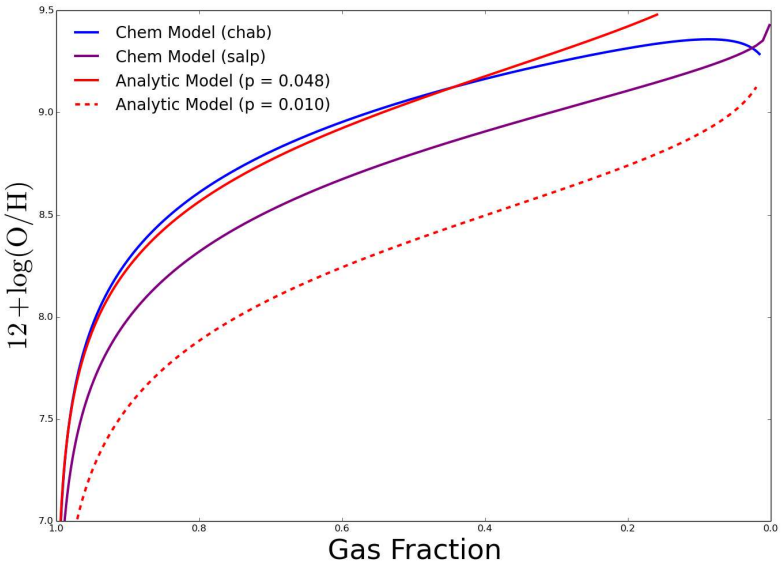

Figure 5.5 Comparison of metallicity (12+log(O/H)) against gas fraction. We see a similar result to Figure 5.4, that is the top heavy IMFs produce more metals. The blue line shows the calculation using a Chabrier IMF and purple line shows the result for the Salpeter IMF. Two models calculated using the analytic solution (with p = 0.01 and 0.048) are also shown for comparison, they diverge from the full integrals at low gas fractions.

5.2.4 Understanding the Evolution of Dust Mass with Gas Fraction

In Figure 5.6 we can see the comparison between the dust mass and gas mass of a galaxy over the evolution of that galaxy, where the dust mass is shown by the red line, and the gas mass is shown in black. For this calculation, we use a Milky Way SFH with initial gas mass of $4 \times 10^{10}\,M_{\odot}$ and a Chabrier IMF. Initially, the gas comprises the full mass of the galaxy, and there is no dust (corresponding to a gas fraction 1.0). Then, following the onset of star formation, the gas mass of the galaxy starts to decrease. At this time, the dust mass of the galaxy rapidly increases, because the high star formation rate produces a large quantity of high mass stars, which very rapidly enrich the ISM. Also, at this time the dust astration is almost zero, since there is little dust in the galaxy.

At a gas fraction of 0.8, where the star formation rate is decreasing, there is a plateau in the dust mass of the galaxy. The reason for this is two fold: firstly with the lower star formation rate there are less high mass stars to produce new dust, and secondly the dust astration will have increased, because now there is a significant

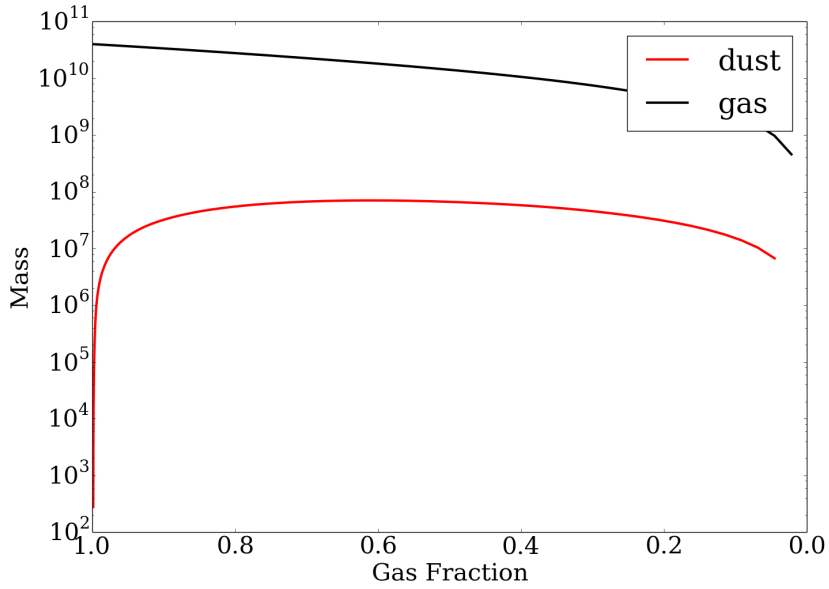

FIGURE 5.6 The dust mass (red) and gas mass (black) in a Milky Way type galaxy against gas fraction. The dust mass rises quickly (in terms of gas fraction)to a maximum around a gas fraction of 0.70, while the gas mass declines as stars are being created.

amount of dust present in the ISM of the galaxy. Past a gas fraction of 0.6, the dust mass of the galaxy starts to decline, although not as rapidly as the gas fraction, since LIMS which formed at higher gas fractions are now producing their dust yield, which is buffering against the astration from the current star formation.

5.2.5 COMPARING THE DUST PRODUCTION OF HIGH AND LOW MASS STARS

In this section, we are concerned with the relative contribution of low and high mass stars tot he dust budget of a galaxy, and how this changes as the galaxy evolves. Figure 5.7 shows the total dust mass produced by a stars of different mass at a given stage in the lifetime of the galaxy. The top panel shows the galaxy 0.25 Gyr into its evolution, and the insert shows that this is just before a significant burst of star formation occurs. The blue portion of the histogram shows the dust yield by stars of mass greater than $8\,M_{\odot}$, these are the stars which produce dust from supernova. The red portion of the histogram shows the dust produced by stars less than $8\,M_{\odot}$, these are the LIMS and produce most of their dust by stellar winds at the end of their lifetime. We can see that at this early stage in the evolution of the galaxy, the dust mass is almost entirely produced by the high mass stars. This is mostly due to

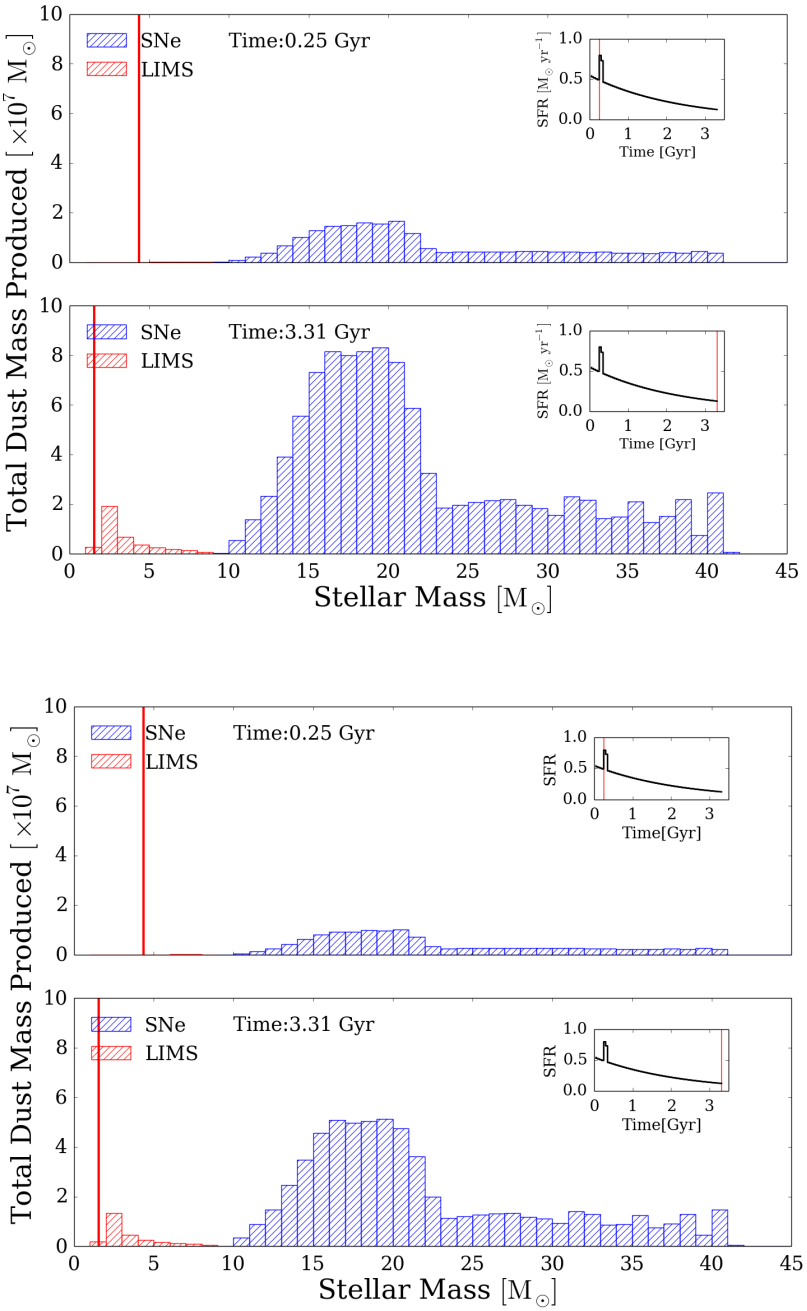

Figure 5.7 *Top Figure:* Here we show the total dust mass contribution of different mass stars over the evolution of a galaxy. The top and bottom plot show snapshots of the galaxy at 0.25 Gyr and 3.31 Gyr after the onset of star formation (with the SFH shown inset), respectively. The contribution of high mass stars is shown in blue while dust from LIMS ($< 8\,M_\odot$) is shown in red. The red vertical line on the inset shows the corresponding position in the SFH of the galaxy. The vertical red line in the main plot highlights the lowest mass of star which can contribute to the dust budget at that time. For the Chabrier IMF used in this calculation, we find that the dust from high mass stars dominates the dust budget of the galaxy at all stages of the evolution. *Bottom:* Similar to above, using a Kroupa IMF for the calculation. The Kroupa IMF is weighted more strongly towards lower mass stars, and therefore we should see a stronger contribution to the dust budget by these stars relative to the Chabrier IMF.

the fact that the LIMS have much longer stellar lifetimes and therefore require more time before they start producing significant quantities of dust. The red line on the plot indicates the lowest mass of star which could be contributing to the dust budget at the current stage in the evolution of the galaxy.

The lower panel in Figure 5.7 shows the same galaxy towards the end of the SFH, 3.31 Gyr since the start of star formation. The red line shows that now most stars can contribute to the dust budget within a galaxy. The dust produced by high mass stars still dominates the dust production, with stars of mass $15 - 20\,M_{\odot}$ having the largest contribution. For this galaxy, we can see that if the dust was only produced by LIMS then the galaxy would have significantly less dust. It is worth noting that the high mass stars dominate the dust budget, while being less numerous than the LIMS. This calculation considers only the total amount of dust which is produced by stars of each mass, and does not consider dust destruction, which would reduce the effective contribution of the high mass stars to the dust budget. The Chabrier IMF used to model the galaxy is biased towards high mass stars, and so therefore we expect that this could explain why these stars contribute so heavily to the dust budget. The lower two plots in Figure 5.7 shows the same calculation, but using a Salpeter IMF. We find that while the contribution of high mass stars has been reduced relative to the Chabrier IMF, these stars still dominate the dust production in the galaxy.

Figure 5.8 (top) lets us look at this in more detail. Here the mass ratio of dust produced and gas returned is shown, against gas fraction. This calculation does not include inflows or outflows of gas, and dust production is limited to stellar sources. When stars form, they remove gas from the interstellar medium, so provide a gas sink. At the end of the stars life, a certain fraction of the initial gas that was locked up is returned to the interstellar medium. Initially the dust created spikes to a high level, and then rapidly falls into a steady decline by gas fraction 0.8. To understand why this is so, we need to consider the independent dust sources in more detail. This is shown for low and high mass stars in the bottom plot of Figure 5.8. The track for high mass stars, shown in blue, traces very closely the track seen in Figure 5.8 (top). High mass stars produce lots of dust initially; since they are short lived their dust production is linked very closely to the star formation rate. Hence, when the star formation rate is high, at high gas fractions in this case, they produce lots of dust. When the the star formation rate falls so does their dust production, as is seen at low gas fractions.

The track for dust production from low mass stars (red) shows us a different trend. The dust production is low initially, since few of the low mass stars created will have evolved to a stage where they can contribute to the dust budget. The dust

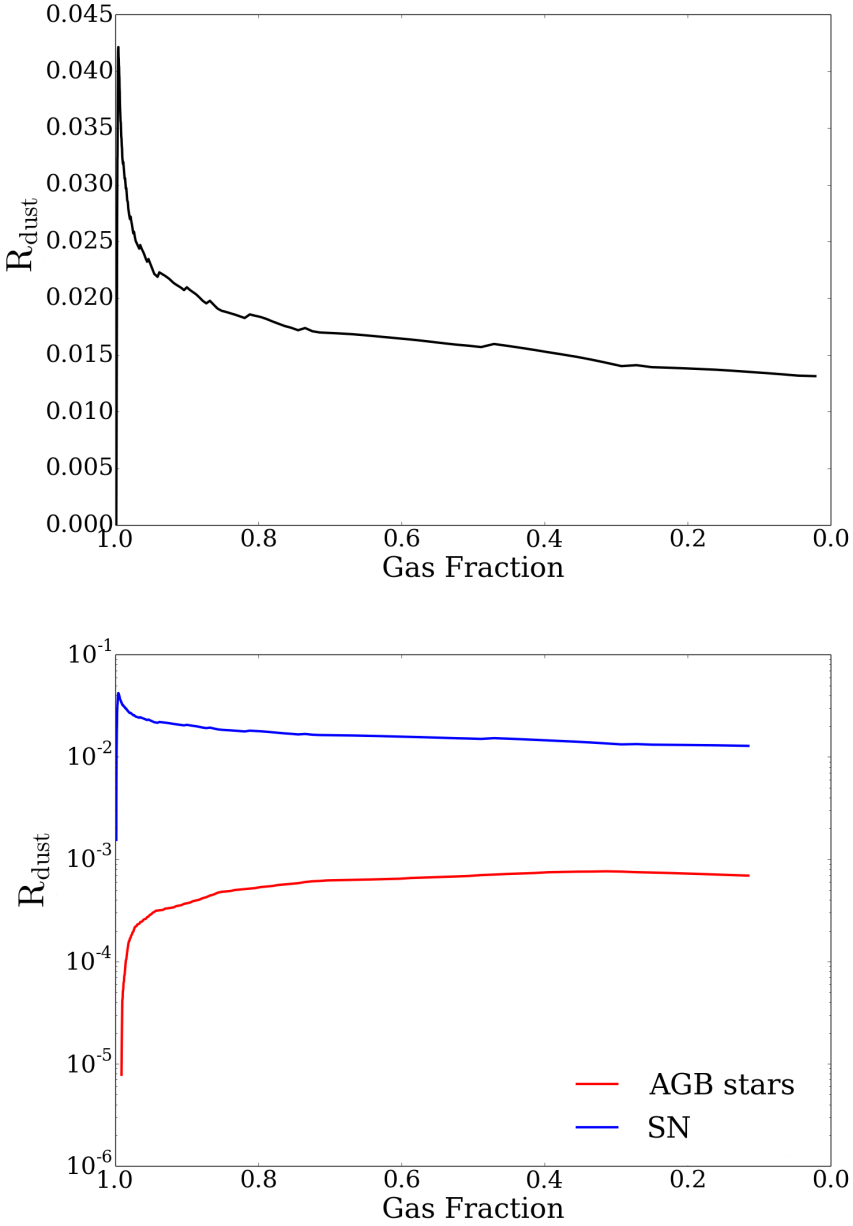

Figure 5.8 *Top:* The ratio of freshly formed dust, normalised by the returned gas from stars (defined here as R_{dust}), in a Milky Way type galaxy as the gas fraction declines. The freshly formed dust comes from stellar sources (both low mass and high mass stars), while the gas comes from the gas returned to the interstellar medium upon the death of a star. *Bottom:* Now split into the two separate dust sources. Dust production by high mass stars is shown in blue, whereas the dust production from low mass stars is shown in red. The dust production from high mass stars dominates the total production, so shows a similar trend to that seen for total dust. The dust from low mass stars is delayed from the onset of star formation, so R_{dust} for these stars is at small at high gas fractions.

production from low mass stars continues to rise against the gas production, as the galaxy evolves to low redshift. This is because the gas production is dominated by the death of high mass stars (linked to the current star formation rate) which is low, while the dust production from low mass stars is linked to the higher star formation rate at the time they formed. The overall trend seen in Figure 5.8 (top) is seen because the dust production is dominated by the high mass stars. If the contribution from low mass stars was higher, then we would see an increase in the total dust production with gas fraction.

5.3 CONCLUSION

In this chapter we have shown how the dust mass of a galaxy evolves using fiducial galaxy models to illustrate how the dust, stars and gas properties vary over time. This includes modelling the dust mass from different fiducial star formation histories and initial mass functions, and illustrating how the results from the full chemical model evolves. Particularly, this allows us to illustrate how the inputs and parameters in Chapter 4 affect the dust and metal yields which are obtained when modelling a galaxy. We have also seen how the relative contribution of the different dust sources and sinks changes over the lifetime of a galaxy. In the final chapter of this thesis, we will apply this model to observations of the nearby galaxies introduced in Chapter 2 to investigate dust sources and galaxy evolution.

Chapter 6
Chemical Evolution of HAPLESS and HIGH

6.1 Introduction

As discussed in Chapter 2, the HAPLESS and HiGH samples allow us to study dust, gas, SFRs and metallicities since when combined with the largest local *Herschel* study of the nearby galaxies, the Herschel Reference Survey (Boselli et al., 2012), these three samples together cover a wide range of gas fraction ($0.05 < f_g < 0.97$). Assuming that the gas fraction can be a proxy for how evolved a galaxy is (eg as a measure of how much of the available gas reservoir has been converted into stars as originally shown in Clark et al. 2015), this provides an opportunity to model the evolution of dust, metals, stars and gas content as galaxies consume their gas into stars and evolve from gas-rich to gas-poor.

In Clark et al. (2015), we attempted to use a simple closed box chemical evolution model to interpret the dust properties of nearby galaxies as observed with *Herschel*, including the dust-selected HAPLESS and stellar-selected HRS sources. To do this, we assumed a Chabrier (2003) IMF and different star formation histories including an exponentially declining function and a SFH with a superimposed burst. This simple model (which I produced) was used to explain our results in the following manner: as galaxies evolve, their dust content first rises steeply, then levels off and reaches its peak about half way through its evolution. The dust content starts declining towards lower gas fractions as more dust is destroyed/consumed than produced. Clark et al. (2015) used our model to provide further evidence that significant quantities of SNe dust (as well as dust from LIMS) must be included otherwise the model cannot account for the dust scaling relations in the dust-selected sample (as

also seen in eg Morgan et al., 2003; Matsuura et al., 2009; Dunne et al., 2011; Gall et al., 2011; Rowlands et al., 2014). However, the HI selected sample of DV16 (the so called HIGH sample, see also Chapter 2), particularly the low stellar mass sources, appear to be offset from this simple evolutionary scenario with low dust-to-gas ratios for the same gas fractions. In this chapter we attempt to explore why these lie offset.

Combining dust-to-gas observations with metallicity information can also provide a way to discriminate between different chemical evolution models (Edmunds, 2001; Dwek, 1998). The dust to gas ratio of Milky Way-type, metal-rich galaxies, appears to scale with metallicity (Z, eg Dwek, 1998). This suggests a constant dust-to-metal ratio in galaxies, with various literature studies quoting values averaging 0.5 ± 0.1 (see Clark, Schofield et al. (2016), Chapter 1) ie half of the metals in galaxies are locked up in dust grains. In low stellar mass galaxies, the dust-to-gas ratios are observed to be somewhat lower than expected at low metallicities (Lisenfeld & Ferrara, 1998; Galliano et al., 2011; Herrera-Camus et al., 2012; Fisher et al., 2014; Rémy-Ruyer et al., 2013, 2015) though these works are hampered by low statistics and (until very recently) lack of observations in the FIR/sub-mm. Zhukovska (2014) compared the largest sample of 48 low metallicity sources surveyed with *Herschel* with a chemical evolution model to show that the observed variation in dust-to-gas ratio and metallicity in local star-forming dwarfs can be explained using models with bursty star formation histories, low dust yields from core-collapse SNe and additional grain growth in the ISM. Feldmann (2015) took the sample from Rémy-Ruyer et al. (2015) and used both an analytic approximation and dynamic one-zone chemical evolution models to fit the observed trends in 126 local galaxies with metallicities $\sim 12 + \log(\mathrm{O/H}) = 7.2$ to $\sim 12 + \log(\mathrm{O/H}) = 9.2$. Their models require very rapid grain growth, which activates at a critical metallicity, to match the observed dust-to-metal ratio in the galaxies. Feldmann (2015) also argues that there is a balance between metal-poor inflows and enriched outflows which regulates the dust-to-metal ratio. While outflows remove dust and metals from the galaxy, it is thought to be inflows which dilute the metal content of the ISM and keep the galaxy from reaching the critical metallicity (and thus maintain a low dust-to-metal ratio for longer).

In this chapter, we add information from other published *Herschel* surveys to the HIGH and HAPLESS samples from Chapter 4, with additional metallicity data provided by De Vis et al (priv. comm., PhD Thesis 2016) to investigate the dust-to-gas and dust-to-metals properties of 425 local galaxies, the largest sample studied to date over such a wide metallicity range. We are particularly interested in trying to determine the contribution from different dust sources and to explain the dust-poor, gas-rich sample seen in the HI selected sample from DV16. The chemical evolution

model from Chapter 4 is applied, as was originally done in C15. However, instead of assuming a somewhat unrealistic simple closed box model, in this chapter we change the following parameters: dust sources, inflows and outflows, SFHs, rate of grain growth in the ISM, rate of dust destruction, and a changing IMF. In this chapter, we choose to use a set of fiducial SFHs to represent the galaxies in our sample; we do this because we have shown in Chapter 2 that it is difficult to uniquely constrain the SFH of individual galaxies using MAGPHYS. Rather we choose a representative range of SFHs (see Section 6.3) which enable us to investigate the contribution from different dust sources during the evolution of the galaxies. In Section 6.2, the ancillary *Herschel* samples are briefly introduced (the HRS and the Dwarf Galaxy Survey, DGS), and we describe the methods used to ensure the different data-sets are consistent.

The results from this thesis have been published in De Vis, Schofield et al *submitted* [hereafter DVS16]. Therefore it is important to outline our roles in this work. De Vis was responsible for deriving the galaxy photometry, compiling the MAGPHYS results for the HRS and for deriving galaxy metallicities for all the samples (and indeed a comparison of different metallicity calibrations is described in DVS16, which does not appear in this thesis). I was responsible for all of the chemical evolution modelling (using the code described in Chapter 4) and the dust-to-metals comparison which will be discussed here. I also carried out the re-evaluation of dust mass for the DGS sources described in Section 6.2. Both De Vis and I were responsible in ultimately determining which models to include in the paper, and the subsequent discussion in that paper.

6.2 The Additional Herschel Samples of Galaxies

The MAGPHYS stellar masses, dust masses, gas fractions and SFRs for the HiGH, HAPLESS and HRS samples are provided in Chapter 2 (HIGH and HAPLESS) and DVS16. Here we briefly describe these samples.

6.2.1 A quasi-stellar mass selected sample

To supplement the dust and gas selected samples taken from H-ATLAS, we use the HRS (Boselli et al., 2010) to provide a (quasi) stellar mass selected sample of nearby sources. This survey targeted 323 galaxies ranging from late-type to early type sources. For consistency when comparing the three samples, DV16 derived galactic properties for HRS using the SED-fitting routine MAGPHYS on photometry from FUV to FIR wavelengths. The photometry was performed in 21 bands spanning GALEX

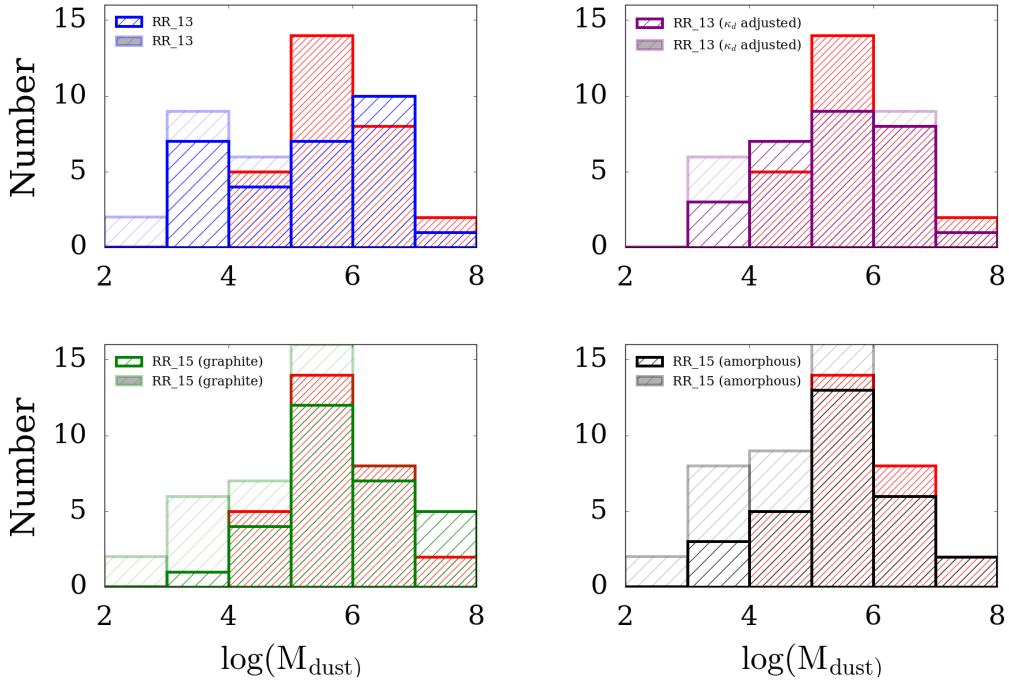

FIGURE 6.1 Comparison of the dust mass which has been derived for the DGS in this work against the dust mass published for the DGS in previous work. The dust masses which have been derived from the two-temperature blackbody fitting in this work are shown as a red histogram on each plot. These exclude the 19 galaxies which are have no detections in the SPIRE bands. *Top Left:* Comparison with unadjusted dust masses from Rémy-Ruyer et al. (2013), shown as the solid blue line. Dust masses from galaxies with only upper limits in SPIRE bands are shown as the transparent blue histogram. *Top Right:* κ_d adjusted dust masses from Rémy-Ruyer et al. (2013) shown in purple. *Bottom Left* Rémy-Ruyer et al. (2015) dust masses assuming a graphite dust grain composition (adjusted to the same κ_d as this work). *Bottom Right:* Comparison with Rémy-Ruyer et al. (2015) dust masses assuming an amorphous carbon dust grain composition (adjusted to the same κ_d as this work).

(Cortese et al., 2012), SDSS (Cortese et al., 2012), 2MASS (Skrutskie et al., 2006), *Spitzer*/IRAC (Sheth et al., 2010), WISE (Ciesla et al., 2014), *Spitzer*/MIPS (Bendo et al., 2012b), *Herschel* /PACS (Cortese et al., 2014) and *Herschel* /SPIRE (Ciesla et al., 2012). HI masses are taken from Boselli et al. (2014). For consistency, galaxy properties were derived using MAGPHYS (DV16, see also Viaene et al. 2015).

6.2.2 THE DWARF GALAXY SURVEY (DGS)

In this work, we also include results from the Dwarf Galaxy Survey (DGS; Madden et al. 2013) to improve our sampling of galaxies at the high gas fraction and low stellar mass regime. The DGS sources were selected from several other surveys

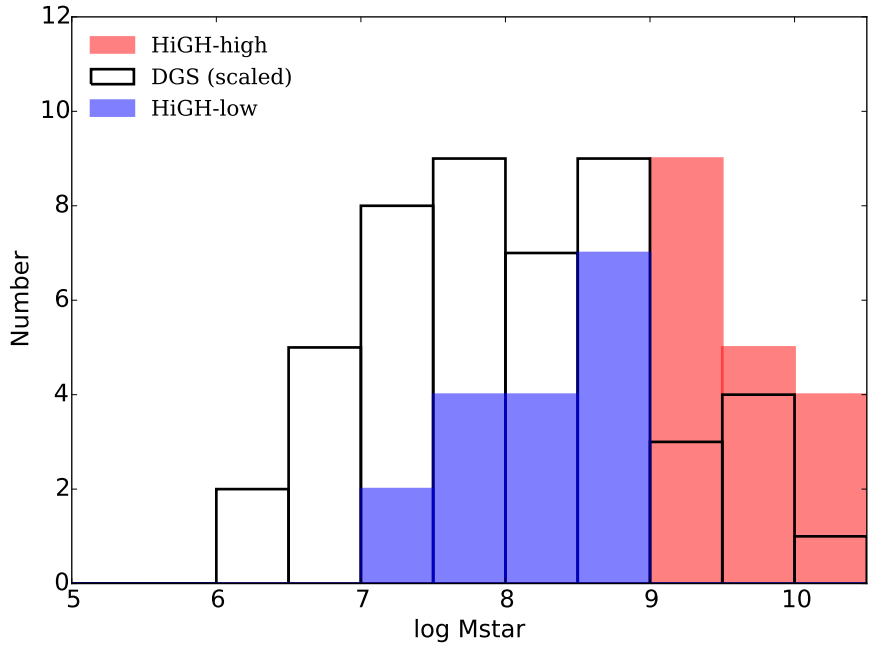

Figure 6.2 Comparison of stellar mass for the HiGH-high (red) and HiGH-low (blue) sources with DGS galaxies (black). Stellar masses were obtained from the MAGPHYS UV-submm SED-fitting routine. The DGS stellar masses from Rémy-Ruyer et al. (2013) have been scaled by a factor of 3.2 to be consistent with the MAGPHYS estimates.

in order to make a broad sample of 50 galaxies ranging from very low ($\sim 1/50\,Z_\odot$) to moderate metallicity ($\sim 1/3\,Z_\odot$). In order to compare the samples, we need consistent methods to calculate the different galactic properties. Unfortunately we do not have the same complete UV-submm coverage for DGS sources as we have available for the H-ATLAS and HRS. Consequently, we redetermined the dust properties of the DGS (following C15) using a modified blackbody (MBB) fit to the 70-500 μm photometry from Rémy-Ruyer et al. (2013, 2015). This method produces consistent results with the dust masses output by MAGPHYS (as shown in DV16), though it tends to produce lower T_d by $3-5$ K for the coldest dusty galaxies. Both methods assume the same dust absorption coefficient of $\kappa_{850} = 0.07\,m^2\,kg^{-1}$, James et al. (2002). The re-evaluated dust masses for the DGS sources in this work are higher than those presented in Rémy-Ruyer et al. (2013) (estimated using one-temperature MBB fitting known to produce lower dust masses - Bendo et al. 2015, C15) and Rémy-Ruyer et al. (2015) (based on amorphous carbon/graphite dust grains consistent with Draine & Li 2007 models).

In Figure 6.1 we compare the RR13 and RR15 (for both graphite and amorphous carbon) dust masses with the values obtained by scaling RR by the difference

in $\kappa_{\rm d}$. In this work we have calculated the dust masses from the two temperature blackbody fit only for sources with a SPIRE detection (there are 19 sources where there are only upper limits for the SPIRE bands). We conclude that the higher dust mass estimates for the DGS sources derived here are entirely consistent with scaling the Rémy-Ruyer et al. (2015) masses to the κ value used in C15 and in MAGPHYS. Therefore in what follows, we simply *scale the Rémy-Ruyer et al. (2015) dust masses for the difference in κ to be consistent across samples.*

We have also compared the DGS stellar mass estimation method (Eskew et al., 2012) to the MAGPHYS stellar masses for all the sources in our sample and found the DGS stellar masses needed to be scaled down by a factor of $\sim$3.2 to be consistent. The re-evaluated stellar masses for the DGS are compared to the HIGH properties in Figure 6.2. The stellar masses of the HIGH-low and DGS samples extend from $10^7 - 10^9$ M$_\odot$ with the latter including galaxies with M = 10^6 M$_\odot$. Despite being called dwarfs, the DGS sample also includes large stellar mass galaxies $> 10^9$ M$_\odot$, these overlap with the HIGH-high sample, HAPLESS and the HRS (for a full comparison with the HRS, we refer the reader to DV16). SFRs for the DGS are taken from Madden et al. (2013) and were estimated using (i) $L_{\rm TIR}$ (Dale & Helou, 2002) if *IRAS* or *Spitzer* data was available or (ii) determined from H$_\alpha$ or H$_\beta$ (Kennicutt, 1998). DVS16 show this method is consistent with MAGPHYS for the HRS. HI gas masses are taken from Madden et al. (2013); the average properties for all the galaxy samples used here are listed in Table 6.1.

Table 6.1 The average properties for the samples used in this work quoted as the mean of the distribution. The upper and lower bounds, indicating the range of the distribution, are obtained from the standard deviation. Where data is not available for all the sample we quote the number of sources in the brackets. We only show the late type galaxies in the HRS (LTGs).

Galaxy Sample	log SFR ($M_\odot\,yr^{-1}$)	log M_{HI} ($M_\odot$)	log M_* ($M_\odot$)	log M_d ($M_\odot$)	f_g
DGS	-0.63 ± 0.85 (45)	8.57 ± 0.78 (35)	8.10 ± 0.99	5.12 ± 1.77	0.74 ± 0.23 (35)
HiGH-low	-1.29 ± -0.48	9.02 ± 0.46	8.17 ± 0.56	5.21 ± 0.97	0.87 ± 0.09
HiGH-high	-0.14 ± 0.45	9.76 ± 0.39	9.89 ± 0.65	7.12 ± 0.43	0.50 ± 0.24
HRS (LTGs)	-0.65 ± 0.55	8.94 ± 0.56 (231)	9.64 ± 0.57	6.70 ± 0.54 (239)	0.28 ± 0.22 (231)

Table 6.2 Parameters for the different chemical evolution models used.

Name	IMF	SFH	Reduced SN dust	Destruction	Grain Growth	Inflow	Outflow
Model I	Chabrier	Milky Way	N	N	N	N	N
Model II	Chabrier	Delayed	N	N	N	N	N
Model III	Chabrier	Delayed	N	N	N	N	Y, 1.5x SFR
Model IV	Chabrier	Delayed	x6	Y, $m_{ISM} = 100$	Y, $\epsilon = 800$	Y, 1.5x SFR	Y, 1.5x SFR
Model V	Chabrier	Delayed	x12	Y, $m_{ISM} = 1000$	Y, $\epsilon = 6000$	Y, 2.0x SFR	Y, 2.0x SFR
Model VI	Chabrier	Delayed/3	x25	Y, $m_{ISM} = 100$	Y, $\epsilon = 10000$	Y, 2.0x SFR	Y, 2.0x SFR
Model VII	Chabrier	Bursty	x12	Y, $m_{ISM} = 100$	Y, $\epsilon = 10000$	Y, 6.0x SFR	Y, 6.0x SFR

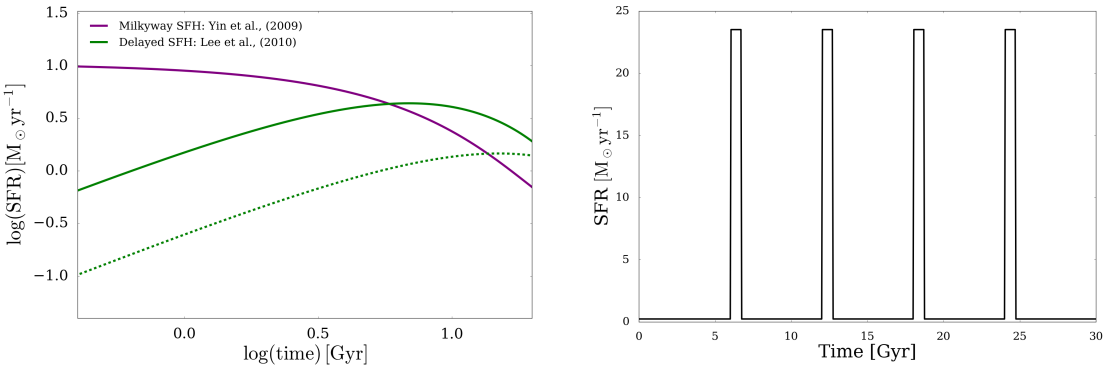

FIGURE 6.3 Star formation histories used in this work. *Left:* Model I has a SFH consistent with the Milky Way (Yin et al., 2009) and Models II-VI use a delayed SFH (Equation 6.1). *Right:* Model VII uses a bursty SFH similar to those used to model the Dwarf Galaxy Survey sources (Zhukovska, 2014).

6.2.3 AN ASIDE ON THE METALLICITIES

Integrated galaxy metallicities for the HRS are taken from (Boselli et al., 2013; Hughes et al., 2013). Fibre metallicities were determined for the HIGH and HAPLESS sources in DVS16 (priv. comm.) using SDSS and GAMA data. Many different metallicity calibrators were used to determine the metallicities of all the samples, including the oft-used Pilyugin & Thuan (2005) (PT05) and Pettini & Pagel (2004) (O3N2) methods. These were thought not to be applicable for these galaxies (see full discussion in DVS16) and instead here we include two calibrators: the N2 method (Pettini & Pagel, 2004) and Pilyugin & Grebel (2016) (PG16S) calibrators. The latter is an updated version of PT05 and is more "stable" in low metallicity regimes. We also use a TO4 metallicity calibrator derived by scaling the N2 values using the conversion in Kewley & Ellison (2008) (hereafter KE08/T04). We do this because this is a commonly used method, but the TO4 prescription is not open access. De Vis et al also re-derived the Dwarf Galaxy Survey metallicities from (Rémy-Ruyer et al., 2013) using these same calibrators.

6.3 THE CHEMICAL EVOLUTION MODELS

We test various parameter combinations in our chemical evolution model from Chapter 4 in order to interpret the observed dust, metal, gas and star formation rates of the samples. First we repeat the simple model used in C15 (parameters for this Model I are listed in Table 6.2). Next, we use different model combinations and relax the closed box assumption, including changing SFHs, IMFs, inflows, outflows

and including different dust sources (Models II-VII in Table 6.2). We have varied inflows and outflows using simple parameterisations where the rate is proportional to $N \times$ SFR and $0 < N < 6$ and different SFHs. We use four representative star formation histories (Figure 6.3) including a Milky Way-type exponentially declining SFR (Yin et al., 2009), and two delayed SFHs parameterised by Lee (2010) as

$$\mathrm{SFR}(t) \propto \frac{t}{\tau^2} e^{-t/\tau} \tag{6.1}$$

where t is the age of the galaxy, τ is the star formation timescale which is set to 6.9 Gyr to provide the best match with the observational data (see Section 6.3.3). The first delayed SFH is normalised to a peak SFR of 4.4 $\mathrm{M_\odot\,yr^{-1}}$ in order to produce the same stellar mass as the Milky Way-type SFH. The second delayed SFH is simply divided by $\sim$3. Finally, a model including a bursty SFH (Figure 6.3) similar to that used in Zhukovska (2014) to explain the SFR properties of the DGS is also used here. (Note we discuss the effect of the SFHs in Section 6.3.3).

6.3.1 The simple model in C15 and DV16

DV16 used dust and gas scaling relations to suggest that as galaxies evolve (ie their gas is consumed in forming stars), the dust content first increases (at the high gas fraction end), then reaches a peak for a gas fraction of $\sim$0.75, plateauing until $\sim$0.5. Beyond this "half way stage", the M_d/M_* decreases and $M_\mathrm{d}/M_\mathrm{g}$ increases. This can be explained as the stellar mass in a galaxy builds monotonically with time as stars are created. On the other hand, dust has a life cycle, being created, mixed in the ISM and then destroyed via astration and destruction. This causes the dust mass doubling time to be longer than the stellar mass doubling time and consequently there is a decrease in M_d/M_*. Yet, at the same time, astration always removes gas at the current $M_\mathrm{d}/M_\mathrm{g}$, and there will be some dust production associated with the stars formed from the consumed ISM. $M_\mathrm{d}/M_\mathrm{g}$ will thus increase with time as a result of astration. Even when the rate of dust destruction is greater than the rate of production, there will still be a larger rate of gas consumption and thus an increase in $M_\mathrm{d}/M_\mathrm{g}$.

Here, we repeat the comparison of our model against the data and figures shown in C15 and DV16; comparing the evolution of the dust-to-baryonic mass ratio ($M_\mathrm{d}/M_\mathrm{bary}$) with gas fraction for the different nearby galaxy samples. We do this to introduce their result (based on our modelling) that the evolution in total dust content of a galaxy changes as it evolves and the dust-selected and stellar mass-selected galaxies are well fit by a simple model of a galaxy with stardust and no inflows or outflows. As we did in those papers, we first define the baryon mass as

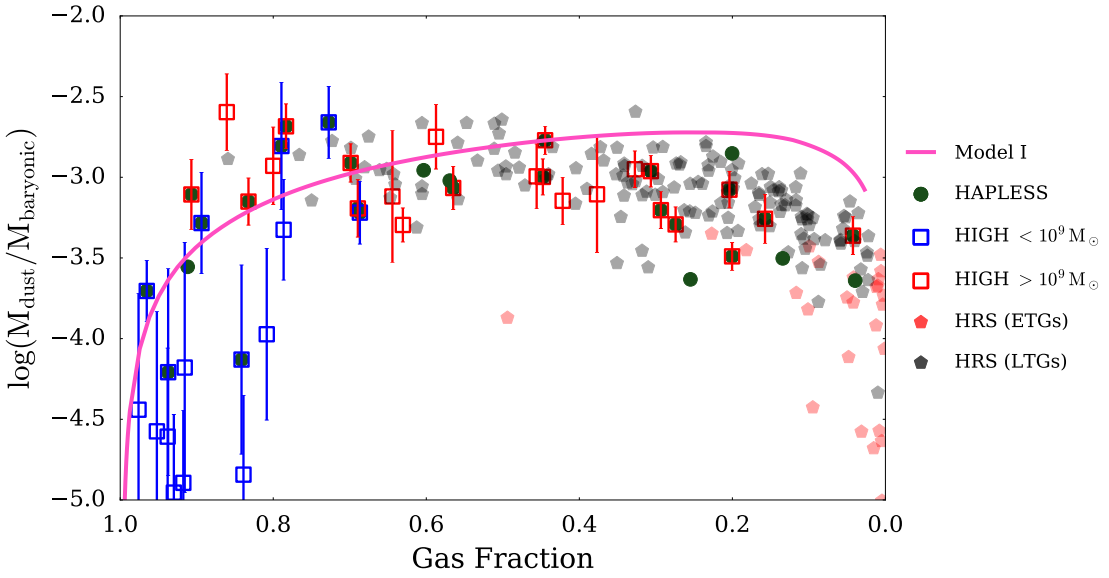

FIGURE 6.4 Variation of M_d/M_{bary} with gas fraction for different samples observed with *Herschel*, including HAPLESS, HRS and HIGH. The gas mass (and therefore gas fraction and baryonic mass) are derived using $M_g = 1.32\,M_{HI}$, not taking into account any molecular component. The dust-selected HAPLESS sample dusty galaxies with a wide range of gas fractions ($0.1 < f_g < 0.99$, C15). The quasi-stellar mass selected HRS (Boselli et al., 2010) also samples a wide range of gas fractions, but most sources tend to cluster at the low gas fraction regime (particularly the ETGs shown in red). The HI sample of DV16 (HIGH) also spans a range of gas fractions, but the low stellar mass subset shown in blue (HIGH-low) tend to have the highest gas fractions. These sources are also dust-poor compared to the prediction shown here. The solid line is a Milky Way-like closed-box chemical evolution model (Model I in Table 6.2) which is similar to the C15 and DV16 model.

$M_{bary} = M_g + M_*$, where $M_g = 1.32\,M_{HI}$ to take into account the mass of neutral helium. Due to the difficulty in obtaining homogeneous sample of CO maps for all the different samples considered here, particularly for low stellar mass sources, we do not take into account any molecular component. This assumption is sensible if the HI mass dominates the total gas mass. Indeed, to affect the subsequent discussions in this paper, the molecular mass would have to be larger than the HI mass which does not agree with the observed M_{HI}/M_{H_2} ratios for some of the sources in our sample that do have both datasets (eg Boselli et al. 2014 for the HRS galaxies). A molecular mass dominated gas component for our sources is also inconsistent with the galaxy gas-scaling laws from Saintonge et al. (2011) and Bothwell et al. (2014) for a wide range of stellar masses, these suggest that M_{H_2}/M_{bary} is small at all evolutionary phases.

When comparing all samples, it appears that M_d/M_{bary} first rises steeply,

then levels off and then drops again as galaxies evolve from high to low gas fractions. This supports the idea of the dust content being built up as galaxies move through the early stages of their evolution (at gas fractions > 0.8). The dust content then plateaus as dust destruction through astration balances the dust production. Note that the position of a galaxy in Figure 6.4 does not depend on its total mass, since both axes are normalised by M. However, on average, massive galaxies go through their evolution faster, and by the current epoch have reached lower gas fractions compared to less massive sources.

Next, in Figure 6.4, we show how the observations from the different samples compare with a chemical evolution track similar to C15 and DV16. This model uses a SFH consistent with the Milky Way (Yin et al., 2009), though here we use our updated code (Model I, Table 6.2). We see that the observed increase and decrease in $M_{\rm d}/M_{\rm bary}$ with gas fraction for the HRS, HiGH-high and HAPLESS samples is well matched within the scatter of the data, albeit with a small offset in the maximum $M_{\rm d}/M_{\rm bary}$. We note that our closed box model peaks at a lower gas fraction ($\sim$0.3) than C15/DV16 ($\sim$0.5) due to the changes made to the assumptions and dust inputs described in Chapter 4. The gas fraction at which the $M_{\rm d}/M_{\rm bary}$ ratio reaches a maximum is in fact determined by the balance of the different dust sources in the galaxy. For the simple closed box model shown in Figure 6.4 we have included only stellar dust sources, therefore it is the balance between the dust contribution of high mass stars and low mass stars which determines at what gas fraction the peak $M_{\rm d}/M_{\rm bary}$ ratio will be reached. High mass stars have short lifetimes and start to contribute dust to dust budget soon after the onset of star formation. High mass stars are therefore the dominant source of dust at high gas fractions. In contrast, low mass stars have longer lifetimes and contribute more of their dust at lower gas fractions. In our revised chemical model we have changed the contribution of SNe[1] compared to the model published in C15 and DV16. Figure 6.5 demonstrates this effect. Here we compare the evolution of the $M_{\rm d}/M_{\rm bary}$ ratio with gas fraction for the Milky Way-like model of C15/DV16 (blue curve), the full chemical model used in this work (purple curve) and three instantaneous analytical chemical models (shown by dashed lines). (Both the metal yields and the return fraction for the analytic models have been chosen to match the Chabrier IMF used in the full chemical models.)

First we compare a analytic model with equal balance between SN and LIMS dust sources ($\chi_1 = \chi_2 = 0.2$, see Equation 4.11), this closely matches the model of C15/DV16. However, if we reduce the SN dust contribution, while keeping the LIMS dust constant (eg $\chi_1 = 0.1$,$\chi_2 = 0.2$), we see a shift in the peak $M_{\rm d}/M_{\rm bary}$ ratio

[1] This is due to subtle changes in the dust yields and interpolation of libraries, see Section 4.4.2.2.

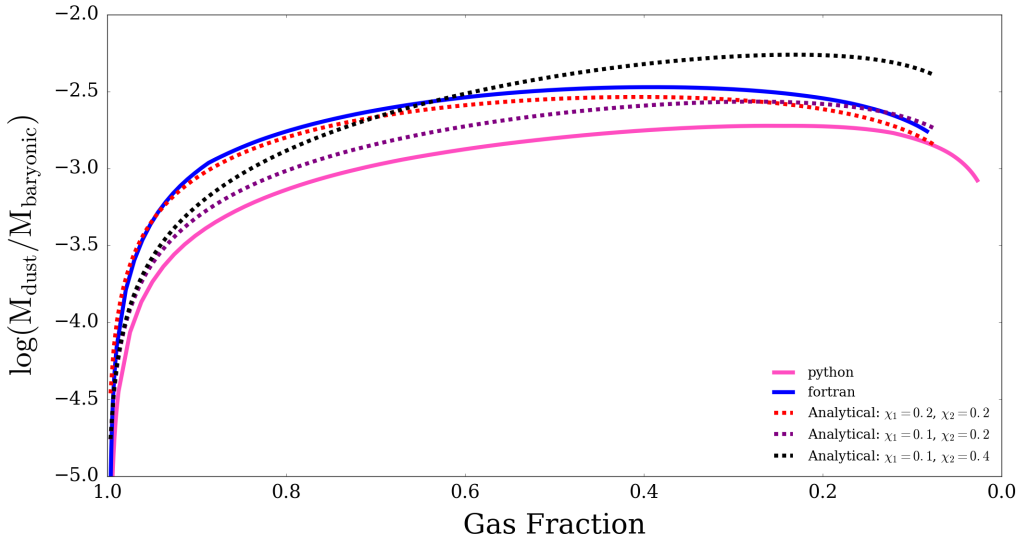

FIGURE 6.5 M_d/M_{bary} ratio against gas fraction for the chemical model used in this work (the updated Python code from this thesis, Chapter 4), the model used in C15 and DV16 (the older Fortran code and model of Morgan et al. (2003)) and three analytical models (based on instantaneous recycling technique). All models shown on this plot have the same initial gas mass of $4.0 \times 10^{10}\,M_\odot$, combined with the Milky Way-type star formation history of Yin et al. (2009).

towards lower gas fractions. If we increase the contribution of LIMS to the dust budget (eg $\chi_1 = 0.1$, $\chi_2 = 0.4$), the peak M_d/M_{bary} ratio for the galaxy continues to shift towards low gas fractions. This confirms that the change in peak M_d/M_{bary} here and in DVS16 compared to C15 and DV16 is due to our reduced SN contribution. Morgan et al. (2003) showed that the dust condensation efficiency of LIMS can range between 0.16-0.45, though the latter value is closer to the highest condensation efficiencies from theoretical models of dust formation in stellar winds (Zhukovska et al., 2008; Ventura et al., 2014, Section 4.4.2.1). By choosing a lower value for the dust condensation efficiency we can obtain a better fit to M_d/M_{bary} at low gas fractions for the closed box model of C15. However, as we show in later Sections, an equally good fit to M_d/M_{bary} can be obtained through the introduction of inflows and outflows when we relax the assumptions of the closed box model.

Perhaps surprisingly, although galaxies are more complex than this simple closed box model, Model I does explain the overall trend in these samples where the gas fraction lies between $80 > f_g > 40\,\%$. However it does not fit the data well at gas fractions outside this range. Model I clearly predicts a steep rise in M_d/M_{bary} at the highest gas fractions ($f_g > 90$ per cent). Since, the addition of the HIGH, DGS and HAPLESS samples has considerably extended the range of gas fraction over which

the models can be studied, particularly at the high gas fraction regime, we can now test this prediction, and Figure 6.4 shows that the highest gas fraction galaxies are indeed offset from the Model I, with significantly lower $M_{\rm d}/M_{\rm bary}$ than expected. It is possible that a different set of chemical model properties are necessary to explain this slower build-up of dust for these high gas fraction sources, we will test this in the following sections.

In summary, by using the new code developed in Chapters 4 and 5 we see that the peak $M_{\rm d}/M_{\rm bary}$ is pushed towards lower gas fractions, of approximately 0.3, compared to the peak $M_{\rm d}/M_{\rm bary}$ of 0.5 in previous studies (Edmunds & Eales, 1998; Morgan & Edmunds, 2003; Rowlands et al., 2014; Clark et al., 2015; De Vis et al., 2016). Furthermore, the dust yields of high mass stars have been reduced by a factor of ~ 1.8 due to changes in the input libraries (see Chapter 4 for further details). Additionally, by using the new code we can relax the closed box model assumptions and include additional sources and sinks of dust in the galaxies (such as grain growth and dust destruction) having realistic timescales which can be compared to other works in the literature.

6.3.2 Relaxing the closed box model

Figure 6.6 now compares the $M_{\rm d}/M_{\rm bary}$ of these samples with different chemical evolution tracks including different SFHs and/or relaxing the closed box assumption from Model I (Models II-VI, Table 6.2). We also add the DGS sample (highlighted with triangles). There are significant differences between some of the models and the data, especially at $f_{\rm g} \sim 80$ per cent. Here we clearly see that even for the same gas fraction, in this regime, nearby low M_* galaxies split into two categories: dust-rich and dust-poor and require *different chemical evolution models* to explain their dust-to-baryonic mass properties. Models I-III show a steep rise in $M_{\rm d}/M_{\rm bary}$ at the highest gas fractions ($f_{\rm g} > 95$ per cent). Given the scatter in the observations, we cannot distinguish between Models I-III at the high gas fraction regime when trying to interpret the HAPLESS, HiGH-high, HRS or some of the DGS sources. Even though the SFH for models I and II are very different (Figure 6.3), their chemical evolution tracks in Figure 6.6 nearly overlap. Independent of the shape of the SFH, the chemical evolution model results predict similar changes in the dust content of galaxies as they evolve from gas rich to gas poor when normalised by baryonic mass. The dust masses of galaxies matched well by models I-III can therefore be explained if core-collapse SNe produce $0.17 - 1.0\,{\rm M}_{\odot}$ of dust per explosion and there is no dust destruction or grain growth (or the net grain growth is matched by equal dust

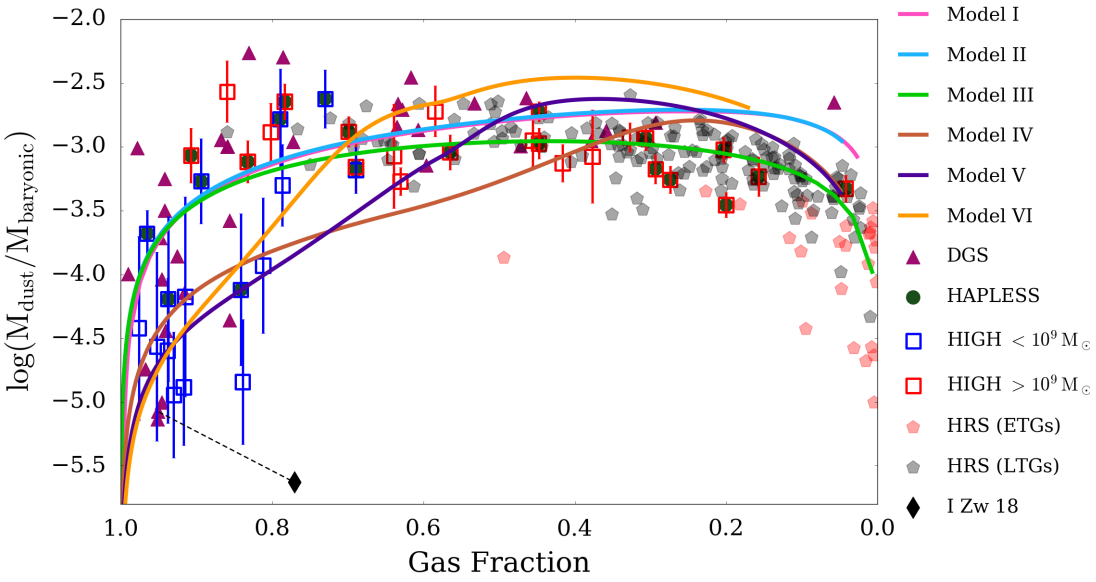

FIGURE 6.6 Variation of $M_{\rm d}/M_{\rm bary}$ with the gas fraction with gas mass defined as $M_{\rm g} = 1.32\,M_{\rm HI}$. After reaching the peak dust mass, the dust per baryonic mass declines as dust is consumed together with the gas in both astration and (where included) destruction via SN shocks which become important in the low gas fraction tail. The solid lines show how galaxies with the same initial gas mass but different combinations of SFHs, inflows, outflows and dust sources evolve as the gas is consumed into stars (Models I-VI defined in Table 6.2). Models I and II overlap on this plot since changing between the two SFHs in Figure 6.3 (top panel) does not change the amount of dust produced when normalised to produce the same stellar mass. The observed properties of dust-poor local galaxy I Zw 18 (black diamond) are also added for comparison (Fisher et al., 2014), with dashed line indicating where this source 'moves' using the methods and calibrations in this work.

destruction).

To reach the regime where the dust-poor HIGH-low and DGS sources are (and to explain their flatter increase in $M_{\rm d}/M_{\rm bary}$ with $f_{\rm g}$), we have to significantly reduce the amount of dust from stars (eg Models IV - VI). Note that changing the IMF to a more bottom heavy form, eg Salpeter, would reduce the dust and metals produced in the first generation of stars. However as the observations are determined using a Chabrier IMF, we would also have to scale these by the appropriate factor between Chabrier-Salpeter. A more bottom heavy IMF therefore does not explain the dust-poor sources (we discuss this further in Section 6.3.4). Models IV-VI therefore require a reduction in the dust production in SNe by a factor of 6-25 compared to the models required to fit the HRS, HIGH-high and HAPLESS. At late times (low gas fractions), Models I and II overestimate the amount of $M_{\rm d}/M_{\rm bary}$ and require inflows and dust-rich outflows of gas or a reduced dust contribution from LIMS (eg a condensation

efficiency of 0.15 instead of 0.45) to explain the observed properties (Models III-VI).

Note that in Figure 6.6 we also highlight the well-studied galaxy I Zw 18 (part of the DGS sample) thought to be a local analogue of low-metallicity, high-redshift systems (eg Herrera-Camus et al. 2012; Fisher et al. 2014). The location of this source on this $M_{\rm d}/M_{\rm bary}$ 'scaling relation' (and in later Sections) is indicated by the black hexagon using the measured properties from Fisher et al. (2014). As we have re-evaluated the DGS measurements to be consistent across all samples (Section 6.2.2), we have indicated where this galaxy moves with our revised measurements (dashed line). We will see in later sections that the dust properties of I Zw 18 are entirely consistent with its gas fraction and metallicity.

6.3.3 Star formation rates and gas mass

Next we briefly attempt to explain the observed SFR properties (derived from magphys for HAPLESS, HRS and HiGH see Chapter 2, Section 2.6; for DGS SFR see Section 6.2.2) with these models by comparing the change in SFR/$M_{\rm bary}$ with gas fraction. Figure 6.7 compares this property for the HAPLESS, HRS, HiGH, and DGS samples. Delayed Milky Way models with varying peak SFRs and SF timescales reduce the amount of SFR/$M_{\rm bary}$ at a given gas fraction (Figure 6.7 top left panel). In the high gas fraction regime ($f_g > 80$ per cent), we see that Model I overpredicts the SFR/$M_{\rm bary}$, particularly in comparison to the HiGH-low sources. Delayed SFH models provides a closer match to the this regime particularly the HiGH-low sample (as used in Models II-VI) by reducing the SFR per unit baryonic mass at early evolutionary stages (Figure 6.7 top right panel). The bottom panel of Figure 6.7 summarizes the final set of SFHs chosen based on the variations seen in the top panels to model our galaxy samples. The values of the delayed SFHs in Figure 6.3 and Eq. 6.1 were chosen to match the data in Figure 6.7, with Model VI reaching the HiGH-low regime.

In models with strong outflows but no inflows (Model III), the baryonic mass is significantly reduced at low gas fractions, and therefore SFR/$M_{\rm bary}$ increases as the gas fraction decreases. Model III thus poorly matches the observed SFR/$M_{\rm bary}$ at low gas fractions and can be discarded as an unrealistic model. However, when the outflow is matched by an equal inflow as in Model V, $M_{\rm bary}$ stays constant and we find the same SFR/$M_{\rm bary}$ track as for the same model without inflows and outflows (ie Models II, IV and V overlap in Figure 6.7).

The DGS sources lie significantly above the HRS, HiGH and HAPLESS samples, with higher SFR/$M_{\rm bary}$ for the same gas fraction. This can be explained given

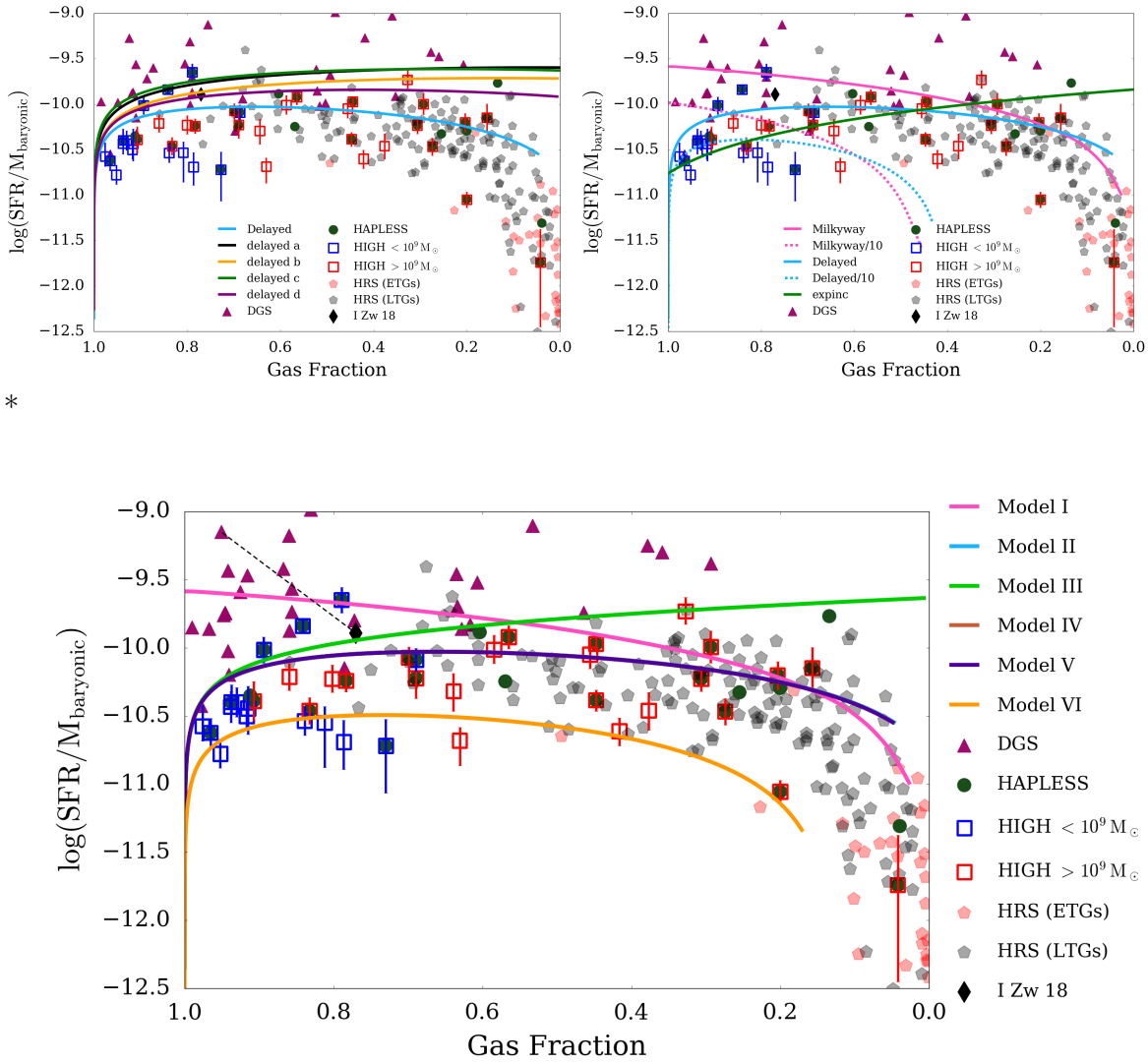

FIGURE 6.7 SFR/$M_{\rm bary}$ against the gas fraction for the samples compared to models with different SFHs to illustrate how the evolution of sources in this parameter space depends on their SFH. *Top Left:* The effect of changing Model I from a MIlky Way SFH to a delayed SFH with the following parameters: delayed SFHs with $4.4\,{\rm M}_\odot\,{\rm yr}^{-1}$, $\tau = 6.9\,{\rm Gyr}$, (a) $6\,{\rm M}_\odot\,{\rm yr}^{-1}$, $\tau = 20\,{\rm Gyr}$, (b) $4\,{\rm M}_\odot\,{\rm yr}^{-1}$, $\tau = 20\,{\rm Gyr}$, (c) $4\,{\rm M}_\odot\,{\rm yr}^{-1}$, $\tau = 10\,{\rm Gyr}$, (d) $2\,{\rm M}_\odot\,{\rm yr}^{-1}$, $\tau = 10\,{\rm Gyr}$. *Top Right:* A medley of different SFHs including Milky Way (Model I), Milky Way SFH reduced by $\times 10$, delayed SFH, delayed SFH reduced by $\times 10$ and an exponential increasing SFH. This reveals the need for adding a delayed SFH (Models II-VI) to explain some of the HIGH-low and HAPLESS sources at high gas fractions (Model I significantly overestimates the SFR/$M_{\rm bary}$ when $f_{\rm g} > 80\%$). *Bottom:* The final models chosen in Table 6.2 to explain the observed trends. These consist of three different SFHs (Figure 6.3). Note that in this parameter space, Model II overlaps with Model IV and partly with Model V as they have the same SFH and their inflows and outflows are balanced. At low gas fractions, a model with only outflows of gas (Model III) has a continuous rise in SFR/$M_{\rm bary}$ due to the ejection of gas from the system, this model does not match the data. Bursty SFHs are needed to explain DGS sources (Figure 6.11, Section 6.3.6)

the different SFRs and gas fractions of the DGS with respect to HIGH-low and HAPLESS sources with similar stellar masses. The DGS has a lower average gas fraction of 0.74 than HIGH-low (0.87, Table 6.1) due to the latter having more atomic gas on average (as expected given this sample is HI-selected). At the highest gas fractions, the HIGH-low and DGS offset is explained by their SFRs: while the SFR in the DGS sample spans four orders of magnitude and includes many quiescent objects, it tends to contain more actively star-forming galaxies (average SFR 1.39 $M_{\odot}\,yr^{-1}$, Table 6.1) than is typical of nearby dwarfs (eg Hunter et al. 2012). Their selection towards more star-forming, low-stellar mass systems could be a consequence of their original selection of galaxies with moderate to very low PT05 metallicities. We return to this in the next section. The intensely SF nature of the DGS was highlighted in Zhukovska (2014) where they found they required bursty SFRs similar to the one in Figure 6.3 to fit the gas and dust properties of their dwarf galaxies. Even with the revised dust masses and metallicities and the different model assumptions in this work, we also find a bursty SFH is required to fit the DGS properties (Section 6.3.6). This demonstrates that despite having similar stellar masses, dust temperatures and gas fractions as the HIGH-low sources, the DGS are more actively star forming than the HIGH galaxies and *do not appear to be the same sources at a different evolutionary stage*. Adding the HIGH-low and HAPLESS samples to the DGS therefore provides additional, new, information of more normal star-forming systems with low Z, high $f_{\rm g}$, and potentially different dust properties.

6.3.4 The metallicity versus gas fraction

We next wish to compare how the metallicity of galaxies changes as they evolve from high to low gas fractions. In Figure 6.8 we see in both the model behaviour and the observations that, in general, the metallicity increases monotonically as galaxies evolve from high to low gas fractions, consistent with an increasing dust-to-gas ratio with increasing Z as gas is consumed into stars. The models are almost indistinguishable at gas fractions > 80 per cent in this parameter space, even when changing the SFH (Models I, II, VI and VII, Figure 6.3). When comparing with the chemical evolution tracks at low gas fractions, Models I and II clearly overestimates the amount of metals. As with the observed SFR/$M_{\rm bary}$ trend, this suggests models with moderate outflows of enriched gas and inflows are necessary (Models V-VI).

In the high gas fraction regime, Models I-VI have difficulty reproducing the high metallicities derived using the N2 and KE08/TO4 calibrators. As Morales-Luis et al. (2014) showed that the N2 calibrator overestimates the oxygen abundance for

the most metal-poor galaxies, we note for the rest of this work, that N2 and KE08/T04 methods should be thought of as upper limits for the lowest metallicity galaxies in HIGH-low and DGS. The PG16S calibrator is well matched by the models at all gas fractions when both inflows and outflows are included.

Figure 6.8 also shows that the HRS galaxies are more metal-rich at a given gas fraction than the DGS, HIGH-low and HAPLESS sources, regardless of whether using the N2, KE08/T04 or PG16S calibrators. The high-gas-fraction DGS sources and HIGH-low lie approximately on the same general trend with increasing metallicity with $f_{\rm g}$ as the HRS and Models I-VI, consistent with their high gas fraction (early stage). However, the DGS appears to have lower metallicities than the HRS at low gas fractions and, to a lesser extent[2], the HIGH-low sources at high gas fractions ie *the DGS are, on average, more metal-poor given their evolutionary state*. From Table 6.1, the average SFR/$M_{\rm HI}$ for the DGS is $\sim$20 times larger than both the HRS and HIGH-low samples, with SFR/M_d higher by $\sim$300 compared to the HRS. If $M_{\rm d}$ is used as a proxy for the molecular gas, this suggests DGS sources have a higher star formation efficiency than the HRS, HAPLESS and HIGH sources. The DGS galaxies are thus, on average, more actively forming stars. This again indicates that the offset in the DGS towards low Z could be a consequence of their selection method. Selecting galaxies ranging from low to moderate metallicity at a given gas fraction could result in a sample selection biased towards galaxies with very high SFRs due to the mass-metallicity fundamental plane (Mannucci et al., 2010). This also explains why a bursty SFH (Zhukovska, 2014) is needed. Although this SFH may match the $M_{\rm d}/M_{\rm bary}-f_{\rm g}$ and SFR/$M_{\rm bary}-f_{\rm g}$ properties, it does not explain their $Z-f_{\rm g}$ properties. Indeed we find it very difficult to reach such low metallicities for a given gas fraction with any of our standard models (I-VI), see Section 6.3.6 for more details.

To increase or decrease the metallicity reached in these models, one can also vary the IMF. For example the offset between models and the HRS at low gas fractions in Figure 6.8 could potentially be explained by changing the model IMF to a Salpeter or bottom-heavy function (eg Cappellari et al. 2012). Similarly at high gas fractions, a top-heavy IMF in the model could increase Z. But to change the model IMF we must also scale the observational parameters which have been determined using the Chabrier function. For example, using a top-heavy IMF with slope $\alpha=-1.5$ (Cappellari et al., 2012; Madau & Dickinson, 2014) we would have to scale the dust mass by a factor of 3, and the stellar mass and SFRs by a factor of 0.32 (Michałowski, 2015). When we do this, we find a slight improvement in comparing the models and data at high f_g for the N2 and KE08/T04 metallicities but this is well within the

[2] this offset is only seen in the N2 calibrator

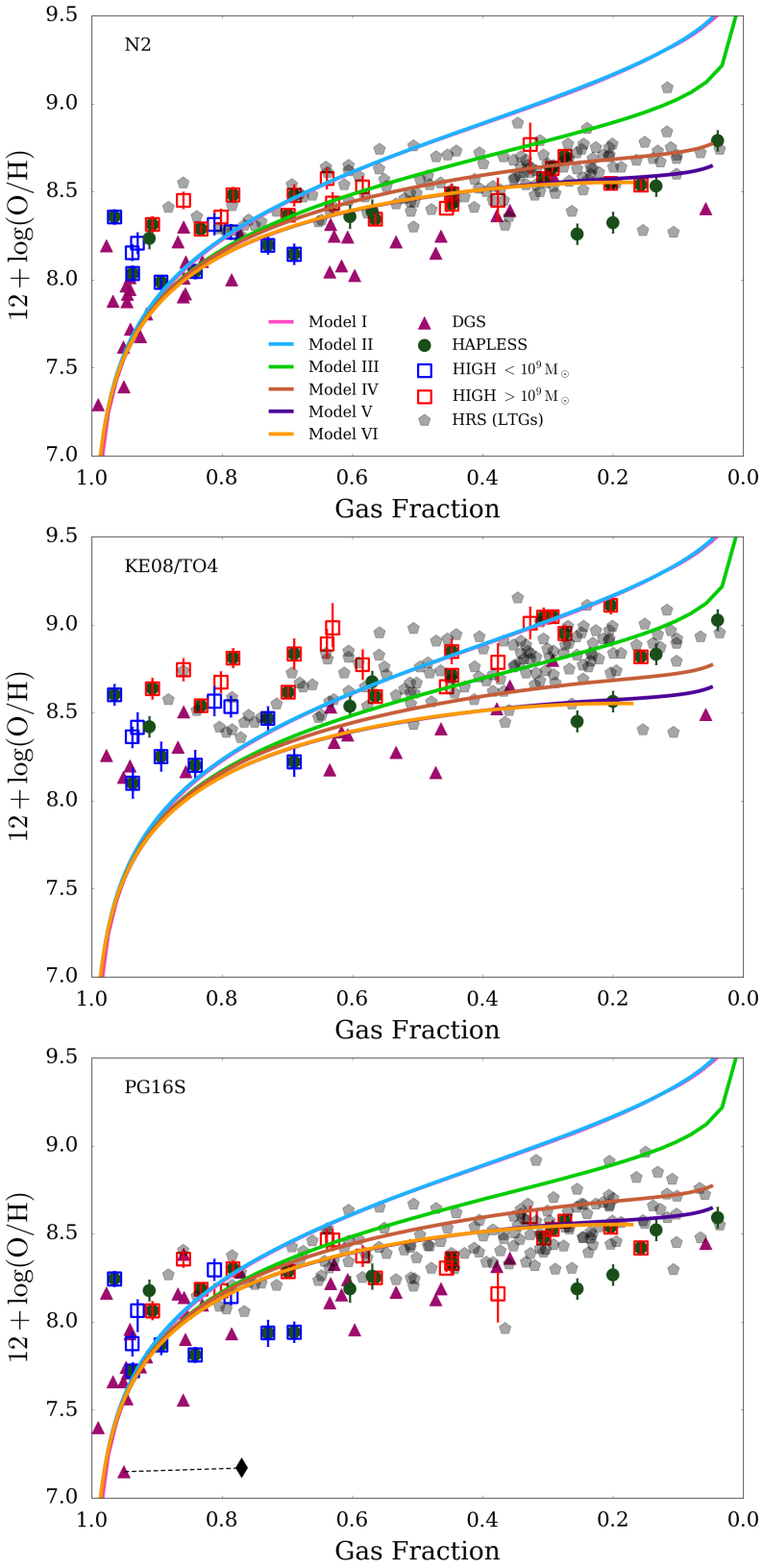

Figure 6.8 Metallicity variation with gas fraction for the different samples using the three different metallicity calibrations (from top to bottom: N2, KE08/T04 and PG16S). The error bars are derived by combining bootstrap uncertainties and an intrinsic scatter of 0.06 dex between fibres. The different chemical evolution models (see text and Table 6.2) are also included.

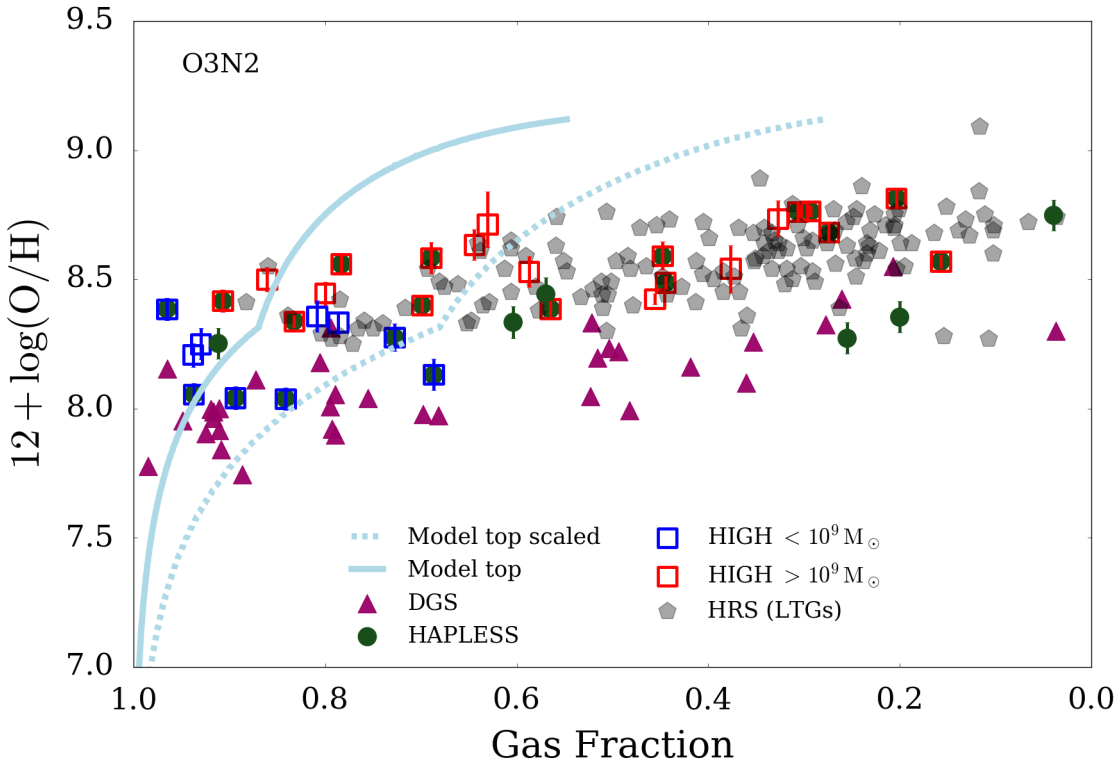

FIGURE 6.9 Metallicity against gas fraction for a top-heavy stellar IMF of slope $\alpha = -1.5$ from Cappellari et al. (2012) (shown as solid blue line). Using a top-heavy IMF causes an enhanced rate of metal production for a given gas fraction, due to an increased number of short lived high mass stars. However, our data was derived using a Chabrier (2003) IMF, so we must apply the scaling of Michałowski (2015) to the model before comparing with the data (dashed blue line). This offers only a slight improvement over our standard models (Models IV-VI) so we remain with the Chabrier (2003) IMF.

scatter, indeed this model is indistinguishable (in terms of a 'good-fit') from Models IV-VI (see Figure 6.9). Similarly there is no strong evidence for a Salpeter IMF to explain the dust properties of the low gas fraction sources. The Salpeter IMF results in a higher fraction of mass locked up in low mass stars and hence produces a lower dust yield when compared to the Chabrier IMF (Madau & Dickinson, 2014). The Salpeter IMF could then be proposed as an alternative to reducing the SN dust yield to match the dust properties of the most dust poor high gas fraction sources. However using a Salpeter IMF makes it more difficult to match the metallicity that is observed at a given gas fraction, and offers no improvement to the overall quality of fit that is obtained.

6.3.5 Dust-to-gas with metallicity

Next we compare metallicity with the dust-to-gas ratio (Figure 6.10). For the DGS, HRS and HAPLESS we see that, in general, galaxies with high dust-to-gas ratios are also sources with high metallicity (as expected if dust traces the metals or a constant fraction of metals remain in dust grains). Some of the galaxies follow a linear trend in increasing dust to gas ratio as the metallicity increases which is well-matched by Models I-III (models with different SFHs are indistinguishable in this parameter space if there is no dust grain growth).

Some of the HiGH-low and DGS sources are consistent with the linear $M_{\rm d}/M_{\rm g} - Z$ relationship, though others are offset from these linear trends. For low stellar mass sources, we observe galaxies that are dust poor given their metallicity regardless of which metallicity calibrator is used (though the N2-derived values are likely upper limits). Thus we caution the use of dust masses as a method to derive gas masses, since in these galaxies, the available atomic (or total) gas mass is not a good tracer of the dust. We also caution against statements made in the literature regarding that low metallicity galaxies are always dust poor (particularly when using local systems such as I Zw 18 as analogues for high redshift galaxies).

This offset from the linear trends was already discussed in Rémy-Ruyer et al. (2013, 2015); Zhukovska (2014) who explained this by suggesting the supernova contribution to the dust budget needs be reduced and a dust grain growth term added. Feldmann (2015) also used reduced supernova dust yields and added dust grain growth to reach the higher dust content at later evolutionary stages. In contrast to Zhukovska (2014), Feldmann (2015) even uses reduced supernova dust yields for sources that are not dust poor given their metallicity. Instead they use extremely fast dust grain growth to obtain the steep rise in dust content at the earliest stages of galaxy evolution. There is thus a degeneracy between using a significant contribution from supernova dust, and using very fast dust grain growth. Their gain growth timescales of $\sim 5\,$Myr are much faster than typically found in nearby galaxies (Mattsson & Andersen, 2012; Mattsson et al., 2014) or from basic theoretical calculations of the underlying growth rate (Draine, 2009). Here we will show that our HiGH-low sample also require a reduced supernova dust production compared to Milky Way-like models (required to fit the HRS) despite having star formation properties that are an order of magnitude lower than the DGS sources. The argument is such: for the highest gas-fraction galaxies in Figure 6.10 the dust mass needs to be significantly suppressed without reducing the metals. The only way to do this is to reduce the amount of dust formed by stars in each stellar population. As the dust-to-gas ratio is already lower than expected from

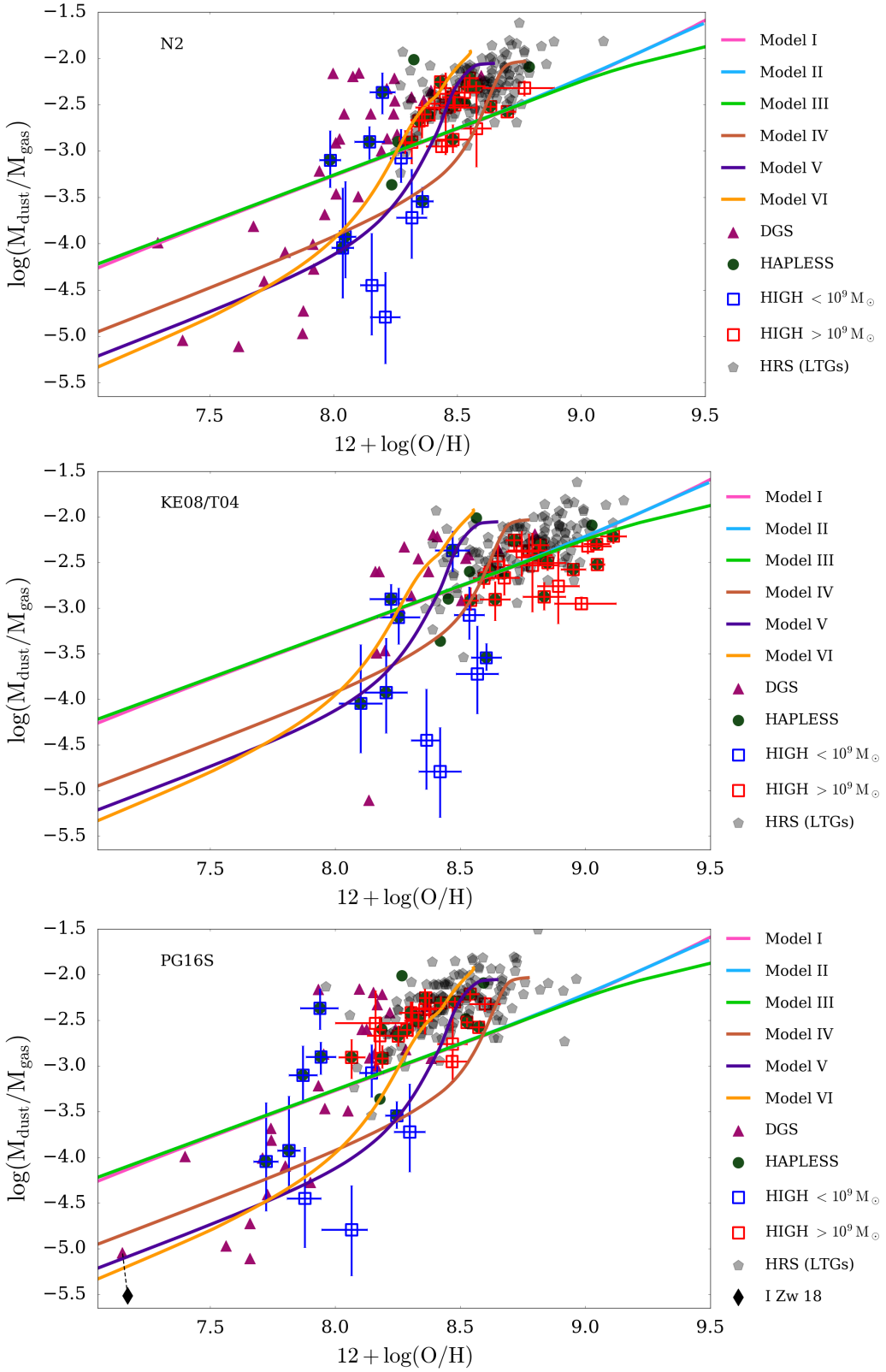

FIGURE 6.10 Metallicity variation with gas-to-dust ratio M_d/M_g with the three different metallicity calibrations shown in Figure 6.8. Models IV, V and VI provides a better match between metallicity and M_d/M_g for the HIGH-low and many DGS sources than Models I-III. Note that metallicities derived using N2 (and therefore KE08/T04) for the most metal-poor systems are likely to be upper limits.

a linear trend at high gas fractions, this suggests the SN dust production must be suppressed. The observed dust-to-gas ratio in the HIGH-low galaxies requires models with a maximum of $0.04\,M_{\odot}$ of dust per core collapse SNe, which corresponds to a condensation efficiency of 0.90 per cent for a $25\,M_{\odot}$ progenitor (assuming $5\,M_{\odot}$ of metals ejected, Woosley & Weaver 1995).

Therefore Models IV, V and VI include a reduced SN dust component (by a factor of 6-25 in mass, Table 6.2) compared to the Milky Way model. Since there is less stardust in these models, if we require galaxies to ultimately evolve to the typical dust-to-gas ratios observed at low $f_{\rm g}$ (Figure 6.10), we need to also include interstellar grain growth. This dust source is strongly metal-dependent and only becomes important once the galaxy reaches a critical metallicity (Asano et al., 2013), this means that different values of the grain growth parameters ϵ, and consequently $\tau_{\rm grow}$, would move the model tracks. An increase of ϵ will steepen the slope of $M_{\rm d}/M_{\rm g}$ (shown by Models IV-VI as they reach the end of their tracks); any offset from the linear trend in Figure 6.10 can therefore be mitigated by changing ϵ such that grain growth starts at a lower metallicity (thereby increasing the dust-to-gas ratio). Alternatively, offsets in Figure 6.10 can also be explained through the use of different bursty SFHs, because long quiescent phases allow accretion of existing metals after short active enrichment episodes (Zhukovska, 2014).

6.3.6 A different model for dwarf galaxies from the DGS

We can test whether the DGS have different star formation properties by including a bursty SFH in the chemical evolution (Model VII, Figure 6.3) following Zhukovska (2014). The results are shown in Figure 6.11 using the original DGS metallicities, and the revised metallicities derived in this work. In the top panel, we compare the $M_{\rm d}/M_{\rm bary}$ of the DGS with Model VII (as we did with the HRS and HAPLESS in Figures 6.4 & 6.6). Model VII matches the observed trend well, again suggesting that the shape of the SFH does not strongly affect the trend in $M_{\rm d}/M_{\rm bary}$ as galaxies evolves from high to low gas fractions. In the bottom panel of Figure 6.11, we compare the predicted SFR/$M_{\rm bary}$ with gas fraction for Model VII. Here we see that the bursty model is required to explain the elevated SFR/$M_{\rm bary}$ of the DGS galaxies compared to the HAPLESS, HRS and HIGH samples (and also the observed metallicity and $M_{\rm d}/M_{\rm HI}$ properties as discussed in Section 6.3.4). In Figure 6.12, the metallicities and dust-to-gas ratios are displayed. Although a bursty model is a good match to the SFR/$M_{\rm bary}$ and $M_{\rm d}/M_{\rm bary}$, we require strong inflows and outflows to fit their metallicities. This was originally suggested in Feldmann (2015). Only Model

VII (see Section 6.3.6), with inflows and outflows a factor of 3 higher than the models (V and VI) used to match the other nearby galaxy samples in this work, can be used to explain the $Z - f_g$ properties of the DGS sample. Therefore the DGS galaxies do require different chemical interpretation to the HIGH-low and HAPLESS galaxies despite their similar metallicities and stellar masses.

To summarize Sections 6.3.2-6.3.5, the best matches for explaining the observed evolution in M_d/M_{bary}, SFR$/M_{bary}$, and now metallicity with gas fraction for most of the galaxies in our sample are Models IV-V, while a better fit for HIGH-low can be obtained with Model VI. The DGS sources require more extreme SFH and outflows (Section 6.3.6, Model VII). The relative contributions to the dust mass budget for Models IV-VI are displayed in Figure 6.13. At gas fractions above 0.8, stellar sources dominate (mostly SN dust, Rowlands et al., 2014, C15). Interstellar grain growth becomes a comparable source of dust mass when the gas fraction falls below $\sim$0.8 (Models V and VI), while for Model IV this does not occur until a gas fraction of $\sim$0.5 due to a lower ϵ value. For each of these models, grain growth is the dominant dust source below 0.4. Asano et al. (2013) showed that the absolute value of the critical metallicity depends on both the dust accretion timescale and the star formation timescale. The metallicity at which dust grain growth exceeds dust production from stars in our model is reached between $0.003 < Z < 0.013$ (or $7.96 < 12 + \log(\mathrm{O/H}) < 8.63$). Higher values of ϵ (Table 6.2) lead to shorter grain growth timescales and lower critical metallicities. By mass, grain growth contributes 73-92 per cent of the total dust budget for models IV-VI (in agreement with estimates of the contribution of grain growth to the dust budget of the Milky Way, Draine 2009). The (Z-dependent) dust grain growth timescales for Models IV, V and VI are shown in Figure 6.13 (right). For Model V and VI, the growth timescale decreases steeply at gas fractions of $\sim 0.9 - 0.6$ (where grain growth switches on). At gas fractions less than 0.5, the timescales for Model V and VI reach a plateau of $\sim$200 Myr. The grain growth timescale for Model IV declines more slowly with f_g and reaches a timescale of $\sim$750 Myr at a gas fraction of 0.5.

6.4 The Dust to Metal Ratio

There is thought to be little variation in the dust-to-metal ratio of galaxies (Mattsson et al., 2014), with only small variations (but increased scatter) observed in low metallicity environments (De Cia et al., 2013) and galaxies at redshifts > 0.1 (Zafar & Watson, 2013) even down to metallicities as low as 1 per cent of solar ($12 + \log(\mathrm{O/H}) = 6.91$). Using the DGS sample, Zhukovska (2014) showed the dust-to-gas

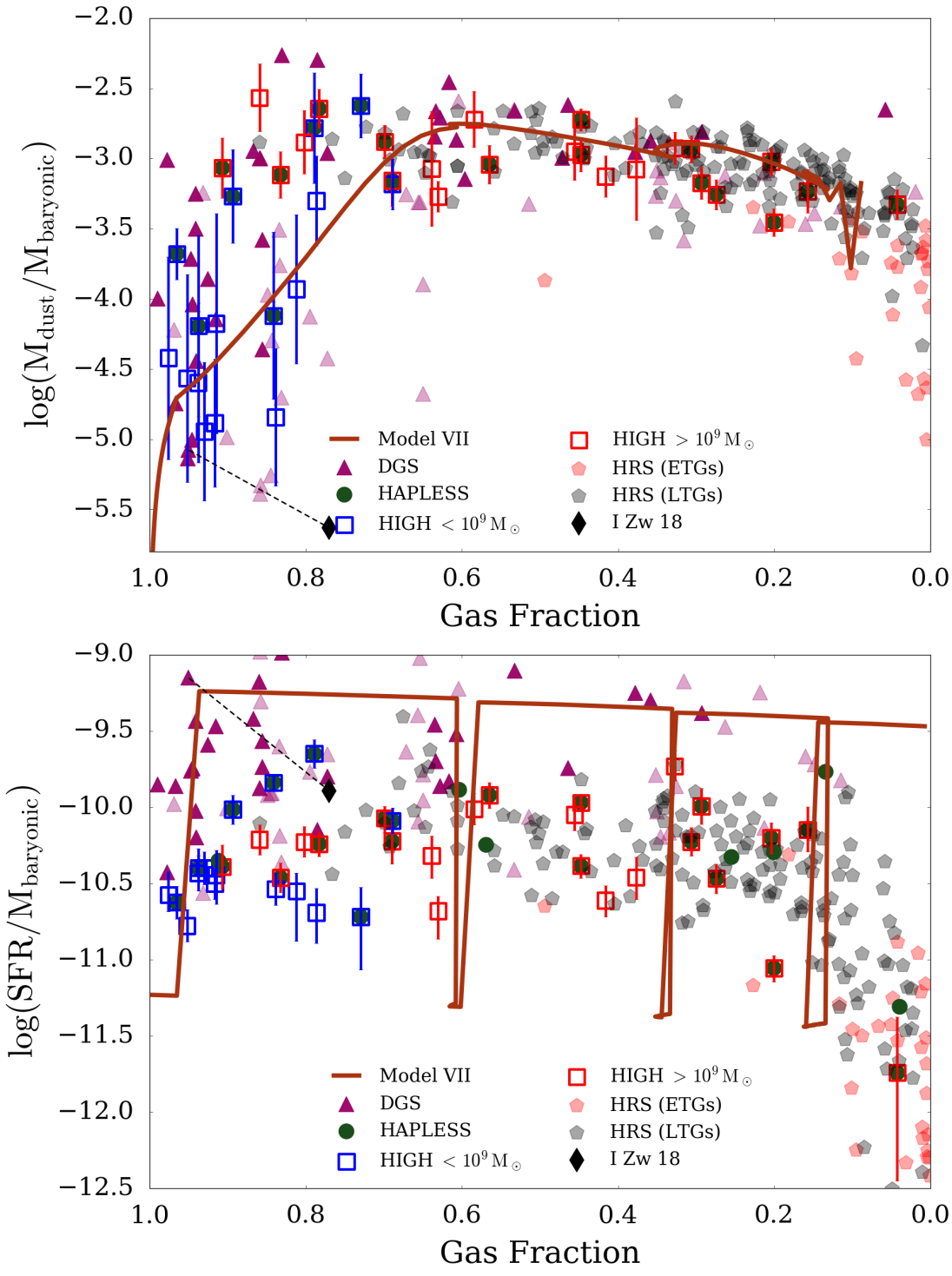

Figure 6.11 *Top:* $M_{\rm d}/M_{\rm bary}$ and *bottom:* SFR/$M_{\rm bary}$ evolution with gas fraction using the bursty SFH in Figure 6.3. As shown in Zhukovska (2014), the DGS sample (purple triangles, transparent ones are from (Zhukovska, 2014)) can be explained with a model undergoing many bursts of star formation (red solid line). The chemical evolution model shown is Model VII (the bursty SFH) which provides a good fit to the DGS galaxies (see also Zhukovska 2014 and Rémy-Ruyer et al. 2015).

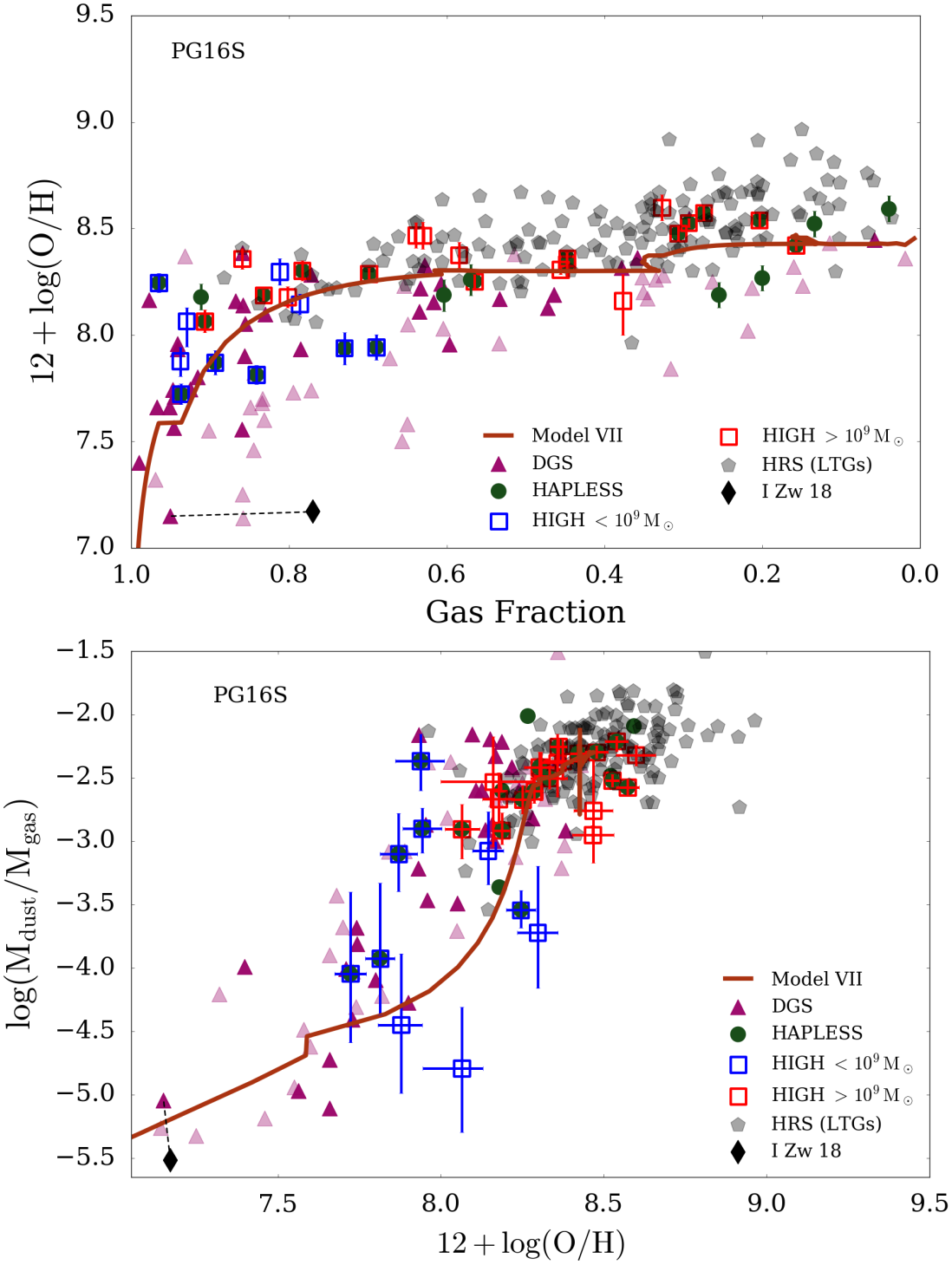

FIGURE 6.12 The DGS are more metal poor at a given gas fraction than the HIGH, HAPLESS and HRS sources, and we require a different model (Model VII) to explain their properties. *Top:* Metallicity against gas fraction. *Bottom:* Dust-to-gas ratio against metallicity. The revised DGS metallicities from this work (opaque purple triangles) require less dust from SNe similarly to the HIGH-low sample. Model VII (the bursty SFH) provides a good fit to the DGS galaxies but as originally proposed in Feldmann (2015), the observed metallicity of the DGS galaxies is best explained by a chemical model which incorporates strong inflows and outflows of gas as well as a bursty SFH.

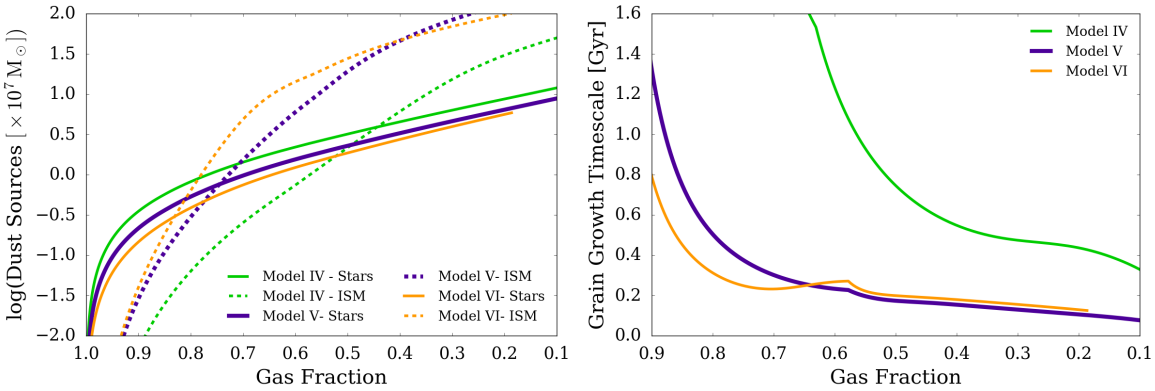

Figure 6.13 (*Left:*) The dust mass produced by the various dust sources in Models IV, V and VI as the galaxy evolves from gas rich to gas poor. At gas fractions above 0.8, only stellar sources (dominated by SN dust - C15, Rowlands et al. 2014) produce significant quantities of dust. The dust grain growth becomes a significant source of dust mass at gas fractions below 0.4. (*Right:*) The variation of the grain growth timescale $\tau_{\rm grow}$ (Equation 4.31) with gas fraction for Models IV, V and VI (Models V and VI overlap on this plot). The timescale is long at high gas fractions, due to the low metallicity of the modelled galaxy at this stage.

ratio is different at low metallicity, finding it increases more steeply with metallicity than can be achieved by stellar dust alone. This hints there is an increase in the dust-to-metal ratio as galaxies evolve due to gain growth. Feldmann (2015) studied this in more detail and attributed it to an increasing efficiency with which dust acquires additional mass from the ISM as galaxies reach their critical metallicity. This critical metallicity is set by the competition between dust grain growth and dilution via dust-poor gas inflows, which are in turn regulated by outflows.

In this Section we explore the variation in the dust-to-metal ratio of the combined samples collated in this work using our sample of 425 sources (67 of which have $Z < 1/3\,{\rm Z}_{\odot}$) following Feldmann (2015). Figure 6.14 and Table 6.3 compares the dust-to-metal ratio in the HiGH, HRS, HAPLESS and DGS samples (for each of the three different metallicity calibrations used in this paper). Adding in HiGH increases the scatter seen in Rémy-Ruyer et al. (2014) and Feldmann (2015). We also note that the dust-to-metal ratio is significantly lower for galaxies in the low metallicity regime regardless of how actively star forming these galaxies are. To estimate the total metal mass M_Z from the observed oxygen abundance from Section 6.3.4, we assume $12 + \log({\rm O/H})_{\odot} = 8.69$ and a Solar metal mass fraction ${\rm Z}_{\odot} = 0.014$ following Asplund et al. (2009). We note the $M_{\rm d}/M_{\rm Z}$ distribution of the HRS galaxies is somewhat bimodal: in the PG16S calibrator panel in Figure 6.14, we see that the peaks occur at $\sim$0.3 and $\sim$0.6 leading to a mean value of $M_{\rm d}/M_{\rm Z} \sim 0.51$. This is in good agreement with the Milky Way value and the recent survey by Davies et al. (2014)

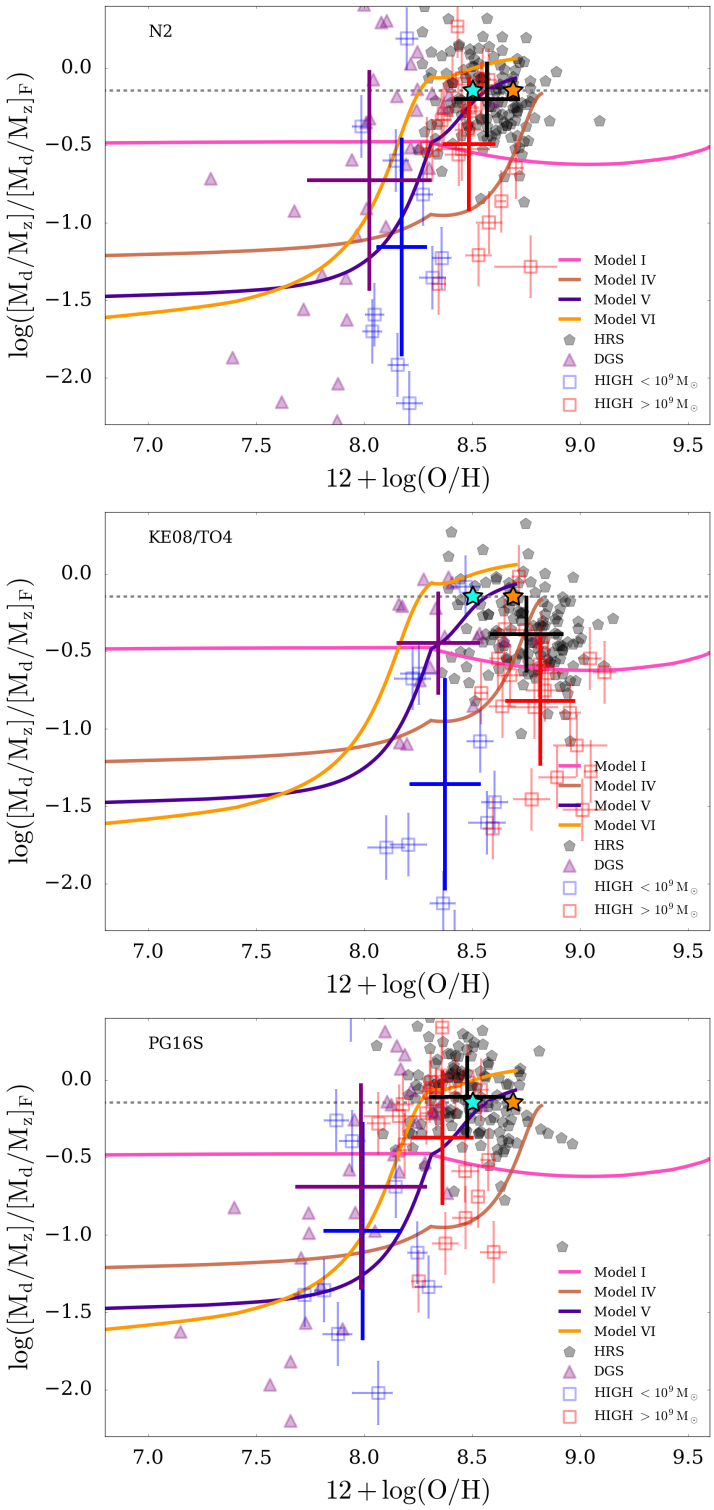

FIGURE 6.14 We follow Feldmann (2015) and compare the dust-to-metal ratio (normalised by the dust-to-metal ratio of a solar metallicity galaxy $[M_d/M_Z]_F = 0.7$) for the HIGH, HRS, HAPLESS and DGS samples against metallicity. The kink at $Z > 0.006$ in Model I is due to an increasing metal mass from stars resulting from changing the input metal yield file (Maeder, 1992). The large crosses show the mean $\pm$ standard deviation of dust-to-gas within the samples. We also highlight the Milky Way ($M_d/M_Z = 0.5$, orange star) and recent estimates for galaxies in the Virgo Cluster (Davies et al., 2014, cyan star).

Table 6.3 Average dust-to-metal ratio for the different galaxy samples quoted as mean ± standard deviation. [a] - Solar measurement from Asplund et al. 2009; [b] - see Clark, Schofield et al. (2016) for a compilation. We include all three metallicity calibrations: N2, KE08/T04, PG16S.

Galaxy Sample	Mean $12 + \log(\mathrm{O/H})$			Mean $log(M_\mathrm{d}/M_Z)$		
MW	-	8.69[a]	-	-	−0.15[b]	-
	N2	KE08/T04	PG16S	N2	KE08/T04	PG16S
DGS	8.02 ± 0.28	8.34 ± 0.19	7.98 ± 0.30	-0.72 ± 0.71	-0.44 ± 0.33	-0.69 ± 0.66
HiGH-low	8.17 ± 0.12	8.37 ± 0.16	7.99 ± 0.18	-1.15 ± 0.70	-1.38 ± 0.69	-0.97 ± 0.70
HiGH-high	8.48 ± 0.12	8.81 ± 0.16	8.36 ± 0.14	-0.49 ± 0.43	-0.82 ± 0.42	-0.37 ± 0.43
HRS (LTGs)	8.57 ± 0.15	8.75 ± 0.17	8.48 ± 0.18	-0.20 ± 0.24	-0.38 ± 0.25	-0.11 ± 0.27

using *Herschel* observations of galaxies in the Virgo Cluster[3].

The location of the low stellar mass samples (HiGH-low and DGS galaxies) is contrary to what we would expect if stellar sources were the dominant source of dust in the galaxies. Additionally we would also expect a constant dust-to-metal ratio if dust destruction and dust grain growth effectively cancel out as shown in Mattsson et al. (2014). The HiGH-low and DGS galaxies ($M_\mathrm{d}/M_\mathrm{Z}(\mathrm{PG16S}) \sim 0.10 - 0.15$) seem to occupy a distinct region of the plot compared to the HiGH-high, HAPLESS and HRS samples ($M_\mathrm{d}/M_\mathrm{Z}(\mathrm{PG16S}) \sim 0.35 - 0.50$), which again indicates different dust production/evolution mechanisms in the different samples. In the previous section, we already saw that reduced supernova dust is necessary to explain the low dust content at the early stages of evolution and that dust grain growth increases the dust mass later on (Models IV, V and VI). This also applies to the dust-to-metal ratio. Before the critical metallicity is reached ($Z < Z_\mathrm{crit}$), the (reduced) stellar dust sources dominate and the dust-to-metal ratio is low, as for HiGH-low and DGS. However for $Z > Z_\mathrm{crit}$, dust grain growth becomes the dominant term and increases the dust-to-metal ratio to the levels seen in HiGH-high, HAPLESS and HRS.

The strong variation in dust-to-metal ratios with metallicity is present regardless of whether the N2, KE08/T04 and PG16S calibrators are used in this work (also seen when using PT05 metallicities; Rémy-Ruyer et al. 2014; Feldmann 2015). By combining the HiGH sample with the DGS and HRS sources, we have increased the sample size (425 instead of 126 sources) at all metallicities compared to the earlier work of Rémy-Ruyer et al. (2014); Zhukovska (2014); Feldmann (2015) and also shown the change in dust-to-gas ratio and dust-to-metals ratio remains for galaxies that are more normal (ie not just the more actively star-forming DGS). The observed trend

[3] calculated using the O3N2 metallicity calibrator and solar abundances from Asplund & García Pérez (2001).

with metallicity for these low stellar mass objects is best matched by Models IV, V and VI, which have reduced stellar dust production (by a factor of $6-25$) and, in the later stages of evolution, we then require ~ 80 per cent of the total dust mass originating from interstellar grain growth.

We note here an important point from Figure 6.14 that is often not considered when modelling dust in galaxies using chemical evolution. It is very difficult for a model with SFH consistent with the Milky Way, with dust from both LIMS combined with *significant* dust production in supernovae and *no dust destruction* (Model I, peak $M_{\rm d}/M_{\rm Z} \sim 0.2$) to reach the observed Milky Way dust-to-metals ratio (~ 0.5; orange star in Figure 6.14) as it evolves. Adding inflow of unenriched gas does help increase $M_{\rm d}/M_{\rm Z}$, but this issue demonstrates why significant interstellar grain growth is needed to supplement the dust mass and reduce the large offset seen between Model I and the observed $M_{\rm d}/M_{\rm Z}$, even in our own galaxy.

6.5 CAVEATS

In the previous sections we have built models to explain the dust properties in the dust-poor low-Z sources, as well as dust rich lower gas fraction sources. We acquire a good fit to the observations by reducing the stardust contribution by a factor of ~ 25 (particularly from core-collapse SNe) and including moderate inflows and outflows, dust destruction and moderate grain growth (timescales ranging from 1 Gyr - 200 Myrs). In this section we discuss potential caveats of our approach.

- **Dust Emissivity** - If the dust emissivity is different across the samples, this could explain the reduced $M_d/M_{\rm HI}$ seen in Figure 6.10 and in $M_{\rm d}/M_{\rm Z}$ (Figure 6.14). For the dust poor HIGH-low sample to have a dust/metals ratio similar to the DGS, HRS and HIGH-high samples (ie $\sim 0.4-0.5$), κ would have to be ~ 4 times lower (ie the dust in the HIGH-low and DGS galaxies would have to be less emissive than evolved spirals such as the Milky Way). This is beyond the scope of this thesis.

- **Missing molecular gas** - We lack sufficient molecular gas information for the HAPLESS and HIGH samples. Though to remove the offset in dust-to-gas ratios observed in the HIGH-low sample, the molecular gas would need to dominate the total gas mass for all the other samples. This does not agree with observed molecular gas masses for the HRS and DGS (see also scaling relations from Saintonge et al. 2011 and Bothwell et al. 2014). This is discussed further in DVS16.

- **Increased dust destruction** - We have investigated whether it is possible to explain the observed dust-to-gas properties of the HiGH galaxies by increasing the amount of dust destruction as opposed to reducing the dust production from SNe. We can model increased dust destruction in two ways. Firstly we can increase the amount of dust which is destroyed per SNe (by adjusting the value of $m_{\rm ISM}$ in Eq. 4.29) and secondly by adjusting the value of $f_{\rm c}$ (the fraction of the ISM in the cold phase). With a larger fraction of the ISM in the warm phase, the efficiency of the dust destruction in the galaxy will be increased. We find that changing dust destruction alone can not match the observed $M_{\rm d}/M_{\rm bary}$ and $M_{\rm d}/M_{\rm g}$ ratios, since an increased dust destruction does not reduce the dust produced at the high gas fractions ($f_{\rm g} > 0.8$). Even an extreme model with $m_{\rm ISM} = 2500\,{\rm M}_{\odot}$ and $f_{\rm c} = 0.01$ would still require significant SNe dust reduction to explain the observed dust-to-gas values. Therefore the conclusion of needing a reduced dust yield from SNe first put forward by Zhukovska (2014) is robust to changes in the values of f_{rmc} and $m_{\rm ISM}$.

6.6 Conclusion

In this chapter, we have brought together the HI-selected HiGH, dust-selected HAPLESS, stellar-mass-selected HRS and the metallicity-selected DGS sources to provide the largest sample of nearby galaxies covering a wide range of gas fraction ($0.05 < f_{\rm g} < 0.97$) and metallicity (over 2 dex). We derived their dust, stars, gas and metallicity properties in a consistent way. The low stellar mass HiGH-low galaxies share similar properties to many sources in the well-studied DGS sample (stellar mass, sub-solar metallicities, high gas fractions), including being dust poor relative to a linear $M_{\rm d}/M_{\rm g}$-metallicity relationship and having different dust-to-metal ratio compared to larger more evolved galaxies. In this work, we have introduced 377 sources from HiGH, HAPLESS and the HRS. We have increased the number of sources with less than $1/5\,{\rm Z}_{\odot}$ by 15 galaxies, and we have an additional 67 sources less than $1/3\,{\rm Z}_{\odot}$ compared to the 126 sources (including 37 DGS sources with $Z < 1/5\,{\rm Z}_{\odot}$) from Rémy-Ruyer et al. (2014). We have therefore increased the sample size in the critical range where sources lie off the typical published scaling relations, derived from benchmark studies of local galaxies with *Herschel* (eg the HRS), in terms of their dust-to-gas and dust-to-metal trends with metallicity.

Following Zhukovska (2014) and Feldmann (2015), we have investigated the dust trends of these samples using an updated version of the chemical evolution model of Rowlands et al. (2014) and Morgan et al. (2003). Additionally, we use gas fraction

as a proxy for the evolutionary state. This allows us to track and constrain the build up of dust and metals as gas is converted into stars, from very high ($f_g = 0.97$) to very low ($f_g = 0.05$) gas fractions. We find that:

- We show that due to the DGS sources being selected to have low metallicities, this consequently leads to a selection of very actively star forming galaxies. These sources require a bursty SFH as originally shown in Zhukovska (2014) and reproduced here. For a given gas fraction or stellar mass, we have found our low M_* HIGH and HAPLESS samples to be more normal in terms of star formation properties and metallicity. Our samples thus complement the DGS, and provide additional, new information on more normal star-forming galaxies in the nearby Universe. Delayed star formation history models are necessary to match the evolution of SFR/$M_{\rm bary}$ for our normal star-forming galaxies.

- To model the dust poor HIGH-low sources, we follow Zhukovska (2014) and Feldmann (2015) and relax the closed box assumption, reduce the contribution from supernova dust, and include dust grain growth in our model. We can model the dust-poor HIGH-low sources using either moderately reduced (factor of 6) supernova dust and moderate (timescale of $\sim$750 Myr) dust grain growth, or strongly reduced (factor of 25) supernova dust and fast (timescale of $\sim$200 Myr) dust grain growth. There are also relatively dust-rich high gas fraction sources, that either have a non-reduced supernova dust contribution, or reduced supernova dust and extremely fast (timescale of $\sim$5 Myr) grain growth (as in Feldmann 2015).

- In order to reproduce the observed metallicity particularly at low gas fractions (late evolutionary stages eg the HRS sources), metal-poor inflows and metal-rich outflows of gas at a rate of twice the SFR are required to keep the metallicity from rising to higher than observed metallicities. The DGS requires inflows and outflows at a rate of 6 times the SFR (Model VII).

- The M_d/M_g ratio correlates with the gas-phase metallicity over a wide range $7.5 < 12 + \log({\rm O/H})_{\rm PG16S} < 9.0$. However we find that low metallicity galaxies can have dust properties that (a) are consistent with a linear $M_d/M_g - Z$ relationship or (b) dust masses well below this trend. Zhukovska (2014) showed the scatter in this relation can be produced by using different bursty SFHs. However, bursty SFHs are inconsistent with our HIGH-low sample. Instead, we show differences in the strength of the contribution of supernova dust, as well as

differences in the dust growth time-scales and galactic winds (and thus critical metallicity) also produce the observed scatter.

- To produce a model which can explain the observed dust-to-gas ratio in the dust-poor HIGH-low and DGS galaxies with moderate grain growth, we require a maximum of $0.04\,M_\odot$ of dust per core collapse SNe which corresponds to a condensation efficiency of 0.90 per cent for a $25\,M_\odot$ progenitor (assuming a Chabrier IMF). This reduced SNe rate is robust to changing dust destruction rates $m_{\rm ISM}$ and the fraction of the ISM in a cold phase $f_{\rm c}$. This sample therefore supports growing evidence that significant grain growth in the ISM is required as a dust source and that the dust-to-metals ratio does vary with metallicity.

- The dust masses of galaxies at the low gas fraction regime can be explained without grain growth only if a typical $25\,M_\odot$ core-collapse SNe produces $0.17-1.0\,M_\odot$ of dust per explosion when there is *no dust destruction*. In contrast, for models with grain growth, grain growth would produce, by mass, 73-92 per cent of the total dust mass produced over the lifetime of these galaxies, in agreement with predictions for the Milky Way (Draine, 2009). For these models, the metallicity at which dust grain growth exceeds stellar dust sources in our model is reached between $7.96 < 12 + \log({\rm O/H}) < 8.63$ (or $0.8 > f_{\rm g} > 0.4$).

- We use our larger sample at low Z to further support the Feldmann (2015) result that the dust-to-metal ratio varies as a function of metallicity. The average dust to metal ratios for the HRS ($M_{\rm d}/M_{\rm Z} = 0.32, 0.46$ and 0.51 for the N2, KE08/T04, PG16S calibrators respectively) is consistent with the Milky Way value as expected given the number of evolved, low gas-fraction spirals in that sample. The DGS sample has $M_{\rm d}/M_{\rm Z} = 0.14$ and the HIGH-low sample (which contains sources with the highest gas fractions observed in the local universe) has $M_{\rm d}/M_{\rm Z} = 0.07, 0.09$ and 0.10.

Chapter 7
Conclusion and Future Work

GANDALF: *'End? No, the journey doesn't end here'*

J.R.R. Tolkien, The Lord of the Rings

7.1 Summary of the thesis

The *Herschel* Astrophysical Terahertz Large Area Survey (H-ATLAS, Eales et al. 2010) provides the largest blind survey of dust in the Universe. When combined with 21-band photometry spanning from the far-ultraviolet (FUV) to far-infrared (FIR) wavelengths, it enables us to study the physical properties of dusty galaxies in unprecedented detail. The dust-selected sample of Clark et al. (2015) and the HI-selected sample of galaxies from De Vis et al. (2016), both drawn from the H-ATLAS field, provide a complementary sample of galaxies at a range of evolutionary stages. By studying these sources, we wish to answer some of the biggest questions relating to dust in galaxies: 'what is the relative balance of dust sources to the dust-budget in a galaxy?', 'how do the dust properties relate to the star formation history?' and 'is the dust-to-metal ratio constant in all galaxies, and if not, what drives the change?'.

In this section, I provide a brief summary of the key findings and results that have been presented in the preceding chapters of this thesis. These are separated into the main subject areas which my research has been focused on.

7.1.1 LIMITATIONS OF SPECTRAL ENERGY DISTRIBUTION MODELLING USING MAGPHYS

In Chapter 2 we explored the spectral energy distribution modelling (SED) tool MAGPHYS (da Cunha et al., 2008) and used it to derive the physical properties of a dust selected sample (HAPLESS, Clark et al. 2015) and a HI selected sample of galaxies (HIGH, De Vis et al. 2016). Subsequently, we found that the cold dust temperature priors from MAGPHYS (15-25 K) were too narrow to successfully fit the coldest galaxies in our sample. Using an extended temperature range of 10-30 K significantly improved the fit obtained for these galaxies. We also showed that these restrictions on the cold dust temperature priors could lead to an underestimate of dust mass for the coldest galaxies in the sample; for example, the dust mass of HAPLESS 11 increased by a factor of 3.5 when the cold dust temperature output by MAGPHYS fell from 15 to 11 K. Additionally we demonstrated that MAGPHYS SED fits are poorly constrained if there was insufficient data in the mid-infrared region of the SED. We obtained IRAS 60 μm photometry for our sample to improve the overall fit and further constrain the SED in this region.

MAGPHYS provides a best-fit star formation history (SFH) for each galaxy. We investigated methods to increase the constraint that could be placed on the SFH obtained from SED modelling, beyond that of using the best-fit model alone. We found that we could create a median SFH for each galaxy by averaging only the 'top'-fitting models for that galaxy (as derived from their χ^2 values, to a probability level of 0.97). From this, we could also estimate the uncertainty in the value of the SFH obtained, by taking the 16^{th} and 84^{th} percentiles. However, we found that any bursts of star formation seen in the best-fit model are 'washed out' in the median SFH. This was because each burst of star formation in the individual SFH models is discreet, and there was not sufficient information in the SED to constrain a burst to a localised region of the SFH of that galaxy. Additionally, since MAGPHYS relies on the SFH to measure the star formation rate (SFR), the uncertainty in the location of the burst can cause a bimodal SFR probability distribution functions (PDF) for some galaxies. If a burst of star formation falls just within the last 10^8 years, then the measure of star formation over the last 10^8 years (the window used by MAGPHYS to average the current SFR across) will be significantly higher than if the burst falls just outside the last 10^8 years. We investigated a method that could be used to limit the impact of the random burst location (both on the stacked SFH and the estimate of SFR) by using a smoothing function, based on UV decay timescales, to make the bursts less localised. However, we found that it was very difficult to 'improve' upon the best-fit SFH for

each galaxy, and that there was no single smoothing function that could be used to obtain an improved SFR for these sources with bimodal SFRs (when compared to the star formation rate from Clark et al. 2015).

We also showed that the standard galaxy template libraries used with MAGPHYS do not contain enough models in specific regions of the parameter space to represent the youngest and most actively star forming galaxies in the HiGH and HAPLESS sample. We have noted that these galaxies are very common, and consist of $\sim$ third of the dust mass at $z = 0$ (Clark et al., 2015), yet MAGPHYS does not seem to fit their star formation properties well. For example, many of these galaxies were located on the extremities of the MAGPHYS parameter space, where the model template density is lower. For these and other such sources the best fit model provides the better estimate of the 'true' value of the physical property of the galaxy, since the median value often becomes biased towards regions of higher template density.

This work has highlighted the limitations of MAGPHYS and shown which galaxies the standard MAGPHYS model should be applied to. We have shown that it is very difficult to improve upon the best-fit SFH, and it is not possible to uniquely constrain the SFH for each galaxy from the broadband photometry. We recommend that, to improve the range of galaxies MAGPHYS can be used to model, an extended library should be created that extends down to $\log(t_{\rm burst}) < 8.5$ and $\log(\rm age_{\it r}) < 9.5$ with $-11 < \log(\rm ssfr_8) < -8$.

7.1.2 The Impact of the Star Formation History on the Physical Properties of Nearby Galaxies

While it does not seem possible to uniquely constrain the SFH of a galaxy from the MAGPHYS SED modelling, can we learn about the more general star formation properties of a population of galaxies (eg by splitting our sample into subsets)? How do these compare to star formation properties derived from alternative methods? In Chapter 3 we investigated the average star formation properties of the combined HiGH and HAPLESS sample. We chose to investigate the differences between groups of galaxies within the sample, since we have shown that it is difficult to uniquely constrain the SFH for an individual galaxy using from SED modelling, and focused our analysis on the best-fit values (since the median can be biased if the galaxy occupies a sparsely populated region of the parameter space).

Initially we split the sample by colour into BADGRS (FUV-$Ks < 3.5$, the blue, gas and dust-rich galaxies) and non-BADGRS, following Clark et al. (2015). We found that, as expected, significant differences could be identified between the star formation

properties of these sub-samples. The average best-fit SFHs showed the non-BADGRS had not experienced a burst of star formation within the last 4 Gyrs, while during the same time period the BADGRS had undergone several bursts. The BADGRS also appeared much younger with a 'light weighted mean age' of (1.89 ± 0.14) Gyr compared to the non-BADGRS (5.32 ± 0.21) Gyr.

We then split the HIGH and HAPLESS samples into dust-rich and dust-poor galaxies, based on their dust-to-gas and dust-to-stellar mass ratios. We found that there was some evidence that the dust-rich galaxies in the HIGH and HAPLESS sample seemed to have experienced bursts of star formation more recently, $t_{\rm burst} = (0.61 \pm 0.16)$ Gyr, than the dust-poor galaxies, $t_{\rm burst} = (1.37 \pm 0.22)$ Gyr. We then compared the star formation properties of HIGH and HAPLESS galaxies derived from SED modelling, to their optical spectra. We found good agreement between the two, with the BADGRS predominantly being identified as starburst galaxies. We also found that all of the galaxies in the dust-rich sub-sample were highly star-forming, while all the more passive quiescent star forming galaxies were in the dust-poor sub-sample.

This work has shown that while SED modelling does not currently present a potential method to constrain detailed individual SFHs for a large number of galaxies, it can be used to investigate general star formation properties of a sample of galaxies. It has also shown that the most dust-rich galaxies in the local universe tend to be the most actively star-forming galaxies.

7.1.3 The Chemical Evolution Model

Chemical evolution modelling can be used to determine how the build up of dust and metals in galaxies relates to their star formation history. In Chapters 4 and 5 we introduced the chemical evolution model of Morgan & Edmunds (2003), used more recently in Rowlands et al. (2014), which we used in the thesis to investigate the evolution of our sample. We updated many of the functions and libraries that are used in the code, to bring them up-to-date with current research in the various fields, and fixed mistakes that were in the previous versions of the code. Here we provide a summery of the key changes.

(i) We no longer interpolate between the stellar yields for stars of a given mass, but choose the nearest neighbour value (this has a small effect on the resulting stellar yields). (ii) We now directly input the dust mass yields of high mass stars from Todini & Ferrara (2001), which reduces the dust mass by a factor of ~ 1.8 for a Milky Way type galaxy at early times (< 0.8 Gyr) compared to the method in Rowlands et al. (2014). (iii) We have updated the remnant mass equation, and account for the fact

that high mass stars ($> 40\,M_\odot$) form a black hole at the end of their lives, and do not contribute metals or gas at this stage. (iv) We included an additional term to account for the cold gas fraction of the galaxy (f_c); grain growth occurs in the cold dense regions of the ISM, whereas dust destruction from SNe shocks will have higher efficiency in the warm diffuse ISM. (v) We have corrected errors in the Rowlands et al. (2014) version of the code which limited the metal contribution of high mass stars, and underestimated the dust grain growth timescale in the ISM.

The code, now written in Python, is freely available for download from GITHUB[1] as an open source package that can be used by the scientific community.

7.1.4 Chemical Evolution Modelling of a Large Sample of Herschel Galaxies

In Chapter 6 we took a combined sample of 425 sources from the *Herschel* surveys DGS, HiGH, HAPLESS and HRS. We re-derived the physical properties of these galaxies in a consistent, coherent manner such that their properties could be reliably compared. We then investigated the evolution of dust, stars and metals in these galaxies using our chemical evolution model.

In summary, we found a very small dust content for some of the high gas fraction, low metallicity sources in our sample. Instead of attributing this result to requiring a balance between metal-poor inflows and enriched outflows with extremely efficient interstellar grain growth (timescales of Myrs needed), as proposed in Feldmann (2015), we suggested a simpler solution following Zhukovska (2014). The dust properties and dust-to-metal ratios in the dust-poor low-Z sources are driven by reducing the stardust contribution by ~ 25 (particularly from core-collapse SNe as the reduced dust component has to act at very high gas fractions) with only moderate outflow, dust destruction and less extreme grain growth (timescales ranging from 1 Gyr - 200 Myrs similar to those quoted for the Milky Way and local galaxies; Draine 2009; Asano et al. 2013; Mattsson & Andersen 2012; Mattsson et al. 2014). We showed this model (our Model VI) is consistent with all of the observed properties of the HiGH-low sources, the first normal star forming population of low stellar mass galaxies studied in this way. Combined with a bursty SFH (as shown originally in Zhukovska 2014) and three times stronger outflows (Feldmann 2015, Model VII), this scenario is also consistent with the DGS galaxies that have similar f_g, M_* and Z. This model therefore adequately explains dust, star and gas properties in nearby galaxies over a wider range than shown before. By increasing the sample of low Z

[1] https://github.com/zemogle/chemevol

sources, we further support the Feldmann (2015) result that the dust-to-metal ratio is non-constant, and seems to vary with metallicity. We argue that this is caused by a reduced SNe dust condensation efficiency, and strong grain growth in these galaxies.

Our work has increased the number of sources at the low stellar mass ($< 10^{10}\,M_{\odot}$) and low metallicity regimes by a factor of ~ 2 using samples selected in different ways. More importantly, the combined sample here covers a wider range of gas fraction and therefore evolutionary state of nearby galaxies. This is particularly important given the relevance of immature, unevolved low metallicity sources as analogues for the first galaxies.

7.2 FUTURE WORK

As highlighted in Section 7.1, the research carried out in this thesis has contributed to our understanding of the evolution of dust and metals in the local universe. In this section we outline future projects and potential avenues for further study which will build upon this research:

1. We would like to take the Herschel-ATLAS SGP and NGP fields and define more dust-selected and HI-selected galaxies following the methods of Clark et al. (2015) and De Vis et al. (2016) respectively. By increasing the sample size of 'blue and dusty gas rich sources' (BADGRS), we could improve the statistics that would be obtained, which may lead to a greater understand of the differences between the star formation properties of the two populations.

2. We would like to collaborate with the authors of MAGPHYS (da Cunha et al., 2008) in order to create new model libraries for the BADGRS (young galaxies which have recently experienced bursts of star formation), which we have shown are currently poorly represented in the MAGPHYS libraries. This would increase the number of galaxies that could be studied using MAGPHYS and could lead to a greater understanding of the star forming properties of these galaxies.

3. We would like to take the dust models from Chapter 6 (produced with the chemical evolution model presented in this work) and predict a dust mass function (space density of galaxies of given dust mass) for $z = 0$. Comparing this against the observed dust mass function could lead to a greater understanding of dusty galaxies in the local universe.

4. Rowlands et al. (2014) take a sample of 26 Submillimetre Galaxies (SMGs) from the literature, located at redshift $z > 1$, and determine the relative contribution

of different sources to the dust budget at high redshift, using the chemical evolution model of Morgan & Edmunds (2003). They find it is difficult to reproduce the observed dust mass in the galaxies using their model, requiring higher supernovae metal yields or substantial grain growth in the ISM. The ALESS sample of 122 SMGs (Hodge et al., 2013) offers the opportunity to revisit and expand upon this work, benefiting from the higher resolution (with source deblending) and increased number of SMGs. Additionally, we could use a method similar to Rodríguez-Muñoz et al. (2015), Smith & Hayward (2015) and Schofield et. al., in prep. to estimate the uncertainty in the SFH derived from SED modelling. This uncertainty enables us to place a limits on the dust mass which we obtain from the chemical modelling of the galaxies.

Chapter 7
Bibliography

[1] Abazajian K. N. et al., 2009, ApJS, 182, 543

[2] Abraham K., Hornbogen E., 1974, Zeitschrift fur Metallkunde, 65, 702

[3] Ahn C. P. et al., 2012, ApJS, 203, 21

[4] Anathpindika S., 2013, 18, 6

[5] Annibali F. et al., 2013, AJ, 146, 144

[6] Asano R. S., Takeuchi T. T., Hirashita H., Inoue A. K., 2013, Earth, Planets, and Space, 65, 213

[7] Asplund M., García Pérez A. E., 2001, A&A, 372, 601

[8] Asplund M., Grevesse N., Sauval A. J., Scott P., 2009, ARA&A, 47, 481

[9] Bailin J., Harris W. E., 2009, ApJ, 695, 1082

[10] Baillard A. et al., 2011, A&A, 532, A74

[11] Baldwin J. A., Phillips M. M., Terlevich R., 1981, PASP, 93, 5

[12] Barai P., Monaco P., Murante G., Ragagnin A., Viel M., 2015, MNRAS, 447, 266

[13] Barlow M. J., Silk J., 1977, ApJ, 211, L83

[14] Barnard E. E., 1919, ApJ, 49

[15] Barnes D. G. et al., 2001, MNRAS, 322, 486

[16] Bastian N., Covey K. R., Meyer M. R., 2010, ARA&A, 48, 339

[17] Bell E. F., de Jong R. S., 2000, MNRAS, 312, 497

[18] Bendo G. J. et al., 2015, MNRAS, 448, 135

[19] Bendo G. J. et al., 2012a, MNRAS, 419, 1833

[20] Bendo G. J., Galliano F., Madden S. C., 2012b, MNRAS, 423, 197

[21] Bendo G. J. et al., 2010, A&A, 518, L65

[22] Blitz L., Shu F. H., 1980, ApJ, 238, 148

[23] Bocchio M., Jones A. P., Slavin J. D., 2014, A&A, 570, A32

[24] Boquien M. et al., 2011, AJ, 142, 111

[25] Boselli A. et al., 2012, A&A, 540, A54

[26] Boselli A., Cortese L., Boquien M., 2014, A&A, 564, A65

[27] Boselli A. et al., 2010, PASP, 122, 261

[28] Boselli A., Hughes T. M., Cortese L., Gavazzi G., Buat V., 2013, A&A, 550, A114

[29] Bothwell M. S. et al., 2014, MNRAS, 445, 2599

[30] Bourne N. et al., 2016, MNRAS, 462, 1714

[31] Boyer M. L. et al., 2012, ApJ, 748, 40

[32] Brown T. M., Ferguson H. C., Smith E., Kimble R. A., Sweigart A. V., Renzini A., Rich R. M., VandenBerg D. A., 2003, ApJ, 592, L17

[33] Bruzual G., Charlot S., 2003, MNRAS, 344, 1000

[34] Calzetti D., 2001, ApJ, 45, 601

[35] Calzetti D. et al., 2010, ApJ, 714, 1256

[36] Cappellari M. et al., 2012, Nature, 484, 485

[37] Casey C. M., 2012, MNRAS, 425, 3094

[38] Casey C. M., Narayanan D., Cooray A., 2014, Phys. Rep., 541, 45

[39] Cenarro A. J. et al., 2007, VizieR Online Data Catalog, 837

[40] Chabrier G., 2001, ApJ, 554, 1274

[41] Chabrier G., 2003, PASP, 115, 763

[42] Charlot S., Fall S. M., 2000, ApJ, 539, 718

[43] Chiaki G., Schneider R., Nozawa T., Yoshida N., Omukai K., Limongi M., Chieffi A., Bianchi S., 2013, in Protostars and Planets VI Posters

[44] Cid Fernandes R. et al., 2009, in Revista Mexicana de Astronomia y Astrofisica, vol. 27, Vol. 35, Revista Mexicana de Astronomia y Astrofisica Conference Series, pp. 127–132

[45] Ciesla L. et al., 2014, A&A, 565, A128

[46] Ciesla L. et al., 2012, A&A, 543, A161

[47] Clark C. J. R. et al., 2015, MNRAS, 452, 397

[48] Clark C. J. R., Schofield S. P., Gomez H. L., Davies J. I., 2016, MNRAS, 459, 1646

[49] Cluver M. E. et al., 2014, ApJ, 782, 90

[50] Cohen R. D., 1983, ApJ, 273, 489

[51] Conroy C., 2013, ARA&A, 51, 393

[52] Corbelli E. et al., 2012, A&A, 542, A32

[53] Cortese L. et al., 2012, A&A, 544, A101

[54] Cortese L. et al., 2014, MNRAS, 440, 942

[55] Couch W. J., Sharples R. M., 1987, MNRAS, 229, 423

[56] da Cunha E., Charlot S., Elbaz D., 2008, MNRAS, 388, 1595

[57] da Cunha E. et al., 2015, ApJ, 806, 110

[58] Dale D. A., Helou G., 2002, ApJ, 576, 159

[59] Davies J. I. et al., 2014, MNRAS, 438, 1922

[60] De Cia A., Ledoux C., Savaglio S., Schady P., Vreeswijk P. M., 2013, A&A, 560, A88

[61] De Vis P. et al., 2016, ArXiv e-prints

[62] Decarli R., Gavazzi G., Arosio I., Cortese L., Boselli A., Bonfanti C., Colpi M., 2007, MNRAS, 381, 136

[63] Dell'Agli F., Ventura P., Schneider R., Di Criscienzo M., García-Hernández D. A., Rossi C., Brocato E., 2015, MNRAS, 447, 2992

[64] Devereux N. A., Young J. S., 1990, ApJ, 359, 42

[65] Dobbs C., 2013, Astronomy and Geophysics, 54, 5.24

[66] Dole H. et al., 2006, A&A, 451, 417

[67] Dolphin A. E., 2000, MNRAS, 313, 281

[68] Draine B. T., 2003, ARA&A, 41, 241

[69] Draine B. T., 2009, in Astronomical Society of the Pacific Conference Series, Vol. 414, Cosmic Dust - Near and Far, Henning T., Grün E., Steinacker J., eds., p. 453

[70] Draine B. T. et al., 2014, ApJ, 780, 172

[71] Draine B. T. et al., 2007, ApJ, 663, 866

[72] Draine B. T., Lee H. M., 1984, ApJ, 285, 89

[73] Draine B. T., Li A., 2007, ApJ, 657, 810

[74] Dressler A., Gunn J. E., 1983, ApJ, 270, 7

[75] Dressler A., Smail I., Poggianti B. M., Butcher H., Couch W. J., Ellis R. S., Oemler, Jr. A., 1999, ApJS, 122, 51

[76] Driver S. P. et al., 2009, in IAU Symposium, Vol. 254, The Galaxy Disk in Cosmological Context, Andersen J., Nordströara, m B., Bland-Hawthorn J., eds., pp. 469–474

[77] Driver S. P. et al., 2011, MNRAS, 413, 971

[78] Dunne L., Eales S., Edmunds M., Ivison R., Alexander P., Clements D. L., 2000, MNRAS, 315, 115

[79] Dunne L., Eales S., Ivison R., Morgan H., Edmunds M., 2003, Nature, 424, 285

[80] Dunne L., Eales S. A., 2001, MNRAS, 327, 697

[81] Dunne L. et al., 2011, MNRAS, 417, 1510

[82] Dunne L. et al., 2009, MNRAS, 394, 1307

[83] Dwek E., 1987, ApJ, 322, 812

[84] Dwek E., 1998, ApJ, 501, 643

[85] Dwek E., Galliano F., Jones A. P., 2007, ApJ, 662, 927

[86] Dwek E., Scalo J. M., 1980, ApJ, 239, 193

[87] Dwek E. et al., 2011, ApJ, 738, 36

[88] Eales S. et al., 2010, PASP, 122, 499

[89] Edmunds M. G., 2001, MNRAS, 328, 223

[90] Edmunds M. G., Eales S. A., 1998, MNRAS, 299, L29

[91] Elbaz D. et al., 2011, A&A, 533, A119

[92] Eminian C., Kauffmann G., Charlot S., Wild V., Bruzual G., Rettura A., Loveday J., 2008, MNRAS, 384, 930

[93] Eskew M., Zaritsky D., Meidt S., 2012, AJ, 143, 139

[94] Fardal M. A., Babul A., Guhathakurta P., Gilbert K. M., Dodge C., 2008, ApJ, 682, L33

[95] Feldmann R., 2015, MNRAS, 449, 3274

[96] Ferreras I., Silk J., 2000, ApJ, 532, 193

[97] Finn R. A. et al., 2010, ApJ, 720, 87

[98] Fisher D. B. et al., 2014, Nature, 505, 186

[99] Foster J. B., Mandel K. S., Pineda J. E., Covey K. R., Arce H. G., Goodman A. A., 2013, MNRAS, 428, 1606

[100] Frayer D. T., Brown R. L., 1997, ApJS, 113, 221

[101] Fumagalli M., O'Meara J. M., Prochaska J. X., 2011, Science, 334, 1245

[102] Gail H.-P., 2009, in EAS Publications Series, Vol. 35, EAS Publications Series, Boulanger F., Joblin C., Jones A., Madden S., eds., pp. 173–194

[103] Gall C., Hjorth J., Andersen A. C., 2011, A&A Rev., 19, 43

[104] Gall E. E. E. et al., 2015, A&A, 582, A3

[105] Galliano F. et al., 2011, A&A, 536, A88

[106] Galliano F., Madden S. C., Jones A. P., Wilson C. D., Bernard J.-P., 2005, A&A, 434, 867

[107] Giovanelli R. et al., 2005, AJ, 130, 2598

[108] Gomez H., 2013, in Proceedings of The Life Cycle of Dust in the Universe: Observations, Theory, and Laboratory Experiments (LCDU2013). 18-22 November, 2013. Taipei, Taiwan. Editors: Anja Andersen, Maarten Baes, Haley Gomez, Ciska Kemper, Darach Watson. Online at http://pos.sissa.it/cgi-bin/reader/conf.cgi?confid=207 id.146, p. 146

[109] Gomez H. L. et al., 2012, ApJ, 760, 96

[110] González Delgado R. M. et al., 2014, A&A, 562, A47

[111] Griffin M. J. et al., 2010, A&A, 518, L3

[112] Groves B. et al., 2012, MNRAS, 426, 892

[113] Gunn J. E., Stryker L. L., 1983, ApJS, 52, 121

[114] Guo R., Hao C.-N., Xia X. Y., Mao S., Shi Y., 2016, ApJ, 826, 30

[115] Hao C.-N., Kennicutt R. C., Johnson B. D., Calzetti D., Dale D. A., Moustakas J., 2011, ApJ, 741, 124

[116] Hayward C. C., Narayanan D., Kereš D., Jonsson P., Hopkins P. F., Cox T. J., Hernquist L., 2013, MNRAS, 428, 2529

[117] Herrera-Camus R. et al., 2012, ApJ, 752, 112

[118] Herschel W., 1785, Philosophical Transactions of the Royal Society of London Series I, 75, 213

[119] Herter T. L. et al., 2012, ApJ, 749, L18

[120] Hildebrand R. H., 1983, QJRAS, 24, 267

[121] Hill T., Motte F., Bontemps S., Zavagno A., Schneider N., Hennemann M., di Francesco J., 2010, in SF2A-2010: Proceedings of the Annual meeting of the French Society of Astronomy and Astrophysics, Boissier S., Heydari-Malayeri M., Samadi R., Valls-Gabaud D., eds., p. 225

[122] Hirashita H., 2000, PASJ, 52, 585

[123] Hirashita H., Kuo T.-M., 2011, MNRAS, 416, 1340

[124] Hodge J. A. et al., 2013, ApJ, 768, 91

[125] Hopkins A. M. et al., 2013, MNRAS, 430, 2047

[126] Hopkins A. M. et al., 2003, ApJ, 599, 971

[127] Hughes T. M., Cortese L., Boselli A., Gavazzi G., Davies J. I., 2013, A&A, 550, A115

[128] Hunt L., Bianchi S., Maiolino R., 2005, A&A, 434, 849

[129] Hunter D. A. et al., 2012, AJ, 144, 134

[130] Ibar E. et al., 2010, MNRAS, 409, 38

[131] Iben, Jr. I., Tutukov A. V., 1984, ApJS, 54, 335

[132] Indebetouw R. et al., 2014, ApJ, 782, L2

[133] Inoue A. K., 2003, PASJ, 55, 901

[134] James A., Dunne L., Eales S., Edmunds M. G., 2002, MNRAS, 335, 753

[135] Jones A. P., 2004, in Astronomical Society of the Pacific Conference Series, Vol. 309, Astrophysics of Dust, Witt A. N., Clayton G. C., Draine B. T., eds., p. 347

[136] Jones A. P., Köhler M., Ysard N., Dartois E., Godard M., Gavilan L., 2016, A&A, 588, A43

[137] Jones A. P., Nuth J. A., 2011, A&A, 530, A44

[138] Juvela M., Montillaud J., Ysard N., Lunttila T., 2013, A&A, 556, A63

[139] Kamijo F., 1963, PASJ, 15, 440

[140] Kapteyn J. C., 1909, ApJ, 30, 284

[141] Karakas A. I., 2010, MNRAS, 403, 1413

[142] Kauffmann G. et al., 2003, Monthly Notices of the Royal Astronomical Society, 341, 33

[143] Kennicutt R. C. et al., 2011, PASP, 123, 1347

[144] Kennicutt, Jr. R. C., 1998, ApJ, 498, 541

[145] Kessler M., Steinz J., Anderegg M., Clavel J., Drechsel G., et al., 1996, Astron.Astrophys., 315, L27

[146] Kewley L. J., Dopita M. A., Sutherland R. S., Heisler C. A., Trevena J., 2001, ApJ, 556, 121

[147] Kewley L. J., Ellison S. L., 2008, ApJ, 681, 1183

[148] Knacke R. F., Gaustad J. E., Gillett F. C., Stein W. A., 1969, ApJ, 155, L189

[149] Könyves V. et al., 2010, A&A, 518, L106

[150] Kozasa T., Hasegawa H., 1987, Progress of Theoretical Physics, 77, 1402

[151] Krabbe A., 2000, in Society of Photo-Optical Instrumentation Engineers (SPIE) Conference Series, Vol. 4014, Airborne Telescope Systems, Melugin R. K., Röser H.-P., eds., pp. 276–281

[152] Kroupa P., Tout C. A., Gilmore G., 1993, MNRAS, 262, 545

[153] Krumholz M. R., 2011, in American Institute of Physics Conference Series, Vol. 1386, American Institute of Physics Conference Series, Telles E., Dupke R., Lazzaro D., eds., pp. 9–57

[154] Ladjal D., Justtanont K., Groenewegen M. A. T., Blommaert J. A. D. L., Waelkens C., Barlow M. J., 2010, A&A, 513, A53

[155] Lagache G., Puget J.-L., Dole H., 2005, Ann.Rev.Astron.Astrophys., 43, 727

[156] Lakićević M. et al., 2015, ApJ, 799, 50

[157] Lee J. C. et al., 2009, ApJ, 706, 599

[158] Lee S.-K. J., 2010, PhD thesis, The Johns Hopkins University

[159] Leroy A. K. et al., 2011, ApJ, 737, 12

[160] Leslie S. K., Kewley L. J., Sanders D. B., Lee N., 2016, MNRAS, 455, L82

[161] Lilly T., Fritze-v. Alvensleben U., 2005, ArXiv Astrophysics e-prints

[162] Lisenfeld U., Ferrara A., 1998, ApJ, 496, 145

[163] Liske J. et al., 2016, VizieR Online Data Catalog, 745

[164] Madau P., Dickinson M., 2014, ARA&A, 52, 415

[165] Madden S. C. et al., 2013, PASP, 125, 600

[166] Maeder A., 1992, A&A, 264, 105

[167] Mancini M., Schneider R., Graziani L., Valiante R., Dayal P., Maio U., Ciardi B., Hunt L. K., 2015, MNRAS, 451, L70

[168] Mannucci F., Cresci G., Maiolino R., Marconi A., Gnerucci A., 2010, MNRAS, 408, 2115

[169] Maraston C., 1998, MNRAS, 300, 872

[170] Maraston C., 2005, MNRAS, 362, 799

[171] Martins F., Schaerer D., Hillier D. J., 2005, in SF2A-2005: Semaine de l'Astrophysique Francaise, Casoli F., Contini T., Hameury J. M., Pagani L., eds., p. 351

[172] Mathis J. S., 1998, ApJ, 497, 824

[173] Mathis J. S., Rumpl W., Nordsieck K. H., 1977, ApJ, 217, 425

[174] Matsuura M. et al., 2009, MNRAS, 396, 918

[175] Matsuura M. et al., 2011, Science, 333, 1258

[176] Mattsson L., Andersen A. C., 2012, MNRAS, 423, 38

[177] Mattsson L. et al., 2014, MNRAS, 444, 797

[178] Matzner C. D., 2002, ApJ, 566, 302

[179] Micelotta E. R., Dwek E., Slavin J. D., 2016, A&A, 590, A65

[180] Michałowski M. J., 2015, A&A, 577, A80

[181] Michałowski M. J., Hayward C. C., Dunlop J. S., Bruce V. A., Cirasuolo M., Cullen F., Hernquist L., 2014, A&A, 571, A75

[182] Miller G. E., Scalo J. M., 1979, ApJS, 41, 513

[183] Miller L., Percival W. J., 1998, ArXiv Astrophysics e-prints

[184] Morales-Luis A. B., Pérez-Montero E., Sánchez Almeida J., Muñoz-Tuñón C., 2014, ApJ, 797, 81

[185] Morgan H. L., Dunne L., Eales S. A., Ivison R. J., Edmunds M. G., 2003, ApJ, 597, L33

[186] Morgan H. L., Edmunds M. G., 2003, MNRAS, 343, 427

[187] Morrissey P. et al., 2007, ApJS, 173, 682

[188] Murray N., Quataert E., Thompson T. A., 2010, ApJ, 709, 191

[189] Neugebauer G., Habing H., 1983, Nature, 305, 578

[190] Neugebauer G., Habing H., van Duinen R., Aumann H., Baud B., et al., 1984, Astrophys.J., 278, L1

[191] Nomoto K., Shigeyama T., Kumagai S., Yamaoka H., 1991, in Supernovae, Woosley S. E., ed., p. 176

[192] Nozawa T., Asano R. S., Hirashita H., Takeuchi T. T., 2015, MNRAS, 447, L16

[193] O'Connell R. W., Thuan T. X., Puschell J. J., 1986, ApJ, 303, L37

[194] Oh K., Sarzi M., Schawinski K., Yi S. K., 2011, ApJS, 195, 13

[195] Oort J. H., van de Hulst H. C., 1946, Bull. Astron. Inst. Netherlands, 10, 187

[196] Ossenkopf V., 1993, A&A, 280, 617

[197] Owen P. J., Barlow M. J., 2015, ApJ, 801, 141

[198] Papovich C., Dickinson M., Ferguson H. C., 2001, ApJ, 559, 620

[199] Pascale E. et al., 2008, ApJ, 681, 400

[200] Pascale E. et al., 2011, MNRAS, 415, 911

[201] Perets H. B., Biham O., 2006, MNRAS, 365, 801

[202] Pettini M., Pagel B. E. J., 2004, MNRAS, 348, L59

[203] Pilbratt G. L. et al., 2010, A&A, 518, L1

[204] Pilyugin L. S., Grebel E. K., 2016, MNRAS, 457, 3678

[205] Pilyugin L. S., Thuan T. X., 2005, ApJ, 631, 231

[206] Poglitsch A. et al., 2010, A&A, 518, L2

[207] Popescu C. C., Tuffs R. J., 2010, in American Institute of Physics Conference Series, Vol. 1240, American Institute of Physics Conference Series, Debattista V. P., Popescu C. C., eds., pp. 35–46

[208] Popping G., Somerville R. S., Trager S. C., 2014, MNRAS, 442, 2398

[209] Prantzos N., Aubert O., 1995, A&A, 302, 69

[210] Prieto Katunaric J. L., 2009, PhD thesis, The Ohio State University

[211] Reichardt C., Jimenez R., Heavens A. F., 2001, MNRAS, 327, 849

[212] Rémy-Ruyer A. et al., 2014, A&A, 563, A31

[213] Rémy-Ruyer A. et al., 2013, A&A, 557, A95

[214] Rémy-Ruyer A. et al., 2015, A&A, 582, A121

[215] Richard J., Kneib J.-P., Ebeling H., Stark D. P., Egami E., Fiedler A. K., 2011, MNRAS, 414, L31

[216] Rodríguez-Muñoz L., Gallego J., Pacifici C., Tresse L., Charlot S., Gil de Paz A., Barro G., Villar V., 2015, ApJ, 799, 36

[217] Rowlands K. et al., 2012, MNRAS, 419, 2545

[218] Rowlands K., Gomez H. L., Dunne L., Aragón-Salamanca A., Dye S., Maddox S., da Cunha E., van der Werf P., 2014, MNRAS, 441, 1040

[219] Saintonge A. et al., 2011, MNRAS, 415, 61

[220] Salpeter E. E., 1955, ApJ, 121, 161

[221] Sanders D. B., Mazzarella J. M., Kim D.-C., Surace J. A., Soifer B. T., 2003, AJ, 126, 1607

[222] Santini P. et al., 2010, A&A, 518, L154

[223] Saunders W. et al., 2004, in Proc. SPIE, Vol. 5492, Ground-based Instrumentation for Astronomy, Moorwood A. F. M., Iye M., eds., pp. 389–400

[224] Schaller G., Schaerer D., Meynet G., Maeder A., 1992, A&AS, 96, 269

[225] Schawinski K., Thomas D., Sarzi M., Maraston C., Kaviraj S., Joo S.-J., Yi S. K., Silk J., 2007, MNRAS, 382, 1415

[226] Seab C. G., Shull J. M., 1983, ApJ, 275, 652

[227] Sharp R. et al., 2006, in Proc. SPIE, Vol. 6269, Society of Photo-Optical Instrumentation Engineers (SPIE) Conference Series, p. 62690G

[228] Sheth K. et al., 2010, PASP, 122, 1397

[229] Shivaei I., Reddy N. A., Steidel C. C., Shapley A. E., 2015, ApJ, 804, 149

[230] Shull J. M., York D. G., Hobbs L. M., 1977, ApJ, 211, L139

[231] Silvia D. W., Smith B. D., Shull J. M., 2012, ApJ, 748, 12

[232] Skrutskie M. F. et al., 2006, AJ, 131, 1163

[233] Smith D. J. B. et al., 2012a, MNRAS, 427, 703

[234] Smith D. J. B. et al., 2011, MNRAS, 416, 857

[235] Smith D. J. B., Hayward C. C., 2015, MNRAS, 453, 1597

[236] Smith M. W. L. et al., 2012b, ApJ, 756, 40

[237] Smith M. W. L. et al., 2012c, ApJ, 748, 123

[238] Spitzer L., 1976, Comments on Astrophysics, 6, 177

[239] Stancliffe R. J., Jeffery C. S., 2007, MNRAS, 375, 1280

[240] Sutherland W., 2012, in Science from the Next Generation Imaging and Spectroscopic Surveys, p. 40

[241] Sweigart A. V., Greggio L., Renzini A., 1990, ApJ, 364, 527

[242] Tabatabaei F. S. et al., 2014, A&A, 561, A95

[243] Talbot, Jr. R. J., Arnett W. D., 1973, ApJ, 186, 69

[244] Taylor E. N. et al., 2011, MNRAS, 418, 1587

[245] Temim T., Dwek E., Tchernyshyov K., Boyer M. L., Meixner M., Gall C., Roman-Duval J., 2014, ArXiv e-prints

[246] Thompson R., Nagamine K., Jaacks J., Choi J.-H., 2014, ApJ, 780, 145

[247] Thornton K., Janka H.-T., Truran J. W., 1997, Nuclear Physics A, 621, 485

[248] Tielens A. G. G. M., McKee C. F., Seab C. G., Hollenbach D. J., 1994, ApJ, 431, 321

[249] Tinsley B. M., 1978, ApJ, 222, 14

[250] Tinsley B. M., 1980, Fund. Cosmic Phys., 5, 287

[251] Todini P., Ferrara A., 2001, MNRAS, 325, 726

[252] Trumpler R. J., 1930, PASP, 42, 214

[253] Valiante E. et al., 2016, MNRAS, 462, 3146

[254] van den Bergh S., 2000, in Bulletin of the American Astronomical Society, Vol. 32, American Astronomical Society Meeting Abstracts, p. 117.01

[255] van den Hoek L. B., Groenewegen M. A. T., 1997, A&AS, 123, 305

[256] Ventura P., D'Antona F., Di Criscienzo M., Carini R., D'Ercole A., vesperini E., 2012, ApJ, 761, L30

[257] Ventura P., Dell'Agli F., Schneider R., Di Criscienzo M., Rossi C., La Franca F., Gallerani S., Valiante R., 2014, MNRAS, 439, 977

[258] Viaene S. et al., 2016, ArXiv e-prints

[259] Viaene S. et al., 2015, A&A, 579, A103

[260] Vincenzo F., Belfiore F., Maiolino R., Matteucci F., Ventura P., 2016, MNRAS, 458, 3466

[261] Walcher C. J. et al., 2008, A&A, 491, 713

[262] Ward-Thompson D., Scott P. F., Hills R. E., Andre P., 1994, MNRAS, 268, 276

[263] Watson D., Christensen L., Knudsen K. K., Richard J., Gallazzi A., Michałowski M. J., 2015, Nature, 519, 327

[264] Watson F. T., Fletcher L., Marshall S., 2011, A&A, 533, A14

[265] Werner M. W. et al., 2004, ApJS, 154, 1

[266] Wesson P. S., 1974, Space Sci. Rev., 15, 469

[267] Whitaker K. E. et al., 2013, ApJ, 770, L39

[268] Whittet D. C. B., ed., 2003, Dust in the galactic environment

[269] Wild V., Kauffmann G., Heckman T., Charlot S., Lemson G., Brinchmann J., Reichard T., Pasquali A., 2007, MNRAS, 381, 543

[270] Wild V., Walcher C. J., Johansson P. H., Tresse L., Charlot S., Pollo A., Le Fèvre O., de Ravel L., 2009, MNRAS, 395, 144

[271] Wilkins S. M., Hopkins A. M., Trentham N., Tojeiro R., 2008, MNRAS, 391, 363

[272] Winnewisser G., 1990, Journal of Molecular Structure, 217, 363

[273] Woosley S. E., Weaver T. A., 1995, ApJS, 101, 181

[274] Worthey G., 1994, ApJS, 95, 107

[275] Wright E. L. et al., 2010, AJ, 140, 1868

[276] Yin J., Hou J. L., Prantzos N., Boissier S., Chang R. X., Shen S. Y., Zhang B., 2009, A&A, 505, 497

[277] York D. G. et al., 2000, AJ, 120, 1579

[278] Zafar T., Watson D., 2013, A&A, 560, A26

[279] Zhukovska S., 2014, A&A, 562, A76

[280] Zhukovska S., Gail H.-P., Trieloff M., 2008, A&A, 479, 453

[281] Zhukovska S., Henning T., 2013, A&A, 555, A99

[282] Zubko V., Dwek E., Arendt R. G., 2003, in Astrophysics of Dust